UNIVERSITAT POLITÈCNICA DE CATALUNYA

Programa de Doctorat:

AUTOMÀTICA, ROBÒTICA I VISIÓ

Tesi Doctoral

UAV PERCEPTION FOR SAFE FLIGHT UNDER PHYSICAL INTERACTION

Julian Fco. Cayero Becerra

Directors: Bernardo Morcego Seix
Josep Cugueró Escofet

Gener de 2018

*To my parents, my wife
and the little thing growing in her*

Abstract

The control of autonomous flying vehicles with navigation purposes is a challenging task. Complexity arises mainly due to the non-linearity and uncertainty inherently present in the flight mechanics and aircraft-air interactions. The potential of many existing flight applications and those that are to come motivates researchers to continuously contribute to this field. Recently, interest has grown for equipping unmanned vehicles with the capacity to interact with their environment, other vehicles or humans. This will enable interesting applications such as autonomous load carrying, aerial refueling or parcel delivering. Having measured the interaction wrenches ease the control problem which can be configured to reject disturbances or to take profit of them to fulfill mission objectives. Approaches present in literature in that direction use dedicated onboard force sensors or use expensive and non-versatile external positioning systems. However, ideal solutions may consider weight, versatility and even budget restrictions in the aircraft equipment.

This thesis will contribute to this area by providing perception solutions which use limited and low cost sensors that enable state and disturbance estimation for possible, but not restricted to, interaction scenarios.

This thesis contain three parts. The first part, introduces basic concepts related to the navigation state, aircraft dynamics, and sensor models. In addition, the platform under study is presented and mathematical models associated to it are calibrated.

The second part is devoted to the observability analysis and the design of state observers. Linear and non-linear observability analysis techniques are used along with models presented in previous chapters to unveil that the state of quadrotors equipped with GPS, magnetometers an IMU sensors cannot be uniquely identified in some specific flight configurations. Results of this section are relevant because the conflicting flight configurations contain hover, a flight maneuverer central in many unmanned aerial missions of Vertical Take-off and Landing vehicles (VToL). For many possible singular configurations, insightful descriptions and interpretations of the solution space known as indistinguishable region are provided. Findings are verified in simulation scenarios where it can be seen how a filter fails to recover the true state of an aircraft when imposing the hover flight condition. We discuss then the design of Extended Kalman Filters for state estimation that considers the available sensors. Issues that are typically not reported in the literature, such as when to update or propagate in the estimator algorithm or which coordinate frame (body or world) should be used to represent each state variable are discussed. This leads to

the formulation of four potentially equivalent but different discrete event-based filters for which precise algorithmic expressions are given. We provide initialization routines and compare the results of the four filters in simulation under known favourable conditions for observability. In order to diminish the effect of flying in the conflicting observability configurations, we provide an alternative filter based on the Schmidt Kalman Filter (SKF). The proposed filter shares the structure of the EKF, behaves better in the instants that the EKF fails and provides similar results in the remaining conditions.

The last part of the thesis deals with the estimation of external disturbances. Disturbance estimation results are based on the derivation of a linear model for the aircraft dynamics. This model is not an approximation but an exact form achieved after a proper choice of coordinates and reference frame. The preceding model is then augmented with a high order disturbance model to enable the estimation of fast varying disturbances. Two estimators following the line of already published external disturbance methods are reviewed and adapted to the new model. Also, two Kalman observers that exploit the linearity of the derived model are presented. A simulation comparison that considers ideal and realistic scenarios is provided demonstrating that the KF disturbance estimators outperform the other. In addition, this part presents a design methodology of generic quadratic bounded observers for linear systems with ellipsoidal bounded uncertainty. The derived observers maximize a user tunable compromise between the estimation convergence speed and the final volume containing the estimation error. This design procedure is then applied to the disturbance estimation problem in aerial vehicles. An observer for disturbances acting on a flying platform is derived considering the high order disturbance model above mentioned. Finally, an analysis of the estimation performance with respect to the design parameters is presented.

Resumen

Controlar la navegación de vehículos autónomos aéreos es un reto. La complejidad de la tarea proviene de las no linealidades y la incertidumbre inherente en la mecánica del vuelo y las interacciones aire-vehículo. El potencial que tienen muchas de las aplicaciones actuales, así como aquellas que están por venir motiva a los investigadores que continuamente contribuyen en este área. Recientemente, ha crecido el interés por dotar a las aeronaves autónomas con la capacidad de interaccionar con su entorno, otros vehículos o humanos. Esto respalda el uso de aeronaves autónomas para aplicaciones como el transporte de carga, el repostaje en vuelo e incluso el reparto de paquetería. En estos casos, conocer las fuerzas y momentos que provienen de la interacción es esencial para facilitar el control que puede ser configurado para rechazar perturbaciones o bien para aprovecharse de ellas si benefician a los objetivos de navegación. Los trabajos presentes en la literatura que lidian con este tipo de problemas suelen usar sensores de fuerza en posiciones muy concretas o bien usan sistemas de posicionamiento externos que son caros y poco versátiles. En cambio, una solución ideal del problema debería considerar, el peso, la versatilidad e incluso restricciones económicas en la elección del equipamiento de la aeronave. Esta tesis, contribuye en este área formulando soluciones de percepción que permiten la estimación del estado y perturbaciones externas en condiciones normales de vuelos así como casos de interacción para UAVs equipados con sensores limitados y de bajo coste.

La tesis se estructura en tres partes. La primera de ellas introduce los conceptos básicos relacionados con el estado de navegación, la dinámica de la aeronave y modelos de sensores. Además, se presenta la plataforma de estudio así como los modelos matemáticos asociados a ella y su calibración.

La segunda parte está destinada al análisis de observabilidad y el diseño de observadores de estado. Se utilizan técnicas de observabilidad lineal y no-lineal junto a los modelos presentados anteriormente para desvelar que el estado de aeronaves equipadas con sensores GPS, magnetómetros y unidades inerciales (IMU) no puede ser únicamente identificado en condiciones específicas de vuelo. Los resultados de esta sección son importantes porque dentro de las condiciones de vuelo conflictivas se encuentra el vuelo a punto fijo, una maniobra de vuelo central en muchas misiones de vehículos con capacidad de despegue y aterrizaje vertical (VToL). Se analizan muchas de estas condiciones críticas de vuelo y para ellas se derivan y describe el espacio de soluciones posible conocido como región indistinguible. Los resultados son verificados en simulación dónde se puede apreciar como un estimador de estado falla al intentar realizar su tarea cuando la aeronave está en vuelo a punto fijo. Seguidamente se presenta el diseño de filtros

extendidos de Kalman (EKF) que proveen estimaciones del estado con la información limitada que proveen los sensores disponibles. Se discuten conceptos que habitualmente no se presentan en la literatura como cuando actualizar o propagar en el algoritmo de estimación o que sistema de referencia (asociados al sistema cuerpo o al sistema mundo) se debe utilizar para representar adecuadamente las variables de estado. Esto lleva a la formulación algorítmica de cuatro filtros discretos basados en eventos, diferentes, pero en esencia equivalentes. Se derivan rutinas de inicialización para los filtros y se comparan los resultados en simulación bajo condiciones favorables de estimación. Con la idea de disminuir el efecto de volar en configuraciones de observabilidad conflictivas, se deriva un filtro alternativo basado en el filtro de Schmidt Kalman (SKF). El filtro propuesto comparte estructura con el EKF, tiene un mejor comportamiento allí dónde le EKF falla y una respuesta similar en el resto de condiciones de vuelo.

La última parte de la tesis trata con la estimación de perturbaciones externas. Los resultados de estimación que se presentan se producen en base a la derivación de un modelo lineal para la dinámica de la aeronave. Este modelo no supone una aproximación de la dinámica, sino un forma exacta obtenida a partir de una elección acertada del estado y el sistema de referencia en el que éste se expresa. Éste modelo se extiende con un modelo de alto orden para la perturbación que habilita la estimación de perturbaciones con rápidas dinámicas. Se estudia su aplicación a dos modelos para la estimación de perturbaciones ya presentes en la literatura. Además, se proponen dos nuevos filtros de Kalman que se aprovechan de la linealidad del modelo. Se presenta una comparativa basada en la simulación de escenarios ideales así como realistas que demuestra que los filtros KF superan al resto. Esta misma parte de la tesis presenta el diseño genérico de estimadores "quadratic bounded" (QB) para sistemas dinámicos lineales cuya incertidumbre se encuentra acotada dentro de elipsoides. Estos estimadores maximizan un compromiso, ajustable por el usuario que contempla la velocidad de convergencia así como el volumen de la solución final que contiene el error de estimación. Este proceso de diseño se aplica a la estimación de perturbaciones en vehículos aéreos. Se deriva un observador de perturbaciones para plataformas aéreas basado en el modelo de alto orden arriba mencionado. Finalmente, se presenta un análisis del desempeño de estimación en función de los parámetros de diseño del filtro.

Resum

Controlar la navegació de vehicles autònoms aeris és un repte. La complexitat de la tasca prové de les no linealitats i la incertesa inherent en la mecànica del vol i les interaccionis aire-vehicle. El potencial que tenen moltes de les aplicacions actuals, així com aquelles que estan per vindre motiva als investigadors que contínuament contribueixen en aquest àrea. Recentment, ha crescut l'interès per dotar a les aeronaus autònomes amb la capacitat d'interaccionar amb el seu entorn, altres vehicles o humans. Això recolza l'ús d'aeronaus autònomes per a aplicacions com el transport de càrrega, el proveïment de carburant en vol i fins i tot el repartiment de paqueteria. En aquests casos, conèixer les forces i moments que provenen de la interacció és essencial per a facilitar el control que pot ser configurat per a rebutjar pertorbacions o bé per a aprofitar-se d'elles si beneficien als objectius de navegació. Els treballs presents en la literatura que estudien aquest tipus de problemes solen usar sensors de força en posicions molt concretes o bé sistemes de posicionament externs que són cars i poc versàtils. En canvi, una solució ideal del problema deuria considerar, el pes, la versatilitat i fins i tot restriccions econòmiques en l'elecció de l'equipament de l'aeronau. Aquesta tesi, contribueix en aquest àrea formulant solucions de percepció que permeten l'estimació de l'estat i pertorbacions externes en condicions normals de vols així com a casos d'interacció per a UAVs equipats amb sensors limitats i de baix cost.

La tesi s'estructura en tres parts. La primera d'elles introdueix els conceptes bàsics relacionats amb l'estat de navegació, la dinàmica de l'aeronau i els models dels sensors. A més, es presenta la plataforma d'estudi així com el calibratge dels models matemàtics associats a ella. La segona part està destinada a l'anàlisi d'observabilitat i el disseny d'observadors d'estat. S'utilitzen tècniques de observabilitat lineal i no-lineal al costat dels models presentats anteriorment. D'aquest estudi es desprèn que l'estat d'aeronaus equipades amb sensors GPS, magnetòmetres i unitats iner-cials (IMU) no pot ser inequívocament identificat en condicions concretes de vol. Els resultats d'aquesta secció són importants perquè dins de les condicions de vol conflictives es troba el vol a punt fix, una maniobra de vol central en moltes missions de vehicles amb capacitat d'enlairament i aterratge vertical (VToL). S'analitzen moltes d'aquestes condicions critiques de vol i per a elles es deriva i descriu l'espai de solucions possible conegut com a regió indistingible. Els resultats són verificats en simulació on es pot apreciar com un estimador d'estat falla en intentar fer la seva tasca quan l'aeronau està en vol a punt fix. Seguidament es presenta el disseny de filtres estesos de Kalman (EKF) que proveeixen estimacions de l'estat amb la informació limitada que proveeixen els sensors disponibles. Es discuteixen conceptes que habitualment no es presen-ten en la literatura com quan actualitzar o propagar en l'algorisme d'estimació o que sistema de

referència (associats al sistema cos o al sistema món) s'ha d'utilitzar per a representar adequadament les variables d'estat. Això porta a la formulació algorítmica de quatre filtres discrets basats en esdeveniments, diferents, però en essència equivalents. Es deriven rutines de inicialització per als filtres i es comparen els resultats en simulació sota condicions favorables d'estimació. Amb la idea de disminuir l'efecte de volar en configuracions d'observabilitat conflictives, es deriva un filtre alternatiu basat en el filtre de Schmidt Kalman (SKF). El filtre proposat comparteix estructura amb el EKF, té un millor comportament allà on l'EKF falla i una resposta similar en la resta de condicions de vol.

L'última part de la tesi tracta amb l'estimació de pertorbacions externes. Els resultats d'estimació que es presenten es produeixen sobre la base de la derivació d'un model lineal per a la dinàmica de l'aeronau. Aquest model no suposa una aproximació de la dinàmica, sinó un forma exacta obtinguda a partir d'una elecció encertada de l'estat i el sistema de referència en el qual aquest s'expressa. Aquest model s'estén amb un model d'alt ordre per a la pertorbació que habilita l'estimació de pertorbacions amb ràpides dinàmiques. S'estudia la seva aplicació a dos models per a l'estimació de pertorbacions ja presents en la literatura. A més, es proposen dos nous filtres de Kalman que s'aprofiten de la linealitat del model. Es presenta una comparativa basada en la simulació d'escenaris ideals i realistes que demostra que els filtres KF superen a la resta. Aquesta mateixa part de la tesi presenta el disseny genèric d'estimadors "quadratic bounded" (QB) per a sistemes dinàmics lineals la incertesa dels quals es troba fitada dins d'el·lipsoides. Aquests estimadors maximitzen un compromís, ajustable per l'usuari que contempla la velocitat de convergència així com el volum de la solució final que conté l'error d'estimació. Aquest procés de disseny s'aplica a l'estimació de pertorbacions en vehicles aeris. Es deriva un observador de pertorbacions per a plataformes aèries basat en el model d'alt ordre a dalt esmentat. Finalment, es presenta una anàlisi dels resultats d'estimació en funció dels paràmetres de disseny del filtre.

Acknowledgement

I would like to thank my supervisors, Prof. Bernardo Morcego and Prof. Pep Cugueró, for their dedication, attention, corrections, advices and a never ending list that I learned from them. This thesis couldn't have been made without their contribution.

I would like to give special thanks to Marta, my wife. She has been the perfect listener to all of my problems and provided me with the proper words at the exact moments when I needed. Her support and advices encouraged me to learn from my errors and never give up.

I really appreciate the interest that my family always showed for the state of my thesis even not exactly knowing what a doctor is or what a doctor does. In particular, I want to thank my parents and sisters for always being proud of me and providing me with the best kind of support, love.

I want to thank all my friends out the university for their patience. They have provide me with useful insights of my world as seen from a distance. I want to thank Javi and Víctor for proof reading many articles and chapters of my thesis and still pretend being interested after that.

I want to express my gratitude to the people of the research group CS2AC, where I had the pleasure to develop the thesis, for creating such a great ambiance and high quality breakfast talks. In particular I want to thank Damiano, for his recommendations and his contribution to some works derived in this thesis; Tomeu for the shared interest in the topic and; Juli, for his honesty and his wise and useful advices that helped me to realise the correct choices in many situations.

Julián Cayero
Terrassa, January 23 2019

Contents

List of Figures

List of Tables

Chapter 1

Introduction

1.1 Motivation

In the era of 70's, Unmanned Aerial Vehicles (UAVs) were initially developed to perform military inspection tasks and to help in tactical attacks. They present the priceless advantage of eliminating completely the possibility to hurt the crew, allowing more aggressive and effective manoeuvres and saving costs in construction and maintenance.

Recently, UAVs have evolved to cover successfully some civilian tasks as exploration, fire inspection in natural areas, agricultural inspection, aerial photography, aerial video recording, terrain mapping and many other tasks related with the environment sensing [39]. USA UAVs, for instance, provided real time imagery and video after the earthquake in Haiti in 2010 and the earthquake that led to a tsunami in Japan in 2011[1].

The high degree of effectiveness in UAV applications [55, 54] and the potential that UAVs have to solve civilian and military missions that are to come, are the main reason for the growing of research related with control of flying vehicles.

Many studies have focused on enhancing the autonomy of unmanned vehicles and, as a consequence, tasks like autonomous guidance and trajectory tracking have been achieved successfully [43, 64]. Even more, some grasping tasks [71, 62], that evolve to autonomous construction tasks [48], art inspired demonstrations [10], and cooperative work between UAVs [74] have been proven successful on well structured environments.

Nowadays, the UAVs are not only able to observe but also to interact with the environment. Recently finished and ongoing European projects exist focused on control techniques that allow safe interaction between UAVs or between UAVs and the external world[2]. Both of them have been motivated by the UAVs potential as tools for damage assessment in critical areas after natural disasters or in hazardous environments, where walls and other physical barriers may exist.

---

[1]http://www.goo.gl/pd4853
[2]AIRobots: Collaborative project ICT-248669 ARCAS: Collaborative project ICT-287617

Even though many technology demonstrators are seen nowadays running impressive UAV control achievements, one aspect remains central for autonomous navigation in non-structured environments, the perception. Any UAV flight application that considers navigation or interaction in an autonomous way is subject to a proper knowledge of the actual UAV status and its surroundings. UAV perception relies primarily on sensors. System measurements allow to infer at least partially the UAV flight state. The requirement of autonomy is a must that forces sensors to be lightweight enough to bring them onboard, which is usually in conflict with required budget and accuracy constraints. To solve this problem, model based estimation techniques are usually used over measurement data to provide better estimates of measured variables and provide estimation of the remaining ones.

1.2 Problem description

Any rigid body can be seen as a dynamical system that transforms input forces into motion. The relation between force and velocity or position is well known and can be derived by basic physical principles.

The same rules apply over a flying vehicle, but in this case the forces are never perfectly known. Without any loss of generality these forces can be divided in three different categories: actuator forces, aerodynamic interaction forces and exogenous forces. The former represent the forces created by the on-board actuators in order to command the aircraft. They are produced by thrusters, propellers or aerodynamic surfaces and show nonlinear, time varying and state dependent behaviour. The second category refers to the external forces that appear due to the interaction of the aircraft with the air. Again this effect is usually nonlinear, time varying and highly dependent on the aircraft velocity state.

The definition of those forces along with the equations of motion represent the dynamics of motion for almost any aircraft in free flight, as depicted in Fig. 1.1
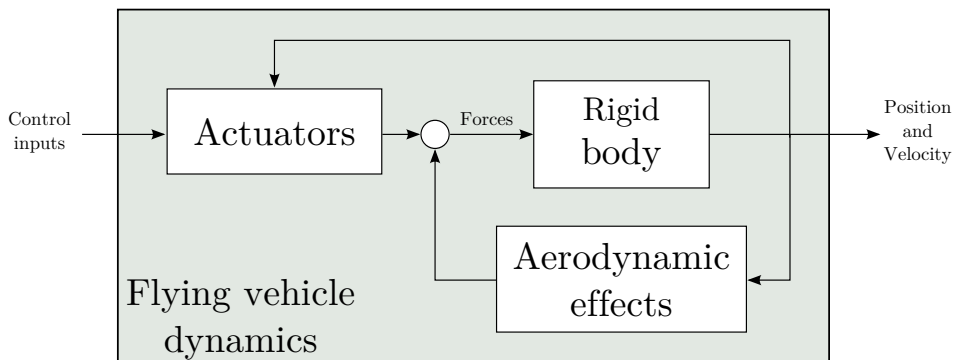
FIGURE 1.1: Aircraft dynamics scheme

State estimation of aerial vehicles in free flight is a challenging task, not only because of the non-linearities and uncertainty present in the system model due to uncertain aerodynamics and uncertain mass parameters but also because of sensors. The unavailability of on-board sensors

to measure specific system states, their accuracy vs. weight or cost ratio and their reliability difficult and even prevent the estimation task.

In the control framework, pose regulation and trajectory tracking for aircraft in free flight has been successfully achieved by many authors [43, 58, 61, 64, 63, 48, 81] either in simulation or by sensor setups dependent on external facilities such as external positioning systems.

The free flight condition is too restrictive in real applications because several sources of exogenous forces often appear. For example, when flying in unstructured environments, contacts can not be predicted or when physical interconnections with the environment or maybe other aircraft exist. In this case, the rigid body equations are fed by an extra term that represents the interaction forces. Note that under the name of exogenous forces, the forces that do not come from actuators nor aerodynamic modelled effects are collected. Taking into account the relation between external forces and the motion of the aircraft is clearly the way to cope with interaction but, at the same time, it provides the advantage to accommodate any other force disturbances.

Since the exogenous forces need not be small, their effects must not be ignored, as they could give raise to important deviations in the aircraft behaviour that may lead to catastrophic accidents. Bearing this in mind, identifying magnitude and direction of the external forces and taking them into account in the controller design could be useful to produce proper control laws that reduce undesired effects.

With the aim to ensure safe flights in presence of physical contacts, this thesis is developed in the framework of UAV perception and it deals with the problem of UAV state and disturbance estimation under interaction. The diagram in Fig. 1.2 shows the interaction and estimation scheme considered here.
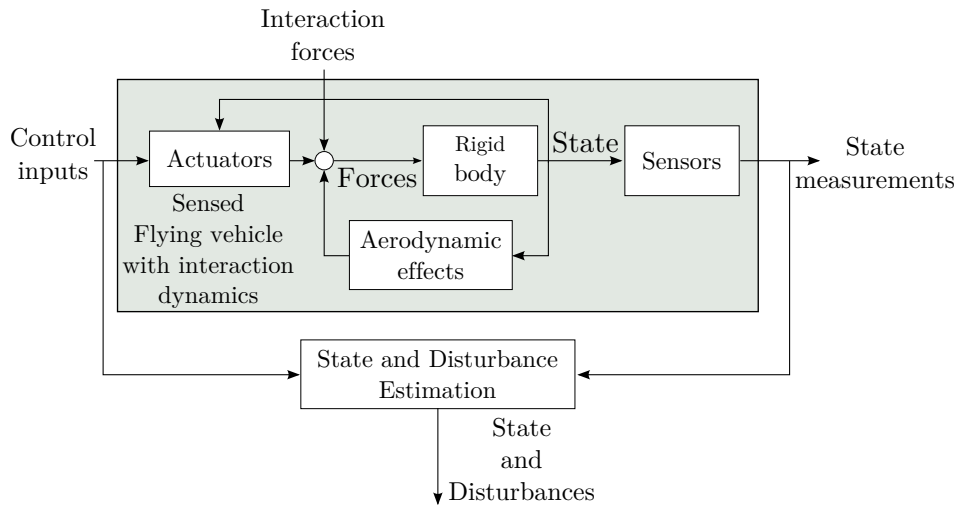
FIGURE 1.2: Aircraft interaction dynamics scheme

1.3   Thesis objectives

Making UAVs interact with their surroundings and provide them with the capacity of dynamically modifying the environment and interact with living entities, expands the current number of applications that can be successfully executed broadly. This topic, appears recently in the literature and represents the edge of today's research.

Most of the provided solutions that deal with interaction are formulated to solve particular tasks in particular scenarios. In addition, in most cases the fulfilment of the task is left to planners that assume a known environment and/or external positioning systems that provide a very accurate feedback to a controller. These facts clearly question the real autonomy achieved by these aircrafts and limits the application of the proposed solutions when applied over any other mission.

It is surprising that, given the high number of UAV related control applications in the literature, only few works deal with the state estimation using low-cost sensor suites and none, to the best of the author knowledge, deals with the most basic and standard sensor suite which incorporates accelerometers, gyroscopes, magnetometers and a GPS.

For those reasons, this thesis is focused on:

The study of estimation techniques that allow the estimation of the UAV state and disturbances appearing in possible interaction scenarios by using a limited and basic set of sensors comprised of a GPS, a three axial magnetometer, a three axial gyroscope and a three axis accelerometer.

The fulfilment of this global objective is achieved by the fulfilment of partial ones. They are:

- Reviewing system dynamics and ways to express the state of UAVs. Finding the most appropriate state description and understand the associated dynamics will be crucial to derive model based estimators.

- Obtaining and calibrating models for the sensors under consideration with the aim to produce reliable simulations and have consistent dynamics when deriving model based estimators.

- Studying the system's state observability for the considered set of sensors and understanding how the number of sensors and its quality or stability may impact, degrade or even prevent the determination of the UAV state.

- Deriving state estimators to infer the system flight configuration, having in mind the implementation efficiency and its practical use. This step may also consider different dynamics representations and study their effect in the final estimation.

- Deriving and implementing disturbance estimators that allow the prediction of external forces and torques acting over the aircraft and comparing the proposals with existing solutions.

1.4 Thesis Outline

This thesis is organised as follows:

- **Chapter 2: Describing the pose and the state of a solid object in the 3D space**

  This chapter analyses the potential parametrizations of the UAV navigation state. Particular emphasis is placed over the parametrization choice for the aircraft attitude. Rotation matrices, Euler angles and quaternions are explored, explained and relations between them are presented. Contents of this chapter will be used throughout the dissertation and their generality will be necessary to link existing and new results.

- **Chapter 3: Mathematical models of the quadrotor dynamics**

  In this chapter many possible ways of deriving the dynamics of the aircrafts are discussed. Even being a priori equivalent, everyone of them presents its benefits and drawbacks. The presented dynamics will serve as a basis for simulation, and will be used to derive state and disturbance estimators in the following chapters.

- **Chapter 4: Platform description**

  This chapter is devoted to the sensor models description and calibration. Particularities of GPS, magnetometer, accelerometer and gyroscope models are analyzed. Calibration of the models is also presented here from two different points of view. First, a conditioning phase is presented which allows to identify and correct three axial sensor misalignments and different per axis gains. Secondly, calibration phase consists in measuring the level of stochasticity present in the sensors measurements. In this chapter geometry and mass properties, hardware, software and principles of UAV actuation are also presented.

- **Chapter 5: Observability of quadrotor's states**

  Analysing the observability of the system is a key point that must be accomplished before the implementation of any state estimator. In this chapter we present the basics for observability and introduce related concepts as indistinguishability, symmetries, indistinguishable regions and singular inputs. Observability analysis is carried out over the non-linear system representing the system and measurement dynamics. A singular input analysis is also provided over a Linear Time Varying (LTV) system and over the Non-Linear (NL) dynamics.

- **Chapter 6: State Estimation**

  Few state estimation designs can be found in the literature considering the full navigation state and none of them have been found that deal with the specific sensor setup under analysis. To this end, this chapter considers model based state estimation through the use of the Extended Kalman Filter (EKF), whose basics are presented at the very beginning of the chapter. Attitude dynamics inherent in the UAV dynamics make the estimation procedure not straightforward given the singularities that minimal parametrizations suffer and the associated constraints that non-minimal representations have associated. The adaptation of the system dynamics and evaluation of filtering strategies to implement our

particular EKF are provided. Issues that are typically not reported in the literature, such as when to update or propagate in the estimator algorithm or which coordinate frame (body or world) should be used to represent each state variable are discussed. This leads to the formulation of four potentially different but equivalent discrete event-based filters for which precise algorithmic expressions are given. We provide initialisation routines and compare the results of the four filters in simulation under known favourable conditions for observability.

The second part of the chapter deals with the use of the presented estimators under low observability conditions. We present the SKF estimator as an alternative to the EKF used when some uncertain parameters want to be neglected in the estimation process. This formulation along with the observability results in Chap. (5) is used to derive an state estimator to fix the estimation results in conflicting observability conditions.

- **Chapter 7: External Disturbances Estimation in UAVs**

  State estimation provided in the previous chapter allows to having accelerometer and gyroscope bias estimations. This quantities, along with the state provided, enables the estimation of external disturbances comprising external wrenches, gravity offsets, actuator and any other unmodelled dynamics whose effect can be interpreted as an external force or torque. In this chapter we make use of the momentum dynamic equations (linear and spin) expressed in the world reference frame as a model of the system dynamics. This model is exploited to derive disturbance estimators based on available implementations but, adapted to our set of measurements. In addition, the linearity of the model is exploited by the consideration of two additional optimal Kalman Filter based disturbance estimators.The three derived observers are compared and their performance is evaluated under simple, challenging, ideal and noisy scenarios.

- **Chapter 8: Quadratic Bounded Observers. Application to UAVs External Disturbances Estimation**

  This chapter is dedicated to the design of Quadratic Bounded (QB) observers and its application to the estimation of external disturbances in UAVs. Firstly, we present a novel design methodology for state observers which guarantees quadratic boundedness of the estimation error. This is achieved by using Lyapunov analysis and convex optimization techniques. The solution of the design problem is optimal in the sense that a gain for the observer is produced that maximizes an user tunable compromise between the estimation convergence speed and the final volume containing the error of the estimation. The filter design contemplates the possibility of selecting the part of the state variables (instead of all the state) whose associated error is to be minimised. This fact is used in the second part of the chapter to derive a QB disturbance observer using the high order model derived in Chap. (7). A performance analysis with respect to the design parameters is presented and finally the effectiveness and main characteristics of the proposed approach are shown using simulation results.

- **Chapter 9: Concluding remarks**

  In this chapter we provide a summary of the thesis' contributions and outline future lines of research.

Part I

System Modelling and Calibration

Chapter 2

Describing the pose and the state of a solid object in the 3D space

The word pose is typically used in robotics and computer vision areas to refer to the concatenation of position and attitude. The position of an object in a 3-dimensional space is not hard to understand and we are used to deal with the problem of describing the position of objects daily. However, it is not the case when we want to describe the attitude of an object in the same 3-dimensional space. In the case that we are interested in the motion of the object further quantities like velocities, accelerations, angular velocities and angular accelerations appear.

This chapter is devoted, firstly, to the basic definition and presentation of the reference frames which enable a proper interpretation of the concepts of position and attitude. Secondly, the most used attitude representations are reviewed. For each of those, benefits and drawbacks are discussed. The relations between them as well as their dependence with the vehicle angular velocity are derived. Finally, a discussion on the chosen navigation state is provided.

2.1   Reference frames

A proper square coordinate system $\{\mathcal{A}\}$ can be represented by a point, called the origin and three orthogonal vectors $\boldsymbol{x}_a$ $\boldsymbol{y}_a$ $\boldsymbol{z}_a$ coming out from the origin for which $\boldsymbol{x}_a \times \boldsymbol{y}_a = \boldsymbol{z}_a$. Such square coordinate system is also known as a frame. By using frames, physical quantities as positions, orientations, velocities and accelerations of rigid bodies can be defined in a comprehensible way.

A division can be done to differentiate two kind of reference frames, inertial and non-inertial frames. Inertial frames are those that are not accelerated. This frames are fixed or translating with constant velocity. Non-inertial frames are accelerated frames, i.e. they have a linear acceleration, or are rotating.

This classification is important since the Euler equations of motion, that most of the people know, are only valid on its standard form when applied over inertial frames. Being strict, since our

planet is travelling through the space, the standard Newton laws are not applicable. However, accelerations perceived in many Earth-fixed reference frames are small enough to apply standard principles without making disproportionate errors.

In this work two basic reference frames are going to be used regularly and are detailed deeply in the next two sections.

2.1.1   Earth-Fixed reference frame

This is a reference frame with its origin on the Earth surface. Its x axis, named $\boldsymbol{x}_w$, is tangent to the Earth surface and points to the North Pole. The z axis, $\boldsymbol{z}_w$, is orthogonal to the Earth surface and it points inwards (to the center of the Earth) and the y axis, $\boldsymbol{y}_w$, given by $\boldsymbol{z}_w \times \boldsymbol{x}_w = \boldsymbol{y}_w$ points to the east, forming a right hand triad. It will be assumed, that this system is inertial even moving with the Earth. In the bibliography, this system is sometimes named NED system by the direction of its axes.
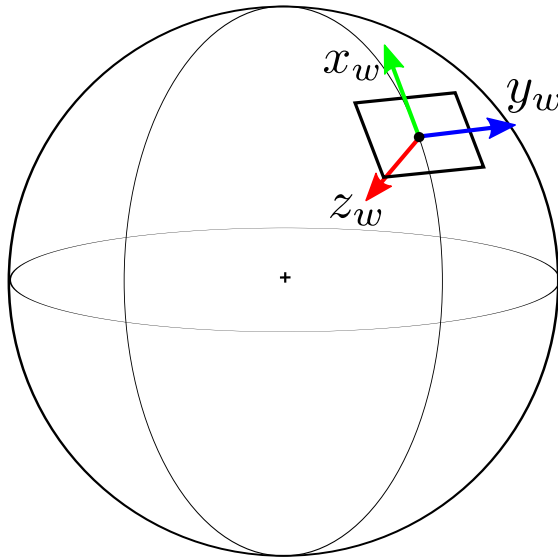
FIGURE 2.1: Representation of the Earth-fixed reference frame

A vector or a point expressed in the Earth frame will be denoted by $^{w}(\bullet)$.

2.1.2   Body fixed reference frame

The body fixed reference frame has its origin on the mass center of the quadrotor. Following the general convention in aeronautics its x axis, $\boldsymbol{x}_b$, points forward, the y axis, $\boldsymbol{y}_b$, points to the right and the z axis, $\boldsymbol{z}_b$ points downwards. The body fixed frame need to be a non-inertial reference frame since most of the time the quadrotor body will be rotating or accelerated.

A vector or a point expressed in the body frame will be denoted by $^{b}(\bullet)$.
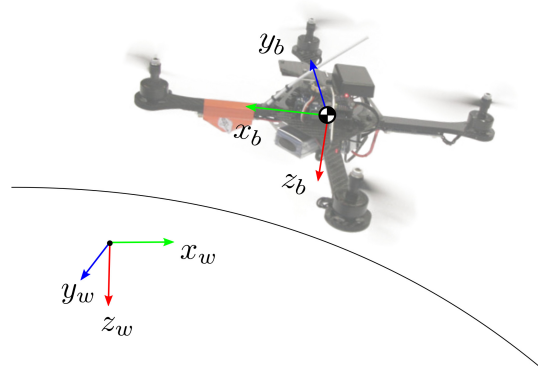
FIGURE 2.2: Representation of the body and Earth reference frames

2.2 Rigid transformation between reference frames

The definition of different reference frames is helpful to understand physical phenomena and to simplify the formulation of the problem. Moreover, they allow to define the position of the vehicle as the distance between the origin of the body frame and the origin of the Earth frame, and the orientation of the vehicle as the orientation of the body frame with respect to the Earth frame.

Since the use of several reference frames is justified, it is necessary to develop relations between them to convert vector and point quantities from one frame to the other.

Rotation matrices

Rotations are linear transformations that allow the orientation of a vector to be modified and thus the orientation of any given frame when applied to each one of its basis vectors. Rotations have special properties:

- Preserve the length of vectors. If a vector $\boldsymbol{v}$ is transformed by a rotation, the resulting vector $\boldsymbol{v}'$ has the same norm as $\boldsymbol{v}$.

$$|\boldsymbol{v}| = |\boldsymbol{v}'|$$

- Preserve angles. Given two vectors $\boldsymbol{v}_1$ and $\boldsymbol{v}_2$, and their respective images after applying rotations $\boldsymbol{v}'_1$ and $\boldsymbol{v}'_2$, the angle between the pair of vectors in the every frame remains the same.

$$\boldsymbol{v}_1^\top \boldsymbol{v}_2 = \boldsymbol{v}_1'^\top \boldsymbol{v}_2'$$

- Preserve volume. Given three vectors $\boldsymbol{v}_1$, $\boldsymbol{v}_2$ and $\boldsymbol{v}_3$ and their respective images after applying rotations $\boldsymbol{v}'_1$, $\boldsymbol{v}'_2$ and $\boldsymbol{v}'_3$,

$$\boldsymbol{v}_1^\top \left(\boldsymbol{v}_2 \times \boldsymbol{v}_3 \right) = \boldsymbol{v}_1'^\top \left(\boldsymbol{v}_2' \times \boldsymbol{v}_3' \right)$$
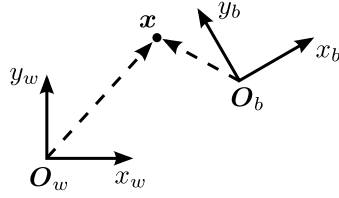
FIGURE 2.3: Point transformation between reference frames

The group of matrices that perform those transformations conforms the special orthogonal group $SO(3)$. The special orthogonal group is a 3-dimensional manifold embedded in a 9-dimensional space. An square $3{\times}3$ matrix $\mathbf{L}$ is said to describe a rotation in $SO(3)$ if its columns, respectively, rows, are orthonormal, i.e.,

$$\mathbf{L} \in SO(3) \iff \det \mathbf{L} = 1 \quad \text{and} \quad \mathbf{L}^{-1} = \mathbf{L}^{\top} \tag{2.1}$$

The purpose of rotation matrices is to transform some vector quantities from an initial frame to a target frame. Regarding the world and the body frames, here we are going to fix the convention that the matrix $\mathbf{L}$ is such that transforms coordinates in body frame to coordinates in Earth frame

$$^{w}\boldsymbol{v} = \mathbf{L}\,^{b}\boldsymbol{v}. \tag{2.2}$$

In an analogue way the inverse transformation from Earth to body frame is carried out by

$$^{b}\boldsymbol{v} = \mathbf{L}^{\top}\,^{w}\boldsymbol{v}. \tag{2.3}$$

The transformations in Eq. (2.2) and Eq. (2.3) allow to transform vector coordinates between different frames. Vectors are quantities without a fixed origin. In the case of transforming points, the origins of both reference frames come into play. If $^{w}\boldsymbol{x}$ represents a point in the Earth frame and, $\boldsymbol{O}_w$ and $\boldsymbol{O}_b$ represent the origin of world and body reference frames respectively, then

$$^{w}\boldsymbol{x} = \left(^{w}\boldsymbol{O}_b - {}^{w}\boldsymbol{O}_w\right) + \mathbf{L}\,^{b}\boldsymbol{x}, \tag{2.4}$$

and vice-versa

$$^{b}\boldsymbol{x} = \left(^{b}\boldsymbol{O}_w - {}^{b}\boldsymbol{O}_b\right) + \mathbf{L}^{\top}\,^{w}\boldsymbol{x}. \tag{2.5}$$

2.3 Representing the attitude

It has been illustrated that the definition of reference frames allows a natural introduction of the attitude definition by means of proper rotation matrices. The orthogonality and determinant constraints imposed over 3×3 generic matrices to produce valid rotations reduces the number of degrees of freedom from nine (one for each matrix entry) to three. This fact has motivated the study of different attitude parametrizations.

The so-called minimal attitude representations define rotations using only three parameters. The Euler's angles, the modified Rodrigues parameters (MRPs), the Gibb's vector or the rotation vector are examples of very common minimal representations. None of these 3D parametrizations are free of singularities (see [82]), being specially unsuitable for tracking the attitude dynamics of highly manoeuvrable flying vehicles. By adding an additional parameter, the unit-quaternions are a singularity-free attitude parametrization that maintain a trade-off between memory usage, usability and efficiency. The increase of efficiency by using unit-quaternions against other lower dimensional parametrizations comes from the fact that in lower dimensional attitude parametrizations, the transformation of vectors is only possible by mapping first the attitude parametrization to a rotation matrix. This mapping is also required for concatenating consecutive rotations (by multiplying the rotation matrices), and its inverse mapping is needed to finally retrieve the three dimensional attitude from the composite rotation matrix. Quaternions, on the other hand, are self-contained. By using quaternion algebra vectors can be directly transformed and composition can be effectively carried out. Although a one-to-one mapping is demonstrated to only exist for 5D orientation parametrizations, the two-to-one mapping that exists between unit-quaternions and the $SO(3)$ does not present any practical disadvantage.

In this section the rotation matrices, Euler angles, quaternions and briefly the rotation vector are introduced as different parametrizations of the attitude. For each of those we discuss benefits and drawbacks and establish the relations between them. In addition, it is shown how every parametrization relates with the angular velocity and how different attitudes can be concatenated to express a composite attitude.

2.3.1 The direct cosine (DCM) rotation matrix

Rotation transformations can be formulated in different ways. The most intuitive one relates the basis vectors of one reference frame with their respective images expressed as a function of the basis vectors of a second reference frame.

To formulate the transformation that converts body frame coordinates to the world frame equivalents, consider first the projection of the x_b axis over the world reference frame

$$^{w}\boldsymbol{x}_b = (\boldsymbol{x}_b^{\top}\boldsymbol{x}_w)^{w}\boldsymbol{x}_w + (\boldsymbol{x}_b^{\top}\boldsymbol{y}_w)^{w}\boldsymbol{y}_w + (\boldsymbol{x}_b^{\top}\boldsymbol{z}_w)^{w}\boldsymbol{z}_w,$$

where the pre-superscript defining the basis of the vectors involved in the scalar product has been intentionally omitted to highlight that the inner product does not depend on the basis chosen.

By repetition over the other body axes, it can be seen that a vector expressed in the body frame $^{b}\boldsymbol{v} = v_1{}^{b}\boldsymbol{x}_b + v_2{}^{b}\boldsymbol{y}_b + v_3{}^{b}\boldsymbol{z}_b$ can be converted to the world frame by

$$^{w}\boldsymbol{v} = \mathbf{L}\,^{b}\boldsymbol{v} \tag{2.6}$$

being

$$\mathbf{L} = \begin{pmatrix} \boldsymbol{x}_b^\top \boldsymbol{x}_w & \boldsymbol{y}_b^\top \boldsymbol{x}_w & \boldsymbol{z}_b^\top \boldsymbol{x}_w \\ \boldsymbol{x}_b^\top \boldsymbol{y}_w & \boldsymbol{y}_b^\top \boldsymbol{y}_w & \boldsymbol{z}_b^\top \boldsymbol{y}_w \\ \boldsymbol{x}_b^\top \boldsymbol{z}_w & \boldsymbol{y}_b^\top \boldsymbol{z}_w & \boldsymbol{z}_b^\top \boldsymbol{z}_w \end{pmatrix} \tag{2.7}$$

Since the dot products in Eq. (2.7) represent the cosine of the angle between a pair of vectors, every entry of the matrix can be calculated from the angle between the unit vectors of the references frames, which is why this matrix is usually called direct cosine matrix (DCM).

Note that if the inverse transformation was desired, that is, transform a vector from the Earth-fixed frame to the body frame, the elements of every entry of the matrix would be exchanged implying that

$$\mathbf{L}^{-1} = \mathbf{L}^\top. \tag{2.8}$$

Kinematic effects over the DCM

When the body frame is rotating with respect to the world frame, the rotation matrix changes in time. The time evolution of the rotation matrix is related kinematically with $\boldsymbol{\omega}$, the angular velocity of the body frame. Note that $\boldsymbol{\omega}$ can be expressed in the inertial frame ${}^w\boldsymbol{\omega}$ or in the body frame ${}^b\boldsymbol{\omega}$. The coordinates in the world and the body frames of a point $\boldsymbol{P}$ rigidly attached to the rotating frame can be related by the transformation matrix $\mathbf{L}$ as in Eq. (2.2).
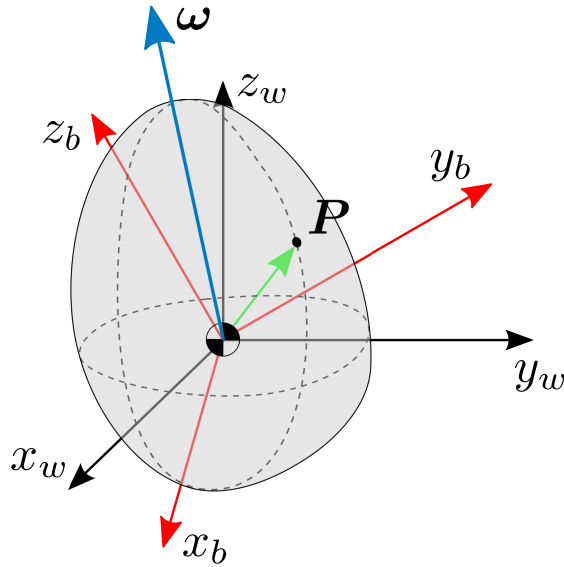
FIGURE 2.4: Rotation effects over a point that is rotating rigidly attached to the body frame

We are interested in determining changes in the transformation matrix due to the rotations of the moving frame. Taking the derivative of Eq. (2.2) having substituted the generic vector $\boldsymbol{v}$ by the point position $\boldsymbol{P}$,

$$^w\dot{\boldsymbol{P}} = \dot{\mathbf{L}}\,^b\boldsymbol{P} + \mathbf{L}\,^b\dot{\boldsymbol{P}} \tag{2.9}$$

Since $\boldsymbol{P}$ is rigidly attached to the rotating frame $^{b}\dot{\boldsymbol{P}} = \boldsymbol{0}$ and then

$$^{w}\dot{\boldsymbol{P}} = \dot{\mathbf{L}}\,^{b}\boldsymbol{P} \tag{2.10}$$

Equivalently, we can find an expression for $^{w}\dot{\boldsymbol{P}}$ by using the kinematic relation

$$^{w}\dot{\boldsymbol{P}} = {}^{w}\boldsymbol{\omega} \times {}^{w}\boldsymbol{P} = \left[{}^{w}\boldsymbol{\omega}\right]_{\times} {}^{w}\boldsymbol{P} \tag{2.11}$$

being $\left[{}^{w}\boldsymbol{\omega}\right]_{\times}$ the skew symmetric matrix associated with the vector $^{w}\boldsymbol{\omega}$ (see Ap. A).

Equating Eq. (2.11) and Eq. (2.10) leads to

$$\dot{\mathbf{L}}\,^{b}\boldsymbol{P} = \left[{}^{w}\boldsymbol{\omega}\right]_{\times} {}^{w}\boldsymbol{P} \tag{2.12}$$

and using Eq. (2.2)

$$\dot{\mathbf{L}} = \left[{}^{w}\boldsymbol{\omega}\right]_{\times} \mathbf{L} \tag{2.13}$$

Eq. (2.13) relates the time derivative of the rotation matrix with $^{w}\boldsymbol{\omega}$. However, when dealing with the attitude of an autonomous aircraft, the angular velocity measures are always available from an on-board set of gyroscopes that measure $^{b}\boldsymbol{\omega}$. To achieve this relationship, we can take advantage of the invariability of the cross product under rotation $(\mathbf{L}\boldsymbol{a}) \times (\mathbf{L}\boldsymbol{b}) = \mathbf{L}\,(\boldsymbol{a} \times \boldsymbol{b})$. Left-multiplying Eq. (2.12) by $\mathbf{L}^{\top}$

$$\dot{\mathbf{L}} = \mathbf{L}\left[{}^{b}\boldsymbol{\omega}\right]_{\times} \tag{2.14}$$

Composition of rotations using DCMs

Theorem 2.3.1 (Euler's Rotation). *Any displacement of a rigid body such that a point on the rigid body remains fixed, is equivalent to a single rotation about some axis that runs through the fixed point.*

The Euler's theorem on rotations simplifies the fact that any orientation of a 3-dimensional rigid body can be seen as the result of a single rotation from a reference orientation (e.g. the inertial frame orientation) instead of being the result of several consecutive rotations. As a consequence the rotation composition can be expressed as a new rotation matrix belonging again to $SO(3)$.

Let $\mathbf{L}_1$ represent a rotation from an initial reference frame to an intermediate one. Let $\mathbf{L}_2$ represent the rotation of the intermediate frame to achieve the orientation of a third one. The matrix that allows to transform directly from the first frame to the third frame is

$$\mathbf{L}_3 = \mathbf{L}_2\mathbf{L}_1 \tag{2.15}$$

Pros and cons of using the DCM to express the attitude

The DCM represents the rotation between a pair of frames and in an equivalent way it encodes the attitude of a second frame with respect to the first one. Therefore, the DCM can be used to represent the attitude of an aircraft. However, it presents some drawbacks

- It is not straightforward to interpret the attitude of the aircraft inspecting the entries of the rotation matrix.

- The differential equation proposed in Eq. (2.13) or Eq. (2.14), does not ensure that, after numerical integration, $\mathbf{L}$ preserves the properties described in Section 2.2. In this way some efforts can be made to renormalize the integrated matrix, but may involve intensive computations.

- The dimension of the $SO(3)$ manifold is three, implying that the minimal attitude representation for a 3D body is given by three parameters, far away from the nine used by the DCM.

There are alternative ways to represent the attitude of rigid bodies that try to cope with the inconveniences presented. In the case of spacecraft, the most used representations are the Euler angles and the quaternions, both based on the Euler's rotation theorem.

2.3.2   Euler Angles

The Euler angles exploit the idea of the principal Euler axis to encode the attitude in three parameters. The basic idea is to decompose the rotation in three consecutive simpler rotations about known axes represented by the basis' unit vectors.

Depending on the selected axis involved and its order, this process leads up to 12 different and valid ways for parametrizing the rotation i.e.

$$
\begin{array}{cccc}
x - y - z & x - z - y & x - y - x & x - z - x \\
y - x - z & y - z - x & y - x - y & y - z - y \\
z - y - x & z - x - y & z - x - z & z - y - z
\end{array}
$$

The standard parametrization in aeronautics known as Tait-Bryan angles $z - y - x$, is presented here.

Consider the Earth reference frame described on Section 2.1.1 and a rotation about the $\boldsymbol{z}_w$ axis a ψ quantity to create an intermediate reference frame with axis $\boldsymbol{x}_1$, $\boldsymbol{y}_1$ and $\boldsymbol{z}_1 = \boldsymbol{z}_w$. After this rotation consider a second rotation around the $\boldsymbol{y}_1$ axis of a quantity θ to create a second intermediate frame with axis $\boldsymbol{x}_2$, $\boldsymbol{y}_2 = \boldsymbol{y}_1$ and $\boldsymbol{z}_2$. Finally, consider the rotation of ϕ around $\boldsymbol{x}_2$ that leads to the desired body reference frame, $\boldsymbol{x}_b = \boldsymbol{x}_2$, $\boldsymbol{y}_b$ and $\boldsymbol{z}_b$. A scheme of the successive rotations that transforms the Earth frame into the body frame is shown in Fig. 2.5.

This convention is so accepted worldwide, that the three rotated angles ϕ, θ and ψ receive the name of roll, pitch and yaw respectively. For the sake of simplicity they are collected in vector form as $\boldsymbol{\eta} = (\phi,\,\theta,\,\psi)^{\top}$.
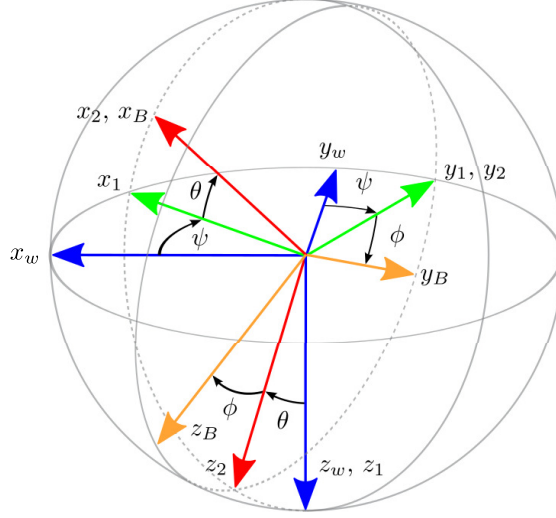
FIGURE 2.5: Euler angles relating the Earth reference frame and the body frame.

A vector in the body frame relates then with its representation in the world frame by the concatenation of consecutive simple rotations

$$^{w}\boldsymbol{v} = \underbrace{\mathbf{R}(\psi)\mathbf{R}(\theta)\mathbf{R}(\phi)}_{\mathbf{L}(\boldsymbol{\eta})}\,^{b}\boldsymbol{v}$$

being

$$\mathbf{R}(\psi) = \begin{pmatrix} \cos(\psi) & -\sin(\psi) & 0 \\ \sin(\psi) & \cos(\psi) & 0 \\ 0 & 0 & 1 \end{pmatrix}$$

$$\mathbf{R}(\theta) = \begin{pmatrix} \cos(\theta) & 0 & \sin(\theta) \\ 0 & 1 & 0 \\ -\sin(\theta) & 1 & \cos(\theta) \end{pmatrix}$$

$$\mathbf{R}(\phi) = \begin{pmatrix} 1 & 0 & 0 \\ 0 & \cos(\phi) & -\sin(\phi) \\ 0 & \sin(\phi) & \cos(\phi) \end{pmatrix}$$

the individual rotation matrices that implement simple rotations about $\boldsymbol{z}_{w}$, $\boldsymbol{y}_{1}$ and $\boldsymbol{x}_{b}$ respectively. The DCM to perform the transformations can be formulated as a function of the Euler

angles as

$$\mathbf{L}(\boldsymbol{\eta}) = \begin{pmatrix} \cos(\theta)\cos(\psi) & \sin(\phi)\sin(\theta)\cos(\psi) - \cos(\phi)\sin(\psi) & \cos(\phi)\sin(\theta)\cos(\psi) + \sin(\phi)\sin(\psi) \\ \cos(\theta)\sin(\psi) & \sin(\phi)\sin(\theta)\sin(\psi) + \cos(\phi)\cos(\psi) & \cos(\phi)\sin(\theta)\sin(\psi) - \sin(\phi)\cos(\psi) \\ -\sin(\theta) & \sin(\phi)\cos(\theta) & \cos(\phi)\cos(\theta) \end{pmatrix}$$

$$(2.16)$$

Kinematic effects over the Euler angles

Now that it has been shown how to represent the attitude by using Euler angles, it is interesting to find the relation that allows us to predict its derivative, as we did for the derivative of the DCM $\dot{\mathbf{L}}$. In this case, taking into account the individual Euler angles derivative magnitudes around their respective axis expressed on body frame, the next expression can be derived

$$\boldsymbol{\omega} = \dot{\phi}\boldsymbol{x}_b + \dot{\theta}\boldsymbol{y}_1 + \dot{\psi}\boldsymbol{z}_h, \qquad (2.17)$$

that converted to matrix form becomes

$$\boldsymbol{\omega} = \begin{pmatrix} 1 & 0 & -\sin(\theta) \\ 0 & \cos(\phi) & \sin(\phi)\cos(\theta) \\ 0 & -\sin(\phi) & \cos(\phi)\cos(\theta) \end{pmatrix} \dot{\boldsymbol{\eta}}. \qquad (2.18)$$

And the inverse transformation is given by inverting the system,

$$\dot{\boldsymbol{\eta}} = \begin{pmatrix} 1 & \sin(\phi)\tan(\theta) & \cos(\phi)\tan(\theta) \\ 0 & \cos(\phi) & -\sin(\phi) \\ 0 & \sin(\phi)/\cos(\theta) & \cos(\phi)/\cos(\theta) \end{pmatrix} \boldsymbol{\omega} \qquad (2.19)$$

Two important details must be mentioned. First, the transformations between $\dot{\boldsymbol{\eta}}$ and $\boldsymbol{\omega}$ do not depend on the yaw angle. Secondly, a singularity, known as gimbal lock, is produced at $\theta = \frac{(2n+1)\pi}{2}$ with $n = 0, 1, ...$, i.e. when the aircraft has its z_b axis on the x_w-y_w plane.

Flying near this singularity is unusual for regular flights of fixed wing aircrafts, and many times it is not taken into account. However, it must be especially considered when performing aerobatic manoeuvres with VToL aircrafts and the Euler angles are used to express the attitude.

Euler angles relations

In 2.16, it has been shown how the euler angles are related with the rotation matrix.

The opposite mapping can be achieved easily by looking at some entries of the rotation matrix $\mathbf{L}$. Let l_{ij} represent the $i-th$ row and $j-th$ column entry of the rotation matrix, then from Eq. (2.16),

$$\phi = \text{atan2}\,(l_{32}, l_{33})$$
$$\theta = -\text{asin}\,(l_{31})$$
$$\psi = \text{atan2}\,(l_{21}, l_{11})$$

(2.20)

In the equation above, the function atan2($\bullet$), represents the inverse tangent function that maps the argument to $[-\pi, \pi]$, while it is admitted that $\theta \in \left[-\frac{\pi}{2}, \frac{\pi}{2}\right]$.

Euler angles composition

Let $\{\mathcal{F}_0\}$, $\{\mathcal{F}_1\}$ and $\{\mathcal{F}_2\}$ represent three reference frames. Let $\boldsymbol{\eta}_1$ and $\boldsymbol{\eta}_2$ be the sets of Euler angles that relate vectors defined in $\{\mathcal{F}_0\}$ with $\{\mathcal{F}_1\}$ and vectors defined in $\{\mathcal{F}_1\}$ with $\{\mathcal{F}_2\}$ respectively. The way of extracting the Euler parameters that links directly $\{\mathcal{F}_0\}$ and $\{\mathcal{F}_2\}$ is not straightforward, in the sense that both vectors of Euler angles need be converted into rotation matrices by using Eq. (2.16) i.e.

$$^{\mathcal{F}_1}\boldsymbol{v} = \mathbf{L}(\boldsymbol{\eta}_1)^{\mathcal{F}_0}\boldsymbol{v} \quad \text{and} \quad {}^{\mathcal{F}_2}\boldsymbol{v} = \mathbf{L}(\boldsymbol{\eta}_2)^{\mathcal{F}_1}\boldsymbol{v}$$

Then, both relations can be composed leading to

$$^{\mathcal{F}_2}\boldsymbol{v} = \mathbf{L}(\boldsymbol{\eta}_2)\mathbf{L}(\boldsymbol{\eta}_1)^{\mathcal{F}_0}\boldsymbol{v}$$

which shows that a composite rotation matrix $\mathbf{L}(\boldsymbol{\eta}_3) = \mathbf{L}(\boldsymbol{\eta}_2)\mathbf{L}(\boldsymbol{\eta}_1)$ can be obtained from the individual rotation matrices. As a consequence, the Euler angles $\boldsymbol{\eta}_3$ that represent the attitude change between the initial anf final frame can be finally retrieved using Eq. (2.20) over $\mathbf{L}(\boldsymbol{\eta}_3)$.

Pros and cons of using Euler angles to express the attitude

Euler angles represent the most understandable attitude parametrization. The consecutive composition of the three different simple rotations make that when θ and ϕ angles are close to null (aircraft body horizontal plane parallel to the world horizontal plane) any small attitude change can be interpreted in an intuitive way. However, it is not easy to understand the resulting attitude when pitch and roll angles are not small.

This representation has two other important drawbacks.

- The concatenation of rotations has to be done by passing through the construction of matrix rotations where the Euler angles enter in a non-linear way. The trigonometric functions that fill the matrix entries are not the class of functions desired when performing estimation or control (the most used techniques are linear techniques that require a linearisation of the system equations).

- The relation of the derivative introduces a singularity known as gimbal lock. Since every triad of Euler angles is associated with one main axis of three different frames, it is possible

for a pair of axes to coincide in a certain configuration. That is the case when in our parametrization the aircraft performs a pitch manoeuvre with the nose up/down until $\theta = \pm\frac{\pi}{2}$ rad. In this new configuration the $\boldsymbol{z}_w$ and the $\boldsymbol{x}_b$ axes are parallel and, therefore, a change in ϕ or ψ angles represents a rotation about the same direction.

This singularity appears explicitly in the equation that transforms the body angular velocity to the derivative of Euler angles. In the configuration $\theta = \pm\frac{\pi}{2}$ rad, the matrix that allows the transformation becomes singular and the mapping is not possible. Moreover, near the singularity, the matrix can be ill-conditioned leading to big round-off errors in the conversion.

2.3.3 Quaternions

Quaternions were proposed by William Rowan Hamilton as an extension of the complex numbers. The idea behind the quaternion formulation was to generalise the effect of rotation that in a 2-dimensional plane produces the multiplication of complex numbers. Under the quaternion multiplication a 3-dimensional vector rotates and changes its magnitude.

A quaternion is defined as the concatenation of a scalar, q_0, and a vector, $\boldsymbol{q} = (q_1, q_2, q_3)^\top$, and it is denoted by $\mathring{q} = (q_0, \boldsymbol{q}^\top)^\top$. An alternative notation is $\mathring{q} = q_0 + q_1\boldsymbol{i} + q_2\boldsymbol{j} + q_3\boldsymbol{k}$. In this case every component of the vector represents a new dimension. As in the complex number case, the multiplication of the imaginary parts is resolved as

$$
\begin{aligned}
\boldsymbol{i}^2 = -1 \quad & \boldsymbol{j}^2 = -1 \quad \boldsymbol{k}^2 = -1 \\
\boldsymbol{ij} = \boldsymbol{k} \quad & \boldsymbol{jk} = \boldsymbol{i} \quad\;\; \boldsymbol{ki} = \boldsymbol{j} \\
\boldsymbol{ji} = -\boldsymbol{k} \quad & \boldsymbol{kj} = -\boldsymbol{i} \quad \boldsymbol{ik} = -\boldsymbol{j}
\end{aligned}
$$

Therefore, the product of two quaternions is another quaternion

$$
\mathring{q}\mathring{p} = \begin{pmatrix} q_0 p_0 - \boldsymbol{q}^\top\boldsymbol{p} \\ q_0\boldsymbol{p} + p_0\boldsymbol{q} + \boldsymbol{q}\times\boldsymbol{p} \end{pmatrix} \tag{2.21}
$$

Quaternion multiplication is not commutative, as can be interpreted by the cross product inside the vector part in Eq. (2.21). However, reverse multiplication requires only the flip of the cross product sign

$$
\mathring{p}\mathring{q} = \begin{pmatrix} q_0 p_0 - \boldsymbol{q}^\top\boldsymbol{p} \\ q_0\boldsymbol{p} + p_0\boldsymbol{q} - \boldsymbol{q}\times\boldsymbol{p} \end{pmatrix} \tag{2.22}
$$

The multiplication operation can be expressed in terms of matrix vector multiplication as

$$
\mathring{q}\mathring{p} = Q(\mathring{q})\mathring{p} = \begin{pmatrix} q_0 & -q_1 & -q_2 & -q_3 \\ q_1 & q_0 & -q_3 & q_2 \\ q_2 & q_3 & q_0 & -q_1 \\ q_3 & -q_2 & q_1 & q_0 \end{pmatrix}\mathring{p} \tag{2.23}
$$

or equivalently

$$\mathring{q}\mathring{p} = \overline{Q}(\mathring{p})\mathring{q} = \begin{pmatrix} p_0 & -p_1 & -p_2 & -p_3 \\ p_1 & p_0 & p_3 & -p_2 \\ p_2 & -p_3 & p_0 & p_1 \\ p_3 & p_2 & -p_1 & p_0 \end{pmatrix}\mathring{q} \tag{2.24}$$

The quaternion algebra defines the addition as the element-wise sum

$$\mathring{s} = \mathring{q} + \mathring{p} \rightarrow s_i = q_i + p_i \quad \forall\, i = 0, 1, 2, 3 \tag{2.25}$$

which has the properties of being associative and commutative.

The conjugate of a quaternion is

$$\overline{\mathring{q}} = \left(q_0, -\boldsymbol{q}^\top\right)^\top \tag{2.26}$$

and the conjugate of products is

$$\overline{\mathring{q}\,\mathring{p}} = \overline{\mathring{p}}\,\overline{\mathring{q}} \tag{2.27}$$

The norm of a quaternion is defined as

$$\|\mathring{q}\| = \sqrt{q_0^2 + \boldsymbol{q}^\top \boldsymbol{q}} \tag{2.28}$$

The norm of a quaternion multiplication is defined as

$$\|\mathring{q}\mathring{p}\| = \|\mathring{q}\|\,\|\mathring{p}\| \tag{2.29}$$

The definition of the quaternion norm allows to define the inverse quaternion. Given $\mathring{q}$, its inverse accomplishes that $\mathring{q}\mathring{q}^{-1} = (1,\, 0,\, 0,\, 0)^\top$. Using Eq. (2.28), it can be seen that

$$\mathring{q}^{-1} = \frac{\overline{\mathring{q}}}{\|\mathring{q}\|^2} \tag{2.30}$$

Quaternions to express attitude

Inside the generality of quaternion algebra, we are interested in using them to represent rotations. In this case, unitary quaternions (i.e. the subgroup of quaternions with unitary norm $\|\mathring{q}\| = q_0^2 + \|\boldsymbol{q}\|^2 = 1$) embed attitude information and some special operations allow to use them to rotate vectors. Note that the norm constraint implies that a unique angle $\vartheta \in [0, \pi]$ exists for which $q_0 = \cos(\vartheta)$ and $\|\boldsymbol{q}\| = \sin(\vartheta)$. As a consequence any unit quaternion can be written as

$$\mathring{q} = \begin{pmatrix} \cos(\vartheta) \\ \sin(\vartheta)\,\boldsymbol{u} \end{pmatrix} \tag{2.31}$$

being $\boldsymbol{u} = \frac{\boldsymbol{q}}{\|\boldsymbol{q}\|}$, a unitary vector that will be related with the rotation direction.

Let the vector $\boldsymbol{v} \in \mathbb{R}^3$ represent a generic vector. Let the pure quaternion $\mathring{v}$ be defined as

$$\mathring{v} = \left(0, \boldsymbol{v}^{\top}\right)^{\top}$$

By using unitary quaternions, the product defined by

$$\mathring{v}' = \mathring{q}\mathring{v}\bar{\mathring{q}}, \tag{2.32}$$

produces a pure quaternion $\mathring{v}' = (0, \boldsymbol{v}'^{\top})^{\top}$ where $\boldsymbol{v}'$ is a rotated version of $\boldsymbol{v}$ about the direction of $\boldsymbol{u}$.

Developing the product in Eq. (2.32) by using Eq. (2.23) and Eq. (2.24) leads to

$$\mathring{v}' = Q(\mathring{q})\overline{Q}(\bar{\mathring{q}})\mathring{v} = Q(\mathring{q})\overline{Q}^{\top}(\mathring{q})\mathring{v} = \begin{bmatrix} 1 & \mathbf{0}_{1\times3} \\ \mathbf{0}_{3\times1} & \mathbf{L}(\mathring{q}) \end{bmatrix}\mathring{v} \tag{2.33}$$

being

$$\mathbf{L}(\mathring{q}) = \begin{pmatrix} q_0^2 + q_1^2 - q_2^2 - q_3^2 & 2q_1q_2 - 2q_0q_3 & 2q_1q_3 + 2q_0q_2 \\ 2q_1q_2 + 2q_0q_3 & q_0^2 - q_1^2 + q_2^2 - q_3^2 & 2q_2q_3 - 2q_0q_1 \\ 2q_1q_3 - 2q_0q_2 & 2q_2q_3 + 2q_0q_1 & q_0^2 - q_1^2 - q_2^2 + q_3^2 \end{pmatrix} \tag{2.34}$$

the rotation matrix responsible for the rotation of vector $\boldsymbol{v}$.

In an equivalent way, by developing Eq. (2.32), the rotated vector $\boldsymbol{v}'$ can be obtained as the application of an operator over $\boldsymbol{v}$

$$\boldsymbol{v}' = \mathcal{R}\left(\mathring{q}, \boldsymbol{v}\right) = \left(q_0^2 - \|\boldsymbol{q}\|^2\right)\boldsymbol{v} + 2\left(\boldsymbol{q}^{\top}\boldsymbol{v}\right)\boldsymbol{q} + 2q_0\left(\boldsymbol{q} \times \boldsymbol{v}\right) \tag{2.35}$$

taking $\boldsymbol{v}$ as common factor by the right in the last equation leads to

$$\boldsymbol{v}' = \mathcal{R}\left(\mathring{q}, \boldsymbol{v}\right) = \mathbf{L}(\mathring{\mathbf{q}})\boldsymbol{v} \tag{2.36}$$

being

$$\mathbf{L}(\mathring{q}) = \left(q_0^2 - \boldsymbol{q}^{\top}\boldsymbol{q}\right)\mathbf{I}_3 + 2\boldsymbol{q}\boldsymbol{q}^{\top} + 2q_0\left[\boldsymbol{q}\right]_{\times} \tag{2.37}$$

or equivalently

$$\mathbf{L}(\mathring{q}) = q_0^2\mathbf{I}_{3\times3} + \boldsymbol{q}\boldsymbol{q}^{\top} + 2q_0\left[\boldsymbol{q}\right]_{\times} + \left[\boldsymbol{q}\right]_{\times}^2 \tag{2.38}$$

$\mathcal{R}$ is a linear operator in terms of $\boldsymbol{v}$ since it can be written as $\mathbf{L}(\mathring{q})\boldsymbol{v}$. Therefore, the superposition principle holds

$$\mathcal{R}\left(\mathring{q}, k_1\boldsymbol{v}_1 + k_2\boldsymbol{v}_2\right) = k_1\mathcal{R}\left(\mathring{q}, \boldsymbol{v}_1\right) + k_2\mathcal{R}\left(\mathring{q}, \boldsymbol{v}_2\right)$$

By analysing the effect of the operator $\mathcal{R}$, or equivalently, the effect of $\mathbf{L}(\mathring{q})$, over $\boldsymbol{v}$ it can be observed that:
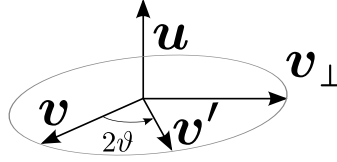
FIGURE 2.6: Effect of the action of quaternion in Eq. (2.31) over an orthogonal vector $\boldsymbol{v}$

- The norm is preserved. By applying Eq. (2.29) over the product in Eq. (2.32) it can be demonstrated that as in any rotation $\|\boldsymbol{v}'\| = \|\boldsymbol{v}\|$.

- A vector in the direction of $\boldsymbol{u}$, equivalently, the direction of $\boldsymbol{q}$, will not change. Taking $\boldsymbol{v} = k\boldsymbol{q}$,

$$
\begin{aligned}
\boldsymbol{v}' = \mathcal{R}\left(\mathring{q}, k\boldsymbol{q}\right) = \left(q_0^2 - \|\boldsymbol{q}\|^2\right)k\boldsymbol{q} + 2k\left(\boldsymbol{q}^\top\boldsymbol{q}\right)\boldsymbol{q} + 2q_0 k\left(\boldsymbol{q}\times\boldsymbol{q}\right) = \\
\left(q_0^2 - \|\boldsymbol{q}\|^2\right)k\boldsymbol{q} + 2k\left(\boldsymbol{q}^\top\boldsymbol{q}\right)\boldsymbol{q} = \left(q_0^2 + \|\boldsymbol{q}\|^2\right)k\boldsymbol{q} = k\boldsymbol{q} = \boldsymbol{v}
\end{aligned}
\tag{2.39}
$$

- A vector perpendicular to $\boldsymbol{u}$, equivalently, perpendicular to $\boldsymbol{q}$, will rotate describing a circle. Let $\boldsymbol{v}$ be orthogonal to $\boldsymbol{q}$. Therefore the rotation operator becomes

$$
\mathcal{R}\left(\mathring{q}, \boldsymbol{v}\right) = \left(q_0^2 - \|\boldsymbol{q}\|^2\right)\boldsymbol{v} + 2\left(\boldsymbol{q}^\top\boldsymbol{v}\right)\boldsymbol{q} + 2q_0\left(\boldsymbol{q}\times\boldsymbol{v}\right) = \left(q_0^2 - \|\boldsymbol{q}\|^2\right)\boldsymbol{v} + 2q_0\left(\boldsymbol{q}\times\boldsymbol{v}\right)
\tag{2.40}
$$

Defining $\boldsymbol{v}_\perp = \frac{(\boldsymbol{q}\times\boldsymbol{v})}{\|\boldsymbol{q}\|}$ as a perpendicular vector to both $\boldsymbol{q}$ and $\boldsymbol{v}$ with the same norm that $\boldsymbol{v}$

$$
\mathcal{R}\left(\mathring{q}, \boldsymbol{v}\right) = \left(q_0^2 - \|\boldsymbol{q}\|^2\right)\boldsymbol{v} + 2q_0\|\boldsymbol{q}\|\boldsymbol{v}_\perp
\tag{2.41}
$$

Now using the definition of the unitary quaternion in Eq. (2.31)

$$
\mathcal{R}\left(\mathring{q}, \boldsymbol{v}\right) = \left(\cos(\vartheta)^2 - \sin(\vartheta)^2\right)\boldsymbol{v} + 2\cos(\vartheta)\sin(\vartheta)\boldsymbol{v}_\perp = \cos(2\vartheta)\boldsymbol{v} + \sin(2\vartheta)\boldsymbol{v}_\perp
\tag{2.42}
$$

From Eq. (2.42) it can be seen that the quaternion in Eq. (2.31) encodes a rotation of 2ϑ about the vector $\boldsymbol{u}$. It is depicted on Fig. 2.6

Given the linearity of the rotation operator over v above stated the superposition principle applies. Then, any vector can be decomposed into its projection over $\boldsymbol{u}$, e.g,

$$
\boldsymbol{v}_\parallel = \left(\boldsymbol{v}^\top\boldsymbol{u}\right)\boldsymbol{u}
$$

and the projection over the perpendicular direction of $\boldsymbol{u}$ that lies in the plane given by $\boldsymbol{v}$ and $\boldsymbol{u}$ e.g

$$
\boldsymbol{v}_\perp = \boldsymbol{v} - \left(\boldsymbol{v}^\top\boldsymbol{u}\right)\boldsymbol{u}
$$

The effect of the rotation can be individually interpreted to affect $\boldsymbol{v}_\parallel$ and $\boldsymbol{v}_\perp$, and the final rotated vector can be reconstructed by the simple addition of them.

As a consequence it can be said that a general quaternion

$$
\mathring{q}^\top = \left(\pm\cos\left(\tfrac{\theta}{2}\right) \pm \sin\left(\tfrac{\theta}{2}\right)\boldsymbol{u}\right)
\tag{2.43}
$$
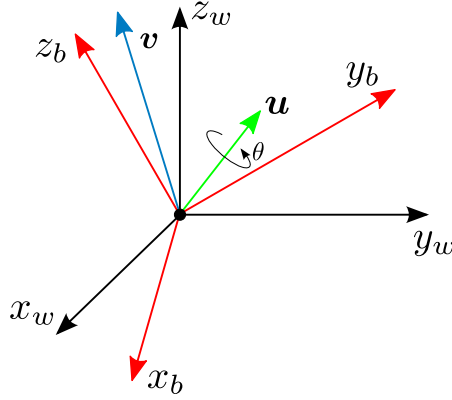
FIGURE 2.7: Reference frame transformations interpretation by using quaternions

through the operator in Eq. (2.32) defines a rotation of an angle θ about the direction of the unit vector $\boldsymbol{u}$.

Note that the $\pm$ sign appears because of the ambiguity of this representation, since the rotations encoded in quaternions $\mathring{q}$ and $-\mathring{q}$ are equivalent as result of applying Eq. (2.32).

This representation shares analogies with the Euler exponential formula for the complex numbers. In this case a quaternion can be expressed as

$$\mathring{q} = \pm \exp\left(\frac{\theta}{2}\boldsymbol{u}\right) = \pm \cos\left(\frac{\theta}{2}\right) \pm \sin\left(\frac{\theta}{2}\right)(u_1 \boldsymbol{i} + u_2 \boldsymbol{j} + u_3 \boldsymbol{k}) \tag{2.44}$$

Transformation between different bases

The previous section describes how quaternions can be used to rotate a vector around a given direction. However, it is not trivial to understand how these rotations allow to formulate the transformations between reference frames that we are dealing with in this document.

When doing transformations between reference frames we are not rotating vectors, but expressing the vector in different basis.

Take the black triad in Fig. 2.7 to be the Earth reference frame. Let the red triad be the body reference frame obtained by the rotation of the basis vectors of the Earth reference frame encoded in a quaternion $\mathring{q}$ such that

$$\begin{aligned}
{}^{w}\boldsymbol{x}_b &= \mathring{q}\, {}^{w}\boldsymbol{x}_w \bar{\mathring{q}} \\
{}^{w}\boldsymbol{y}_b &= \mathring{q}\, {}^{w}\boldsymbol{y}_w \bar{\mathring{q}} \\
{}^{w}\boldsymbol{z}_b &= \mathring{q}\, {}^{w}\boldsymbol{z}_w \bar{\mathring{q}}
\end{aligned} \tag{2.45}$$

Given the vector ${}^{w}\boldsymbol{v}$ expressed in the world frame, the same vector in the body frame will be given by

$$ {}^{b}\mathring{v} = \bar{\mathring{q}}\, {}^{w}\mathring{v}\, \mathring{q} \tag{2.46}$$

where ${}^{b}\mathring{v}^{\top} = [0;\, {}^{b}\boldsymbol{v}^{\top}]$ and ${}^{w}\mathring{v}^{\top} = [0;\, {}^{w}\boldsymbol{v}^{\top}]$.

This quaternion operation is the inverse of the operation in Eq. (2.32). It can be interpreted as the rotation of the vector $\boldsymbol{v}$ about $\boldsymbol{u}$ by a quantity $-\theta$ or as the rotation of the coordinate frame about $\boldsymbol{u}$ of θ magnitude keeping the vector $\boldsymbol{v}$ fixed.

As a consequence, the rotation matrix in Eq. (2.34) represents the rotation from body to Earth frames i.e. $\mathbf{R}(\mathring{q}) = \mathbf{L}$

Kinematic effects over quaternions

As shown for Euler angles and rotation matrices, the time derivative of the attitude expressions can be related with the angular velocity.

From the formulation of Eq. (2.44) and differentiating it with respect to time

$$\dot{\mathring{q}} = \frac{\mathrm{d}\left(\exp\left(\frac{\theta}{2}\boldsymbol{u}\right)\right)}{\mathrm{d}t} \tag{2.47}$$

Since the rotation represented by the quaternion maintains the direction of the vector $\boldsymbol{u}$

$$\dot{\mathring{q}} = \frac{\dot{\theta}}{2}\boldsymbol{u}\exp\left(\frac{\theta}{2}\boldsymbol{u}\right) = \frac{1}{2}{}^{w}\mathring{\omega}\mathring{q} \tag{2.48}$$

An equivalent expression can be found to relate the derivative of the quaternion with the body angular velocity. By using Eq. (2.46)

$${}^{b}\mathring{q} = \bar{\mathring{q}}{}^{w}\mathring{q}\mathring{q} \tag{2.49}$$

And using this result in Eq. (2.48),

$$\dot{\mathring{q}} = \frac{1}{2}\mathring{q}{}^{b}\mathring{\omega} \tag{2.50}$$

The quaternion derivative can be written in matrix vector multiplication form by using the relations in Eq. (2.23) and Eq. (2.24), so that

$$\dot{\mathring{q}} = \frac{1}{2}\boldsymbol{\Gamma}(\mathring{q})\,{}^{b}\boldsymbol{\omega} \tag{2.51}$$

and

$$\dot{\mathring{q}} = \frac{1}{2}\tilde{\boldsymbol{\Gamma}}(\mathring{q})\,{}^{b}\boldsymbol{\omega} \tag{2.52}$$

being

$$\boldsymbol{\Gamma}(\mathring{q}) = \begin{pmatrix} \boldsymbol{q}^{\top} \\ q_0\mathbf{I}_3 + [\boldsymbol{q}]_{\times} \end{pmatrix} \tag{2.53}$$

$$\tilde{\boldsymbol{\Gamma}}(\mathring{q}) = \begin{pmatrix} \boldsymbol{q}^{\top} \\ q_0\mathbf{I}_3 - [\boldsymbol{q}]_{\times} \end{pmatrix} \tag{2.54}$$

Composition of rotations with quaternions

Let a rotation of a vector $\boldsymbol{v}$ be represented as in Eq. (2.32). A successive rotation encoded in a second unit quaternion $\mathring{w}$ can be calculated as

$$\boldsymbol{v}''_q = \mathring{w}\left(\mathring{u}\mathring{v}\overline{\mathring{u}}\right)\overline{\mathring{w}} = \left(\mathring{w}\mathring{u}\right)\mathring{v}\left(\overline{\mathring{u}}\,\overline{\mathring{w}}\right). \tag{2.55}$$

The previous equation shows that rotations expressed in quaternions are simply concatenated by quaternion multiplication.

DCM to quaternions.

Up until now, we have seen how a rotation matrix is composed by using quaternions, Eq. (2.34). Now we are looking for the inverse relation. The fact that we have 4 parameters to represent a quaternion versus 9 parameters in the rotation matrix case, makes redundancy appear.

Let l_{ij} represent the $i-th$ row and $j-th$ column entry of the rotation matrix $\mathbf{L}$ in Eq. (2.34) .

By operating with the diagonal terms of $\mathbf{L}$ and applying the unity norm constraint, the following can be obtained:

$$\begin{aligned}
4q_0^2 &= 1 + l_{11} + l_{22} + l_{33} = 1 + \text{trace}(\mathbf{L}) \\
4q_1^2 &= 1 + l_{11} - l_{22} - l_{33} = 1 - \text{trace}(\mathbf{L}) + 2l_{11} \\
4q_2^2 &= 1 - l_{11} + l_{22} - l_{33} = 1 - \text{trace}(\mathbf{L}) + 2l_{22} \\
4q_3^2 &= 1 - l_{11} - l_{22} + l_{33} = 1 - \text{trace}(\mathbf{L}) + 2l_{33}
\end{aligned} \tag{2.56}$$

In a similar way, using the off-diagonal terms

$$\begin{aligned}
4q_0q_1 &= l_{32} - l_{23} \\
4q_0q_2 &= l_{13} - l_{31} \\
4q_0q_3 &= l_{21} - l_{12} \\
4q_1q_2 &= l_{21} + l_{12} \\
4q_1q_3 &= l_{13} + l_{31} \\
4q_2q_3 &= l_{32} - l_{23}.
\end{aligned} \tag{2.57}$$

By using the Eq. (2.56) and Eq. (2.57) it is possible to recover the quaternion values from the individual entries of the rotation matrix. However, note that Eq. (2.56) by itself cannot be used to solve for every quaternion parameter given the ambiguity of sign in the squared power. In a similar way, retrieving all the quaternion parameters from Eq. (2.57) implies solving a non-linear system of equations, moreover, large round errors can occour when some quaternion parameter take near zero values. The final procedure consists in using Eq. (2.56) to determine one parameter of the quaternion and then using Eq. (2.57) to determine the remaining ones, provided that the parameter determined by the first equation is far from zero, which can be known beforehand by only checking the values of $\mathbf{L}$. This procedure damps possible numeric problems that can arise from round off errors in the rotation matrix [80, 57]. This method is described next.

Let the highest component of the quaternion $\mathring{q}$ be q_i. This implies that

$$q_i^2 - q_j^2 > 0 \quad \text{for } j \neq i \wedge j = 0, 1, 2, 3 \tag{2.58}$$

The addition of the three previous equations leads to

$$3q_i^2 > \sum_{\substack{j=0 \\ j \neq i}}^{j=3} q_j^2 \tag{2.59}$$

By the unity norm constraint $1 - q_j^2 = \sum_{\substack{j=0 \\ j \neq i}}^{j=3} q_j^2$, therefore

$$q_i^2 > \frac{1}{4} \tag{2.60}$$

which is far away from 0. This is useful to decide how to perform the reverse transformation.

Case1 : In case that $q_0^2 > q_i^2$ for $i = 1, 2, 3$, which is achieved iff trace($\mathbf{L}$) ≥ 0 based on Eq. (2.56)

$$\mathring{q} = \frac{1}{2} \begin{bmatrix} \sqrt{1 + l_{11} + l_{22} + l_{33}} \\ \frac{l_{32} - l_{23}}{\sqrt{1 + l_{11} + l_{22} + l_{33}}} \\ \frac{l_{13} - l_{31}}{\sqrt{1 + l_{11} + l_{22} + l_{33}}} \\ \frac{l_{21} - l_{12}}{\sqrt{1 + l_{11} + l_{22} + l_{33}}} \end{bmatrix} \tag{2.61}$$

Case2 : In case that $q_1^2 > q_i^2$ for $i = 0, 2, 3$ which is achieved iff trace($\mathbf{L}$) < 0 and $l_{11} = \max(l_{11}, l_{22}, l_{33})$ based on Eq. (2.56)

$$\mathring{q} = \frac{1}{2} \begin{bmatrix} \frac{l_{32} - l_{23}}{\sqrt{1 + l_{11} - l_{22} - l_{33}}} \\ \sqrt{1 + l_{11} - l_{22} - l_{33}} \\ \frac{l_{21} + l_{12}}{\sqrt{1 + l_{11} - l_{22} - l_{33}}} \\ \frac{l_{13} + l_{31}}{\sqrt{1 + l_{11} - l_{22} - l_{33}}} \end{bmatrix} \tag{2.62}$$

Case3 : In case that $q_2^2 > q_i^2$ for $i = 0, 1, 3$ which is achieved iff trace($\mathbf{L}$) < 0 and $l_{22} = \max(l_{11}, l_{22}, l_{33})$ based on Eq. (2.56)

$$\mathring{q} = \frac{1}{2} \begin{bmatrix} \frac{l_{13} - l_{31}}{\sqrt{1 - l_{11} + l_{22} + l_{33}}} \\ \frac{l_{21} + l_{12}}{\sqrt{1 - l_{11} + l_{22} + l_{33}}} \\ \sqrt{1 - l_{11} + l_{22} + l_{33}} \\ \frac{l_{32} + l_{23}}{\sqrt{1 - l_{11} + l_{22} + l_{33}}} \end{bmatrix} \tag{2.63}$$

Case4 : In case that $q_3^2 > q_i^2$ for $i = 0, 1, 2$ which is achieved iff trace($\mathbf{L}$) < 0 and $l_{33} = \max(l_{11}, l_{22}, l_{33})$ based on Eq. (2.56)

$$\mathring{q} = \frac{1}{2} \begin{bmatrix} \frac{l_{21} - l_{12}}{\sqrt{1 - l_{11} - l_{22} + l_{33}}} \\ \frac{l_{13} + l_{31}}{\sqrt{1 - l_{11} - l_{22} + l_{33}}} \\ \frac{l_{32} + l_{23}}{\sqrt{1 - l_{11} - l_{22} + l_{33}}} \\ \sqrt{1 - l_{11} - l_{22} + l_{33}} \end{bmatrix} \tag{2.64}$$

Quaternions to Euler angles.

There is no a direct relation between quaternions and Euler angles. However, simple relations can be achieved by first construct the rotation matrix from quaternions by using Eq. (2.34) and then using the mapping from the DCM to Euler angles presented in Eq. (2.20).

This process reduces to

$$\begin{aligned} \phi &= \text{atan2}\left(2q_2q_3 - 2q_0q_1,\, q_0^2 - q_1^2 - q_2^2 + q_3^2\right) \\ \theta &= -\text{asin}\left(2q_1q_3 + 2q_0q_2\right) \\ \psi &= \text{atan2}\left(2q_1q_2 - 2q_0q_3,\, q_0^2 + q_1^2 - q_2^2 - q_3^2\right) \end{aligned} \tag{2.65}$$

Euler angles to quaternions.

This mapping can be done in a very straightforward way. Since every rotation in a sequence of Euler angles represents a rotation over a different axis it can also be represented by quaternion concatenation.

Let $\mathring{q}(\vartheta, \boldsymbol{u})$ be the quaternion that represents a rotation of an angle theta about the axis of the vector $\boldsymbol{u}$. Therefore,

$$\mathring{q} = \mathring{q}(\phi, \boldsymbol{x})\mathring{q}(\theta, \boldsymbol{y})\mathring{q}(\psi, \boldsymbol{z}). \tag{2.66}$$

Pros and cons of using quaternions to express the attitude

- Quaternions avoid singularities when representing the attitude. However, the arbitrariness of sign makes the representation non unique (two quaternions for one attitude) and this can be a problem when trying to force convergence to a certain attitude configuration.

- Quaternions are well suited to concatenate rotations, as they require less operations than composing rotations by using DCMs.

- Obtaining a quaternion from its derivative by simple integration is not reliable. The time integration process always carries error propagation and this does not guarantee the norm of the obtained quaternion to be unitary.

- Understanding which attitude is encoding a quaternion by looking at its 4 component vector is not straightforward. However, expressing the quaternion in function of the Euler principal axis and angle produces an interpretable formulation.

2.3.4 Rotation vector representation

Based on Euler's theorem for rotations, Thm. (2.3.1), any pure rotation can be seen as a rotation of an angle θ about a fixed axis ($\boldsymbol{u}$). The rotation vector representation is given by a 3-dimensional vector $\boldsymbol{r} \in \mathbb{R}^3$ that takes advantage of the Euler axis theorem, defined so that

$$\boldsymbol{r} = \theta \boldsymbol{u} \tag{2.67}$$

$$\begin{aligned} \|r\| &= \theta \\ \frac{r}{\|r\|} &= \boldsymbol{u} \end{aligned} \tag{2.68}$$

The skew symmetric matrices $[\boldsymbol{r}]_\times$ formed by the rotation vectors $\boldsymbol{r} \in \mathbb{R}^3$ represent the lie algebra of $SO(3)$ which is denoted by $\mathfrak{so}(3)$. This makes the exponential map $\mathbf{A} \to \exp(\mathbf{A})$ map any skew symmetric matrix $[\boldsymbol{r}]_\times$ into a rotation matrix in $SO(3)$. This leads to the relation

$$\mathbf{L} = \mathbf{I}_{3x3} + \frac{\sin(\|\boldsymbol{r}\|)}{\|\boldsymbol{r}\|} [\boldsymbol{r}]_\times + \frac{(1 - \cos(\|\boldsymbol{r}\|))}{\|\boldsymbol{r}\|^2} [\boldsymbol{r}]_\times^2 \tag{2.69}$$

And the inverse of the exponential map is the logarithmic map for which $SO(3) \to \mathfrak{so}(3)$

$$[\boldsymbol{r}]_\times = \frac{\theta}{2\sin(\theta)} \left(\mathbf{L} - \mathbf{L}^\top\right) \tag{2.70}$$

This representation shares analogies with the unit quaternion and in fact uses the conversion

$$\mathring{q} = \begin{pmatrix} \cos\left(\frac{\|\boldsymbol{r}\|}{2}\right) \\ \frac{\boldsymbol{r}}{\|\boldsymbol{r}\|} \sin\left(\frac{\|\boldsymbol{r}\|}{2}\right) \end{pmatrix}, \tag{2.71}$$

to concatenate rotations and to convert the attitude measures to other attitude representations.

In addition, this representation is interesting for one special reason, which will be used in next chapters. Let

$$\Delta \boldsymbol{a} = \int_{t_0}^{t_1} {}^b\boldsymbol{\omega}(t)\mathrm{d}t \tag{2.72}$$

represent a rotation vector resulting from the integration of the body angular velocity in the time interval t_0 and t_1.

Therefore, if at time t_0 the attitude of the body frame was known and represented by the quaternion $\mathring{q}_{t_0}$, the attitude of the body frame at time t_1 can be calculated as

$$\mathring{q}_{t_1} = \mathring{q}_{t_0} \begin{pmatrix} \cos(\|\Delta \boldsymbol{a}\|/2) \\ \frac{\Delta \boldsymbol{a}}{\|\Delta \boldsymbol{a}\|} \sin\left(\frac{\|\Delta \boldsymbol{a}\|}{2}\right) \end{pmatrix} \tag{2.73}$$

2.4   Navigation state

The state of a rigid body is composed of all the variables that determine its position and attitude (pose) and information about how they are evolving in time (their derivatives). Different parametrizations for the attitude and how they are related with the angular velocity of the body have been introduced in the last section. In contrast, nothing has been said about the remaining states.

For every physical magnitude representing the state, there is still some degree of freedom related with the vector realization of that quantity, e.g. in the literature it is very common to take position as the directed distance of the body frame with respect to the world frame expressed over direction of the world frame's vectors, but equivalent information is contained in the directed distance of the world frame with respect to the body frame expressed over the direction vectors of the body frame or even the world frame. Taking one representation or the other is many times a matter of choice, convenience or thoughtlessness. Below, we discuss the choices done in this work.

Position: In this work, the position will be defined as the directed distance of the platform's center of mass measured from the world reference frame origin and projected over its unit axes. This is the choice that can be seen in many works. It is also the selection made here, given that our position sensor delivers direct measures of this state, ${}^{w}\boldsymbol{\xi}$. For concision, since there is no source of misunderstanding throughout the thesis it will be many times denoted by $\boldsymbol{\xi}$.

Translational velocity: Velocity is defined as the rate of change of the defined position. Measures of this state are not provided by any sensor and as consequence it is not possible to fix any a priori predilection between the two possible choices that still exist, the velocity expressed in world frame ${}^{w}\boldsymbol{v}$ or in body frame ${}^{b}\boldsymbol{v}$. Both representations, will lead to different dynamic equations and hence to different filter implementations.

Angular velocity: Following the same reasoning that has been used for the position, the angular velocity used here will be the angular velocity of the body frame with respect to the world frame expressed in the body frame and denoted as ${}^{b}\boldsymbol{\omega}$. Gyroscopes provide direct measurements of this state and by using it we avoid the use of extra mathematical relations. Again, for brevity ${}^{b}\boldsymbol{\omega} = \boldsymbol{\omega}$.

Attitude: Selecting the correct parametrization to express the attitude is a mater of choice. However, quaternions offer the benefits of being a minimal non-singular representation with efficient composition. In most of this work the attitude will be represented by the quaternion $\mathring{q}$ which encodes the attitude and relates world and body frames by:

$$ {}^{w}\boldsymbol{u} = \mathbf{L}(\mathring{q})\,{}^{b}\boldsymbol{u} \tag{2.74} $$

Exceptionally, Chap. (3) deals with the attitude without explicitly chosing a unique parametriza-
tion and a three dimensional parametrization based on the Gibbs vector is introduced in Chap. (5)
and used also in Chap. (6) to work with incremental attitudes.

The collection of the presented variables represent the navigation states $\boldsymbol{x}_n$. The derivation
and formulation of the aircraft motion equations, an observability study and state estimation
processes by considering

$$\boldsymbol{x}_{n_1} = \left(\boldsymbol{\xi}^\top,\ {}^w\boldsymbol{v}^\top,\ \boldsymbol{\zeta}^\top,\ \boldsymbol{\omega}^\top\right)^\top \tag{2.75a}$$

$$\boldsymbol{x}_{n_2} = \left(\boldsymbol{\xi}^\top,\ {}^b\boldsymbol{v}^\top,\ \boldsymbol{\zeta}^\top,\ \boldsymbol{\omega}^\top\right)^\top \tag{2.75b}$$

with the variable ζ representing any of the possible attitude parametrizations, will be shown
throughout the thesis.

Chapter 3

Mathematical models of the quadrotor dynamics

Equations of motion provide a mathematical way to express the dynamics of a system. The general way of doing that is by means of differential equations that involve time the state and possible inputs of the system

$$\dot{\boldsymbol{x}} = \boldsymbol{f}\left(t, \boldsymbol{x}(t), \boldsymbol{u}(t)\right) \tag{3.1}$$

where t represents the time, $\boldsymbol{x}$ represents the state of the system and $\boldsymbol{u}$ represents the control input that allows to modify at least partially the state by affecting its time derivative $\dot{\boldsymbol{x}} = \frac{\mathrm{d}\boldsymbol{x}}{\mathrm{d}t}$.

Mechanical systems, normally are controlled systems for which the equations of motion are formulated from physical principles related with Newton's second law and usually depends on the time in an implicit way through the time dependent state an input. Many mechanical system's state equations can be written as

$$\ddot{\boldsymbol{q}} = \boldsymbol{f}\left(\boldsymbol{q}, \dot{\boldsymbol{q}}, \boldsymbol{u}\right). \tag{3.2}$$

where every component of the state q_i represents the displacement of a degree of freedom and its derivatives $\dot{q}_i$ and $\ddot{q}_i$ are interpreted as the associated velocity and acceleration.

In many cases, depending on the system structure, the equations become even simpler reducing the dynamics to what is known as affine controlled differential form

$$\ddot{\boldsymbol{q}} = \boldsymbol{f}_1\left(\boldsymbol{q}, \dot{\boldsymbol{q}}\right) + \boldsymbol{f}_2\left(\boldsymbol{q}, \dot{\boldsymbol{q}}\right)\boldsymbol{u}. \tag{3.3}$$

A quadrotor can be interpreted as a rigid body under the action of external forces and torques. What differentiates this kind of platforms from other mechanical systems is the way that external wrenches, such as those produced by actuators, aerodynamic effects and wrench disturbance act over them. A simple diagram depicting the system dynamics can be seen in Fig. 1.1.

This chapter is devoted to the derivation of the equations of motion that describe the dynamics of UAVs. We present several ways of deriving rigid body dynamics (Section 3.1), and how forces created by actuators affect the system (Section 3.2). Aerodynamic wrenches are very complex to model and are highly dependent on the UAV geometry and flight condition (velocity, attitude etc.). In addition, the effect of body-air is small when compared with weight forces or actuator forces at the velocity regimes that the quadrotor uses which is the main reason why aerodynamic effects are obviated in this chapter. This does not mean that aerodynamic interactions are not important. In fact, drag forces allow the aircraft to reduce the velocity in case of static force equilibrium and prevents the system equations from diverging in presence of constant force or torque actions. Note that by ignoring aerodynamic interactions in the dynamic model we are intentionally creating a discrepancy between the behaviour of a real plant and the model predictions. Given that one of the aims of this work is to estimate external disturbances, those unmodelled aerodynamics along with the unmodelled actuator dynamics or any model discrepancy will be present in the estimation results.

3.1 Rigid body equations of motion

The dynamic equations that describe the behaviour of a rigid body in space are founded in first principles such as Newton-Laws or energy conservation. From the physics, different methods, the consideration of different reference frames (inertial and non-inertial ones) and the choice of many possible states allows to derive different and, in essence, equivalent system dynamics. In this section we present three different representations for the dynamics of a rigid body floating in space and under the action of external forces. The first one, based on the direct application of the Newton-Euler equations is, maybe the most known form of dynamics. For this representation we discuss the effect of choosing the world or the body frame to express the platform dynamics and we give explicit motion equations. In second place, we present a Lagrangian formulation of the system dynamics. This formulation is based in a energy balance of the system and produce a set of second order dynamic equations where some generalized terms like mass and damping are well identified for both translational and rotational dynamics. The benefit of the Lagrangian formulation is exploited by the third formulation provided, the Legendre formulation. Te Legendre formulation allows to simplify the system dynamics under a change of variables. The Newton-Euler derivations serve as basis for analysing the system observability and deriving state estimators in Chap. (5), Chap. (6). The Legendre formulation is used to derive external disturbance and wrench estimators and observers in Chap. (7).

3.1.1 Newton-Euler equations of motion

The Newton-Euler equations are the generalized version of Newton's second law, which establish the dynamic evolution of the position and attitude of a rigid body.

Their mathematical expression is well known

$$\frac{\mathrm{d}\, m\dot{\boldsymbol{\xi}}}{\mathrm{d}t} = \boldsymbol{F}$$
$$\frac{\mathrm{d}\, \mathbf{J}\boldsymbol{\omega}}{\mathrm{d}t} = \boldsymbol{\tau} \tag{3.4}$$

being $\dot{\boldsymbol{\xi}} = (\dot{x}, \dot{y}, \dot{z})^{\top}$ the translational velocity of the mass center, $\boldsymbol{\omega}$ the angular velocity of the body frame, both expressed in an inertial frame, m the mass, $\mathbf{J}$ the inertia in the inertial frame, $\boldsymbol{F}$ the sum of the external forces acting over the mass center and $\boldsymbol{\tau}$ the sum of the torques produced over the body expressed on the inertial frame.

When the Earth-fixed reference is used, assuming that the gravity acts always as a constant pointing in the ^{w}z direction, the first equation of Eq. (3.4) can be expressed as

$$m\, {}^{w}\ddot{\boldsymbol{\xi}} - mg \begin{pmatrix} 0 \\ 0 \\ 1 \end{pmatrix} = {}^{w}\boldsymbol{F}, \tag{3.5}$$

where $^{w}\boldsymbol{F}$ now excludes the weight force.

Developing the second equation in Eq. (3.4) is much more complicated since the inertia matrix $\mathbf{J}$ depends on the body orientation in the inertial frame.

The Newton-Euler equations can be formulated in a non-inertial frame by taking into account that the moving frame is continuously accelerated due to the effect of its rotation, in this case,

$$\frac{\mathrm{d}\left(m\, {}^{b}\dot{\boldsymbol{\xi}}\right)}{\mathrm{d}t} + {}^{b}\boldsymbol{\omega} \times \left(m\, {}^{b}\dot{\boldsymbol{\xi}}\right) = {}^{b}\boldsymbol{F}$$
$$\frac{\mathrm{d}\, {}^{b}\mathbf{J}\, {}^{b}\boldsymbol{\omega}}{\mathrm{d}t} + {}^{b}\boldsymbol{\omega} \times \left({}^{b}\mathbf{J}\, {}^{b}\boldsymbol{\omega}\right) = {}^{b}\boldsymbol{\tau} \tag{3.6}$$

where now $^{b}\dot{\boldsymbol{\xi}}$ represents the velocity of the vehicle's center of mass expressed in the body frame, $^{b}\boldsymbol{\omega}$ the angular velocity of the body expressed in the body frame and $^{b}\mathbf{J}$ is the inertia of the vehicle on the body frame which is constant.

In the body frame the translational equations become

$$m\, {}^{b}\ddot{\boldsymbol{\xi}} - \mathbf{L}^{T}(0,0,mg)^{\top} + m\, {}^{b}\boldsymbol{\omega} \times {}^{b}\dot{\boldsymbol{\xi}} = {}^{b}\boldsymbol{F} \tag{3.7}$$

And the angular equations of motion turn up to be

$$^{b}\mathbf{J}\, {}^{b}\dot{\boldsymbol{\omega}} + {}^{b}\boldsymbol{\omega} \times \left({}^{b}\mathbf{J}\, {}^{b}\boldsymbol{\omega}\right) = {}^{b}\boldsymbol{\tau} \tag{3.8}$$

The previous two systems of equations can be combined with the kinematic relations to complete the dynamic system equations.

As an example, let the state be defined as

$$\boldsymbol{x} = \left({}^{w}\boldsymbol{\xi}, \boldsymbol{\zeta}, {}^{b}\boldsymbol{v}, \boldsymbol{\omega}^{b} \right)^{\top}, \tag{3.9}$$

with $\boldsymbol{\zeta}$ representing any attitude parametrization for which the relation $\dot{\boldsymbol{\zeta}} = \mathbf{A}\,{}^{b}\boldsymbol{\omega}$ is known, and let ${}^{w}\boldsymbol{g} = (0, 0, g)^{\top}$, then, the equations of motion become

$$
\begin{aligned}
{}^{w}\dot{\boldsymbol{\xi}} &= \mathbf{L}(\boldsymbol{\zeta})\,{}^{b}\boldsymbol{v} \\
\dot{\boldsymbol{\zeta}} &= \mathbf{A}(\boldsymbol{\zeta})\,{}^{b}\boldsymbol{\omega} \\
{}^{b}\dot{\boldsymbol{v}} &= \mathbf{L}^{T\,w}\boldsymbol{g} - {}^{b}\boldsymbol{\omega} \times {}^{b}\boldsymbol{v} + \frac{1}{m}\,{}^{b}\boldsymbol{F} \\
{}^{b}\dot{\boldsymbol{\omega}} &= {}^{b}\mathbf{J}^{-1}\left({}^{b}\boldsymbol{\tau} - {}^{b}\boldsymbol{\omega} \times \left({}^{b}\mathbf{J}\,{}^{b}\dot{\boldsymbol{\omega}} \right) \right)
\end{aligned}
\tag{3.10}
$$

The most used version of Newton-Euler equations make use of a mixture of both, the world and body reference frames. Given the simplicity of the translational motion equations in the inertial (world) frame, the equations of motion are usually also written as

$$
\begin{aligned}
{}^{w}\dot{\boldsymbol{\xi}} &= {}^{w}\boldsymbol{v} \\
\dot{\boldsymbol{\zeta}} &= \mathbf{A}(\boldsymbol{\zeta})\,{}^{b}\boldsymbol{\omega} \\
{}^{w}\dot{\boldsymbol{v}} &= {}^{w}\boldsymbol{g} + \frac{1}{m}\,{}^{w}\boldsymbol{F} \\
{}^{b}\dot{\boldsymbol{\omega}} &= {}^{b}\mathbf{J}^{-1}\left({}^{b}\boldsymbol{\tau} - {}^{b}\boldsymbol{\omega} \times \left({}^{b}\mathbf{J}\,{}^{b}\dot{\boldsymbol{\omega}} \right) \right)
\end{aligned}
\tag{3.11}
$$

3.1.2   Lagrangian equations of motion

The Lagrangian approach is a general method to extract the equations of motion from energetic metrics. The lagrangian function is defined as function of the kinetic and potential energy $L = T - U$ and is related with the equations of motion by

$$\frac{\mathrm{d}}{\mathrm{d}t}\left(\frac{\partial L}{\partial \dot{q}_i} \right) - \frac{\partial L}{\partial q_i} = W_i \tag{3.12}$$

where q_i stands for the $i-th$ degree of freedom. The term W_i represents the generalized wrench, i.e., the action (force or torque) component of the vector that acts over the $i-th$ degree of freedom.

Let us consider the state vector partition $\boldsymbol{q} = \left(\boldsymbol{\xi}^{\top}, \boldsymbol{\zeta}^{\top} \right)^{\top}$ that allows to distinguish between translational and rotational degrees of freedom. Let the inertial earth reference system be selected as the inertial triad where to express the equations of motion. As a consequence $\boldsymbol{\xi} = {}^{w}\boldsymbol{\xi}$ and $\boldsymbol{\zeta}$ is a parametrization for the attitude such that $\dot{\boldsymbol{\zeta}} = \mathbf{A}\,{}^{w}\boldsymbol{\omega}$.

The kinetic and potential energies for the translational equations of motion become

$$T_{\xi} = \tfrac{1}{2}m\,{}^{w}\boldsymbol{\xi}^{\top\,w}\boldsymbol{\xi} \quad U_{\xi} = -mgz_w \tag{3.13}$$

and equivalently for the rotational degrees of freedom

$$T_{\zeta} = \tfrac{1}{2}\,{}^{w}\boldsymbol{\omega}^{\top\,w}\mathbf{J}\,{}^{w}\boldsymbol{\omega}^{\top} \quad U_{\zeta} = 0 \tag{3.14}$$

Using the Lagrange equation defined in Eq. (3.12) for the translational degrees of freedom, the equations of motion result in

$$m\,{}^{w}\ddot{\boldsymbol{\xi}} = mg\begin{pmatrix}0\\0\\1\end{pmatrix} + {}^{w}\boldsymbol{F} \tag{3.15}$$

where ${}^{w}\boldsymbol{F}$ represents the forces vector affecting the translational degrees of freedom expressed on the world frame.

Applying the Lagrangian approach over the rotational degrees of freedom the next equation can be obtained

$$\mathbf{J}_{\zeta}(\boldsymbol{\zeta})\ddot{\boldsymbol{\zeta}} + \mathbf{C}_{\zeta}\left(\boldsymbol{\zeta},\dot{\boldsymbol{\zeta}}\right)\dot{\boldsymbol{\zeta}} = \boldsymbol{\tau} \tag{3.16}$$

where

$$\begin{aligned}\mathbf{J}_{\zeta}(\zeta) &= \mathbf{A}^{\top}{}^{w}\mathbf{J}\mathbf{A}\\ \mathbf{C}_{\zeta}\left(\boldsymbol{\zeta},\dot{\boldsymbol{\zeta}}\right)\dot{\boldsymbol{\zeta}} &= \dot{\mathbf{J}}\dot{\zeta} - \tfrac{1}{2}\dot{\zeta}^{\top}\tfrac{\partial \mathbf{J}}{\partial \zeta}\dot{\zeta}\end{aligned} \tag{3.17}$$

and $\boldsymbol{\tau}$ represents how the external torques affect the translational degrees of freedom represented by $\boldsymbol{\zeta}$.

Both systems of equations can be stacked to create a complete system of equations of the form

$$\mathbf{M}(\boldsymbol{q})\ddot{\boldsymbol{q}} + \mathbf{C}\left(\boldsymbol{q},\dot{\boldsymbol{q}}\right)\dot{\boldsymbol{q}} + \boldsymbol{g} = \boldsymbol{W} \tag{3.18}$$

being

$$\begin{aligned}\mathbf{M}(\boldsymbol{q}) &= \text{blkdiag}\left(m\mathbf{I}_3, \mathbf{J}_{\zeta}(\boldsymbol{\zeta})\right)\\ \mathbf{C} &= \text{blkdiag}\left(\mathbf{0}_{3\times 3}, \mathbf{C}_{\zeta}(\boldsymbol{\zeta},\dot{\boldsymbol{\zeta}})\right)\end{aligned} \tag{3.19}$$

For a deeper derivation of the above equations see Ap. B.

Compared to Eq. (3.11) or Eq. (3.10), Eq. (3.18) is more compact, considers explicitly the velocity and acceleration of the attitude degrees of freedom and is a second order system in which if $\ddot{\boldsymbol{q}}$ is known, $\dot{\boldsymbol{q}}$ and $\boldsymbol{q}$ can be found by direct integration.

3.1.3 Legendre representation

Let the generalized momentum, $\boldsymbol{p}$, be defined as

$$\boldsymbol{p} = \mathbf{M}\dot{\boldsymbol{q}}. \tag{3.20}$$

with $\boldsymbol{q}$ defined as before, $\boldsymbol{q} = \left(\boldsymbol{\xi}^{\top}, \boldsymbol{\zeta}^{\top}\right)^{\top}$, and $\mathbf{M} = \mathbf{M}(\boldsymbol{q})$ as in Eq. (3.18). Given that the mass matrix is square, symmetric and positive definite, its inverse exists and velocities can be calculated from the momentum as

$$\dot{\boldsymbol{q}} = \mathbf{M}^{-1}\boldsymbol{p} \tag{3.21}$$

and

$$\dot{\boldsymbol{p}} = \dot{\mathbf{M}}\dot{\boldsymbol{q}} + \mathbf{M}\ddot{\boldsymbol{q}} = \dot{\mathbf{M}}\dot{\boldsymbol{q}} - \mathbf{C}\dot{\boldsymbol{q}} - \boldsymbol{g} + \boldsymbol{W} \tag{3.22}$$

Note that $\mathbf{C} = \mathbf{C}(\boldsymbol{q}, \dot{\boldsymbol{q}})$ that appears in Eq. (3.18) is bilinear in terms of $\dot{\boldsymbol{q}}$. As a consequence, multiple choices for $\mathbf{C}$ can be made such that the product $\mathbf{C}(\boldsymbol{q}, \dot{\boldsymbol{q}})\dot{\boldsymbol{q}}$ is not modified. Among them, $\mathbf{C}$ can be selected such that $\dot{\mathbf{M}} = \mathbf{C} + \mathbf{C}^T$ (see Ap. C), which simplifies the system equations to

$$\begin{bmatrix} \dot{\boldsymbol{q}} \\ \dot{\boldsymbol{p}} \end{bmatrix} = \begin{bmatrix} \mathbf{M}^{-1}\boldsymbol{p} \\ \mathbf{C}^{\top}\dot{\boldsymbol{q}} + \boldsymbol{W} \end{bmatrix} \tag{3.23}$$

Eq. (3.23) is a first order dynamic system of equations as the Newton-Euler equations were still representing energy balances in the system. The new state variables allow a simplification of the system dynamics, which benefits are clear in Chap. (7).

3.2   Quadrotor actuation principles

The quadrotor is actuated by means of four independent motors that turn four propellers with fixed pitch. The equivalence principle of forces and couples allow to state that the aerodynamical force and torque produced for every actuator along with its particular spatial disposition can be reduced to a single force acting on a given point plus a torque.

In standard quadrotors, the four propellers are equal and are contained in the same plane. This causes that when the propellers rotate at the same velocity, the individual propeller torques are compensated and a pure force appears as the summation of the individual thrusts.

Antisymmetric deviations of the angular velocity of opposite rotors with respect to the pure force condition produces torques in the perpendicular direction to the resultant thrust.

Finally, symmetric deviations of the angular velocity of opposite rotors with respect to the pure force condition break the compensation of torques and induce a torque in the motor axis of rotation direction.

These four basic actuation principles, depicted in Fig. 3.1, are the most basic actuation laws. Mixing these four cases allows the quadrotor to produce angular accelerations that modify its attitude and to produce linear accelerations that modify its position.

In a generic frame of reference $\{\mathcal{F}\}$ with its origin at point o, the six dimensional wrench vector produced by the actuators is given by

$$\boldsymbol{W} = \sum_{r_i=1}^{4} \begin{pmatrix} \boldsymbol{T}_{r_i} \\ \boldsymbol{d}_{r_i} \times \boldsymbol{T}_{r_i} + \boldsymbol{Q}_{r_i} \end{pmatrix} \tag{3.24}$$

being $\boldsymbol{T}_{r_i}$, $\boldsymbol{Q}_{r_i}$ and $\boldsymbol{d}_i$ the individual force vector, the torque vector and the distance from o to any point of the hub axis, respectively, all expressed in $\{\mathcal{F}\}$.

Given the standard configuration of propellers in quadrotors, aerodynamic forces are usually expressed in the body reference frame, where the greatest contribution of thrust and individual torques point in the $-z_b$ direction.

(A) Identical thrust in all rotors to produce net thrust.

(B) Antisymmetric thrust in rotors 2 and 4 to produce net thrust + torque on $\boldsymbol{x}_b$ direction.

(C) Antisymmetric thrust in rotors 1 and 3 to produce net thrust + torque on $\boldsymbol{y}_b$ direction.

(D) Equal radially symmetric angular velocities but different in groups of two to produce net thrust and torque on $\boldsymbol{z}_b$
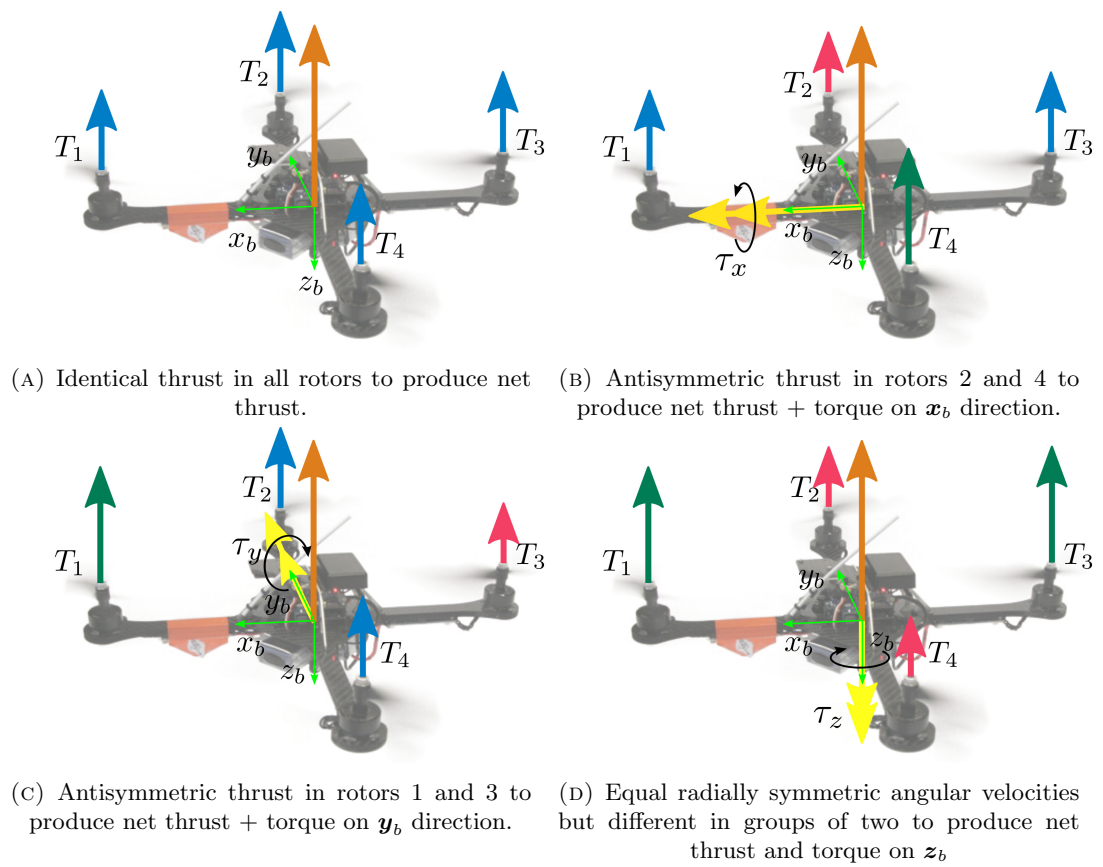
FIGURE 3.1: Quadrotor actuation principles

Chapter 4

Platform description

The main issue of this thesis is to develop estimation techniques with potential application to aerial vehicles and in particular to quadrotors. Although the derived methodologies will remain tuneable and adaptable to the platform of application, this chapter is focused on our test platform, an AscTec Hummingbird quadrotor. The purpose of this chapter is twofold. Firstly, it is intended to serve as a description of the physical platform from the equipment, hardware and software points of view. And secondly, it will present the aircraft parameters that will be used in subsequent chapters.

4.1   Geometric and mass Properties

The geometric and mass properties of the original AscTec quadrotor are detailed in Fig. 4.1 and a drawing of the platform is presented in Table 4.1.

Size	$540 \times 540 \times 85.5\,\mathrm{mm}$
Mass	$0.53057\,\mathrm{kg}$
Propeller diameter	$20.32\,\mathrm{cm}$
Inertia	$10^{-3}\begin{pmatrix} 3.65 & -0.057 & -0.015 \\ -0.057 & 3.675 & 0.0043 \\ -0.015 & 0.0043 & 7.03 \end{pmatrix}\mathrm{kg\,m^2}$

TABLE 4.1: AscTec default parameters
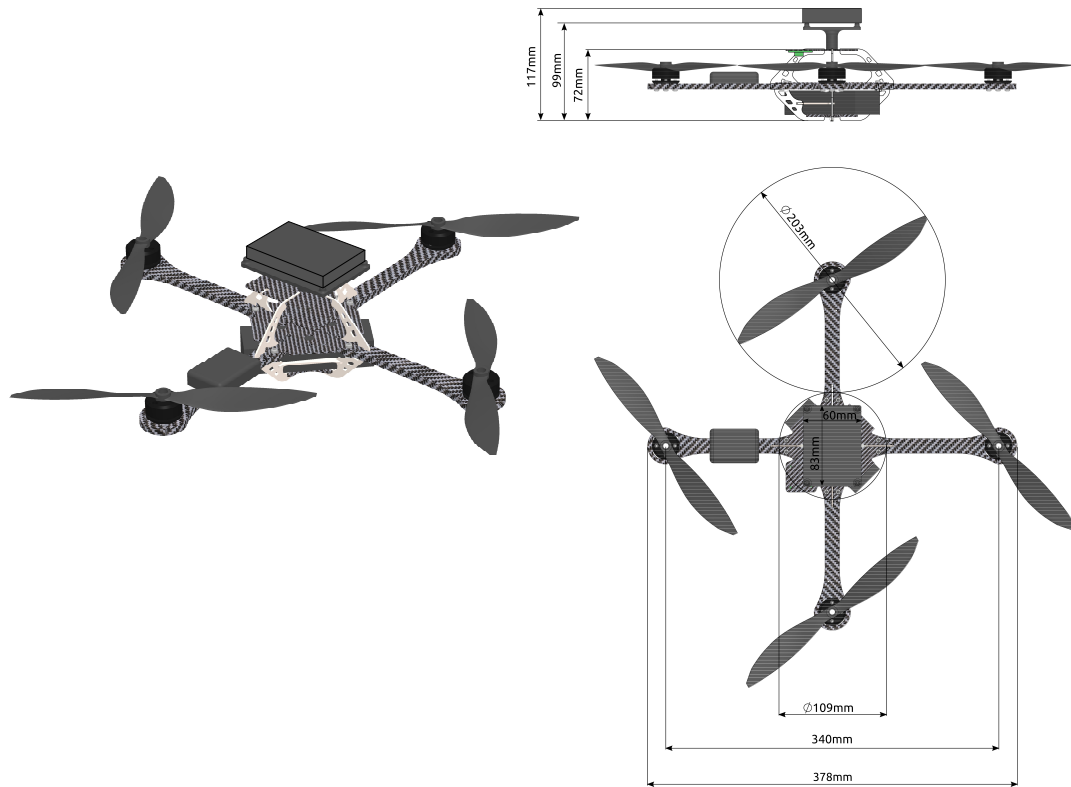
FIGURE 4.1: AscTec Hummingbird draft with tan added computer housing and board.

The Inertia, there shown, have been provided by the manufacturer on its website and is calculated as if the center of mass was situated in the geometric center of the platform.

The additional computer installed on the top of the aircraft modifies the mass properties of the platform, obviously the weight changes but in addition the inertia of the aircraft and the center of mass position does. Calculating the new mass is as simple as estimate the new weight with a simple scale or adding the weight of the additional part to the old one. Estimating the center of mass requires the knowledge of the individual center of masses, but the symmetry conditions of the pieces involved and some gross assumptions do not lead to big errors. The most difficult part is then to estimate the new inertia, which is a central point in this script. The effect of the mass parameters change could be problematic in many different aspects related with the simulation, the estimation and the control.

Simulation:

- Hypotheses: The simulated aircraft does not have the same exact mass and inertia but shares the center of mass position with the original platform. In this case angular acceleration and linear acceleration estimations will differ from the real ones in the measurements as the mass and inertial differ from the original ones. The presence of non-diagonal terms in the inertia does not allow to make a direct relation, but one can expect a similar motion under the same actions.

- Hypotheses: The simulated aircraft has the mass and inertia of the original platform but does not share the center of mass position. In this case equations of motion will describe well the center of mass and rotation motion of the platform but around the gravity center. So any angular velocity will affect to the old center of gravity with additional linear velocity.

A mixing of both hypothesis will lead to a mixing of the effects

Control:

The change of mass changes the equilibrium condition for the controller, admitting that the new condition for the updated platform is still far form the actuator saturation limits, the effect of an increase in mass will imply a change in the controllers gain in the case that the controller does not compensate the error in the dynamics by itself. In the case of inertia, the attitude controller could loose effectiveness making controllers less reactive which, at the same time, will lead to a degradation of the position or linear velocity performance. The center of gravity shift, however, could be more problematic, in the sense that it can change the torque created by the actuators thus making that a controller that stabilized the initial platform may not work in the new one.

Estimation:

Mass parameters does not appear in the estimation made in Chap. (6), given that IMU measurements feed the dynamics instead of external forces and torques. However, since the estimated state depends on the sensor measurements, the estimation will continue being valid as long as the measurement model is. Magnetometer and IMU measurements are not dependent of the center of mass position, however the position measurement of the GPS is. The error in the GPS will then be increased by the center of mass change in a changing direction that depends on the orientation.

The added computer and the housing have weigh $75\,\text{g}$, the dimensions are depicted in Fig. 4.1 and its associated inertia have been estimated as

$$\mathbf{J}_c = 10^{-4} \begin{pmatrix} 0.3996 & 0 & 0 \\ 0 & 0.7435 & 0 \\ 0 & 0 & 1.06200 \end{pmatrix} \text{kg}\,\text{m}^2$$

with a reference frame parallel to the platform one, but centered in the computer center of mass.

The modified platform has a total weight equal to the sum of the two parts

$$m = 0.605\,\text{kg}$$

The center of mass has been shifted in the vertical direction, by an amount of $6\,\text{mm}$ with respect the geometric center of the platform and the new inertia have been calculated by using [4], which

lead to a joint inertia of

$$\mathbf{J} = 10^{-3} \begin{pmatrix} 3.9242 & -0.0567 & -0.014 \\ -0.0567 & 3.9688 & 0.00426 \\ -0.0149 & 0.00426 & 7.0927 \end{pmatrix} \mathrm{kg\,m}^2$$

4.2   Sensor suite

Navigation implies interaction with the environment. Sensors provide partial readings of what is really happening. By using them, it is possible to mitigate errors that appear when only dynamic models are considered to predict future states.

Inertial Measurement Units or IMU sensors measure accelerations and angular velocities at high rates. IMU sensors are used in the vast majority of navigation solutions because they can be carried on board and do not depend on any external source. In the last years microelectromechanical systems (MEMS) have emerged to mitigate almost completely weight limitations, providing very affordable solutions at the expense of precision and sensor readings stability.

Accelerometers inside IMUs sense the specific force vector, i.e., the acceleration of external and actuator forces acting over the body expressed in the $\{B\}$ frame. The specific force appeared previously as $\frac{1}{m}{}^b\boldsymbol{F}$ in Eq. (3.10). However, given that the specific force will appear recurrently, it will be simply denoted by $\boldsymbol{a}$ and it is convenient to further extend its model as

$$\boldsymbol{a} = \frac{1}{m}\left(\boldsymbol{f}_{act} + \mathbf{L}^\top \boldsymbol{f}_{ext}\right). \tag{4.1}$$

where $\boldsymbol{f}_{act}$ and $\boldsymbol{f}_{ext}$ represent respectively the actuator and exhogenous forces.

Let $\boldsymbol{a}_m$ be the measured value of $\boldsymbol{a}$, $\boldsymbol{b}_a$ the accelerometer bias and $\boldsymbol{\eta}_a$ the noise in the measurement. In a similar way $\boldsymbol{\omega}_m$ represents the measurement of the angular velocity in body frame ${}^b\boldsymbol{\omega}$ (denoted by $\boldsymbol{\omega}$ from now in absence of ambiguity), $\boldsymbol{b}_\omega$ the bias present in the gyroscopes and $\boldsymbol{\eta}_\omega$ the noise. Then

$$\boldsymbol{a} = \boldsymbol{a}_m - \boldsymbol{b}_a - \boldsymbol{\eta}_a \tag{4.2a}$$

$$\boldsymbol{\omega} = \boldsymbol{\omega}_m - \boldsymbol{b}_\omega - \boldsymbol{\eta}_\omega \tag{4.2b}$$

$$\dot{\boldsymbol{b}}_a = \boldsymbol{\eta}_{b_a} \tag{4.2c}$$

$$\dot{\boldsymbol{b}}_\omega = \boldsymbol{\eta}_{b_\omega} \tag{4.2d}$$

where the biases have been modeled by zero mean random processes driven by white noises $\boldsymbol{\eta}_{b_a}$ and $\boldsymbol{\eta}_{b_\omega}$. This sensor model, used throughout the thesis, has been used in several works. In [26] the gyro model is used as a basis for many attitude estimation techniques applied to satellites. And the complete model is considered in [41, 77, 93, 92].

Magnetometers measure the local electromagnetic field strength. If this value is known in the world frame $\boldsymbol{H}$, then measurements in the body frame given by $\boldsymbol{h_H}$ can be used to infer the attitude of the aircraft except for one degree of freedom represented by a rotation about the

measured vector (see Fig. 4.2). Again, magnetometer sensors are carried onboard and do not depend on external facilities. The problem associated with magnetometers comes from the fact that the magnetic field is easily disturbed by the presence of external ferric objects. However, magnetometers are rarely disturbed during flight. A model of the magnetometer is usually represented by

$$h_H = H_m = \mathbf{L}^{\top w}H + \eta_H \tag{4.3}$$

with η_H representing white noises.

Finally, the GPS is intended to deliver the position of the platform with respect to an earth fixed frame through measurements of latitude, longitude and altitude with respect to a geoid model for the earth shape. Position for the ground vehicle is decrypted in the receiver by solving a trilateration problem concerning more than four satellite messages which contain information of the satellite position and time of broadcast. The error on the measurement is dependent on the satellite coverage and satellite relative positions. The latitude, longitude and altitude information can be converted to a local horizon frame, e.g., the NED frame, by firstly transforming the information to cartesian coordinates on the Earth Centered Earth Fixed (ECEF) reference frame and then translating and rotating the data to refer it to the local frame whose pose in ECEF has to be previously known. More information about this transformation is provided in the Ap. D. After this process, the GPS data can be interpreted as the cartesian position from the world frame to the aircraft on-board receiver position.

The expected model for the position is represented by

$$h_\xi = \xi_m = \xi + \eta_\xi \tag{4.4}$$

IMU, GPS and magnetometer models differ by the consideration of biases and the position of the noise in Eq. (4.2), Eq. (4.3) and Eq. (4.4). The necessity of acounting for biases in the IMU model will be verified later in this chapter, whereas the noise position has been intentionally swapped to favour the particular use of each model in Chap. (5) and Chap. (6).

4.3 Sensor Calibration

4.3.1 3-axial Data sensor conditioning

In ideal conditions, the measurement of a constant vector in the world frame sensed by the three perpendicular axis of a sensor attached to the frame of a platform under different orientations should describe a sphere. This is implicit in the IMU and magnetometer models shown in Eq. (4.2) and Eq. (4.3). Nevertheless, this may be not happening in the real world where data conditioning process of the data may help to improve the fidelity of the models. In the case of a three axial magnetometer, the sensed vector is the Earth magnetic field which is supposed to be known. The exact value of the magnetic field is not important, but its orientation is. It allows to
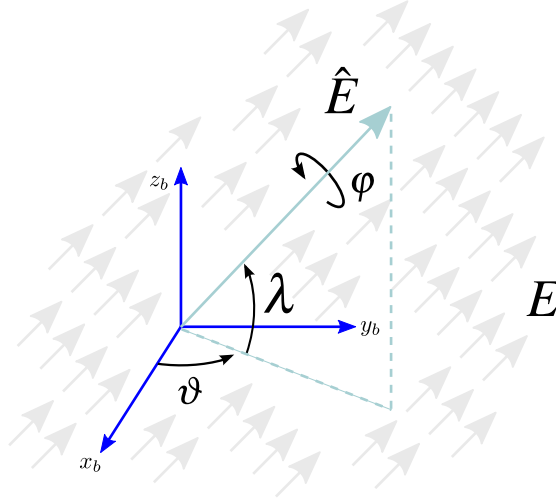
FIGURE 4.2: Earth magnetic field sensed in the body frame. ϑ and λ can be estimated from the measurement, but φ cannot.

partially infer the aircraft attitude with respect to the world frame as Fig. 4.2 depicts. However, non-ideal measurements are usually affected by different scales of the individual magnetometers, their possible misalignment, and the existence of a hard iron bias created by on-board magnetic, electric and electronic components. In the case of the IMU, three axial accelerometers and gyroscopes provide measurements of the acceleration created by external forces and angular velocity respectively. Contrary to the magnetometer, the physical units are important for IMU propagation since the magnitude impacts directly on the value of the navigation states from the measurement time onward. Again, misalignment of the axial sensors, different scales and possible constant biases can affect the sensor providing different outputs for identical excitation.

Under these assumptions, measurements will not describe a perfect sphere anymore, but a three dimensional not centered ellipsoid with a generic orientation. Points over the boundary of an ellipsoid can be represented by the scalar equation

$$f(x, y, z) = Ax^2 + By^2 + Cz^2 + 2Dxy + 2Exz + 2Fyz + 2Gx + 2Hy + 2Iz + J = 0 \qquad (4.5)$$

being the parameters $A, B, ..., J$ the responsibles for the exact shape of the ellipsoid. By using homogeneous coordinates, the quadratic equation Eq. (4.5) can be rewritten as

$$\bar{\boldsymbol{x}}^\top \mathbf{M} \bar{\boldsymbol{x}} = 0 \qquad (4.6)$$

where $\bar{\boldsymbol{x}} = (x, y, z, 1)^\top$ and

$$\mathbf{M} = \begin{pmatrix} A & D & E & G \\ D & B & F & H \\ E & F & C & I \\ G & H & I & J \end{pmatrix}$$

is symmetric and positive definite.

It is worth to note that the 10 parameters defining M are not unique, they are defined up to a degree of freedom since $\lambda\mathbf{M}$ is a valid solution of Eq. (4.6) $\forall \lambda \neq 0$.

Knowing the matrix $\mathbf{M}$, which represents the uncalibrated measurement space, is useful because firstly, it will allow a calibration of the measurements, by transforming the ellipsoid into a centered sphere and secondly, because it will allow the creation of a model to generate synthetic data useful in simulation. The next subsections are devoted to studying the mapping between the ellipsoid to the sphere (calibration mapping) and to finding the ellipsoid parameters from uncalibrated data (parameter calibration).

Calibration mapping

In this section we are interested in finding the transformation which allows to map any point of the ellipsoid to a centered unit sphere and viceversa. A usual procedure with similar effect consists in normalizing the sensor's measurements, so that any measurement is mapped to a unit sphere. However, this practice is not recommended, because the ellipsoid has to be centered in the origin to obtain good results. Secondly, the covariance pattern of the measurements is restricted to live in the tangent plane of the sphere, and thus the covariance of the projected measurement depends on the measured direction. Finally, it supposes a non-linear mapping containing square roots in contrast with the ellipsoid to sphere transformation which will be shown to correspond to a linear transformation.

Let the partitioned matrix

$$\mathbf{M} = \begin{pmatrix} \mathbf{M}' & \boldsymbol{k} \\ \boldsymbol{k}^\top & J \end{pmatrix}$$

define a generic ellipsoid whose boundary will be described by Eq. (4.6). Note that the points of the shifted ellipsoid can be though of as points of an ellipsoid centered in the origin under a translation. Let the homogeneous vector $\bar{\boldsymbol{x}}'$ define the unshifted points. The homogeneous transformation between those points can be represented by

$$\bar{\boldsymbol{x}} = \begin{pmatrix} \mathbf{I}_3 & \boldsymbol{t} \\ \mathbf{0}_{1\times 3} & 1 \end{pmatrix} \bar{\boldsymbol{x}}' \tag{4.7}$$

which certainly leads to

$$\begin{pmatrix} x \\ y \\ z \end{pmatrix} = \begin{pmatrix} x' \\ y' \\ z' \end{pmatrix} + \boldsymbol{t}$$

By introducing this change into Eq. (4.6), an equivalent ellipsoid equation can be obtained

$$\bar{\boldsymbol{x}}'^\top \begin{pmatrix} \mathbf{I}_3 & \mathbf{0}_{3\times 1} \\ \boldsymbol{t}' & 1 \end{pmatrix} \begin{pmatrix} \mathbf{M}' & \boldsymbol{k} \\ \boldsymbol{k}^\top & J \end{pmatrix} \begin{pmatrix} \mathbf{I}_3 & \boldsymbol{t} \\ \mathbf{0}_{1\times 3} & 1 \end{pmatrix} \bar{\boldsymbol{x}}' =$$

$$\bar{\boldsymbol{x}}'^\top \begin{pmatrix} \mathbf{M}' & \mathbf{M}'\boldsymbol{t} + \boldsymbol{k} \\ \boldsymbol{t}^\top \mathbf{M}' + \boldsymbol{k}^\top & \boldsymbol{t}^\top \mathbf{M}'\boldsymbol{t} + 2\boldsymbol{t}^\top \boldsymbol{k} + J \end{pmatrix} \bar{\boldsymbol{x}}' = 0$$

Given that an ellipsoid centered at the origin will have null G, H and I coefficients, by equating $\mathbf{M}'\boldsymbol{t} + \boldsymbol{k}$ to $\mathbf{0}_{3\times1}$ it can be found that

$$\boldsymbol{t} = -\mathbf{M}'^{-1}\boldsymbol{k} \tag{4.8}$$

which leads to

$$\bar{\boldsymbol{x}}'^{\top}\begin{pmatrix} \mathbf{M}' & \mathbf{0}_{3\times1} \\ \mathbf{0}_{1\times3} & J - \boldsymbol{k}^{\top}\mathbf{M}'^{-1}\boldsymbol{k} \end{pmatrix}\bar{\boldsymbol{x}}' = 0$$

or the equivalent representation

$$\bar{\boldsymbol{x}}'^{\top}\begin{pmatrix} \mathbf{M}'' & \mathbf{0}_{3\times1} \\ \mathbf{0}_{1\times3} & -1 \end{pmatrix}\bar{\boldsymbol{x}}' = 0 \tag{4.9}$$

with

$$\mathbf{M}'' = \frac{\mathbf{M}'}{\boldsymbol{k}^{\top}\mathbf{M}'^{-1}\boldsymbol{k} - J} \tag{4.10}$$

In a similar way to what has been done before to obtain the mapping between the points of the shifted ellipsoid and the unshifted one, it is possible to relate points of a centered unit sphere to a centered ellipsoid with generic orientation. For that purpose, an stretching can be applied to the principal axis of the sphere followed by a rotation. Let the homogeneous vector $\bar{\boldsymbol{x}}''$ define the points over the sphere, the homogeneous transformation between $\bar{\boldsymbol{x}}''$ and $\bar{\boldsymbol{x}}'$ can be represented by

$$\bar{\boldsymbol{x}}' = \begin{pmatrix} \mathbf{RD} & \mathbf{0}_{3\times1} \\ \mathbf{0}_{1\times3} & 1 \end{pmatrix}\bar{\boldsymbol{x}}'' \tag{4.11}$$

where $\mathbf{R}$ represents the rotation matrix and $\mathbf{D}$ is a diagonal matrix with the value of each semi-axis length at its diagonal

$$\mathbf{D} = \begin{pmatrix} r_x & 0 & 0 \\ 0 & r_y & 0 \\ 0 & 0 & r_z \end{pmatrix}$$

Introducing the change of coordinates from Eq. (4.11) into Eq. (4.9), the quadratic form for the sphere is obtained

$$\bar{\boldsymbol{x}}''^{\top}\begin{pmatrix} \mathbf{DR}^{\top} & \mathbf{0}_{3\times1} \\ \mathbf{0}_{1\times3} & 1 \end{pmatrix}\begin{pmatrix} \mathbf{M}'' & \mathbf{0}_{3\times1} \\ \mathbf{0}_{1\times3} & -1 \end{pmatrix}\begin{pmatrix} \mathbf{RD} & \mathbf{0}_{3\times1} \\ \mathbf{0}_{1\times3} & 1 \end{pmatrix}\bar{\boldsymbol{x}}'' = \tag{4.12}$$

$$\bar{\boldsymbol{x}}''^{\top}\begin{pmatrix} \mathbf{DR}^{\top}\mathbf{M}''\mathbf{RD} & \mathbf{0}_{3\times1} \\ \mathbf{0}_{1\times3} & -1 \end{pmatrix}\bar{\boldsymbol{x}}'' = 0 \tag{4.13}$$

Given that the quadratic form of a unit sphere takes the form

$$\bar{\boldsymbol{x}}''^{\top}\begin{pmatrix} \mathbf{I}_3 & \mathbf{0}_{3\times1} \\ \mathbf{0}_{1\times3} & -1 \end{pmatrix}\bar{\boldsymbol{x}}''$$

$$\mathbf{DR}^{\top}\mathbf{M}''\mathbf{RD} = \mathbf{I}_3 \Rightarrow \mathbf{M}'' = \mathbf{R}\left(\mathbf{D}^2\right)^{-1}\mathbf{R}^{\top} \tag{4.14}$$
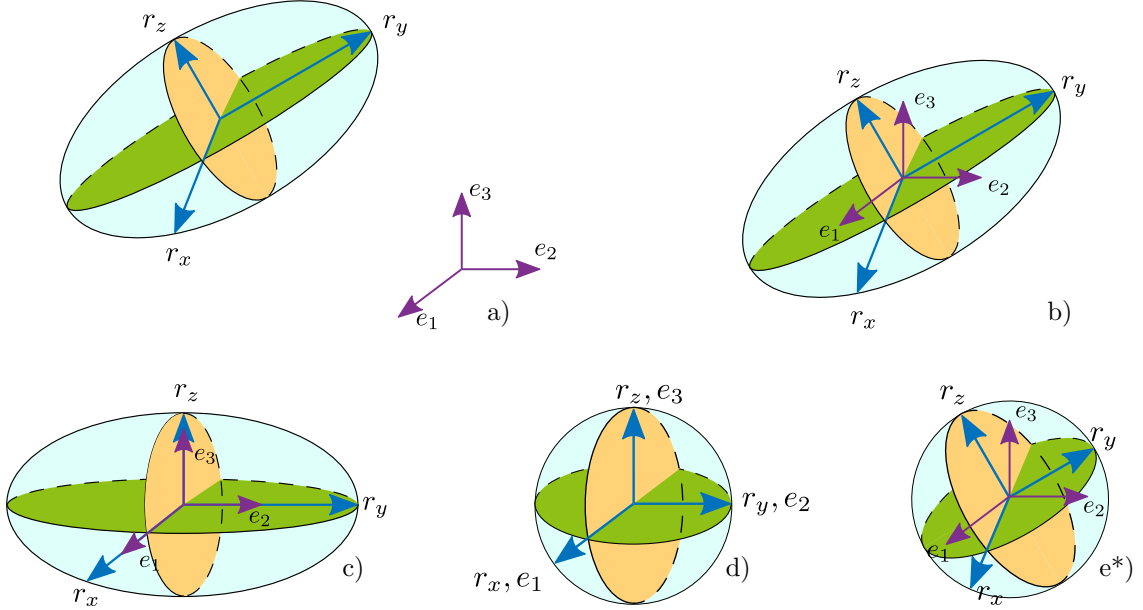
FIGURE 4.3: Steps for sensor calibration. a) Uncalibrated ellipsoid. b) Uncalibrated ellipsoid centered. c) Uncalibrated ellipsoid centered and derotated. d) Derotated sphere. e) Calibrated Sphere.

Note that $\mathbf{R}$ and $\mathbf{D}$ are closely related with the eigenvalue decomposition of $\mathbf{M}''$. In particular, the rotation matrix represents the matrix of eigenvectors and $\mathbf{D}$ as the square root of the inverse of eigenvalues of $\mathbf{M}''$.

The mapping between points in the sphere and the shifted ellipsoid can be described by using Eq. (4.7) and Eq. (4.11)

$$\boldsymbol{x} = \mathbf{R}\mathbf{D}\boldsymbol{x}'' + \boldsymbol{t} \tag{4.15}$$

whilst points in the ellipsoid map to points on the unit sphere by

$$\boldsymbol{x}'' = \mathbf{D}^{-1}\mathbf{R}^{\top}(\boldsymbol{x} - \boldsymbol{t}) \tag{4.16}$$

The parameters in the transformations, $\boldsymbol{t}$, $\mathbf{D}$ and $\mathbf{R}$, can be obtained from the original quadratic matrix $\mathbf{M}$ by using Eq. (4.8) and the eigenvalue decomposition of $\mathbf{M}''$ in Eq. (4.10).

The transformation in Eq. (4.16) ensures that points at the extremes of semi-axis map to vectors $\boldsymbol{e}_1 = (1, 0, 0)^{\top}$, $\boldsymbol{e}_2 = (0, 1, 0)^{\top}$, $\boldsymbol{e}_3 = (0, 0, 1)^{\top}$. However, the rotation matrix $\mathbf{R}$, as extracted from the eigenvalue decomposition, does not guarantee the correspondence $r_x \rightarrow \boldsymbol{e}_1$, $r_y \rightarrow \boldsymbol{e}_2$ or $r_x \rightarrow \boldsymbol{e}_3$, but instead provides an arbitrary ordering based on the eigenvalue calculation method. The rotation matrix $\mathbf{R}$ can be used to rotate the sphere and align the sphere basis with the sensor frame to fully define the calibration. Fig. 4.3 depicts the transformations involved in the calibration process and the final calibration mapping is described by Eq. (4.17), where x_{uncal} represents the raw data and $\boldsymbol{x}_{cal}$ the calibrated version.

$$\boldsymbol{x}_{cal} = \mathbf{R}\mathbf{D}^{-1}\mathbf{R}^{\top}(\boldsymbol{x}_{uncal} - \boldsymbol{t}) \tag{4.17}$$

Parameter calibration

This section describes how to proceed with the magnetometer calibration, i.e., how to estimate the magnetometer ellipsoid given a set of measurements represented by N readings of three dimensional points (x_i, y_i, z_i).

Algebraic ellipsoidal fit An algebraic approach to solve the calibration is based on the extraction of the ellipsoid parameters that minimize in the least square sense the errors of Eq. (4.5). As stated before, the 10 parameters are not unique, and they represent the ellipsoid with an additional degree of freedom. The most direct approach would be to fix one parameter of the ellipsoid to restrict the degree of freedom, and then try to estimate the remaining ones. The choice of the parameter to fix has to be done with care, since several orders of magnitude may exist between them depending on the ellipsoid size, which may lead to numerical inaccuracies in the estimation. By definition, Eq:ellipsoidMag0 represents an ellipsoid if A, B and C share sign. Assuming that these parameters are positive, the extra degree of freedom can be eliminated by fixing one of them or the sum of them, $A + B + C = T$, being T a positive constant as suggested in [87]. In this case, the parameters A, B and C can be substituted by a linear combination of two modified parameters, say U_1 and U_2 as

$$A = U_1 + U_2 + \frac{T}{3}$$
$$B = U_1 - 2U_2 + \frac{T}{3}$$
$$C = U_2 - 2U_1 + \frac{T}{3}$$

Once the system is constrained, a linear regression model can be constructed. For each set of three dimensional data (x_i, y_i, z_i) a scalar equation linear on parameters can be formulated as

$$\boldsymbol{\phi}\boldsymbol{\theta} = b \tag{4.18}$$

with

$$\boldsymbol{\phi}_i = \left((x_i^2 + y_i^2 - 2z_i^2),\ (x_i^2 - 2y_i^2 + z_i^2),\ 2x_iy_i,\ 2x_iz_i,\ 2y_iz_i,\ 2x_i,\ 2y_i,\ 2z_i,\ 1\right)$$

$$\boldsymbol{\theta} = (U_1,\ U_2,\ D,\ E,\ F,\ G,\ H,\ I,\ J)^\top$$

$$b_i = -(x_i^2 + y_i^2 + z_i^2)$$

for having constrained $A + B + C = 3$, or which is equivalent having set $T = 3$.

Stacking N $\boldsymbol{\phi}_i$ vectors and N b_i independent values, an $N \times 9$ linear system can be constructed

$$\underbrace{\begin{pmatrix} \boldsymbol{\phi}_1 \\ \boldsymbol{\phi}_2 \\ \vdots \\ \boldsymbol{\phi}_N \end{pmatrix}}_{\Phi} \boldsymbol{\theta} = \underbrace{\begin{pmatrix} b_1 \\ b_2 \\ \vdots \\ b_N \end{pmatrix}}_{b}$$

whose least square error solution can be found for $N > 9$ as

$$\boldsymbol{\theta}_{LS} = \left(\boldsymbol{\Phi}^\top \boldsymbol{\Phi}\right) \boldsymbol{\Phi}^\top \boldsymbol{b}$$

Geometric ellipsoidal fit   The algebraic solution of the ellipsoid fitting provided in the last section is an exact solution only for unperturbed data. When noise is present in the data set, the ellipsoid obtained minimizes the quadratic error of the solution of Eq. (4.5). However, this does not guarantee that the obtained ellipsoid represents the obtained data.

In order to obtain a more representative ellipsoid, a geometric fitting can be used, which consists in minimizing the geometrical distance. The ellipsoid geometrical fit tries to fit the ellipsoid parameters so that the distance of the measured points to the boundary of the ellipsoid is minimized. The distance of a generic point to the boundary of an ellipsoid represented by a matrix $\mathbf{M}$ is not straightforward, since it will depend on the relative orientation of the point with respect to the ellipsoid main axis. By mapping ellipsoid points to a unit sphere Eq. (4.16), the distance from the mapped point i to the unit sphere can be simply calculated as

$$d_i = \left|1 - \boldsymbol{x}_i''^\top \boldsymbol{x}_i''\right| = \left|1 - (\boldsymbol{x}_i - \boldsymbol{t})^\top \mathbf{R}(\mathbf{D}^{-1})^2 \mathbf{R}^\top (\boldsymbol{x}_i - \boldsymbol{t})\right| = \\ \left|1 - (\boldsymbol{x}_i - \boldsymbol{t})^\top \mathbf{M}'' (\boldsymbol{x}_i - \boldsymbol{t})\right|$$

The associated matrix of the ellipsoid which minimizes the geometric distance can be obtained as the solution of the next minimization problem

$$\mathbf{M}^\star = \underset{\mathbf{M}}{\operatorname{argmin}} \frac{1}{N} \sum_{i=1}^{N} d_i(\boldsymbol{x}_i, \mathbf{M}) \tag{4.19}$$

In practice, the minimization problem in Eq. (4.19) is not well-posed from a numerical perspective when the data set contains noise. If that is the case, a very big ellipsoid, with center out of the data set, and at least one semi-axis bigger that the nominal data set size could be proposed such that after the mapping, all the transformed points are concentrated in a small neighbourhood of a sphere boundary point in such a way that the geometrical error is minimized.

To avoid that issue, the optimization problem is formulated as a function of the matrix $\mathbf{M}''$ and the distance vector $\boldsymbol{t}$, which is constrained to be confined to the interior of a bounding box containing the data set, i.e, $\underline{\boldsymbol{t}} \leq \boldsymbol{t} \leq \bar{\boldsymbol{t}}$ with $\underline{\boldsymbol{t}}$ and $\bar{\boldsymbol{t}}$ representing respectively the minimum and maximum x, y and z values in the dataset. The minimization problem can be read as

$$\begin{aligned} \left(\mathbf{t}^\star, (\mathbf{M}'')^\star\right) \quad &= \underset{\mathbf{t}, \mathbf{M}''}{\operatorname{argmin}} \frac{1}{N} \sum_{i=1}^{N} d_i(\boldsymbol{x}_i, \mathbf{t}, \mathbf{M}'') \\ \text{subject to} \quad &\quad \boldsymbol{t} \geq \underline{\boldsymbol{t}} \\ &\quad \underline{\boldsymbol{t}} \leq \boldsymbol{t} \end{aligned} \tag{4.20}$$

Solutions of that problem can been obtained by using constrained minimization algorithms. In particular in this thesis this problem is solved by using the `fmincon` solver in MatLab .
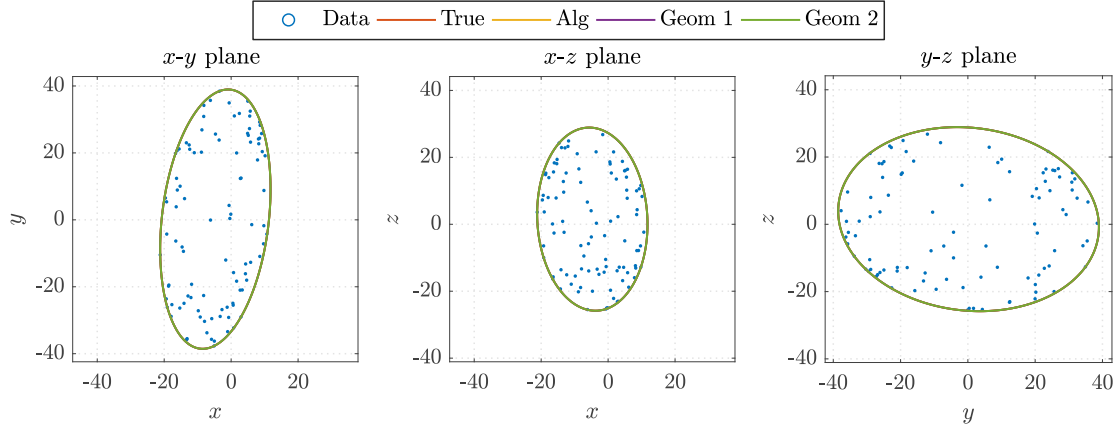
FIGURE 4.4: Ellipsoid fitting of ideal data.

3-axial sensor synthetic calibration results

In order to show the results of the fitting techniques presented, synthetic data with random points distributed over the boundary of a known ellipsoid have been used. Three scenarios are presented: with perfect known data, with noisy data in a case where the geometric fit in Eq. (4.19) delivers a solution for the ellipsoid center outside the data set, and a scenario with noisy data where results of Eq. (4.19) and Eq. (4.20) coincide. The used data could represent any generic physical quantity as seen for a 3-axial sensor, so no units are used to give generality to the results.

Ideal Data   For the first scenario a set of 100 points have been generated over an ellipsoid. The parameters used are shown in Table 4.2, and the fitting results are shown in Fig. 4.4, where the projection of the ellipsoid over the x-y, x-z and y-z planes. In this case it can be seen that all the fittings collapse in the true results.

Parameter	t	$\mathbf{R}$			diag $(\mathbf{D})$
Sim. True	$\begin{pmatrix} 3.38 \\ 4.29 \\ -3.46 \end{pmatrix}$	$\begin{pmatrix} 0.37 & 0.45 & 0.81 \\ 0.66 & 0.49 & -0.57 \\ -0.66 & 0.75 & -0.12 \end{pmatrix}$			$\begin{pmatrix} 23.24 \\ 30.25 \\ 12.15 \end{pmatrix}$

TABLE 4.2: Ideal data parameters

Noisy data   Next, we present a simulation for which the optimization problem in Eq. (4.19) delivers a solution for the ellipsoid center outside the data set. Again, 100 points have been generated over an ellipsoid whose parameters appear in the first column of Table 4.3. In this case, noise has been added to the raw data as a Gaussian random variable with null mean and unit covariance. Information of the estimated ellipsoid parameters is provided also in Table 4.3. In addition, we present the sum of the geometric distance for each point to the boundaries of each ellipsoid considered. It can be seen that in this case, the ideal ellipsoid does not represent the best fit to the noisy data. Moreover, the values obtained by the geometric fit based on
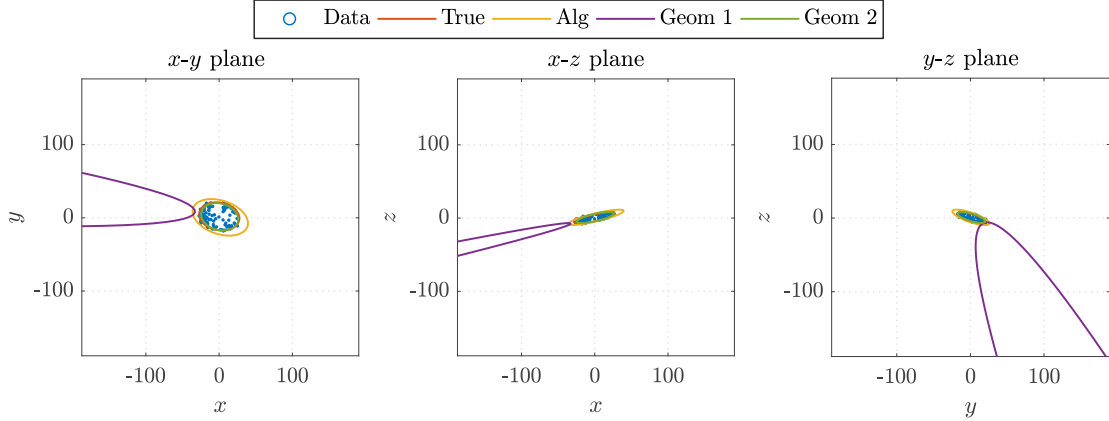
FIGURE 4.5: Results of the fitted ellipsoids when Eq. (4.19) provides a center estimation out of the data set range.

Eq. (4.19), are not representative despite having low geometrical distance (in the sphere space). Figs. 4.5 and 4.6 show the projection of the calculated ellipsoid over the x-y, x-z and y-z planes.

Parameter	t	$\mathbf{R}$			diag $(\mathbf{D})$	$\sum_{i=1}^{N} d_i$
Sim. True	$\begin{pmatrix} -0.25 \\ 1.94 \\ 0.38 \end{pmatrix}$	$\begin{pmatrix} 0.95 & 0.25 & -0.17 \\ -0.21 & 0.95 & 0.23 \\ 0.22 & -0.18 & 0.96 \end{pmatrix}$			$\begin{pmatrix} 28.4 \\ 19.20 \\ 1.16 \end{pmatrix}$	0.270
Alg.Fit	$\begin{pmatrix} 1.64 \\ 0.63 \\ 1.00 \end{pmatrix}$	$\begin{pmatrix} 0.91 & 0.37 & -0.18 \\ -0.32 & 0.95 & 0.22 \\ 0.24 & -0.14 & 0.96 \end{pmatrix}$			$\begin{pmatrix} 40.35 \\ 23.10 \\ 1.33 \end{pmatrix}$	0.266
Geom. Fit Eq. (4.19)	$\begin{pmatrix} -4.60 \\ 0.49 \\ -1.2 \end{pmatrix} 10^6$	$\begin{pmatrix} 0.97 & 0.15 & -0.18 \\ -0.10 & 0.97 & 0.24 \\ 0.22 & -0.22 & 0.95 \end{pmatrix}$			$\begin{pmatrix} 3.93 \cdot 10^2 \\ 4.54 \cdot 10^3 \\ 4.74 \cdot 10^6 \end{pmatrix}$	$1.3 \cdot 10^{-5}$
Geom. Fit Eq. (4.20)	$\begin{pmatrix} -0.76 \\ 1.34 \\ 0.86 \end{pmatrix}$	$\begin{pmatrix} 0.92 & 0.34 & -0.18 \\ -0.29 & 0.3 & 0.23 \\ 0.24 & -0.16 & 0.96 \end{pmatrix}$			$\begin{pmatrix} 26.48 \\ 18.41 \\ 2.50 \end{pmatrix}$	0.14

TABLE 4.3: Calibration transformation parameters for noisy data where the unconstrained geometric fitting results in an ellipsoid with center out of the data range.

The convergence of the geometric fit in Eq. (4.19) will usually depend on the data set and the noise present in it. Even though a divergence of the fit was a possible result, it did not take place for the experiments carried out. In the case of Eq. (4.19) producing an ellipsoid with center inside the data set, both Eq. (4.19) and Eq. (4.20) deliver exactly the same solution. Table 4.4 and Fig. 4.7 show the simulation results where this took place. Again 100 points have been selected and the have been corrupted with a Gaussian noise of zero mean and unit covariance.

Magnetometer experimental data

We have selected a data set containing 4975 points of the magnetometer measurements during 165 s approx. Units of the magnetic field are not provided by the manufacturer, under the argument of not being necessary for direction determination, thus units are not provided in the
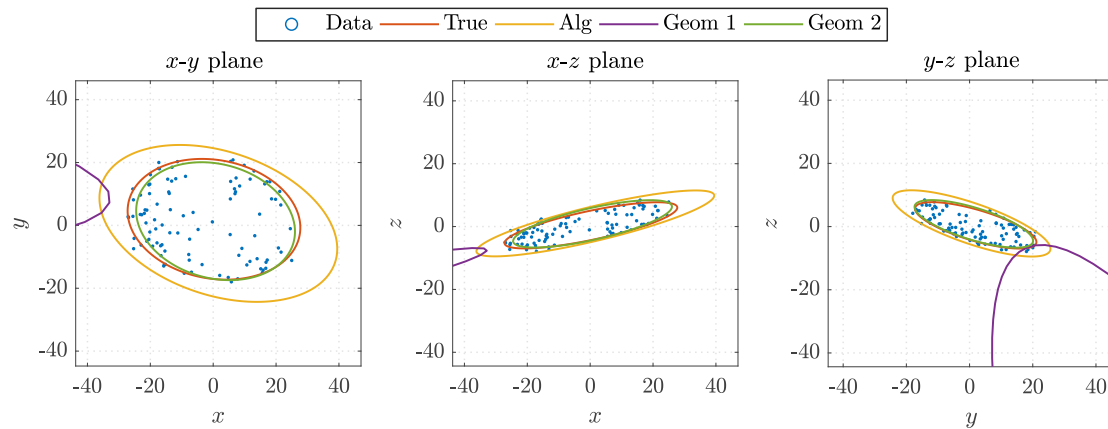
FIGURE 4.6: Detail of the fitted ellipsoids when Eq. (4.19) provides a center estimation out of the data set range.
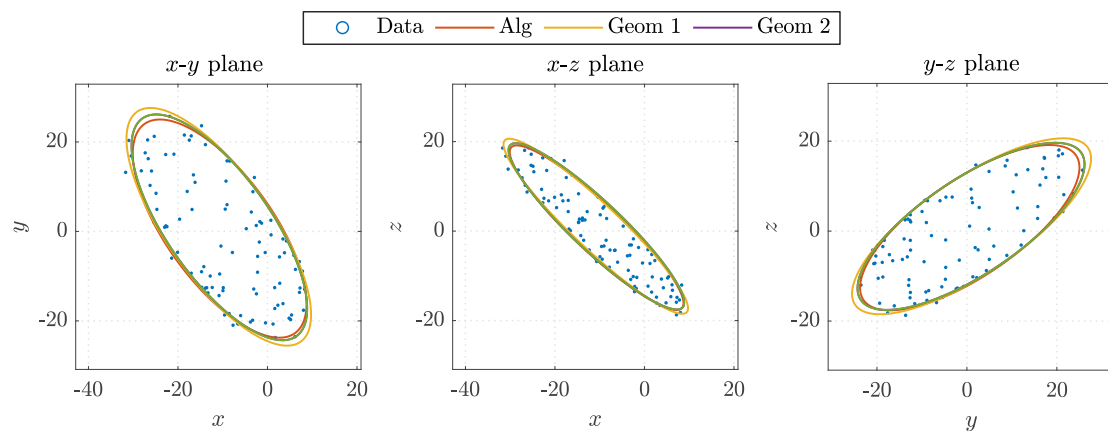
FIGURE 4.7: Results of the fitted ellipsoid in the case that Eq. (4.19) provides a centre's estimation contained in the data range.

Parameter	t	$\mathbf{R}$			diag $(\mathbf{D})$	$\sum\limits_{i=1}^{N} d_i$
Sim. True	$\begin{pmatrix} -10.68 \\ 0.63 \\ 0.76 \end{pmatrix}$	$\begin{pmatrix} 0.66 & 0.53 & -0.53 \\ -0.06 & 0.74 & 0.67 \\ 0.75 & -0.41 & 0.51 \end{pmatrix}$			$\begin{pmatrix} 5.3 \\ 13.35 \\ 33.21 \end{pmatrix}$	0.077
Alg.Fit	$\begin{pmatrix} -10.88 \\ 1.03 \\ 1.08 \end{pmatrix}$	$\begin{pmatrix} 0.66 & 0.53 & -0.53 \\ -0.044 & 0.73 & 0.68 \\ 0.75 & -0.43 & 0.51 \end{pmatrix}$			$\begin{pmatrix} 5.00 \\ 13.22 \\ 36.24 \end{pmatrix}$	0.078
Geom. Fit Eq. (4.19) & Eq. (4.20)	$\begin{pmatrix} -10.75 \\ 0.92 \\ 1.05 \end{pmatrix}$	$\begin{pmatrix} 0.66 & 0.53 & -0.53 \\ -0.04 & 0.73 & 0.68 \\ 0.75 & -0.44 & 0.50 \end{pmatrix}$			$\begin{pmatrix} 5.47 \\ 13.03 \\ 34.16 \end{pmatrix}$	0.74

TABLE 4.4: Calibration transformation parameters for noisy data where the unconstrained geometric fitting have converged, naturally.

magnetometer data that follows. A visual representation of the data is provided in Figs. 4.8 and 4.9. It can be observed that measurements are not centered at the origin and that an ellipsoid elongation near the sensor z axis is greater than in the other directions.

The calibration procedure has been tuned to produce magnetometer measurements with an approximate norm of 1000, to maintain sensor output levels in the ideal undistorted case by dividing the ellipsoid semiaxis by this amount. The obtained parameters are presented in Table 4.5, and the fitted ellipsoids are shown along with the projected data in Fig. 4.9. In this case, the transformation parameters derived by the algebraic and geometric fittings are very close and produce very similar accumulated geometric distances.

Parameter	t	$\mathbf{R}$			diag $(\mathbf{D})$	$\sum\limits_{i=1}^{N} d_i$
Alg.Fit	$\begin{pmatrix} 74.27 \\ 92.00 \\ -891.67 \end{pmatrix}$	$\begin{pmatrix} 0.97 & 0.16 & 0.18 \\ -0.21 & 0.94 & 0.28 \\ -0.13 & -0.31 & 0.94 \end{pmatrix}$			$\begin{pmatrix} 2.77 \\ 3.27 \\ 3.43 \end{pmatrix}$	$3.83 \cdot 10^{-2}$
Geom. Fit Eq. (4.19) & Eq. (4.20)	$\begin{pmatrix} 86.22 \\ 90.26 \\ -886.96 \end{pmatrix}$	$\begin{pmatrix} 0.97 & 0.18 & 0.17 \\ -0.22 & 0.92 & 0.33 \\ -0.09 & -0.35 & 0.93 \end{pmatrix}$			$\begin{pmatrix} 2.7883 \\ 3.2703 \\ 3.4159 \end{pmatrix}$	$3.8 \cdot 10^{-2}$

TABLE 4.5: Calibration parameters for the experimental magnetometer measurements.

The calibrated data set is shown in Figs. 4.11, 4.12 and 4.13 for the algebraic parameters under the transformation in Eq. (4.17). Results show the improvement of covariance of the magnetometer norm, the range of measurements in every direction and a better detection of spurious values.

Accelerometer experimental data

The measurement of accelerometers represent the acceleration of external forces. Calibrating those sensors using the previously presented methods requires a constant measurement in the world frame. This can be achieved by measuring the reaction force of the weight in static
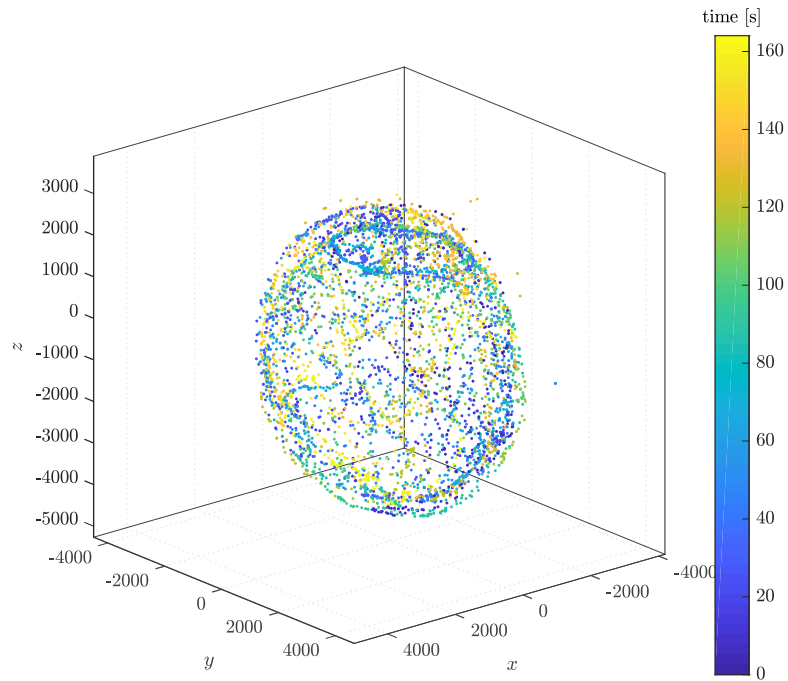
FIGURE 4.8: 3D representation of the magnetometer data.
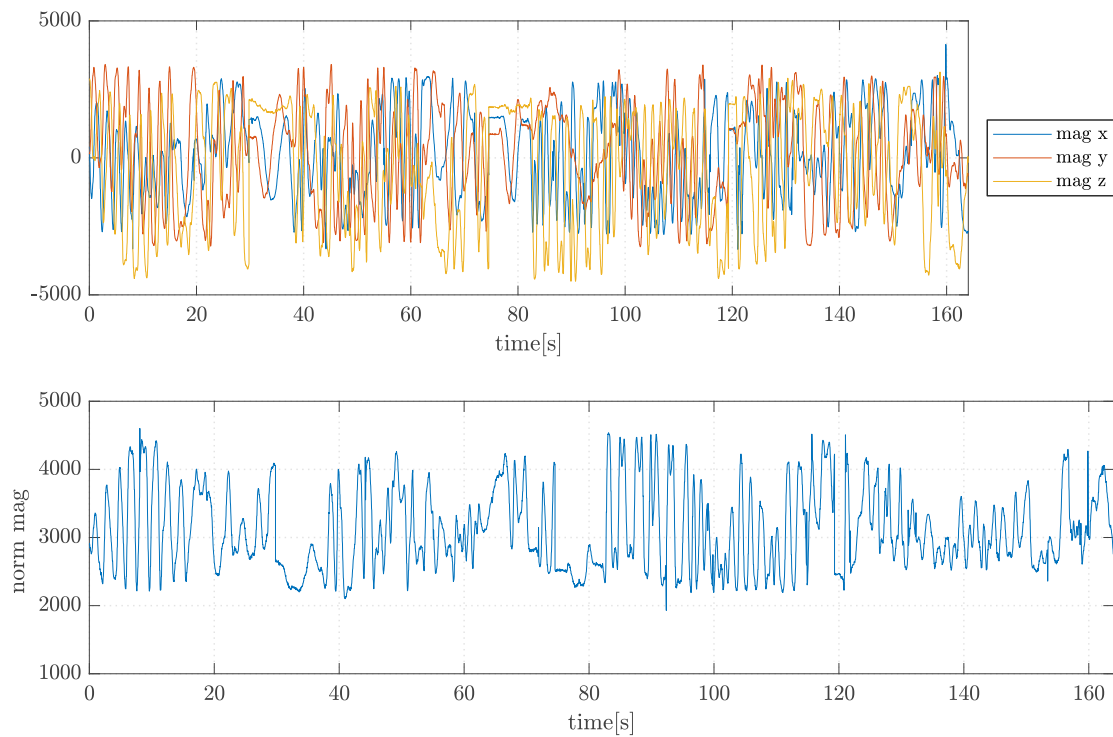
FIGURE 4.9: Temporal representation of the magnetometer components and norm.
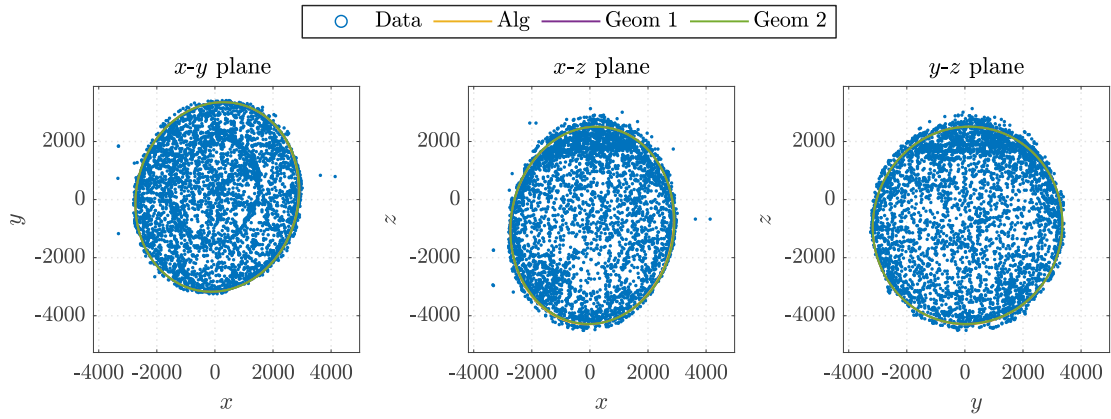
FIGURE 4.10: Projection of experimental data over the x-y, x-z and y-z planes and projection of the algebraic and geometric fitted ellipsoids.
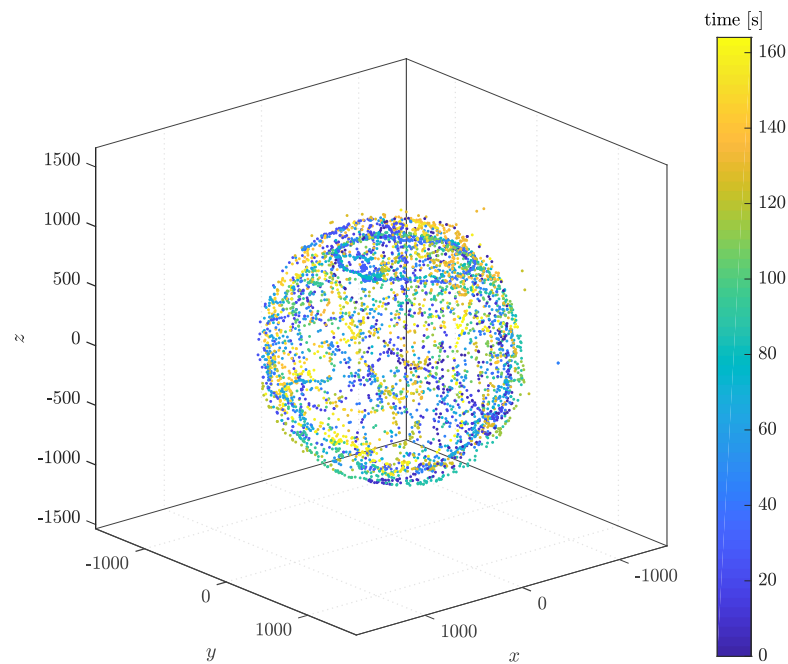
FIGURE 4.11: 3D calibrated points
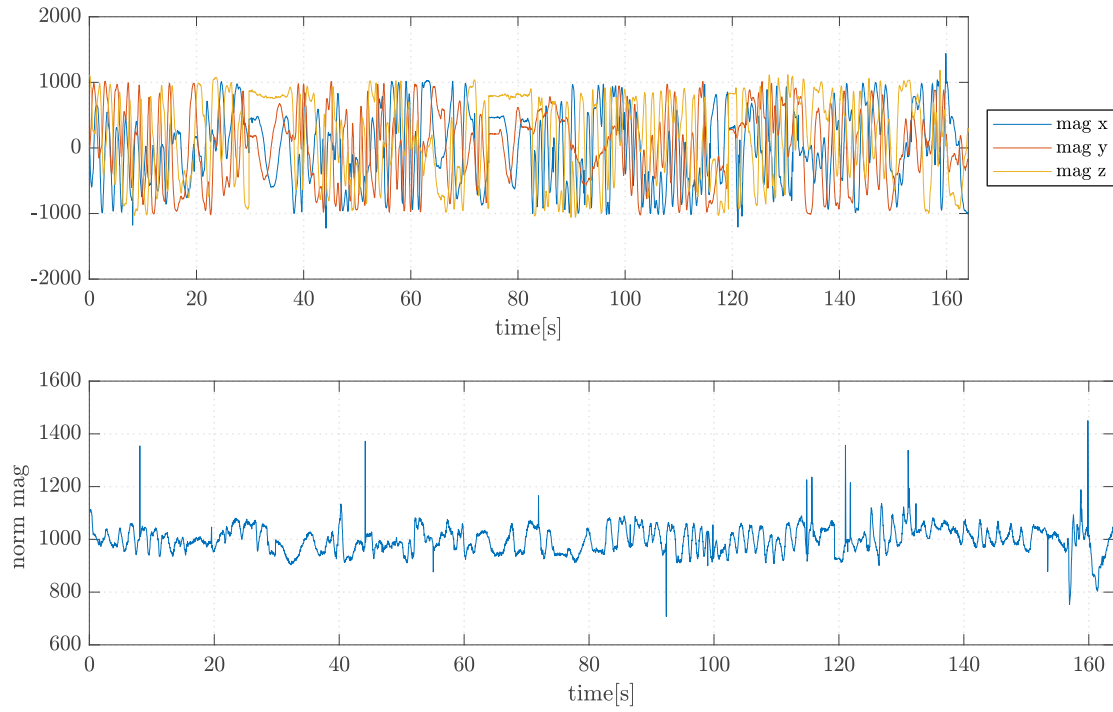
FIGURE 4.12: Temporal representation of the magnetometer calibrated measurements and their norm.
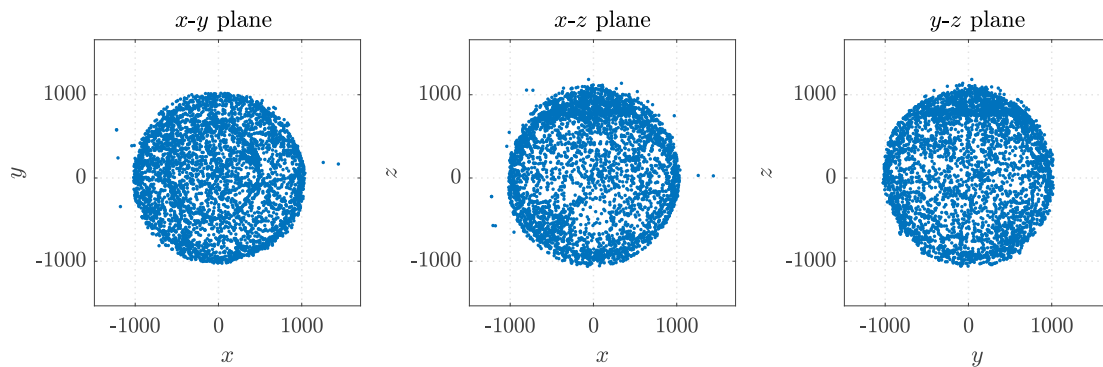
FIGURE 4.13: Projection of the calibrated data over the x-y, x-z and y-z planes
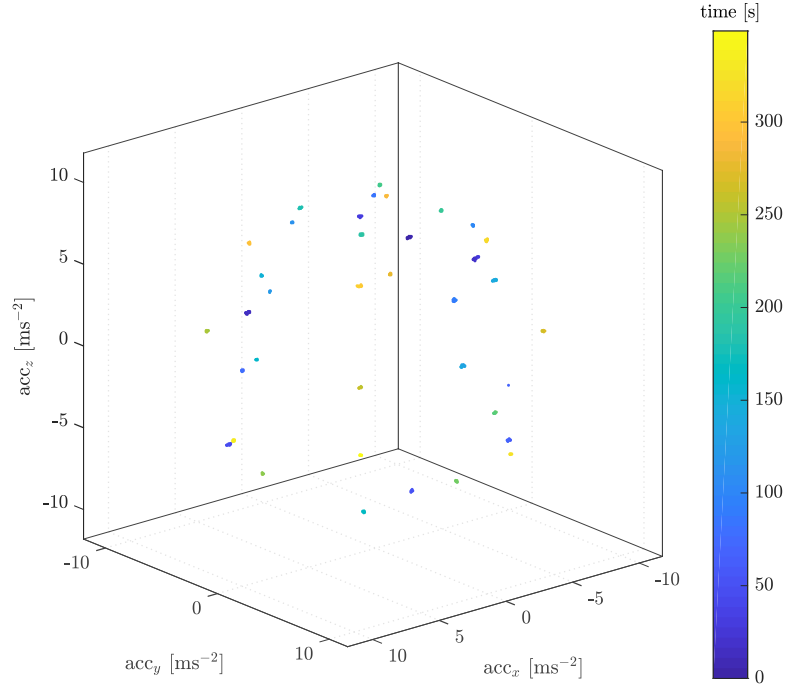
FIGURE 4.14: Accelerometer raw data

conditions through different orientations. Data of accelerometers at 36 different attitude configurations has been collected with the aircraft at rest covering the possible ellipsoid for a period of approximately 10s at 100Hz. The results of the uncalibrated data are shown in Fig. 4.14.

The model fitting over the ellipsoid has produced the results shown in Table 4.6 where the mapping has been fixed to reproduce a ball of radius $9.81 \, \mathrm{ms}^{-2}$. Note that results are very similar except for the rotation matrix. This is not surprising taking into account the roundness of the raw data that can be observed in Fig. 4.15, where the projection of the fitted ellipsoid to the raw data is shown. The more similar the initial data to a sphere is, less effect has the rotation matrix. In the extreme case in which the raw data describes a perfect sphere, the rotation matrix does not affect the result.

Parameter	t	$\mathbf{R}$			$\mathrm{diag}\,(\mathbf{D})$	$\sum_{i=1}^{N} d_i$
Alg.Fit	$\begin{pmatrix} 0.038 \\ -0.089 \\ -0.027 \end{pmatrix}$	$\begin{pmatrix} -0.18 & 0.37 & -0.9100 \\ -0.73 & -0.67 & -0.1300 \\ -0.66 & 0.64 & 0.39 \end{pmatrix}$			$\begin{pmatrix} 0.99 \\ 1.00 \\ 1.01 \end{pmatrix}$	$4.16 \cdot 10^{-3}$
Geom. Fit Eq. (4.19) & Eq. (4.20)	$\begin{pmatrix} 0.031 \\ -0.094 \\ -0.027 \end{pmatrix}$	$\begin{pmatrix} -0.18 & 0.37 & -0.91 \\ -0.73 & -0.67 & -0.13 \\ -0.66 & 0.64 & 0.39 \end{pmatrix}$			$\begin{pmatrix} 0.99 \\ 1.00 \\ 1.01 \end{pmatrix}$	$4.11 \cdot 10^{-3}$

TABLE 4.6: Calibration parameters for the experimental accelerometer measurements.

Given the finite number of configurations and despite the similarity of the results, the algebraic calibration results have been taken over the goemetric ones to avoid the possible shift of the geometric solution towards more densely sampled areas. Differences between raw and calibrated
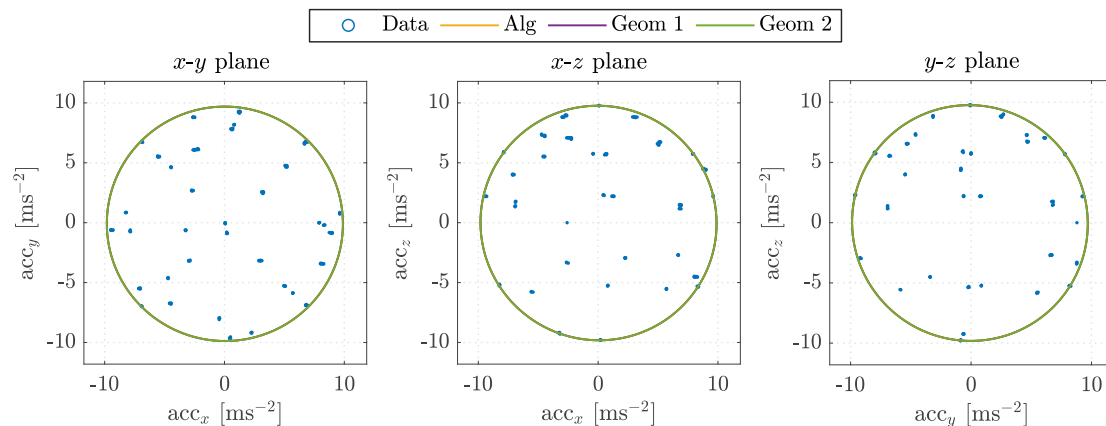
FIGURE 4.15: Accelerometer raw data projection and ellipsoidal fit projection.
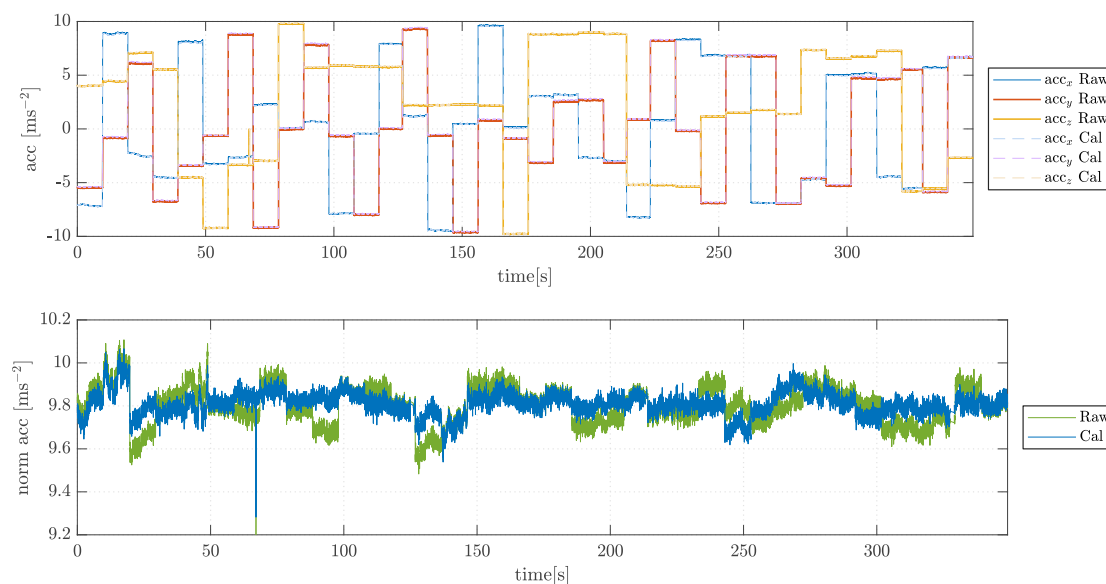
FIGURE 4.16: Raw data and calibrated data comparison.

measurements are presented in Fig. 4.16 where it can be seen that the calibration effect almost does not affect single axis measurements, but it has an impact over the acceleration norm. This can be observed in Fig. 4.17, where the distribution of the magnitude of the calibrated and raw data are presented. It can be stated that after calibration, the data dispersion shifts from a bi-modal shape to a symmetric uni-modal one.

Gyroscope experimental data

Calibrating gyroscopes has an increased difficulty compared with the previous sensors. It is difficult to reproduce a situation in which a constant and well known angular velocity acts over the aircraft. In this case, the assumption of unit per axis gain will be made for the gyroscope measurements.
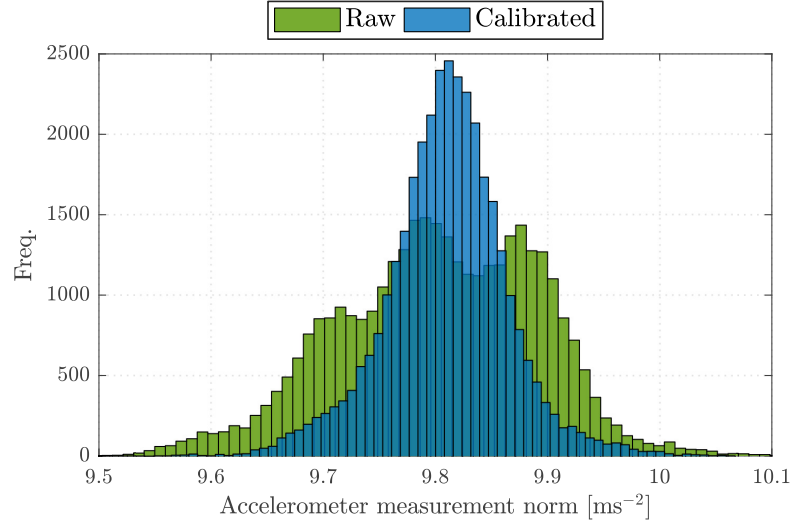
FIGURE 4.17: Raw data and calibrated data norm distribution.

4.3.2   Sensor error estimation

Sensor models in Eqs. 4.4, 4.3 and 4.2 include stochastic terms that reproduce the random behaviour or noise noticeable at the real sensors output. The study and quantification of this error fluctuation is interesting since it provides a measure of the precision and accuracy of the sensor outputs and thus a measure of the reliability when using this sensors to feed a controller. Under the hypothesis of Gaussian white noise, i.e., the noise is a random process that take values for any time instant t and is represented by a zero mean, finite covariance random variable which is independent of previous realizations,

$$\boldsymbol{\eta}(t) \sim \mathcal{N}\left(\mathbf{0}, \mathbf{Q}\right) \quad \text{and} \quad E\left(\boldsymbol{\eta}(t)\boldsymbol{\eta}^{\top}(\tau)\right) = \mathbf{Q}\delta(t - \tau)$$

where $E\left(\bullet\right)$ represents the expected value function, $\mathbf{Q}$ represents the signal covariance and $\delta(t-\tau)$ represents the dirac's delta function

$$\delta(t-\tau)\begin{cases} 1 & \text{if } t = \tau \\ 0 & \text{otherwise} \end{cases}$$

The sensor models presented in Section 4.2 are continuous. However, the estimation of noise will be made from the sensor's output sampled at constant rates. To this end, we need to relate the discrete and continuous versions of variables involved and their covariance. To this purpouse, let the algebraic model

$$\boldsymbol{z}_1(t) = \boldsymbol{\eta}_1(t)$$

being $\boldsymbol{\eta}_1$ a random Gaussian variable with covariance $\mathbf{Q}_1\delta(t-\tau) \in \mathbb{R}^{n \times n}$. For every time interval limited by consecutive sample times, $t \in [t_0, t_0 + \Delta t]$ we can estimate the discrete version of $\boldsymbol{z}(t)$

as its mean in the interval represented by

$$\boldsymbol{z}_1(k) \approx \bar{\boldsymbol{z}}(t_0 + \Delta t) = \frac{1}{\Delta t} \int_{t_0}^{t_0 + \Delta t} \boldsymbol{\eta}_1(t) \mathrm{d}t$$

The covariance of $\boldsymbol{z}_1(k)$ is then

$$\mathbf{Q}_{d_1} = E\left(\bar{\boldsymbol{z}}(t_0 + \Delta t) \bar{\boldsymbol{z}}^{\top}(t_0 + \Delta t)\right) = \frac{1}{(\Delta t)^2} \int_{t_0}^{t_0 + \Delta t} \boldsymbol{\eta}(t) \mathrm{d}t \int_{t_0}^{t_0 + \Delta t} \boldsymbol{\eta}(\tau) \mathrm{d}\tau =$$

$$\frac{\mathbf{Q}_1}{(\Delta t)^2} \int_{t_0}^{t_0 + \Delta t} \int_{t_0}^{t_0 + \Delta t} \delta(t - \tau) \mathrm{d}t \mathrm{d}\tau = \frac{\mathbf{Q}_1}{\Delta t} \qquad (4.21)$$

hence

$$\boldsymbol{z}_1(k) \sim \mathcal{N}\left(\mathbf{0}, \frac{\mathbf{Q}_1}{\Delta t}\right) \quad \text{and} \quad \boldsymbol{\eta}(k)\boldsymbol{\eta}^{\top}(l) = \mathbf{Q}_{d_1} \text{ for } k = l$$

In a similar way, given a dynamic variable $\boldsymbol{z}(t) \in \mathbb{R}^n$ for which it is known that

$$\dot{\boldsymbol{z}}(t) = \boldsymbol{\eta}_2(t)$$

being $\boldsymbol{\eta}_2$ a random Gaussian variable with covariance $\mathbf{Q}_2 \delta(t - \tau) \in \mathbb{R}^{n \times n}$, its discrete counterpart at time $t_0 + \delta t$ can be calculated by knowing the value of z at time t_0, $z(t_0)$, by

$$\boldsymbol{z}(t_0 + \Delta t) = \boldsymbol{z}(t) + \int_{t_0}^{t_0 + \Delta t} \boldsymbol{\eta}_2(t) \mathrm{d}t,$$

as a consequence the discrete model will have an stochastic noise represented by

$$\boldsymbol{\eta}_d = \int_{t_0}^{t_0 + \Delta t} \boldsymbol{\eta}_2(t) \mathrm{d}t$$

with null mean and covariance

$$\mathbf{Q}_{d_2} = E\left(\left(\int_{t_0}^{t_0 + \Delta t} \boldsymbol{\eta}_2(t) \mathrm{d}t\right)\left(\int_{t_0}^{t_0 + \Delta t} \boldsymbol{\eta}_2^{\top}(\tau) \mathrm{d}\tau\right)\right) = \mathbf{Q}_2 \int_{t_0}^{t_0 + \Delta t} \int_{t_0}^{t_0 + \Delta t} \delta(t - \tau) \mathrm{d}t \mathrm{d}\tau = \mathbf{Q}_2 \Delta t$$

$$(4.22)$$

resulting in

$$\boldsymbol{z}(k+1) \sim \mathcal{N}\left(\boldsymbol{z}(k), \mathbf{Q}_2 \Delta t\right) \quad \text{and} \quad \boldsymbol{\eta}_2(k)\boldsymbol{\eta}_2^{\top}(l) = \mathbf{Q}_{d_2} \text{ for } k = l$$

subsequently,

$$\boldsymbol{\eta}_2(k) \sim \mathcal{N}\left(\mathbf{0}, \mathbf{Q}_2 \Delta t\right)$$

The sample covariance $\tilde{\mathbf{Q}}$, an unbiased estimator of any discrete covariance $\mathbf{Q}_d$ can be obtained from a set of N discrete measurements of the vector $\boldsymbol{z}$. Let z_{ij} define the j-th measurement of the i-th component of $\boldsymbol{z}$, then the sample covariance is a matrix $\tilde{\mathbf{Q}} \in \mathbb{R}^{n \times n}$ where each i, j entry is defined as

$$\tilde{Q}_{ij} = \frac{1}{N-1} \sum_{k=1}^{N} \left(a_{ik} - \frac{1}{N} \sum_{j=1}^{N} (a_{ij})\right)\left(a_{jk} - \frac{1}{N} \sum_{i=1}^{N} (a_{ji})\right) \qquad (4.23)$$

GPS error estimation

Real GPS measurements suffer from smooth random walks that cannot be obviated in general. An example of GPS measurement taken during a lapse of 5 min with the receiver at rest can be seen in Fig. 4.18 and Fig. 4.20, being φ, λ and h, the latitude, longitude and altitude of the reciever with respect the WGS84 frame (see Ap. D). The representation in the local world NED frame with origin given by the first instance of the GPS measurement, φ_0 = 41.5610803 deg, λ_0 = 2.0209686 deg, h_0 = 3.46813 m, of the measurements is achieved by applying the transformation in Eq. (D.5) and is shown in Fig. 4.19 and Fig. 4.21.
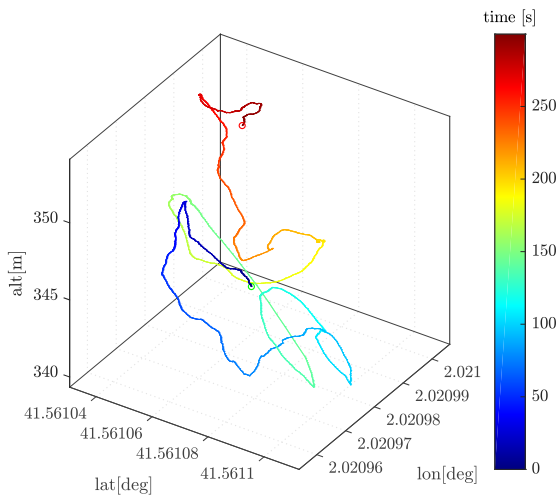
FIGURE 4.18: GPS raw data
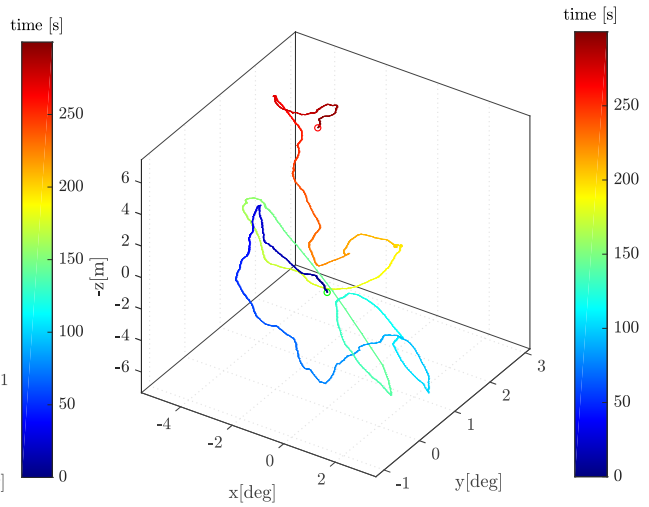
FIGURE 4.19: GPS raw data transformed to NED frame. The z coordinate have been reversed in order to make a direct visual comparison with Fig. 4.18

Taking into account internal dynamics on the GPS, in a similar way to what is done with accelerometers and gyroscopes is not feasible given that there is no other measurement of postition to compare with, and information integrated from accelerometers does not allow to correct bias of the position. In spite of this fact, measurements of the GPS are not useless as they provide position measurements with a prescribed degree of accuracy and in an incremental way they could be used to provide better estimations of the velocity. To this end it is desired to find a covariance for the GPS model in Eq. (4.4) with the additional restriction of being consistent with the velocity quantities inherent to the GPS.

An approximation of the derivative of the GPS readings by using finite differences is presented in Fig. 4.22 and a histogram representing its distribution is shown in Fig. 4.23.

In Eq. (4.23) it can be observed that the error distributions are approximately symmetric and that the central values are contained in the neighbourhood of zero. Here, the hypotheses of admitting the derivatives of the GPS measurements distributed as normal random variables with null mean is justified. The estimated sample variances for the estimated velocities have
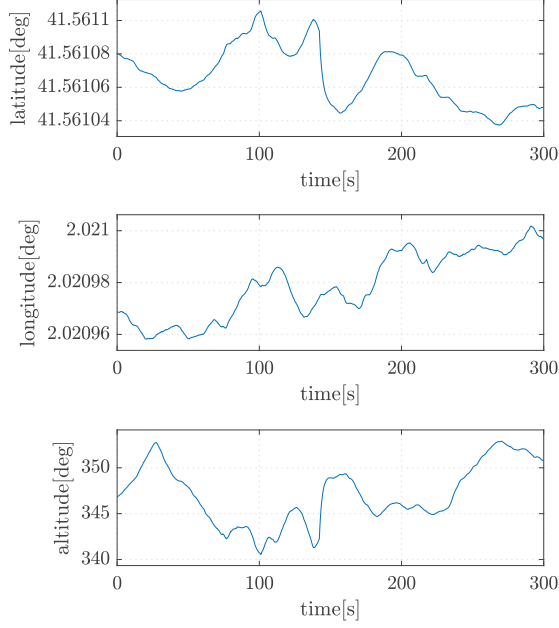
FIGURE 4.20:   GPS latitude, longitude
and altitude data time historic
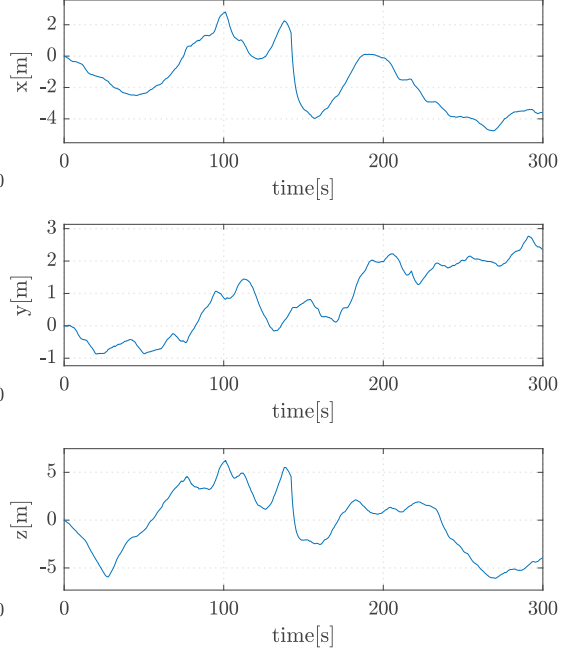
FIGURE 4.21: GPS x,y and z coordinates
time historic

been calculated using Eq. (4.23) leading to

$$\mathbf{Q}_{d_{\dot{\varphi}\dot{\lambda}\dot{h}}} = \text{diag}\left(1.244 \cdot 10^{-12},\, 6.0301 \cdot -13,\, 0.0491\right)^{\top}$$

Using the relations in Eq. (4.21) and Eq. (4.22), the discrete covariance $\mathbf{Q}_{d_{\dot{\varphi}\dot{\lambda}\dot{h}}}$ can be related with the discrete covariance of the GPS measurements by

$$\mathbf{Q}_{d_{\varphi\lambda h}} = \mathbf{Q}_{d_{\dot{\varphi}\dot{\lambda}\dot{h}}}\Delta t^2 = \text{diag}\left(4.9780 \cdot 10^{-14},\, 2.4123 \cdot 10^{-14},\, 0.002\right)^{\top} \tag{4.24}$$

The equivalent covariance in the NED frame can be achieved by doing a similar analysis after transforming the latitude, longitude and altitude data or, given the proximity of the data to the origin of the frame, making use of the jacobian in Eq. (D.6) by

$$\mathbf{Q}_{\boldsymbol{\xi}} = \mathbf{J}\mathbf{Q}_{d_{\varphi\lambda h}}\mathbf{J}^{\top} = \text{diag}\left(5.9723 \cdot 10^{-4},\, 1.6788 \cdot 10^{-4},\, 0.002\right)^{\top} \tag{4.25}$$

It is important to have in mind that the derived covariance matrix for $\mathbf{Q}_{gps}$ is smaller than what it would have to be to cover the size of variability that can be observed in Fig. 4.19. The use of the model in Eq. (4.4) with the derived covariance matrix for state filtering, as it will be proposed in Chap. (6), will result in a position estimation which will closely follow the gps position (which can be biased), but with a more trustworthy velocity estimation. One may discuss that the ad-hoc proposed solution can be also achieved by using a model for the velocity related with the covariance in Eq. (4.24), instead of a model for the position. However, the proposed solution has
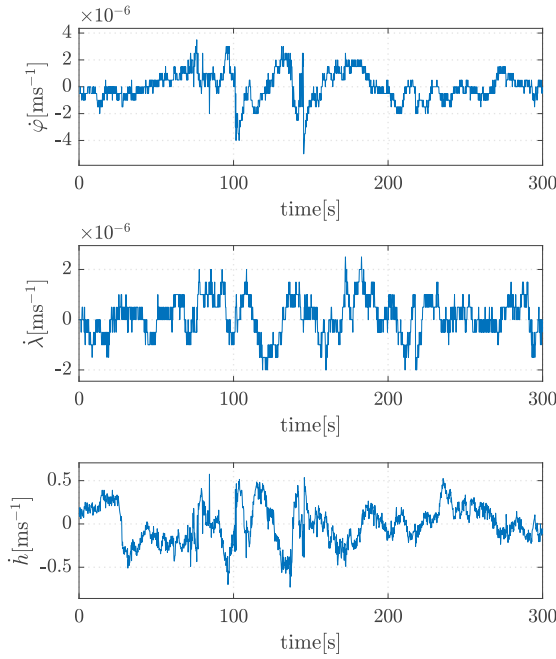
FIGURE 4.22: GPS latitude, longitude and altitude velocities approximation
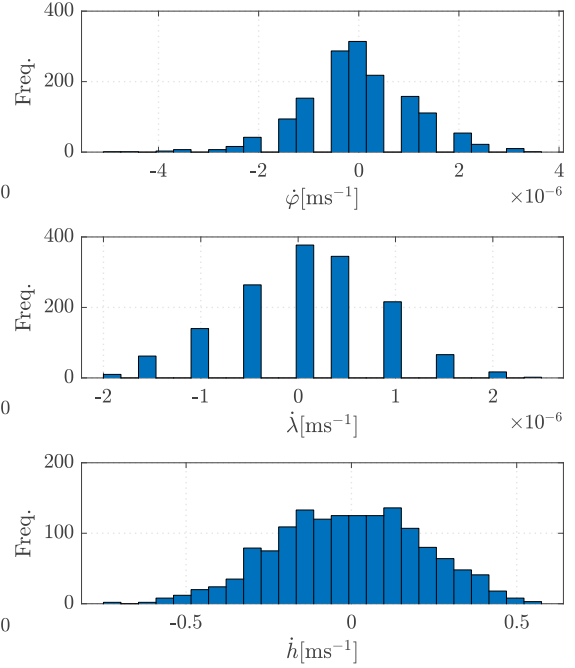
FIGURE 4.23: GPS latitude, longitude and altitude velocities approximation histogram

been preferred for its wider applicability in case of using more accurate position sensors, e.g., differential GPS or motion capture systems.

Magnetometer error estimation

Magnetometer measurements are principally affected by quantization noise. This can be observed in Fig. 4.24 and Fig. 4.25 which show 830 raw and calibrated (geometric fit in Table 4.5) point measurements of the sensor in a steady position after having removed the means of every axis.

A normal Gaussian (continuous) distribution has been constructed to approximate the error in the data set by computing the covariance as presented in Eq. (4.23) which has lead to

$$\mathbf{Q}_H = \begin{pmatrix} 71.76 & -40.67 & 72.87 \\ -40.67 & 90.42 & 16.33 \\ 72.87 & 16.33 & 249.64 \end{pmatrix} \tag{4.26}$$

The validity of the approximation is verified by Fig. 4.26, which shows a histogram comparing the experimental data against synthetic errors generated by simulation using Eq. (4.26). In this case, the total frequency of the plots has been normalized to sum one and the bin length has been chosen as half of the quantum size in order to better compare the results.
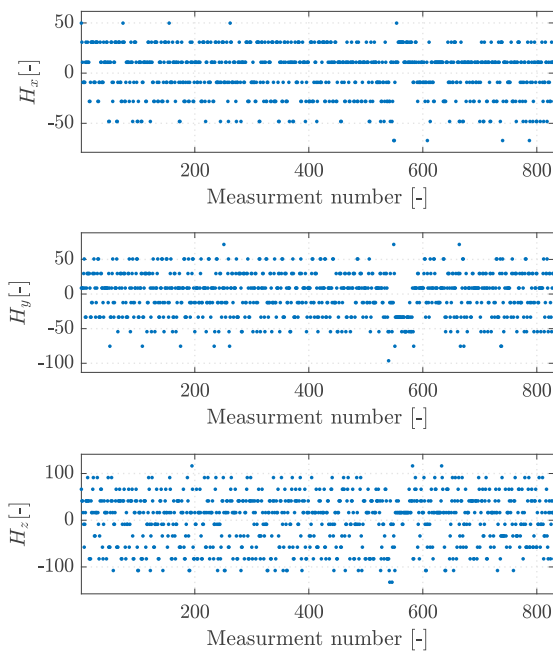
FIGURE 4.24: Magnetometer raw measurement error
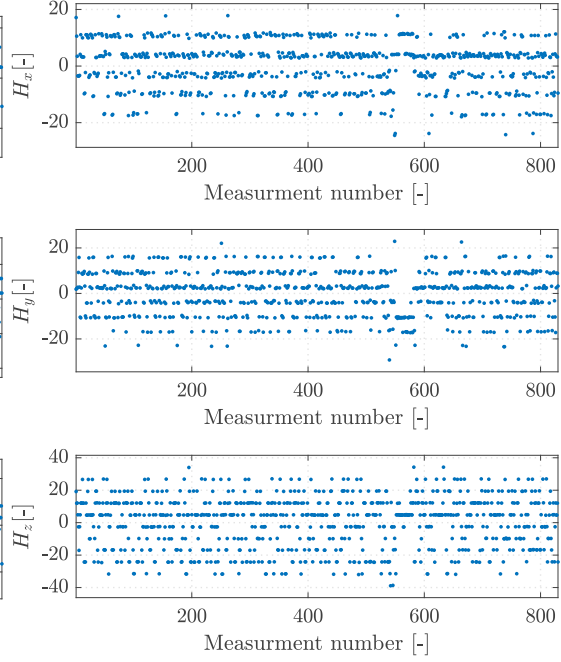
FIGURE 4.25: Magnetometer calibrated measurement error

IMU error estimation

Accelerometers and gyroscopes share the model, as shown in Eq. (4.2a) and Eq. (4.2b). Estimating the noise covariance of both, bias and gyroscope (equivalently bias and accelerometer), from only measurements of the gyroscope (equivalently accelerometer) is not straightforward. For this purpose, the discrete model of Eq. (4.2) presented in [25] and only developed for the gyro model is used

$$\boldsymbol{\omega}_m(k+1) = \boldsymbol{\omega}(k+1) + \frac{1}{2}\left(\boldsymbol{b}_\omega(k+1) + \boldsymbol{b}_\omega(k)\right) + \left(\frac{\mathbf{Q}_\omega}{\Delta t} + \frac{1}{12}\mathbf{Q}_{b\omega}\Delta t\right)^{\frac{1}{2}} \boldsymbol{n}_\omega \tag{4.27a}$$

$$\boldsymbol{b}_\omega(k+1) = \boldsymbol{b}_\omega(k) + (\mathbf{Q}_{b\omega}\Delta t)^{\frac{1}{2}} \boldsymbol{n}_{b\omega} \tag{4.27b}$$

Where $(\mathbf{P})^{\frac{1}{2}}$ must be interpreted as the Cholesky factorization of the covariance matrix $\mathbf{P}$, i.e., $\mathbf{L} = (\mathbf{P})^{\frac{1}{2}}$ such that $\mathbf{L}\mathbf{L}^\top = \mathbf{P}$, and $\boldsymbol{n}_\bullet$ are instances of random vectors obtained from a normal distribution.

This discrete model can be used in simulation to provide synthetic values of the measurements $\boldsymbol{\omega}_m$ for null $\boldsymbol{\omega}$ as a function of $\mathbf{Q}_\omega$, $\mathbf{Q}_{b\omega}$ and the initial value of $\boldsymbol{b}_\omega$.

In order to determine the values of the covariance matrices, the temporal and spectral representation of both measured and synthetic generated data are compared for zero initial conditions of the bias. In addition, diagonal structures for the covariance matrices have been assumed so that the per axis sensor measurements are implicitly supposed independent, which is not a strong assumption when calibrating the data following the methodology described in Section 4.3.1.
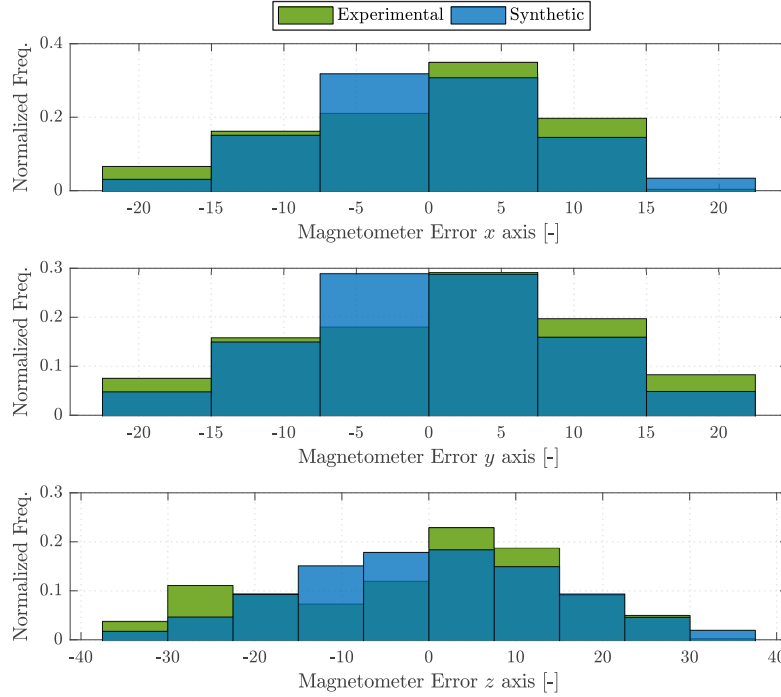
FIGURE 4.26: Magnetometer error histogram.

Figs. 4.27 and 4.28 show the value of time and frequency spectra for real and simulated data of IMU accelerometers with estimated matrix covariances

$$\mathbf{Q}_a = \mathrm{diag}\,(1.85,\ 1.60,\ 1.60) \cdot 10^{-5}$$

$$\mathbf{Q}_{ba} = \mathrm{diag}\,(1.69,\ 1.44,\ 1.44) \cdot 10^{-6}$$

In a similar way, Figs. 4.29, 4.30 show the value of time and frequency spectra for experimental and simulated data of IMU gyroscopes with estimated matrix covariances

$$\mathbf{Q}_\omega = \mathrm{diag}\,(6.72,\ 9.21,\ 9.21) \cdot 10^{-7}$$

$$\mathbf{Q}_{b\omega} = \mathrm{diag}\,(0.36,\ 4.0,\ 4.0) \cdot 10^{-10}$$

Figs. 4.29, 4.30, reveal that the model chosen for gyroscopes match the experimental results and that the effect of the gyroscope bias is small enough to not affect the temporal signal trend in the analyzed period of time. Whereas for the case of accelerometers shown in Figs. 4.27 and 4.28, it can be seen that the spectral response of the measurements is not represented by the provided model. However the the tuning of the model have been done taking into account a covering of the of the spectral response. This results in higher covariance of the time signal as can be appreciated in 4.27.
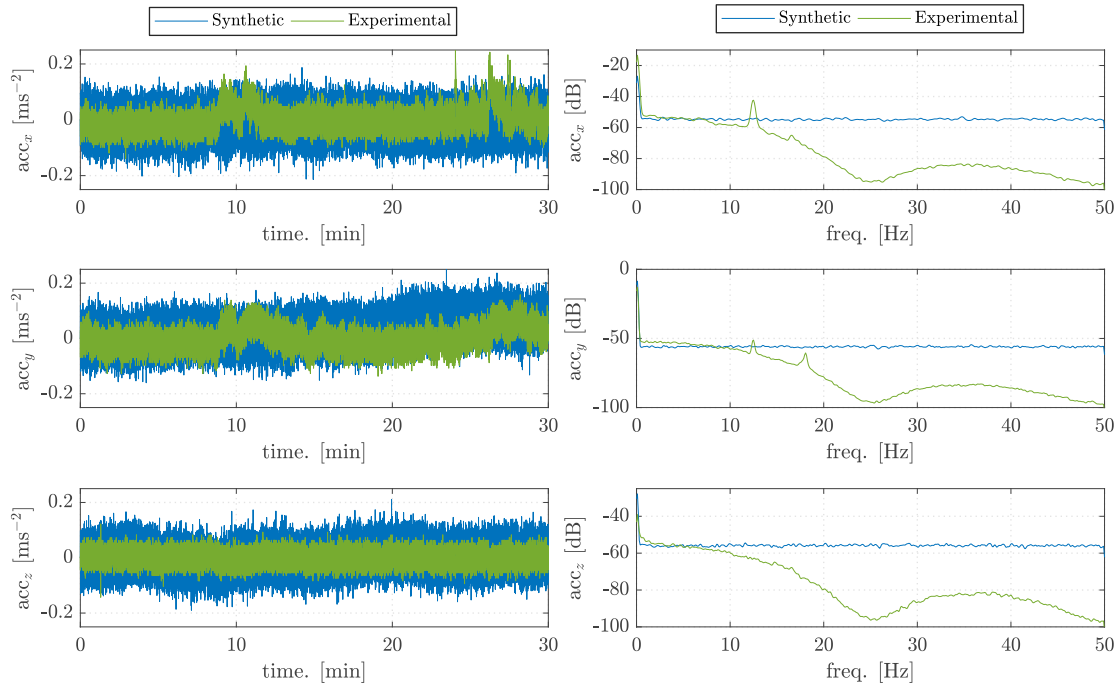
FIGURE 4.27: Simulated model vs. real data for the accelerometer.

FIGURE 4.28: Frequency spectra. Simulated model vs. real data for the accelerometer.
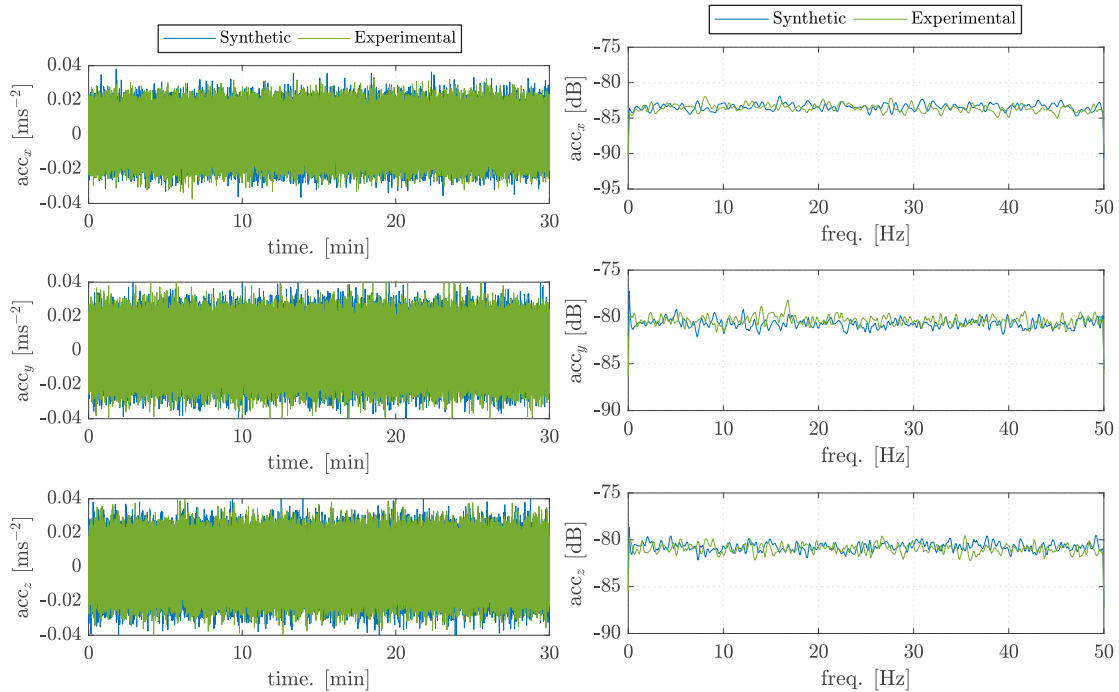
FIGURE 4.29: Simulated model vs. real data for the gyroscope.

FIGURE 4.30: Frequency spectra. Simulated model vs. real data for the gyroscope.

4.4 Actuators

Quadrotors are actuated by four propellers usually driven by electric motors. As a consequence an acuator model must contain: 1) the dynamical system representing the electric motor dynamics, and 2) a model of the aerodynamic actions created by the air-propeller interaction. Inputs for the actuation model are desired angular velocity references and the outputs are the actuation forces and torques.

4.4.1 Electric subsystem, Motor+ESC

Electric motors used on small scale UAVs are usually Brushless DC motors. This kind of electric machines are efficient motors whose velocity is controlled at high frequencies by the use of external hardware implemented controllers named electronic speed controllers or ESC. The ESC transforms the DC power into a three phase AC output to feed the motor. The speed is controlled by controlling the energizing sequence of the windings in the stator.

The presence of the ESC makes a model of the open loop dynamics of the motor irrelevant as long as the controller implemented in the ESC is not known. In this situation, the dynamics of the closed loop system are often approximated as first order systems with parameters estimated during tests as done in [64].

$$\dot{\omega} = k_1 \left(k_2 u - \omega \right) \tag{4.28}$$

being u an escalated input coming from the RC.

In many other works, the motor dynamics are directly neglected [43, 70, 72] or obviated [11] arguing that the time constant of this closed loop system is several orders of magnitude greater than the time constant of the attitude dynamics. In these cases it is assumed that desired angular velocities for the rotors are achieved instantaneously and the model simplifies in

$$\omega = k_1 u \tag{4.29}$$

Four X-BL-52S 80 W motors with four dedicated ESC translate commanded power to the propellers. We have estimated the time constant of the first order model for the motor to be $k_1 = \frac{1}{0.076} \, \text{s}^{-1}$. However this value is only used for simulations while we admit instantaneously achievement of the commanded velocity when using the actuator model for state estimation purposes.

4.4.2 Individual thrust and torque models

Aerodynamic forces over the blades of a quadrotor appear as a consequence of the interaction of the propeller's geometry with the local flow. The state of the flow in the surroundings of the propeller depends on the fluid properties and flow conditions which are mainly affected by the rotational velocity of the rotor.

In general terms, aerodynamic forces and torques depend on the square of the angular velocity. However, inflow speed, inflow direction, turbulence and wake interferences make accurate models to be unavailable.

The Navier Stoke's equations are a set of differential equations that describe the flow behaviour. However they depend on the flow state (velocity, pressure, temperatures etc.) at different size scales which prevents from obtaining a closed solution for complex geometries or general non-stationary surrounding conditions. Instead, burdensome computations have to be carried out to analyse particular configurations to obtain approximations of the solution, which at the moment is far away to be achievable in real time.

For real sized rotors, simplified theories that rely on the hypotheses of inviscid and incompressible flows such as the Momentum Conservation (MC), the Blade element method (BE) or the junction of both named Blade Element Momentum (BEM) allow the prediction of a good approximation of aerodynamic forces and torques over the rotors on hover, climbing, descent and forward manoeuvres.

The size and different rotational speeds of the small-scale rotors make the flow conditions around the rotor different from the flow conditions around a real-size rotor. In particular, small-scale rotors fly on a low-Reynolds number environment for which the classical theories are not fully proven [85]. The only work found in this direction, [60], presents a verified and tested model based in BEM for predicting aerodynamic thrust and torque, and different performance metrics of propellers. However this work applies only to flight conditions in which the flow is parallel to the hub axis, which is only the case of propellers mounted in fixed-wing UAVs.

For miniature helicopters or quadrotors the forward flight represents the majority of operation time and currently there is no a model that accounts for all possible modes in the literature.

As a consequence, many works that deal with control, e.g. [64, 14] among many others, assume models of the form

$$
\begin{aligned}
\boldsymbol{T} &= k_T \omega_p^2 \\
\boldsymbol{Q} &= k_Q \omega_p^2,
\end{aligned}
\tag{4.30}
$$

for all the flight operational modes, being k_T and k_Q constants that hasve to be estimated empirically. In the previous model, both $\boldsymbol{T}$ and $\boldsymbol{Q}$ are vectors pointing in the hub direction.

A slightly more precise model can be found in the works [70, 53], where blade flapping and the induced drag (effects of forward flight) are taken into account. These effects disturb the norm of the thrust and slightly tilt it, making $\boldsymbol{T}$ have non null components on the $x_b - y_b$ plane.

The Hummingbird implements four APC 8×3.8 propellers. Values of the thrust and torque coefficients for this propeller can be found in [15] for different flow conditions (Reynolds numbers) and with or without advance flight. A rough value for k_t and k_q have been obtained by fitting a second order polynomial with null independent and linear terms to the data using least squares which results in

$$
\begin{aligned}
k_T &= 5.6031 \cdot 10^{-6} \, \mathrm{Ns^2} \\
k_Q &= 8.0974 \cdot 10^{-8} \, \mathrm{Nms^2}
\end{aligned}
\tag{4.31}
$$

The thrust coefficient leads to a hover angular speed of about 4553 rpm which is very close to the value that has been experienced in numerous real flight tests.

4.5 Onboard computers and hardware

4.5.1 AscTec AutoPilot Board

The AscTec Hummingbird has an on-board flight control unit (FCU) pre-installed named AscTec AutoPilot Board. The Autopilot Board embeds two ARM7 microprocessors, accelerometers and gyroscopes, a pressure sensor, I/O ports to communicate with the GPS, the magnetometer and the motors and other external devices.

The two processors of the FCU have different purposes. The Low Level Processor (LLP) reads information directly from all sensors with the exception of the GPS and contains factory algorithms for sensor fusion and control that are always running and can not be accessed. The LL is also directly connected to the R/C inputs and is in charge of commanding actions to the motor controllers. In contrast, the High Level Processor (HLP) is open to modifications through an SDK provided by AscTec and can interact with the information in the LL using SPI protocols. The HL has been flashed with a modified firmware `AscTec_hl_firmware`[2] to work as a bridge between sensor readings and the second onboard computer.

4.5.2 Odroid XU4

The platform has been modified to hold a second computer to extend computation capabilities for algorithms that do not fit in the HLP of the FCU and to house possible new sensors. The Odroid XU4 is a card-sized computer with 2GB of RAM and eight Samsung Exynos 5422 @ 2 GHz. The computer runs an Ubuntu 16.04LTS desktopless operative system, with ROS as middleware. The computer has the `asctec_mav_framework` [1] package that works as a driver to receive information provided by the `AscTec_hl_firmware` at the UART serial port of the vehicle in the ODROID. Thus, providing the aircraft information such as sensor readings, battery and motor states among some other information in a standard and readable format via UDP.

The ROS middleware [73] provides libraries for Python and C++ programming languages that allow the access and writing of the UDP information to easily derive new applications. In this case, the implementation of algorithms derived in the next sections make use of those libraries to communicate with the aircraft. An additional communication port is provided via an AD-HOC WIFI network, which is automatically created when the the computer boots. Using this network, external computers can monitorize the process running on the ODROID and have access to the aircraft information.

A communication/architecture diagram depicting the aircraft-computer setup is given in Fig. 4.31.
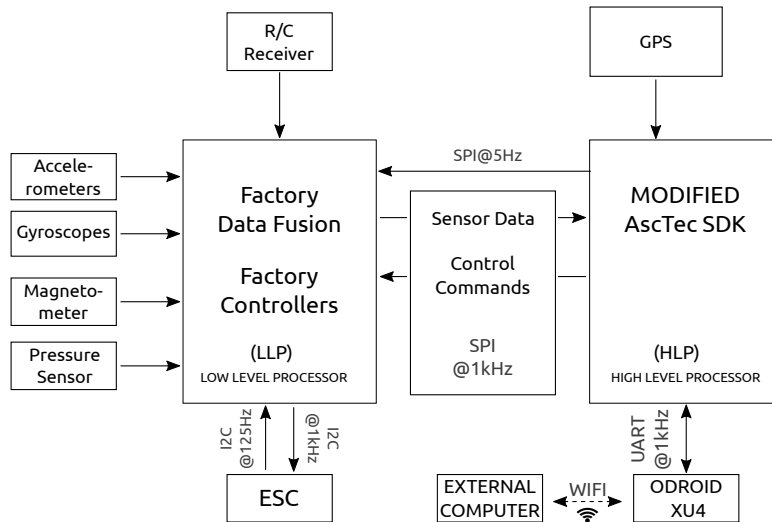
FIGURE 4.31: Architecture/scheme describing our setup. Based on the original diagram of AscTec wiki [9].

Part II

System Observabilty and State Estimation

Chapter 5

Observability of quadrotor's states

This chapter is devoted to study the observability of VToL vehicles equipped with a specific sensor suite. In particular, it is desired to unveil which states of an VToL vehicle can be determined when making use of IMU, GPS and magnetometer readings.

Observability is a system's property related to the possibility of recovering the system states from the system input-output data. Observability of linear systems is a well understood property. However, non-linear observability analysis relies on richer concepts which in turn lead to more complex treatment. Non-linear analysis results are not easy to interpret and usually need a good understanding of the system behaviour to be meaningful.

The structure of this chapter is as follows: First, in Section 5.1 fundamentals of non-linear observability, and the essential concepts used along the chapter are presented. A review of non-linear observability analysis applications to self-localization and attitude estimation done by some authors is detailed in Section 5.2. In Section 5.3 the dynamics of the system under analysis are given. By including IMU measurements in the system dynamics, IMU internal states representing non-constant bias can be taken into consideration for estimation. This state extension implies a state increase from thirteen to sixteen state variables and the benefit of avoiding uncertain terms related to external external forces and torques. The resulting dynamic system is a basis for IMU, GPS and magnetometer integration for localization and auto-calibration. After that, we introduce the application of observability analysis present in the literature to our specific case in Section 5.4 and Section 5.5. In Section 5.4 we demonstrate the observability of the system by using the well known observability rank criterion over the system non-linear dynamic equations. However this analysis does not match our needs since, for the derived system, the inputs are externally determined and then, no longer manipulable. In Section 5.5 it is shown, by using methods present in the literature, that for the linearized system there exist singular inputs i.e. inputs that do not allow full-state reconstruction. Finally, those results are extended by using non-linear analysis on the non-linear system in Section 5.6. For the provided singular inputs, the indistinguishable regions associated to them, i.e, the connected set of states which

cannot be distinguished from the true state, are presented. Observability issues in presence of singular inputs are shown by using simulations. Comparisons of the linear and non-linear results are presented showing that the non-linear analysis provides a better and more accurate description of the observability issues. The results derived take relevance by demonstrating that the conflicting inputs match those inputs needed to perform flight configurations central to missions of VToL platforms.

5.1 Observability of non-linear systems

This section revises the basic concepts of non-linear observability present in [34, 38, 13] using own notation.

Let a non-linear system of the form

$$\Sigma : \begin{cases} \dot{\boldsymbol{x}}(t) = \boldsymbol{f}(\boldsymbol{x}(t), \boldsymbol{u}(t)) \\ \boldsymbol{y}(t) = \boldsymbol{h}(\boldsymbol{x}(t)) \end{cases} \tag{5.1}$$

with $\boldsymbol{x} \in \mathcal{X}$ a smooth infinite differentiable manifold (C^{∞}) contained in $\mathbb{R}^n$, $\boldsymbol{u} \in \mathbb{U} \subseteq \mathbb{R}^p$, $\boldsymbol{y} \in \mathbb{Y} \subseteq \mathbb{R}^m$ with $\boldsymbol{f}$ and $\boldsymbol{h}$ representing smooth infinitely differentiable functions. Let the space of admissible input functions be represented by $\mathcal{U}$. It will be assumed that the dynamic system is complete, i.e. for every control input $\boldsymbol{u}(t) \in \mathcal{U}$ and initial state $\boldsymbol{x}_0 \in \mathcal{X}$ the differential equation accepts a finite solution. By accepting the notation $(\boldsymbol{v}(t), [t_0, t_1])$ to represent vector valued functions in the time interval $T : [t_0, t_1]$, the system in Eq. (5.1) with initial state $\boldsymbol{x}_0$ can be seen as a mapping between inputs $(\boldsymbol{u}(t), [t_0, t_1])$ and outputs $(\boldsymbol{y}(t), [t_0, t_1])$. The mapping produced by the pair $(\Sigma, \boldsymbol{x}_0)$ can be denoted as

$$\Sigma_{\boldsymbol{x}_0} : (\boldsymbol{u}(t), [t_0, t_1]) \to (\boldsymbol{y}(t), [t_0, t_1])$$

Definition 5.1.1 (Indistinguishability). *Two states $\boldsymbol{x}_1 \in \mathcal{X}$ and $\boldsymbol{x}_2 \in \mathcal{X}$ are said to be indistinguishable if the pairs $(\Sigma, \boldsymbol{x}_1)$ and $(\Sigma, \boldsymbol{x}_2)$ produce the same input output map, i.e, for every admissible input $(\boldsymbol{u}(t), [t_0, t_1])$*

$$\Sigma_{\boldsymbol{x}_1} : (\boldsymbol{u}(t), [t_0, t_1]) = \Sigma_{\boldsymbol{x}_2} : (\boldsymbol{u}(t), [t_0, t_1])$$

Definition 5.1.2 (Observability). *Let $\mathcal{I}(\boldsymbol{x})$ represent the set of points indistinguishable from $\boldsymbol{x}$, a dynamic system is observable at $\boldsymbol{x} = \boldsymbol{x}_1$ if $\mathcal{I}(\boldsymbol{x}_1) = \boldsymbol{x}_1$. The whole system is said to be observable if $\mathcal{I}(\boldsymbol{x}) = \boldsymbol{x} \, \forall \boldsymbol{x} \in \mathcal{X}$.*

The definition of observability is said to be a global concept in the sense that a system is observable even if the system's input-output map only fails to be equal after a long time or having deviated a lot from the initial point. A more restrictive observability property can be formulated by restricting the state distinguishability to be present from the initial times. To this end, let the concepts of V-indistinguishability and local observability be defined as

Definition 5.1.3 (V-Indistinghishability)**.** *Let $\mathcal{V}$ represent a subset of $\mathcal{X}$. The set of initial state points in $\mathcal{V}$ whose associated trajectories $(\boldsymbol{x}(t), [t_0, t_1])$ under the same input $(\boldsymbol{u}(t), [t_0, t_1])$ are contained in $\mathcal{V}$ and are indistinguishable from $\boldsymbol{x}$ is represented by $\mathcal{I}_{\mathcal{V}}(\boldsymbol{x})$.*

Definition 5.1.4 (Local Observability)**.** *A system is said to be locally observable (LO) at $\boldsymbol{x}_1$ if **for every** open neighbourhood $\mathcal{V}$ of $\boldsymbol{x}_1$ $\mathcal{I}_{\mathcal{V}}(\boldsymbol{x}_1) = \boldsymbol{x}_1$. The system is said to be locally observable if the previous statement is accomplished $\forall \boldsymbol{x} \in \mathcal{X}$.*

In practice observability is a hard property for a system to fulfil so it can be weakened by restricting the indistinguishability comparison to a neighbourhood of each state.

Definition 5.1.5 (Weak Observability)**.** *A system is said to be weakly observable (WO) at $\boldsymbol{x}_1$ if there exists a neighbourhood $\mathcal{V}$ of $\boldsymbol{x}_1$, such that $\mathcal{I}(\boldsymbol{x}_1) \cap \mathcal{V} = \boldsymbol{x}_1$. The system is said to be weakly observable if the previous statement is accomplished $\forall \boldsymbol{x} \in \mathcal{X}$.*

Definition 5.1.6 (Weak Local Observability)**.** *A system is said to be weakly locally observable (WLO) at $\boldsymbol{x}_1$ if there exists an open neighbourhood $\mathcal{V}$ of $\boldsymbol{x}_1$, such that for every open neighbourhood $\mathcal{W}$ of $\boldsymbol{x}_1$ contained in $\mathcal{V}$, $\mathcal{I}_{\mathcal{W}}(\boldsymbol{x}_1) = \boldsymbol{x}_1$. The system is said to be locally weakly observable if the previous statement is accomplished $\forall \boldsymbol{x} \in \mathcal{X}$.*

Roughly speaking, a system is locally observable if every state can be uniquely identified without the need of having the state to travel too far or for a long time. A system is weakly observable if the state can be distinguished from its neighbours. Finally, a system is weakly locally observable if every state can be distinguished from its neighbours without having to travel too far or for a long time.

WLO is preferred over the other kinds of observability due to its simplicity of verification. WLO of a system can be checked by means of a binary test, known as observability rank condition.

5.1.1   Observability rank conditon

Let the output of the system $\boldsymbol{h}(\boldsymbol{x})$ be interpreted as a set of scalar measurement equations $h_j(\boldsymbol{x})$, $j = 1, 2, ..., p$.

Definition 5.1.7 (Observation Space)**.** *The observation space, denoted by $\mathcal{S}$, is the smallest real vector space of C^{∞} functions which contain the components of the measurement function $\boldsymbol{h}(\boldsymbol{x})$ and closed under Lie differentiation along the vector flows $\boldsymbol{f}_{u^q} = \boldsymbol{f}(., u^q)$, for some constant $\boldsymbol{u}^q \in \mathbb{U}$, i.e., $h_j \in \mathcal{S}$ as well as $L_{\boldsymbol{f}_{u^i}} ... L_{\boldsymbol{f}_{u^k}} ... h_j \in \mathcal{S}$, $j = 1, 2, ... p$ and $i, k = 1, 2, ...$*

In the previous definition $L_{\boldsymbol{\gamma}} \phi$ represent the Lie derivative of the scalar function ϕ along the direction of the vector field $\boldsymbol{\gamma}$ calculated as

$$L_{\boldsymbol{\gamma}} \phi = (\nabla_{\boldsymbol{x}} \phi) \boldsymbol{\gamma}$$

being $\nabla_{\boldsymbol{x}} \phi = \frac{\partial \phi}{\partial \boldsymbol{x}}$ the gradient of ϕ, expressed as a row.

Definition 5.1.8 (Observable Codistribution)**.** *The observable codistribution, denoted by $\Omega(\boldsymbol{x})$ is the vector space spanned by the gradients of the elements of the observation space $\mathcal{S}$, i.e.,*

$$\Omega(\boldsymbol{x}) = \operatorname{span}\left(\nabla_{\boldsymbol{x}} h, ... \nabla_{\boldsymbol{x}} L_{\boldsymbol{f}_{u^i}}...L_{\boldsymbol{f}_{u^k}}...h_j\right) \quad j = 1, 2, ...p \; and \; i, k = 1, 2, ... \tag{5.2}$$

Elements of the observable codistribution are known as covectors, dual elements to vector fields.

Definition 5.1.9 (Observability rank condition)**.** *The system satisfies the observability rank condition at $\boldsymbol{x}_0$ if*

$$\dim\left(\Omega(\boldsymbol{x}_0)\right) = n$$

being n the state dimension. The system is said to satisfy the observability rank condition if $\dim\left(\Omega(\boldsymbol{x})\right) = n \; \forall \boldsymbol{x} \in \mathcal{X}$.

Theorem 3.11 in [34] establishes that a system in the form of Eq. (5.1) satisfying the observability rank condition is WLO. Note that the test depends on the many possible choices for $\boldsymbol{f}_{u^q}$ and it may be necessary to consider multiple (maybe infinite) vector fields and their Lie derivatives in multiples orders to determine the dimension of the codistribution. However, in practice it may suffice to consider only an a priori unknown but finite set of them for which $\dim\left(\Omega(\boldsymbol{x})\right) = n$.

For input control affine systems of the form

$$\begin{cases} \dot{\boldsymbol{x}} = \boldsymbol{f}_0(\boldsymbol{x}) + \sum_{i=1}^{m} \boldsymbol{f}_i(\boldsymbol{x})\boldsymbol{u}_i & \text{(5.3a)} \\[3mm] \boldsymbol{y} = \boldsymbol{h}(\boldsymbol{x}) & \text{(5.3b)} \end{cases}$$

this analysis is simplified since the set of vector fields under consideration is finite. In [38], algorithm 1 is provided to derive the observability codistribution in at most n-1 steps.

Algorithm 1: Calculation of codistribution Ω

  Data: $h_i \quad$ for $i = 1, 2, ..., p$
  Result: Ω
  begin
    $\Omega^k = \{\varnothing\}$
    $\Omega^{k+1} = \operatorname{span}\left(\nabla_x h_i\right) \quad i = 1, ..., p$
    while $\Omega^{k+1} > \Omega^k$ **do**
      $\Omega^k = \Omega^{k+1}$
      $\Omega^{k+1} = \Omega^k + L_{\boldsymbol{f}_0}\Omega^k + \sum_{j=1}^{m} L_{\boldsymbol{f}_j}\Omega^k$
    $\Omega = \Omega^k$

---

where the sum operator over two vector fields must be understood as the span of all generators of both spaces, $L_{\boldsymbol{f}}\Omega = \operatorname{span}\left(L_{\boldsymbol{f}}\boldsymbol{w} \; \forall \boldsymbol{w} \in \Omega\right)$, with $L_{\boldsymbol{f}}\boldsymbol{w}$ representing the Lie derivative of a covector defined as

$$L_{\boldsymbol{f}}\boldsymbol{w} = \boldsymbol{f}^{\top}\frac{\partial \boldsymbol{w}^{\top}}{\partial \boldsymbol{x}} + \boldsymbol{w}^{\top}\frac{\partial \boldsymbol{f}}{\partial \boldsymbol{x}}$$

Ap. 1 presented is related to Eq. (5.2) given that for a scalar function ϕ (as $h_i(\boldsymbol{x})$ or $L_{\boldsymbol{f}}^k h_i(\boldsymbol{x})$ are) its partial derivative can be interpreted as a covector, called exact differential, for which it

can be stated that

$$\frac{\partial L_{\boldsymbol{f}}\phi(\boldsymbol{x})}{\partial \boldsymbol{x}} = L_{\boldsymbol{f}}\frac{\partial \phi(\boldsymbol{x})}{\partial \boldsymbol{x}}$$

Using Algorithm. 1, the computation of the observability codistribution is still not straightforward since the convergence criteria should be evaluated for all $\boldsymbol{x} \in \mathcal{X}$. As an alternative, some works [41, 92] analyse the WLO by studying the rank of an observability matrix $\mathcal{O}$, a matrix whose rows are given by covectors of Ω.

5.1.2 Analytic conditions for observability

WLO of a system implies that there exist inputs for which the state can be fully recovered form input-output data. It is worth noting that a system can be WLO and still exist some inputs for which the state can not be fully inferred. Inputs that allow the discrimination of the initial state are known as universal inputs.

Definition 5.1.10 (Universal inputs). *An input $(\boldsymbol{u}(t), [t_0, t_1])$ is universal for system in Eq. (5.1) if $\forall \boldsymbol{x}_0 \neq \boldsymbol{x}_1$*

$$\Sigma_{\boldsymbol{x}_0} : (\boldsymbol{u}(t), [t_0, t_1]) \neq \Sigma_{\boldsymbol{x}_1} : (\boldsymbol{u}(t), [t_0, t_1])$$

There exist systems for which, under any input, the state of the system can be reconstructed.

Definition 5.1.11 (Uniform observability). *The system in Eq. (5.1) is said to be uniformly observable if every input $\boldsymbol{u}(t)$ is universal.*

Definition 5.1.12 (Local uniform observability). *The system in Eq. (5.1) is said to be locally uniformly observable if every input $\boldsymbol{u}(t)$ is universal in the interval $[0, t]$.*

In practice, real dynamic systems are not necessarily uniformly observable and the inputs to be command them need not be universal. In these cases it is interesting to determine the singular inputs and the effect that they have on the system.

5.1.3 Univalence of the state-output map

Although nonlinear geometric analysis has received attention in the literature to determine observability properties of UAVs, given the input dependence that observability has in the nonlinear case, it could be interesting to consider a more basic formulation as the ones in [44, 32].

Let $y_i = h_i(x)$ be the i-th output of the measurement vector of Eq. (5.12b). The successive time derivatives of every output function can be recovered by using the system dynamic equation e.g. Eq. (5.1) as

$$
\begin{aligned}
y_i &= h_i(\boldsymbol{x}) \\
\dot{y}_i &= (\nabla_{\boldsymbol{x}} y_i)\, \boldsymbol{f}(\boldsymbol{x}, \boldsymbol{u}) \\
\ddot{y}_i &= (\nabla_{\boldsymbol{x}} \dot{y}_i)\, \boldsymbol{f}(\boldsymbol{x}, \boldsymbol{u}) + (\nabla_{\boldsymbol{u}} \dot{y}_i)\, \dot{\boldsymbol{u}} \\
\dddot{y}_i &= (\nabla_{\boldsymbol{x}} \ddot{y}_i)\, \boldsymbol{f}(\boldsymbol{x}, \boldsymbol{u}) + (\nabla_{\boldsymbol{u}} \ddot{y}_i)\, \dot{\boldsymbol{u}} + (\nabla_{\boldsymbol{u}} \dot{y}_i)\, \ddot{\boldsymbol{u}} \\
&\;\;\vdots
\end{aligned}
\tag{5.4}
$$

Let the vector $\boldsymbol{U}$, contain the input and its time derivatives

$$\boldsymbol{U} = \left(\boldsymbol{u}^\top, \dot{\boldsymbol{u}}^\top, \ddot{\boldsymbol{u}}^\top, ... \right)^\top,$$

then, Eq. (5.4) formulated for every output can be grouped under what is known as observability mapping of the system

$$\boldsymbol{Y} = \boldsymbol{F}(\boldsymbol{x}, \boldsymbol{U})$$

The system is weakly locally observable at a given point $\boldsymbol{x}^\star$ if the mapping $\boldsymbol{F}(\boldsymbol{x}^\star, \boldsymbol{U})$ is a local dipheomorfism in the neighbourhood of $\boldsymbol{x}^\star$, i.e. if it is smooth, if it has an inverse and if this inverse is also smooth. A sufficient condition for bijectivity on the neighbourhood $\boldsymbol{x}^\star$, given that $\boldsymbol{F}$ is smooth by construction (from smooth conditions of $\boldsymbol{f}$ and $\boldsymbol{h}$), is that the gradient of $\boldsymbol{F}$, a linearized version of the mapping, is full column rank, or equivalently

$$\mathrm{rank}\left(\nabla_{\boldsymbol{x}} \boldsymbol{F}(\boldsymbol{x}, \boldsymbol{U})\right)\big|_{\boldsymbol{x}=\boldsymbol{x}^\star} = n.$$

By ensuring the full column rank of $\nabla_{\boldsymbol{x}} \boldsymbol{F}(\boldsymbol{x}, \boldsymbol{U})$ it is ensured that the mapping F is invertible at least locally, meaning that by knowing values of $\boldsymbol{Y}$ and $\boldsymbol{U}$, the state $\boldsymbol{x}$ can be recovered.

It is not difficult to realise, given the similarities between Eq. (5.2) and Eq. (5.4), that the jacobian of the mapping is related under a row swap with the definition of observability matrix $\mathcal{O}$ mentioned in the previous subsection. The equivalence of the space spanned by the right hand side of Eq. (5.4) and Ω in Eq. (5.2) is demonstrated in [90]. Since the rank of a matrix does not vary under row swapping, abusing notation it is considered that

$$\mathcal{O} = \nabla_{\boldsymbol{x}} \boldsymbol{F}(\boldsymbol{x}, \boldsymbol{U}) \tag{5.5}$$

Note that, in contrast with previous definitions, the assumption of constant $\boldsymbol{u}$ has not been made. The observability matrix in this case is still input dependant. This will be useful to formulate results in Section 5.6.

5.1.4   System symmetries and indistinguishable regions

If a system is not observable at a given point $\boldsymbol{x}^\star$ it does not mean that no state can be identified, instead there may exist some states or combination of the states that are still observable.

In [38, propositions 1.6.1 and 1.7.2] it is demonstrated that if $\dim\left(\Omega(\boldsymbol{x}^\star)\right) = d < n$, a coordinate transformation in the neighbourhood of $\boldsymbol{x}^\star$ of the form

$$\begin{pmatrix} \boldsymbol{z}_1 \\ \boldsymbol{z}_2 \end{pmatrix} = \boldsymbol{\Xi}(\boldsymbol{x})$$

with $\boldsymbol{z}_1 \in \mathbb{R}^{n-d}$ and $\boldsymbol{z}_2 \in \mathbb{R}^d$ can be found, such that the system in Eq. (5.3) can be locally represented by

$$\dot{\boldsymbol{z}}_1 = \boldsymbol{g}_1(\boldsymbol{z}_1, \boldsymbol{z}_2) + \sum_{i=1}^{m} \boldsymbol{g}_{1i}(\boldsymbol{z}_1, \boldsymbol{z}_2)\boldsymbol{u}_i \tag{5.6a}$$

$$\dot{\boldsymbol{z}}_2 = \boldsymbol{g}_2(\boldsymbol{z}_2) + \sum_{i=1}^{m} \boldsymbol{g}_{2i}(\boldsymbol{z}_2)\boldsymbol{u}_i \tag{5.6b}$$

$$\boldsymbol{y} = \boldsymbol{h}(\boldsymbol{z}_2) \tag{5.6c}$$

The subsystem given by Eq. (5.6b) and Eq. (5.6c) is by construction WLO of dimension d, while subsystem in Eq. (5.6a) is not observable.

The relation between state and input $(\boldsymbol{x}, \boldsymbol{u})$ and the system output $\boldsymbol{y}$ is given in Eq. (5.2) or equivalently in Eq. (5.4). As a consequence, state regions for which Lie derivatives of the output function do not change will be formed by indistinguishable points.

Definition 5.1.13 (Indistinghishable region [59]). *Given a system described by Eq. (5.1) or Eq. (5.3), an indistinguishable region associated with the point $\boldsymbol{x}^\star$ is a connected set which contains the point $\boldsymbol{x}^\star$ and the points where all Lie derivatives have the same value as in $\boldsymbol{x}^\star$.*

Definition 5.1.14 (Continuous symmetry [59]). *The vector field $\boldsymbol{w}_s(\boldsymbol{x})$ is a continuous symmetry of the system described by Eq. (5.3) at the point $\boldsymbol{x}^\star$ if, and only if, it is a non-null vector belonging to the null space of the observability matrix $\mathcal{O}$.*

$$\mathcal{O}(\boldsymbol{x}^\star)\boldsymbol{w}_s = \boldsymbol{0}$$

Given a state $\boldsymbol{x}^\star$ for which $\text{rank}(\mathcal{O}) = d < n$, the system has $n - d$ symmetries associated to $\boldsymbol{x}^\star$ $(\boldsymbol{w}_{s_1}, \boldsymbol{w}_{s_2}, ..., \boldsymbol{w}_{s_{n-d}})$. An indistinguishable region $\boldsymbol{x}_I(\tau, \boldsymbol{x}^\star)$ can be identified as the solution of the ordinary differential equation (ODE)

$$\frac{\mathrm{d}\boldsymbol{x}_I}{\mathrm{d}\tau} = \sum_{i=1}^{n-d} \boldsymbol{w}_{si}(\boldsymbol{x}_I)\eta_i(\tau)$$

with $\boldsymbol{w}_i$ representing the i-th symmetry of the system, initial condition $\boldsymbol{x}_I = \boldsymbol{x}^\star$ and for every possible choice of $\boldsymbol{\eta}_i$ compatible with the uniqueness of the ODE solution.

5.2 Observability in the field of navigation and self-calibration

There are many works dealing with the problem of estimation for autonomous positioning and navigation of satellites, cars, unmanned aerial vehicles and underwater autonomous vehicles. However the problem of observability does not precede the majority of these studies. This is because in the majority of applications the vehicle is highly equipped with multiple sensors, mostly of high quality and many times even redundant. Since observability depends mainly on the system dynamics and outputs, the topic must be revised any time that a new sensor

configuration is considered or if the same set of sensors equips a new platform. It turns out that the dynamics of those vehicles are not so different and they are commonly described by the same basic principles. If any platform is seen as a rigid body, the equations of motion that describe its pose are the ones derived in Chap. (3). Differences arise in the kind of inputs and constraints that limit vehicle motion.

While many sensors may be necessary to determine the state of a generic vehicle, inertial measurement units (IMU) play an important role in navigation. An IMU is usually composed of a set of 3 orthogonal accelerometers and 3 orthogonal gyroscopes that provide measurements of the specific acceleration (acceleration produced by external forces ignoring weight) and angular velocity in the body frame. As we will see explicitly in the next subsection, IMU measurements can be used to replace many uncertain and unknown terms in the system equations. The obtained dynamics rely primarily on kinematic relations comprising acceleration, velocity, position, angular velocity and attitude, then being generic and representing a wider range of systems. When using a low-precision (usually associated to low-cost) IMU, this choice can be done at a cost of enlarging the system state to consider internal calibration parameters of the IMU. This is why many works related to the topic talk about self-calibration.

Following this line, [41] makes use of the non-linear analysis introduced in the previous sections to verify the observability of camera-IMU self-calibrating system. The analysis reveals that full state recovery requires the camera–IMU platform to undergo rotational and accelerated motion about at least two IMU axes directions.

The work [93, sec. 3.4.3], offers an overview of observability of UAVs equipped with several sets of sensors with special focus on camera-IMU integration. It is stated there that the combination of GPS and IMU sensors represent a minimal and self-calibrating sensor suite for globally consistent position and attitude navigation. The results are established based on weak local observability tests over the non-linear system and under the assumption of controllable inputs.

Observability of integrated IMU and GPS systems has been assessed in [36] by using motion equations in incremental error form by means of LTV analysis. The approach differs from the previous ones in that it does not assume constant inputs. Instead generic inputs are used to derive an LTV observability matrix whose rank condition is evaluated for specific values of the input.

It is surprising that the sensor configuration given by IMU-GPS-Magnetometers has not recieved attention in literature given that is the standard for outdoor navigation of unmanned aerial vehicles. In the following section, different system dynamics that enable the system observability analysis corresponding to this setup are derived.

5.3 IMU driven dynamics for observability and estimation

5.3.1 Motion equations

Dynamics equation of the aircraft platform can be formulated by considering the Newton-Euler equations in the mixed body-world reference frames as was shown in Eq. (3.11). When the attitude is represented by quaternions the system equations can be written as

$$
\dot{\boldsymbol{x}}_n = \begin{pmatrix} \dot{\boldsymbol{\xi}} \\ \dot{\boldsymbol{v}} \\ \dot{\mathring{q}} \\ \dot{\boldsymbol{\omega}} \end{pmatrix} = \begin{pmatrix} \boldsymbol{v} \\ \boldsymbol{g} + \mathbf{L}(\mathring{q})\frac{\boldsymbol{f}_{act}}{m} + \frac{\boldsymbol{f}_{ext}}{m} \\ \frac{1}{2}\boldsymbol{\Gamma}(\mathring{q})\boldsymbol{\omega} \\ \mathbf{J}^{-1}\left(\boldsymbol{\tau}_{act} + \boldsymbol{\tau}_{ext} - \boldsymbol{\omega} \times \mathbf{J}\boldsymbol{\omega}\right) \end{pmatrix} \tag{5.7}
$$

where $\boldsymbol{g}$ represents the gravity vector expressed in $\{W\}$, $\boldsymbol{f}_{act}$ are the forces coming from the actuators expressed in $\{B\}$, $\boldsymbol{f}_{ext}$ are external force disturbances expressed in $\{W\}$, $\boldsymbol{\tau}_{act}$ are the torques coming from the actuators expressed in $\{B\}$, $\boldsymbol{\tau}_{ext}$ are external torque disturbances expressed in $\{B\}$, m represents the mass of the body, $\mathbf{J}$ its inertia as seen from frame $\{B\}$ and $\mathbf{L}(\mathring{q})$ and $\boldsymbol{\Gamma}(\mathring{q})$ are the rotation matrix and quaternion kinematic matrix defined respectively in Eq. (2.37) and Eq. (2.53).

5.3.2 IMU driven nonlinear model

The time dependency of the unknown biases in Eq. (4.2) prevents the straightforward use of the IMU measurements to correct the navigation state of the platform. Moreover, there is always some degree of uncertainty in Eq. (5.7) associated to the actuator and unknown external forces and torques. Considering the accelerometer and gyroscope bias as additional states, the vector given by

$$
\boldsymbol{x}^\top = \left(\boldsymbol{\xi}^\top, \boldsymbol{v}^\top, \mathring{q}^\top, \boldsymbol{b}_a^\top, \boldsymbol{b}_\omega^\top\right) \tag{5.8}
$$

describes the state of the system. Note that if $\boldsymbol{x}$ is known, the only navigation variable left, $\boldsymbol{\omega}$, can be recovered by using Eq. (4.2b).

The dynamics of $\boldsymbol{x}$ can be derived by using Eq. (5.7), eliminating the equation of angular velocity, substituting the linear forces using Eq. (4.1) and taking into account the IMU model in Eq. (4.2) leading to

$$
\dot{\boldsymbol{x}} = \boldsymbol{f}(\boldsymbol{x}, \boldsymbol{u}) = \begin{pmatrix} \boldsymbol{v} \\ \boldsymbol{g} + \mathbf{L}(\mathring{q})\left(\boldsymbol{a}_m(t) - \boldsymbol{b}_a - \boldsymbol{\eta}_a\right) \\ \frac{1}{2}\boldsymbol{\Gamma}(\mathring{q})\left(\boldsymbol{\omega}_m(t) - \boldsymbol{b}_\omega - \boldsymbol{\eta}_\omega\right) \\ \boldsymbol{\eta}_{b_a} \\ \boldsymbol{\eta}_{b_\omega} \end{pmatrix} \tag{5.9}
$$

The resulting dynamic system is not driven anymore by controllable inputs, in contrast the dynamic system input $\boldsymbol{u}$ composed by IMU outputs

$$\boldsymbol{u} = \begin{pmatrix} \boldsymbol{a}_m \\ \boldsymbol{\omega}_m \end{pmatrix}$$

Observations of the system come from the GPS and magnetometer outputs presented in Eq. (4.3) and Eq. (4.4) respectively. In addition, since using the quaternion implies considering an additional state (enlarging the state dimension by one) when compared with any other minimal attitude representation, it is usually considered necessary to add an additional virtual measure to ensure the quaternion unit norm and reduce the non-observable degrees of freedom

$$h_{\mathring{q}} = \left(q_0^2 + \boldsymbol{q}_v^\top \boldsymbol{q}_v \right) \tag{5.10}$$

The final vector of measurements of the system is taken as

$$\boldsymbol{y} = \boldsymbol{h}(\boldsymbol{x}) = \begin{pmatrix} \boldsymbol{h}_{\boldsymbol{\xi}}(\boldsymbol{x}) \\ \boldsymbol{h}_{\boldsymbol{H}}(\boldsymbol{x}) \\ h_{\mathring{q}}(\boldsymbol{x}) \end{pmatrix} \tag{5.11}$$

As it is common, the observability analysis will be performed over the nominal system neglecting the noise sources, in that case the system equations are

$$\dot{\boldsymbol{x}} = \begin{pmatrix} \boldsymbol{v} \\ \boldsymbol{g} + \mathbf{L}(\mathring{q})\,(\boldsymbol{a}_m - \boldsymbol{b}_a) \\ \frac{1}{2}\boldsymbol{\Gamma}(\mathring{q})\,(\boldsymbol{\omega}_m - \boldsymbol{b}_\omega) \\ \mathbf{0} \\ \mathbf{0} \end{pmatrix} \tag{5.12a}$$

$$\boldsymbol{y} = \boldsymbol{h}(\boldsymbol{x}) = \begin{pmatrix} \boldsymbol{\xi} \\ \mathbf{L}^\top \boldsymbol{H} \\ q_0^2 + \boldsymbol{q}_v^\top \boldsymbol{q}_v \end{pmatrix} \tag{5.12b}$$

Eq. (5.12a) as it is, will be used in Section 5.6, while the input affine factorization

$$\dot{\boldsymbol{x}} = \underbrace{\begin{pmatrix} \boldsymbol{v} \\ \boldsymbol{g} - \mathbf{L}(\mathring{q})\boldsymbol{b}_a \\ -\frac{1}{2}\boldsymbol{\Gamma}(\mathring{q})\boldsymbol{b}_\omega \\ \mathbf{0} \\ \mathbf{0} \end{pmatrix}}_{\boldsymbol{f}_0(\boldsymbol{x})} + \underbrace{\begin{pmatrix} \mathbf{0}_{3\times3} & \mathbf{0}_{3\times3} \\ \mathbf{L}(\mathring{q}) & \mathbf{0}_{3\times3} \\ \mathbf{0}_{4\times3} & \frac{1}{2}\boldsymbol{\Gamma}(\mathring{q}) \\ \mathbf{0}_{3\times3} & \mathbf{0}_{3\times3} \\ \mathbf{0}_{3\times3} & \mathbf{0}_{3\times3} \end{pmatrix}}_{\mathbf{F}(\boldsymbol{x})} \underbrace{\begin{pmatrix} \boldsymbol{a}_m \\ \boldsymbol{\omega}_m \end{pmatrix}}_{\boldsymbol{u}} \tag{5.13}$$

where every column and entry i of the matrix $\mathbf{F}$ and vector $\boldsymbol{u}$ can be interpreted as the i-th vector field $\boldsymbol{f}_i$ and i-th input u_i appearing in Eq. (5.3), will be used to analyse the WLO of the system in Section 5.4.

5.3.3 IMU driven error based model

Considering the non-linear model with quaternions as attitude parametrization leads to a 16-dimensional state and the inclusion of an additional constraint. To avoid the additional state and the added equation, some works [51, 56, 92, 77] use an error model to enable the use of minimal attitude representations and achieve a 15-dimensional state without the need of extra constraints. Minimal attitude representations have the weakness of being singular at some points of its domain [82]. However, if the system is formulated in an error form, the state represents deviations from a nominal point, and if these deviations are small enough so that they are always far from the singularity, then the use of minimal attitude parametrizations is justified.

Composition of any three dimensional quantity conforming the state, positions, velocities and biases is simply made by addition. However, composition of orientations is not so simple given the structure of $SO(3)$. The usual way to compose two different attitudes is to map them to rotation matrices, compose the attitude by matrix multiplication and then perform the inverse mapping to recover the final attitude in the expected representation form. This process is different depending on the representation choice but identical results can be expected after interpreting the calculated attitude. However, given the way attitude is composed, deriving the error formulation is not so straightforward.

For a quaternion $\mathring{q}$ representing the true attitude, and a quaternion $\hat{\mathring{q}}$ representing the nominal orientation, the attitude error can be denoted by $\delta\mathring{q}$. This incremental rotation can be thought as the necessary attitude that, composed by the left (or the right) with the nominal quaternion, leads to the true attitude

$$\mathring{q} = \delta\mathring{q}_L \, \hat{\mathring{q}} \tag{5.14a}$$

$$\mathring{q} = \hat{\mathring{q}} \, \delta\mathring{q}_R \tag{5.14b}$$

The interpretation of these attitude errors is as follows. $\delta\mathring{q}_R$ is known as the body frame attitude error. It represents a small rotation applied to the body frame such that, when followed by the nominal rotation, the resulting frame and the world frame coincide Eq. (5.14b). Conversely, the world frame attitude error, $\delta\mathring{q}_L$ considers that the misalignment is produced near the world reference frame as described by Eq. (5.14a).

The error quaternion $\delta\mathring{q}$ still maintains the problem of the unit-norm, but as commented, it can be easily related to any 3-dimensional attitude parametrization, as long as the attitude error remains far enough from the singularity.

In [56] different 3D parametrizations for the error quaternion are considered and are claimed equivalent up to second order. To the purpose of this section the attitude error $\boldsymbol{\alpha}$ will be represented by the Gibb's vector multiplied by two. This choice is made based on some computational

savings that the particular parametrization choice brings to the estate estimation implementations (this model will be used also in the estimation chapter)

The error attitude can be obtained from $\delta\mathring{q}$ as

$$\boldsymbol{\alpha} = 2\frac{\delta\boldsymbol{q}}{\delta q_0}, \tag{5.15}$$

the inverse mapping is given by

$$\delta\mathring{q} = \frac{1}{\sqrt{4 + \boldsymbol{\alpha}^\top\boldsymbol{\alpha}}}\begin{pmatrix} 2 \\ \boldsymbol{\alpha} \end{pmatrix} \tag{5.16}$$

and a rotation matrix can be constructed from Eq. (2.35) as

$$\mathbf{L}(\boldsymbol{\alpha}) = \frac{4}{4 + \boldsymbol{\alpha}^\top\boldsymbol{\alpha}}\left(\mathbf{I}_3 + \boldsymbol{\alpha}\right) + \frac{1}{4 + \boldsymbol{\alpha}^\top\boldsymbol{\alpha}}\left(2\boldsymbol{\alpha}\boldsymbol{\alpha}^\top - \boldsymbol{\alpha}^\top\boldsymbol{\alpha}\mathbf{I}_3\right) \tag{5.17}$$

The derivative of the error quaternion $\delta\mathring{q}_L$ can be derived from

$$\dot{\mathring{q}} = \delta\dot{\mathring{q}}_L\hat{\mathring{q}} + \delta\mathring{q}_L\dot{\hat{\mathring{q}}}$$

Taking into account the quaternion dynamics in Eq. (2.50) and taking as nominal angular velocity $\hat{\boldsymbol{\omega}} = \boldsymbol{\omega}_m - \hat{\boldsymbol{b}}_\omega$

$$\delta\dot{\mathring{q}}_L\hat{\mathring{q}} = \dot{\mathring{q}} - \delta\mathring{q}_L\dot{\hat{\mathring{q}}} \rightarrow$$

$$\delta\dot{\mathring{q}}_L\hat{\mathring{q}} = \tfrac{1}{2}\mathring{q}\begin{pmatrix} 0 \\ \boldsymbol{\omega} \end{pmatrix} - \tfrac{1}{2}\delta\mathring{q}_L\hat{\mathring{q}}\begin{pmatrix} 0 \\ \hat{\boldsymbol{\omega}} \end{pmatrix} \rightarrow$$

$$\delta\dot{\mathring{q}}_L = \tfrac{1}{2}\delta\mathring{q}_L\hat{\mathring{q}}\begin{pmatrix} 0 \\ \boldsymbol{\omega} \end{pmatrix}\hat{\mathring{q}}^{-1} - \tfrac{1}{2}\delta\mathring{q}_L\hat{\mathring{q}}\begin{pmatrix} 0 \\ \hat{\boldsymbol{\omega}} \end{pmatrix}\hat{\mathring{q}}^{-1} \rightarrow$$

$$\delta\dot{\mathring{q}}_L = \tfrac{1}{2}\delta\mathring{q}_L\hat{\mathring{q}}\begin{pmatrix} 0 \\ \boldsymbol{\omega} - \hat{\boldsymbol{\omega}} \end{pmatrix}\hat{\mathring{q}}^{-1} \rightarrow$$

$$\delta\dot{\mathring{q}}_L = \tfrac{1}{2}\delta\mathring{q}_L\hat{\mathring{q}}\begin{pmatrix} 0 \\ \hat{\boldsymbol{b}}_\omega - \boldsymbol{b}_\omega - \eta_\omega \end{pmatrix}\hat{\mathring{q}}^{-1}$$

by defining $\boldsymbol{b}_\omega - \hat{\boldsymbol{b}}_\omega$ as $\delta\boldsymbol{b}_\omega$ finally the next relation is achieved

$$\delta\dot{\mathring{q}}_L = -\frac{1}{2}\boldsymbol{\Gamma}(\delta\mathring{q}_L)\left(\mathbf{L}(\hat{\mathring{q}})\left(\delta\boldsymbol{b}_\omega + \eta_\omega\right)\right) \tag{5.18}$$

A different relation can be obtained when considering the error quaternion $\delta\mathring{q}_R$, in this case

$$\dot{\mathring{q}} = \dot{\hat{\mathring{q}}}\delta\mathring{q}_R + \hat{\mathring{q}}\delta\dot{\mathring{q}}_R$$

which leads to

$$\hat{\mathring{q}} \delta \dot{\mathring{q}}_R = \dot{\mathring{q}} - \dot{\hat{\mathring{q}}} \delta \mathring{q}_R \rightarrow$$

$$\hat{\mathring{q}} \delta \dot{\mathring{q}}_R = \frac{1}{2} \mathring{q} \begin{pmatrix} 0 \\ \boldsymbol{\omega} \end{pmatrix} - \frac{1}{2} \hat{\mathring{q}} \begin{pmatrix} 0 \\ \hat{\boldsymbol{\omega}} \end{pmatrix} \delta \mathring{q}_R \rightarrow$$

$$\delta \dot{\mathring{q}}_R = \frac{1}{2} \left(\delta \mathring{q}_R \begin{pmatrix} 0 \\ \boldsymbol{\omega} \end{pmatrix} - \begin{pmatrix} 0 \\ \hat{\boldsymbol{\omega}} \end{pmatrix} \delta \mathring{q}_R \right) \rightarrow$$

$$\delta \dot{\mathring{q}}_R = \frac{1}{2} \left(\begin{pmatrix} -\delta \boldsymbol{q}_{vR}^\top \boldsymbol{\omega} \\ \delta q_{0R} \boldsymbol{\omega} + \delta \boldsymbol{q}_{vR} \times \boldsymbol{\omega} \end{pmatrix} - \begin{pmatrix} -\delta \boldsymbol{q}_{vR}^\top \hat{\boldsymbol{\omega}} \\ \delta q_{0R} \hat{\boldsymbol{\omega}} + \delta \hat{\boldsymbol{\omega}} \times \boldsymbol{q}_{vR} \end{pmatrix} \right)$$

Finally,

$$\delta \dot{\mathring{q}}_R = \frac{1}{2} \begin{pmatrix} -\delta \boldsymbol{q}_{vR}^\top \delta \boldsymbol{b}_\omega \\ \delta q_{0R} \delta \boldsymbol{b}_\omega + \delta \boldsymbol{q}_{vR} \times (\boldsymbol{\omega} + \hat{\boldsymbol{\omega}}) \end{pmatrix} \tag{5.19}$$

The derivative of the Gibbs vector can be related with the error quaternion derivative by using the chain rule

$$\dot{\boldsymbol{\alpha}} = 2 \frac{(\delta \dot{\boldsymbol{q}} \delta q_0 - \delta \boldsymbol{q} \delta \dot{q}_0)}{(\delta q_0)^2} = \sqrt{4 + \boldsymbol{\alpha}^\top \boldsymbol{\alpha}} \left(-\frac{\boldsymbol{\alpha}}{2} \mid \mathbf{I}_{3 \times 3} \right) \delta \dot{\mathring{q}} \tag{5.20}$$

Eq. (5.20) can be particularised for $\delta \mathring{q}_R$, respectively $\delta \mathring{q}_L$, by substituting the respective quaternion derivative in Eq. (5.18) and Eq. (5.19) which leads to

$$\dot{\boldsymbol{\alpha}}_L = -\frac{1}{2} \left(2\mathbf{I}_3 + \frac{\boldsymbol{\alpha}_L \boldsymbol{\alpha}_L^\top}{2} + [\boldsymbol{\alpha}_L]_\times \right) \mathbf{L}(\hat{\mathring{q}}) \left(\boldsymbol{b}_\omega - \hat{\boldsymbol{b}}_\omega + \boldsymbol{\eta}_\omega \right) \tag{5.21a}$$

$$\dot{\boldsymbol{\alpha}}_R = -\left(\mathbf{I}_3 + \frac{\boldsymbol{\alpha}_R \boldsymbol{\alpha}_R^\top}{4} \right) \left(\boldsymbol{b}_\omega - \hat{\boldsymbol{b}}_\omega + \boldsymbol{\eta}_\omega \right) + \frac{1}{2} \boldsymbol{\alpha}_R \times \left(2\boldsymbol{\omega}_m - \boldsymbol{b}_\omega - \hat{\boldsymbol{b}}_\omega - \boldsymbol{\eta}_\omega \right) \tag{5.21b}$$

Let the true state be denoted as $\boldsymbol{x}$, and the nominal estate

$$\hat{\boldsymbol{x}} = \begin{pmatrix} \hat{\boldsymbol{\xi}} \\ \hat{\boldsymbol{v}} \\ \hat{\mathring{q}} \\ \hat{\boldsymbol{b}}_a \\ \hat{\boldsymbol{b}}_\omega \end{pmatrix}$$

Then, the error state can be denoted as

$$\delta \boldsymbol{x}_L = \begin{pmatrix} \delta \boldsymbol{\xi} \\ \delta \boldsymbol{v} \\ \boldsymbol{\alpha}_L \\ \delta \boldsymbol{b}_a \\ \delta \boldsymbol{b}_\omega \end{pmatrix} = \begin{pmatrix} \boldsymbol{\xi} - \hat{\boldsymbol{\xi}} \\ \boldsymbol{v} - \hat{\boldsymbol{v}} \\ \boldsymbol{\alpha}_L \\ \boldsymbol{b}_a - \hat{\boldsymbol{b}}_a \\ \boldsymbol{b}_\omega - \hat{\boldsymbol{b}}_\omega \end{pmatrix} \tag{5.22}$$

or equivalently

$$\delta \boldsymbol{x}_R = \begin{pmatrix} \delta \boldsymbol{\xi} \\ \delta \boldsymbol{v} \\ \boldsymbol{\alpha}_R \\ \delta \boldsymbol{b}_a \\ \delta \boldsymbol{b}_\omega \end{pmatrix} = \begin{pmatrix} \boldsymbol{\xi} - \hat{\boldsymbol{\xi}} \\ \boldsymbol{v} - \hat{\boldsymbol{v}} \\ \boldsymbol{\alpha}_R \\ \boldsymbol{b}_a - \hat{\boldsymbol{b}}_a \\ \boldsymbol{b}_\omega - \hat{\boldsymbol{b}}_\omega \end{pmatrix} \tag{5.23}$$

The error state dynamics can be obtained then as

$$\dot{\delta \boldsymbol{x}}_L = \begin{pmatrix} \dot{\delta \boldsymbol{\xi}} \\ \dot{\delta \boldsymbol{v}} \\ \dot{\boldsymbol{\alpha}}_L \\ \dot{\delta \boldsymbol{b}}_a \\ \dot{\delta \boldsymbol{b}}_\omega \end{pmatrix} = \begin{pmatrix} \delta \boldsymbol{v} \\ \mathbf{L}(\boldsymbol{\alpha}_L)\mathbf{L}(\hat{\bar{q}})\left(\boldsymbol{a}_m - \boldsymbol{b}_a - \boldsymbol{\eta}_a\right) - \mathbf{L}(\hat{q})\left(\boldsymbol{a}_m - \hat{\boldsymbol{b}}_a\right) \\ -\frac{1}{2}\left(2\mathbf{I}_3 + \frac{\boldsymbol{\alpha}_L\boldsymbol{\alpha}_L^\top}{2} + [\boldsymbol{\alpha}_L]_\times\right)\mathbf{L}(\hat{\bar{q}})\left(\boldsymbol{b}_\omega - \hat{\boldsymbol{b}}_\omega + \boldsymbol{\eta}_\omega\right) \\ \boldsymbol{\eta}_{b_a} \\ \boldsymbol{\eta}_{b_\omega} \end{pmatrix} \tag{5.24}$$

respectively

$$\dot{\delta \boldsymbol{x}}_R = \begin{pmatrix} \dot{\delta \boldsymbol{\xi}} \\ \dot{\delta \boldsymbol{v}} \\ \dot{\boldsymbol{\alpha}}_R \\ \dot{\delta \boldsymbol{b}}_a \\ \dot{\delta \boldsymbol{b}}_\omega \end{pmatrix} = \begin{pmatrix} \delta \boldsymbol{v} \\ \mathbf{L}(\hat{\bar{q}})\mathbf{L}(\boldsymbol{\alpha}_R)\left(\boldsymbol{a}_m - \boldsymbol{b}_a - \boldsymbol{\eta}_a\right) - \mathbf{L}(\hat{q})\left(\boldsymbol{a}_m - \hat{\boldsymbol{b}}_a\right) \\ -\left(\mathbf{I}_3 + \frac{\boldsymbol{\alpha}_R\boldsymbol{\alpha}_R^\top}{4}\right)\left(\boldsymbol{b}_\omega - \hat{\boldsymbol{b}}_\omega + \boldsymbol{\eta}_\omega\right) + \frac{1}{2}\boldsymbol{\alpha}_R \times \left(2\boldsymbol{\omega}_m - \boldsymbol{b}_\omega - \hat{\boldsymbol{b}}_\omega - \boldsymbol{\eta}_\omega\right) \\ \boldsymbol{\eta}_{b_a} \\ \boldsymbol{\eta}_{b_\omega} \end{pmatrix} \tag{5.25}$$

By assuming $\boldsymbol{\alpha} \ll 1$ and neglecting second order terms, Eq. (5.17) reduces to

$$\mathbf{L}(\boldsymbol{\alpha}) = \mathbf{I}_3 + [\boldsymbol{\alpha}]_\times ,$$

and Eq. (5.24) and Eq. (5.25) can be written as

$$\dot{\delta \boldsymbol{x}}_L = \begin{pmatrix} \delta \boldsymbol{v} \\ -\mathbf{L}(\hat{\bar{q}})\delta \boldsymbol{b}_a - \mathbf{L}(\hat{\bar{q}})\boldsymbol{\eta}_a - \left[\mathbf{L}(\hat{\bar{q}})\left(\boldsymbol{a}_m - \boldsymbol{b}_a\right)\right]_\times \boldsymbol{\alpha}_L \\ -\mathbf{L}(\hat{\bar{q}})\delta \boldsymbol{b}_\omega - \mathbf{L}(\hat{\bar{q}})\boldsymbol{\eta}_\omega \\ \boldsymbol{\eta}_{b_a} \\ \boldsymbol{\eta}_{b_\omega} \end{pmatrix} \tag{5.26}$$

and

$$\dot{\delta \boldsymbol{x}}_R = \begin{pmatrix} \delta \boldsymbol{v} \\ -\mathbf{L}(\hat{\bar{q}})\delta \boldsymbol{b}_a - \mathbf{L}(\hat{\bar{q}})\boldsymbol{\eta}_a - \mathbf{L}(\hat{\bar{q}})\left[\left(\boldsymbol{a}_m - \boldsymbol{b}_a\right)\right]_\times \boldsymbol{\alpha}_R \\ -\delta \boldsymbol{b}_\omega - \left[\boldsymbol{\omega}_m - \boldsymbol{b}_\omega\right]_\times \boldsymbol{\alpha}_R \\ \boldsymbol{\eta}_{b_a} \\ \boldsymbol{\eta}_{b_\omega} \end{pmatrix} \tag{5.27}$$

respectively.

Considering the measurement equations, Eq. (5.26) and Eq. (5.27) can be rewritten as

$$\dot{\boldsymbol{x}}_L = \mathbf{A}_L(t)\boldsymbol{x}_L$$
$$\boldsymbol{y} = \mathbf{C}_L(t)\boldsymbol{x}_L$$

with

$$\boldsymbol{x}_L = (\delta\boldsymbol{\xi}, \delta\boldsymbol{v}, \alpha_L, \delta\boldsymbol{b}_a, \delta\boldsymbol{b}_\omega)^\top \tag{5.28a}$$

$$\mathbf{A}_L(t) = \begin{pmatrix} \mathbf{0}_3 & \mathbf{I}_3 & \mathbf{0}_3 & \mathbf{0}_3 & \mathbf{0}_3 \\ \mathbf{0}_3 & \mathbf{0}_3 & -\left[\mathbf{L}\boldsymbol{a}\right]_\times & -\mathbf{L} & \mathbf{0}_3 \\ \mathbf{0}_3 & \mathbf{0}_3 & \mathbf{0}_3 & \mathbf{0}_3 & -\mathbf{L} \\ \mathbf{0}_3 & \mathbf{0}_3 & \mathbf{0}_3 & \mathbf{0}_3 & \mathbf{0}_3 \\ \mathbf{0}_3 & \mathbf{0}_3 & \mathbf{0}_3 & \mathbf{0}_3 & \mathbf{0}_3 \end{pmatrix} \tag{5.28b}$$

$$\mathbf{C}_L(t) = \begin{pmatrix} \mathbf{I}_3 & \mathbf{0}_3 & \mathbf{0}_3 & \mathbf{0}_3 & \mathbf{0}_3 \\ \mathbf{0}_3 & \mathbf{0}_3 & \mathbf{L}^\top\left[\boldsymbol{H}\right]_\times & \mathbf{0}_3 & \mathbf{0}_3 \end{pmatrix} \tag{5.28c}$$

or

$$\dot{\boldsymbol{x}}_R = \mathbf{A}_R(t)\boldsymbol{x}_R$$
$$\boldsymbol{y} = \mathbf{C}_R(t)\boldsymbol{x}_L$$

with

$$\boldsymbol{x}_R = (\delta\boldsymbol{\xi}, \delta\boldsymbol{v}, \alpha_R, \delta\boldsymbol{b}_a, \delta\boldsymbol{b}_\omega)^\top \tag{5.29a}$$

$$\mathbf{A}_R(t) = \begin{pmatrix} \mathbf{0}_3 & \mathbf{I}_3 & \mathbf{0}_3 & \mathbf{0}_3 & \mathbf{0}_3 \\ \mathbf{0}_3 & \mathbf{0}_3 & -\mathbf{L}\left[\boldsymbol{a}\right]_\times & -\mathbf{L} & \mathbf{0}_3 \\ \mathbf{0}_3 & \mathbf{0}_3 & -\left[\boldsymbol{\omega}\right]_\times & \mathbf{0}_3 & -\mathbf{I}_3 \\ \mathbf{0}_3 & \mathbf{0}_3 & \mathbf{0}_3 & \mathbf{0}_3 & \mathbf{0}_3 \\ \mathbf{0}_3 & \mathbf{0}_3 & \mathbf{0}_3 & \mathbf{0}_3 & \mathbf{0}_3 \end{pmatrix} \tag{5.29b}$$

$$\mathbf{C}_R(t) = \begin{pmatrix} \mathbf{I}_3 & \mathbf{0}_3 & \mathbf{0}_3 & \mathbf{0}_3 & \mathbf{0}_3 \\ \mathbf{0}_3 & \mathbf{0}_3 & \left[\mathbf{L}^\top\boldsymbol{H}\right]_\times & \mathbf{0}_3 & \mathbf{0}_3 \end{pmatrix} \tag{5.29c}$$

The models in Eq. (5.28) and Eq. (5.29) are linear time varying systems where the time dependency is implicit in the inputs $\boldsymbol{a}_m = \boldsymbol{a}_m(t)$, $\boldsymbol{\omega}_m = \boldsymbol{\omega}_m(t)$ and in the rotation matrix $\mathbf{L}(\hat{\bar{q}})$ which depends on the system angular velocity $\boldsymbol{\omega}$.

The same equations can be found in [77] with the difference of being derived considered a different error attitude representation.

5.4 WLO test over the non-linear IMU driven dynamics

The observability of the system in Eq. (5.12) can be assessed by using the tools derived in Section 5.1. This section reproduces the results derived in [41] and [93] for visual inertial integration but particularised to our navigation system i.e considering GPS, IMU and magnetometers as sensors.

Theorem 5.4.1. *The dynamic system in Eq. (5.13), under measurement equations in Eq. (5.11) is Weakly locally observable.*

Proof. The demonstration is founded in finding a subset of the observation space represented by some rows of the observability matrix in Eq. (5.5) which is demonstrated to have maximum dimension under generic input conditions.

Let the matrix $\mathbf{O}$ be composed by elements of $\mathcal{O}$ corresponding to the GPS mearuments and some specific Lie derivatives

$$
\mathbf{O} = \begin{pmatrix} \frac{\partial}{\partial \boldsymbol{x}}(h_{\boldsymbol{\xi}}) \\ \frac{\partial}{\partial \boldsymbol{x}}(L_{\boldsymbol{f}_0}h_{\boldsymbol{\xi}}) \\ \frac{\partial}{\partial \boldsymbol{x}}(L_{\boldsymbol{f}_0}^2 h_{\boldsymbol{\xi}}) \\ \frac{\partial}{\partial \boldsymbol{x}}(L_{\boldsymbol{f}_1}L_{\boldsymbol{f}_0}h_{\boldsymbol{\xi}}) \\ \frac{\partial}{\partial \boldsymbol{x}}(L_{\boldsymbol{f}_2}L_{\boldsymbol{f}_0}h_{\boldsymbol{\xi}}) \\ \frac{\partial}{\partial \boldsymbol{x}}(L_{\boldsymbol{f}_3}L_{\boldsymbol{f}_0}h_{\boldsymbol{\xi}}) \\ \frac{\partial}{\partial \boldsymbol{x}}(L_{\boldsymbol{f}_0}L_{\boldsymbol{f}_1}L_{\boldsymbol{f}_0}h_{\boldsymbol{\xi}}) \\ \frac{\partial}{\partial \boldsymbol{x}}(L_{\boldsymbol{f}_0}L_{\boldsymbol{f}_2}L_{\boldsymbol{f}_0}h_{\boldsymbol{\xi}}) \\ \frac{\partial}{\partial \boldsymbol{x}}(L_{\boldsymbol{f}_0}L_{\boldsymbol{f}_3}L_{\boldsymbol{f}_0}h_{\boldsymbol{\xi}}) \end{pmatrix} = \left(\begin{array}{c|c|c|c} \mathbf{I}_6 & \mathbf{0}_{6\times 4} & \mathbf{0}_{6\times 3} & \mathbf{0}_{6\times 3} \\ \hline \mathbf{0}_{3\times 6} & \mathbf{U}_1(\mathring{q}, \boldsymbol{b}_a) & -\mathbf{L}(\mathring{q}) & \mathbf{0}_{3\times 3} \\ \hline \mathbf{0}_{9\times 6} & \mathbf{A}(\mathring{q}) & \mathbf{0}_{9\times 3} & \mathbf{0}_{9\times 3} \\ \hline \mathbf{0}_{9\times 6} & \mathbf{U}_2(\mathring{q}, \boldsymbol{b}_\omega) & \mathbf{0}_{9\times 3} & \mathbf{B}(\mathring{q}) \end{array} \right) \tag{5.30}
$$

where

$$
\mathbf{U}_1(\mathring{q}, \boldsymbol{b}_a) = -\frac{\partial(\mathbf{L}\boldsymbol{b}_a)}{\partial \mathring{q}}, \quad \mathbf{U}_2(\mathring{q}, \boldsymbol{b}_w) = -\frac{1}{2}\frac{\partial}{\partial \mathring{q}}\begin{pmatrix} \frac{\partial \mathbf{L}_1}{\partial \mathring{q}}\boldsymbol{\Gamma}(\mathring{q})\boldsymbol{b}_w \\ \frac{\partial \mathbf{L}_2}{\partial \mathring{q}}\boldsymbol{\Gamma}(\mathring{q})\boldsymbol{b}_w \\ \frac{\partial \mathbf{L}_3}{\partial \mathring{q}}\boldsymbol{\Gamma}(\mathring{q})\boldsymbol{b}_w \end{pmatrix},
$$

$$
\mathbf{A}(\mathring{q}) = \frac{\partial}{\partial \mathring{q}}\begin{pmatrix} \mathbf{L}_1 \\ \mathbf{L}_2 \\ \mathbf{L}_3 \end{pmatrix}, \tag{5.31}
$$

$$
\mathbf{B}(\mathring{q}) = \frac{1}{2}\mathbf{A}(\mathring{q})\boldsymbol{\Gamma}(\mathring{q}), \tag{5.32}
$$

with $\mathbf{L}_i$ representing the i-th column of $\mathbf{L}$.

Let $\mathbf{O}'$ be a permutated version of $\mathbf{O}$ obtained by circle-shifting block columns two, three and four and exchanging block rows three and four of Eq. (5.30), i.e.,

$$
\boldsymbol{O}' = \left(\begin{array}{c|c|c|c} \mathbf{I}_6 & \mathbf{0}_{6\times 3} & \mathbf{0}_{6\times 3} & \mathbf{0}_{6\times 4} \\ \hline \mathbf{0}_{3\times 6} & -\mathbf{L}(\mathring{q}) & \mathbf{0}_{3\times 3} & \mathbf{U}_1(\mathring{q}, \boldsymbol{b}_a) \\ \hline \mathbf{0}_{9\times 6} & \mathbf{0}_{9\times 3} & \mathbf{B}(\mathring{q}) & \mathbf{U}_2(\mathring{q}, \boldsymbol{b}_\omega) \\ \hline \mathbf{0}_{9\times 6} & \mathbf{0}_{9\times 3} & \mathbf{0}_{9\times 3} & \mathbf{A}(\mathring{q}) \end{array} \right)
$$

By considering the properties in [37]

- For a generic block diagonal matrix $\mathbf{M} = \begin{pmatrix} \mathbf{M}_{11} & \mathbf{0} \\ \mathbf{0} & \mathbf{M}_{22} \end{pmatrix}$,

$$\operatorname{rank}(\mathbf{M}) = \operatorname{rank}(\mathbf{M}_{11}) + \operatorname{rank}(\mathbf{M}_{22})$$

- For a generic upper block triangular matrix $\mathbf{M} = \begin{pmatrix} \mathbf{M}_{11} & \mathbf{0} \\ \mathbf{M}_{12} & \mathbf{M}_{22} \end{pmatrix}$,

$$\operatorname{rank}(\mathbf{M}) \geq \operatorname{rank}(\mathbf{M}_{11}) + \operatorname{rank}(\mathbf{M}_{22})$$

the rank of $\mathbf{O}'$ must acomplish the next relation

$$\operatorname{rank}(\mathbf{O}') \geq \operatorname{rank}(\mathbf{I}_6) + \operatorname{rank}(-\mathbf{L}(\mathring{q})) + \operatorname{rank}(\mathbf{B}(\mathring{q})) + \operatorname{rank}(\mathbf{A}(\mathring{q})) \tag{5.33}$$

A singular value decomposition of matrices $\mathbf{A}(\mathring{q})$ and $\mathbf{B}(\mathring{q})$ reveals 4 and 3 non-zero singular values respectively, represented by

$$\boldsymbol{\sigma}_{\mathbf{A}} = 2\left(q_0^2 + \boldsymbol{q}^\top \boldsymbol{q}\right)\left(\sqrt{2}, \sqrt{2}, \sqrt{2}, \sqrt{3}\right) = 2\left(\sqrt{2}, \sqrt{2}, \sqrt{2}, \sqrt{3}\right)^\top$$

$$\boldsymbol{\sigma}_{\mathbf{B}} = 2\sqrt{2}\left(q_0^2 + \boldsymbol{q}^\top \boldsymbol{q}\right)(1, 1, 1) = 2\sqrt{2}\,(1, 1, 1)^\top$$

As a consequence $\operatorname{rank}(\mathbf{A}) = 4$ and $\operatorname{rank}(\mathbf{B}) = 3$, equivalently $\mathbf{A}$ and $\mathbf{B}$ are full column rank matrices.

The use of Eq. (5.33) and the fact that $\operatorname{rank}(\mathbf{O}') \leq \min\{m, n\} = n$ and $\operatorname{rank}(\mathbf{L}(\mathring{q})) = 3$, leads to $\operatorname{rank}(\mathbf{O}') = \operatorname{rank}(\mathbf{O}) = n$ or equivalently $\mathbf{O}$ is full column rank. Given that $\mathbf{O}$ is formed by elements of the observability matrix $\mathcal{O}$, the dimension of the observable codistribution will equal the rank of $\mathbf{O}$, which by the observability rank criterion discussed in Section 5.1.1 guarantees the weak local observability of the system. $\qquad\square$

The derived result reveals that the weak local observability of the system can be guaranteed without the need of considering measures of the magnetometer, (the quaternion unit norm constraint has been used in the singular value decomposition of $\mathbf{A}$ and $\mathbf{B}$). Moreover, this result is independent of the system state configuration since it does not depend on $\boldsymbol{\xi}$, $\boldsymbol{v}$, $\boldsymbol{b}_a$ nor $\boldsymbol{b}_\omega$ and it is valid for any quaternion $\mathring{q}$.

5.5   Singular inputs of the IMU driven error based linear model

The work [36] deals with observability issues of a navigation system composed by an INS (Inertial Navigation System, called IMU in this work) and a GPS. The approach makes use of the system error equations to derive a linear time varying (LTV) dynamic model of the system in an equivalent form of what has been done in Section 5.3.3. In particular the body frame attitude

error is considered under the argument of simplifying the observability analysis. Eq. (5.28b) coincides with Eq. (22) in [36], except for the column related to the distance between the center of mass and the antenna, not considered here. In addition, biases are considered as state, while here only the errors of biases are considered. Given the linearity of biases dynamics, estimating the state or the error of the state is equivalent except for an added shift value. There is also a sign discrepancy in the entries related to the biases, which arises from considering biases and noises as subtracting terms instead of additive ones.

The results of that paper are based in the observability analysis of LTV system provided [20]. The findings presented there are not directly comparable to the ones given here because both states and measurements are different. However, the methodology presented in [36] can be used to reconstruct the unobservable regions of the system described in Eq. (5.12) using similar hypothesis. We will refer to this procedure as LTV observability analysis method.

A direct implication of using linear models in the observability tests is that the nullspace of the observability matrix can be directly related with the indistinguishable region instead of its dynamics, then further integration is not needed to reconstruct the indistinguishable region from the symmetry.

Analysing the possibility of recovering the state from the input-output mapping for every of the possible combinations of inputs and input derivatives may be a hard task. However, in the remaining part of this section (and also the next one Section 5.6) we are going to restrict this analysis to the case of constant inputs, i.e, null derivative signals. The case of constant inputs is meaningful since constant input values represent many of the flight modes characteristic of VTOL vehicles, such as, constant velocity vertical take-off and landing, and most importantly, hover.

In this section, the LTV observability analysis is applied to systems in Eq. (5.28) and Eq. (5.29) to find the constant singular inputs that make the state unrecoverable.

When the inputs of the system, $\boldsymbol{a}_m$ and $\boldsymbol{\omega}_m$, are considered constant, the system specific force $\boldsymbol{a}$ and the system angular velocitiy $\boldsymbol{\omega}$ can be considered constant too given that in the ideal case (absence of disturbance) biases of the system have null derivative. In this case, the platform rotates at a constant rate (the angular velocity is integrated into the nominal quaternion $\hat{\bar{q}}$) and matrices $\mathbf{A}(t)$ and $\mathbf{C}(t)$ in Eq. (5.28) and Eq. (5.29) take explicit time dependence. In particular the rotation matrix

$$\mathbf{L}(\hat{\bar{q}}(t)) = \mathbf{L}(\hat{\bar{q}}(0)) \left(\mathbf{I}_3 \cos(\|\boldsymbol{\omega}\| t) + \frac{(1 - \cos(\|\boldsymbol{\omega}\| t))}{\|\boldsymbol{\omega}\|^2} (\boldsymbol{\omega}\boldsymbol{\omega}^\top) \frac{\sin(\|\boldsymbol{\omega}\| t)}{\|\boldsymbol{\omega}\|} [\boldsymbol{\omega}]_\times \right) \qquad (5.34)$$

where $\mathbf{L}(\hat{\bar{q}}(0))$ is a constant matrix that determines the vehicle attitude at the initial time just before the platform starts rotating. It can be shown that the derivative of $\mathbf{L}(\hat{\bar{q}}(t))$ fulfils Eq. (2.14), is infinitely differentiable and its k derivative, defined by

$$\overset{(k)}{\mathbf{L}} = \mathbf{L} [\boldsymbol{\omega}]_\times^k \qquad (5.35)$$

make matrices $\mathbf{A}(t)$ and $\mathbf{C}(t)$ also infinitely differentiable.

The singular input analysis is finds the values of the input variables variables $\boldsymbol{a}_m$ and $\boldsymbol{\omega}_m$ and states that make the matrix

$$\mathbf{O}(t) = \begin{pmatrix} \mathbf{N}_0(t) \\ \mathbf{N}_1(t) \\ \mathbf{N}_2(t) \\ \vdots \\ \mathbf{N}_{n-1}(t) \end{pmatrix} \tag{5.36}$$

rank deficient [20], being n the system dimension and

$$\mathbf{N}_{k+1}(t) = \mathbf{N}_{k-1}(t)\mathbf{A}(t) + \dot{\mathbf{N}}_{k-1}$$
$$\mathbf{N}_0(t) = \mathbf{C}(t) \tag{5.37}$$

The connected sets of states that make the observability matrix full column rank for a given input constitutes and indistinguishable region. The observability matrix in Eq. (5.36) and Eq. (5.37) are obtained from Eq. (5.5) in the case that the system is described by a linear time varying model.

It is useful in the present analysis to consider a partition of the measurement matrix $\mathbf{C}(t)$ as

$$\mathbf{C}(t) = \begin{pmatrix} \mathbf{C}_1(t) \\ \mathbf{C}_2(t) \end{pmatrix}$$

where $\mathbf{C}_1(t)$ represent the first three rows and $\mathbf{C}_2(t)$ the last three rows of Eq. (5.28c) or Eq. (5.29c) respectively. With this partition and given that the rank of a matrix is invariant under permutation of rows

$$\text{rank}\left(\mathbf{O}(t)\right) = \text{rank}\begin{pmatrix} \mathbf{O}_1(t) \\ \mathbf{O}_2(t) \end{pmatrix}$$

where

$$\mathbf{O}_1 = \begin{pmatrix} \mathbf{N}_0'(t) \\ \mathbf{N}_1'(t) \\ \mathbf{N}_2'(t) \\ \vdots \\ \mathbf{N}_{n-1}'(t) \end{pmatrix} \quad \mathbf{O}_2 = \begin{pmatrix} \mathbf{N}_0''(t) \\ \mathbf{N}_1''(t) \\ \mathbf{N}_2''(t) \\ \vdots \\ \mathbf{N}_{n-1}''(t) \end{pmatrix}$$

with $\mathbf{N}_k'(t)$ and $\mathbf{N}_k''(t)$ generated by Eq. (5.37) with $\mathbf{C}(t) = \mathbf{C}_1(t)$ and $\mathbf{C}(t) = \mathbf{C}_2(t)$ respectively.

In the next, a nullspace analysis will be presented for the observability matrices generated for the LTV systems in Eq. (5.28) and Eq. (5.29). Six conflicting flight configurations are studied based in the particular values of $\boldsymbol{a}$ and $\boldsymbol{\omega}$ present $\mathbf{A}(t)$ and $\mathbf{C}(t)$. The explicit dependence of time in matrices and variables will be omitted from now on for clarity purposes.

5.5.1   Singular input analysis of the world frame attitude error equations

This section deals with the singular input analysis of the LTV system in Eq. (5.28). The study of this case is simplified noting that the matrix $\mathbf{A}_L$ in Eq. (5.28b) is idempotent, i.e., $\mathbf{A}_L^i = 0$ for some integer $i > 0$, which in this case is $i = 4$ and that the k-th time derivative of $\mathbf{A}_L$ can be written as

$$\overset{(k)}{\mathbf{A}_L} = \begin{pmatrix} \mathbf{0}_3 & \mathbf{0}_3 & \mathbf{0}_3 & \mathbf{0}_3 & \mathbf{0}_3 \\ \mathbf{0}_3 & \mathbf{0}_3 & -\left[\overset{(k)}{\mathbf{L}a}\right]_\times & -\overset{(k)}{\mathbf{L}} & \mathbf{0}_3 \\ \mathbf{0}_3 & \mathbf{0}_3 & \mathbf{0}_3 & \mathbf{0}_3 & -\overset{(k)}{\mathbf{L}} \\ \mathbf{0}_3 & \mathbf{0}_3 & \mathbf{0}_3 & \mathbf{0}_3 & \mathbf{0}_3 \\ \mathbf{0}_3 & \mathbf{0}_3 & \mathbf{0}_3 & \mathbf{0}_3 & \mathbf{0}_3 \end{pmatrix} \quad \forall k \geq 1$$

Noting that $\dot{\mathbf{C}}_{1L} = \mathbf{0}$ and that $\mathbf{C}\dot{\mathbf{A}}_L = \mathbf{0}$, the observability matrix $\mathbf{O}_1$ after eliminating null rows reduces to

$$\mathbf{O}_{L1} = \begin{pmatrix} \mathbf{C}_{L1} \\ \mathbf{C}_{L1}\mathbf{A}_L \\ \mathbf{C}_{L1}\mathbf{A}_L^2 \\ \mathbf{C}_{L1}\mathbf{A}_L^3 \end{pmatrix} = \begin{pmatrix} \mathbf{I}_3 & \mathbf{0}_3 & \mathbf{0}_3 & \mathbf{0}_3 & \mathbf{0}_3 \\ \mathbf{0}_3 & \mathbf{I}_3 & \mathbf{0}_3 & \mathbf{0}_3 & \mathbf{0}_3 \\ \mathbf{0}_3 & \mathbf{0}_3 & -[\mathbf{L}a]_\times & -\mathbf{L} & \mathbf{0}_3 \\ \mathbf{0}_3 & \mathbf{0}_3 & \mathbf{0}_3 & \mathbf{0}_3 & [\mathbf{L}a]_\times \mathbf{L} \end{pmatrix} \tag{5.38}$$

The general analysis of $\mathbf{O}_{L2}$ is more intricate given that $\dot{\mathbf{C}}_2 \neq \mathbf{0}$. However noting that

$$\mathbf{C}_{L2}\mathbf{A}_L^2 = \mathbf{0} \qquad \overset{(k)}{\mathbf{C}_{L2}}A^2 = \mathbf{0}$$
$$\overset{(k)}{\mathbf{C}_{L2}}\dot{\mathbf{A}}_L\mathbf{A}_L = \mathbf{0} \quad \overset{(k)}{\mathbf{C}_{L2}}\mathbf{A}_L\dot{\mathbf{A}}_L = \mathbf{0}$$

$\forall k \geq 1$, the matrix $\mathbf{O}_{L2}$ can be expressed as

$$\mathbf{O}_{L2} = \begin{pmatrix} \mathbf{C}_{L2} \\ \dot{\mathbf{C}}_{L2} + \mathbf{C}_{L2}\mathbf{A}_L \\ \ddot{\mathbf{C}}_{L2} + 2\dot{\mathbf{C}}_{L2}\mathbf{A}_L + \mathbf{C}_{L2}\dot{\mathbf{A}}_L \\ \dddot{\mathbf{C}}_{L2} + 3\ddot{\mathbf{C}}_{2L}\mathbf{A}_L + 3\dot{\mathbf{C}}_{2L}\dot{\mathbf{A}}_L + \mathbf{C}_{2L}\ddot{\mathbf{A}}_L \\ \vdots \end{pmatrix} = \begin{pmatrix} \mathbf{0}_3 & \mathbf{0}_3 & \mathbf{D}_1 & \mathbf{0}_3 & \mathbf{0}_3 \\ \mathbf{0}_3 & \mathbf{0}_3 & \mathbf{D}_2 & \mathbf{0}_3 & \mathbf{E}_1 \\ \mathbf{0}_3 & \mathbf{0}_3 & \mathbf{D}_3 & \mathbf{0}_3 & \mathbf{E}_2 \\ \vdots & \vdots & \vdots & \vdots & \vdots \\ \mathbf{0}_3 & \mathbf{0}_3 & \mathbf{D}_{15} & \mathbf{0}_3 & \mathbf{E}_{15} \end{pmatrix} \tag{5.39}$$

The binomial-like form of the left hand side matrix in Eq. (5.39) can be exploited along with Eq. (5.35) to derive

$$\mathbf{D}_i = (-1)^{i-1}[\boldsymbol{\omega}]_\times^{i-1}\mathbf{L}^\top[\boldsymbol{H}]_\times \; \forall i \geq 1$$

and

$$\mathbf{E}_{i+1} = \sum_{l=1}^{i}\binom{i}{l}[\boldsymbol{\omega}]_\times^{i-l}\mathbf{L}^\top[\boldsymbol{H}]_\times\mathbf{L}[\boldsymbol{\omega}]_\times^{l-1} \; \forall i > 1$$

As a consequence, the observability matrix for the system in Eq. (5.28) can be expressed as

$$
\mathbf{O}_L \begin{pmatrix}
\mathbf{I}_3 & \mathbf{0}_3 & \mathbf{0}_3 & \mathbf{0}_3 & \mathbf{0}_3 \\
\mathbf{0}_3 & \mathbf{I}_3 & \mathbf{0}_3 & \mathbf{0}_3 & \mathbf{0}_3 \\
\mathbf{0}_3 & \mathbf{0}_3 & -\left[\mathbf{L}a\right]_\times & -\mathbf{L} & \mathbf{0}_3 \\
\mathbf{0}_3 & \mathbf{0}_3 & \mathbf{0}_3 & \mathbf{0}_3 & \left[\mathbf{L}a\right]_\times \mathbf{L} \\
\mathbf{0}_3 & \mathbf{0}_3 & \mathbf{D}_1 & \mathbf{0}_3 & \mathbf{0}_3 \\
\mathbf{0}_3 & \mathbf{0}_3 & \mathbf{D}_2 & \mathbf{0}_3 & \mathbf{E}_1 \\
\mathbf{0}_3 & \mathbf{0}_3 & \mathbf{D}_3 & \mathbf{0}_3 & \mathbf{E}_2 \\
\vdots & \vdots & \vdots & \vdots & \vdots \\
\mathbf{0}_3 & \mathbf{0}_3 & \mathbf{D}_{15} & \mathbf{0}_3 & \mathbf{E}_{15}
\end{pmatrix}
\tag{5.40}
$$

A nullspace analysis over $\mathbf{O}_L$ reveals that:

- In the case that both a and ω are null, after eliminating null rows matrix $\mathbf{O}_L$ reduces to

$$
\mathbf{O}_L = \begin{pmatrix}
\mathbf{I}_3 & \mathbf{0}_3 & \mathbf{0}_3 & \mathbf{0}_3 & \mathbf{0}_3 \\
\mathbf{0}_3 & \mathbf{I}_3 & \mathbf{0}_3 & \mathbf{0}_3 & \mathbf{0}_3 \\
\mathbf{0}_3 & \mathbf{0}_3 & \mathbf{0}_3 & -\mathbf{L} & \mathbf{0}_3 \\
\mathbf{0}_3 & \mathbf{0}_3 & \mathbf{L}^\top\left[H\right]_\times & \mathbf{0}_3 & \mathbf{0}_3 \\
\mathbf{0}_3 & \mathbf{0}_3 & \dot{\mathbf{L}}^\top\left[H\right]_\times & \mathbf{0}_3 & -\mathbf{L}^\top\left[H\right]_\times \mathbf{L}
\end{pmatrix}
$$

  Elements in the nullspace of the reduced $\mathbf{O}_L$ have the form

$$
n_{L1} = \begin{pmatrix}
\mathbf{0}_{6\times1} \\
H \\
\mathbf{0}_{3\times1} \\
\mathbf{L}^\top H
\end{pmatrix}
$$

  and singular inputs can be identified as

$$
u_{s1} = \begin{pmatrix}
b_a \\
b_\omega
\end{pmatrix}
$$

- If the platform is not rotating, i.e, $\omega = \mathbf{0}$ and assuming non null value of the specific forces $a \neq \mathbf{0}$, matrices $\mathbf{D}_i = \mathbf{0}\,\forall i \geq 2$ and $\mathbf{E}_i = \mathbf{0}\,\forall i \geq 3$, reducing the observability matrix to

$$
\mathbf{O}_L = \begin{pmatrix}
\mathbf{I}_3 & \mathbf{0}_3 & \mathbf{0}_3 & \mathbf{0}_3 & \mathbf{0}_3 \\
\mathbf{0}_3 & \mathbf{I}_3 & \mathbf{0}_3 & \mathbf{0}_3 & \mathbf{0}_3 \\
\mathbf{0}_3 & \mathbf{0}_3 & -\left[\mathbf{L}a\right]_\times & -\mathbf{L} & \mathbf{0}_3 \\
\mathbf{0}_3 & \mathbf{0}_3 & \mathbf{0}_3 & \mathbf{0}_3 & \left[\mathbf{L}a\right]_\times \mathbf{L} \\
\mathbf{0}_3 & \mathbf{0}_3 & \mathbf{L}^\top\left[H\right]_\times & \mathbf{0}_3 & \mathbf{0}_3 \\
\mathbf{0}_3 & \mathbf{0}_3 & \mathbf{0}_3 & \mathbf{0}_3 & -\mathbf{L}^\top\left[H\right]_\times \mathbf{L}
\end{pmatrix}
$$

The nullspace is again non-empty and contains elements of the form

$$
\boldsymbol{n}_{L2} = \begin{pmatrix} \mathbf{0}_{6\times 1} \\ \boldsymbol{H} \\ -\left[\boldsymbol{a}\right]_{\times}\mathbf{L}^{\top}\boldsymbol{H} \\ \mathbf{0}_{3\times 1} \end{pmatrix}
$$

and singular inputs can be identified as

$$
\boldsymbol{u}_{s2} = \begin{pmatrix} \boldsymbol{k} \\ \boldsymbol{b}_{\omega} \end{pmatrix} \forall \boldsymbol{k} \in \mathbb{R}^3, \boldsymbol{k} \neq \boldsymbol{b}_a
$$

- In the case that $\boldsymbol{a} = \mathbf{0}$, and the platform is rotating in a generic direction $\boldsymbol{\omega} \neq \mathbf{0}$, $\mathbf{O}_{L1}$ simplifies whereas $\mathbf{O}_{L2}$ does not. The resulting observability matrix is represented by

$$
\mathbf{O}_L = \begin{pmatrix}
\mathbf{I}_3 & \mathbf{0}_3 & \mathbf{0}_3 & \mathbf{0}_3 & \mathbf{0}_3 \\
\mathbf{0}_3 & \mathbf{I}_3 & \mathbf{0}_3 & \mathbf{0}_3 & \mathbf{0}_3 \\
\mathbf{0}_3 & \mathbf{0}_3 & \mathbf{0}_3 & -\mathbf{L} & \mathbf{0}_3 \\
\mathbf{0}_3 & \mathbf{0}_3 & \mathbf{D}_1 & \mathbf{0}_3 & \mathbf{0}_3 \\
\mathbf{0}_3 & \mathbf{0}_3 & \mathbf{D}_2 & \mathbf{0}_3 & \mathbf{E}_2 \\
\vdots & \vdots & \vdots & \vdots & \vdots
\end{pmatrix}
$$

Noting that matrices $\mathbf{E}_i$ share the nullspace represented by the vector $\boldsymbol{H}$ and that for a generic $\boldsymbol{\omega}$ matrices $\mathbf{D}_i$ do not, the nullspace of $\mathbf{O}_L$ is spanned by the vector

$$
\boldsymbol{n}_{L3} = \begin{pmatrix} \mathbf{0}_{6\times 1} \\ \boldsymbol{H} \\ \mathbf{0}_{6\times 1} \end{pmatrix}
$$

and singular inputs can be identified as

$$
\boldsymbol{u}_{s3} = \begin{pmatrix} \boldsymbol{b}_a \\ \boldsymbol{k} \end{pmatrix} \forall \boldsymbol{k} \in \mathbb{R}^3, \boldsymbol{k} \neq \boldsymbol{b}_{\omega}
$$

- If $\boldsymbol{\omega}$ is parallel to the magnetic field direction, i.e, $\boldsymbol{\omega} = \kappa \mathbf{L}^{\top}\boldsymbol{H}$ and $\boldsymbol{a}$ take generic values, matrices $\mathbf{E}_i$ share the same nullspace than $\mathbf{D}_i$. From a rank perspective this means that block rows given by $\mathbf{D}_i$ and $\mathbf{E}_i$ $\forall i > 2$ are redundant. As a consequence the nullspace analysis can be made over the smaller matrix

$$
\mathbf{O}'_L = \begin{pmatrix}
\mathbf{I}_3 & \mathbf{0}_3 & \mathbf{0}_3 & \mathbf{0}_3 & \mathbf{0}_3 \\
\mathbf{0}_3 & \mathbf{I}_3 & \mathbf{0}_3 & \mathbf{0}_3 & \mathbf{0}_3 \\
\mathbf{0}_3 & \mathbf{0}_3 & -\left[\mathbf{L}\boldsymbol{a}\right]_{\times} & -\mathbf{L} & \mathbf{0}_3 \\
\mathbf{0}_3 & \mathbf{0}_3 & \mathbf{0}_3 & \mathbf{0}_3 & \left[\mathbf{L}\boldsymbol{a}\right]_{\times}\mathbf{L} \\
\mathbf{0}_3 & \mathbf{0}_3 & \mathbf{L}^{\top}\left[\boldsymbol{H}\right]_{\times} & \mathbf{0}_3 & \mathbf{0}_3 \\
\mathbf{0}_3 & \mathbf{0}_3 & \dot{\mathbf{L}}^{\top}\left[\boldsymbol{H}\right]_{\times} & \mathbf{0}_3 & -\mathbf{L}^{\top}\left[\boldsymbol{H}\right]_{\times}\mathbf{L}
\end{pmatrix}
$$

As it can be observed this is the same observability matrix than the one presented when $\boldsymbol{\omega} = \mathbf{0}$. As a consequence, the nullspace is spanned by the same vector

$$\boldsymbol{n}_{L4} = \begin{pmatrix} \mathbf{0}_{6 \times 1} \\ \boldsymbol{H} \\ -\left[\boldsymbol{a}\right]_{\times} \mathbf{L}^{\top} \boldsymbol{H} \\ \mathbf{0}_{3 \times 1} \end{pmatrix}$$

and singular inputs can be identified as

$$\boldsymbol{u}_{sL4} = \begin{pmatrix} \boldsymbol{k}_1 \\ \boldsymbol{b}_\omega + k_2 \mathbf{L}^{\top} \boldsymbol{H} \end{pmatrix} \forall \boldsymbol{k}_1 \in \mathbb{R}^3, \boldsymbol{k}_1 \neq \boldsymbol{b}_a, k_2 \in \mathbb{R}$$

Note that this case includes the case $\boldsymbol{\omega} = 0$ if $k_2 = 0$.

- In the case that the vehicle rotates about the magnetic field vector and the specific force also points in that direction, i.e., $\boldsymbol{\omega} = \kappa_1 \mathbf{L}^{\top} \boldsymbol{H}$, $\boldsymbol{a} = \kappa_2 \mathbf{L}^{\top} \boldsymbol{H}$, $\mathbf{O}_{L1}$ reduces to

$$\mathbf{O}_{L1} = \begin{pmatrix} \mathbf{I}_3 & \mathbf{0}_3 & \mathbf{0}_3 & \mathbf{0}_3 & \mathbf{0}_3 \\ \mathbf{0}_3 & \mathbf{I}_3 & \mathbf{0}_3 & \mathbf{0}_3 & \mathbf{0}_3 \\ \mathbf{0}_3 & \mathbf{0}_3 & -\kappa_1 \left[\boldsymbol{H}\right]_{\times} & -\mathbf{L} & \mathbf{0}_3 \\ \mathbf{0}_3 & \mathbf{0}_3 & \mathbf{0}_3 & \mathbf{0}_3 & \kappa_2 \left[\boldsymbol{H}\right]_{\times} \mathbf{L} \end{pmatrix}$$

When is it the case, block columns three and five of $\mathbf{O}_{L1}$ share the nullspace of $\mathbf{D}_i$ and $\mathbf{E}_i$. Then elements in the nullspace of $\mathbf{O}_L$ have the form

$$\boldsymbol{n}_{L5} = \begin{pmatrix} \mathbf{0}_{6 \times 1} \\ \boldsymbol{H} \\ \mathbf{0}_{3 \times 1} \\ \mathbf{L}^{\top} \boldsymbol{H} \end{pmatrix}$$

and singular inputs are then

$$\boldsymbol{u}_{sL5} = \begin{pmatrix} \boldsymbol{b}_a + k_1 \mathbf{L}^{\top} \boldsymbol{H} \\ \boldsymbol{b}_\omega + k_2 \mathbf{L}^{\top} \boldsymbol{H} \end{pmatrix} \forall k1, k2 \in \mathbb{R}$$

- In the case that $\boldsymbol{a}$ and $\boldsymbol{\omega}$ are constant and do not fulfil any of the previous requirements, the nullspace of $\mathbf{O}_L$ does not simplify in any special way, however its kernel its still non-empty and it is spanned by the vector

$$\boldsymbol{n}_{L6} = \begin{pmatrix} \mathbf{0}_{6 \times 1} \\ \boldsymbol{H} \\ -\left[\boldsymbol{a}\right]_{\times} \mathbf{L}^{\top} \boldsymbol{H} \\ \mathbf{0}_{3 \times 1} \end{pmatrix}$$

The vector spanning the nullspace represents a rotation about the direction of the magnetic field for the attitude and an increment of accelerometer bias that is orthogonal to

the direction of the magnetic field and the specific force. The constant singular inputs compatible with this condition are given by

$$\boldsymbol{u}_{sL6} = \begin{pmatrix} \boldsymbol{k}_1 \\ \boldsymbol{k}_2 \end{pmatrix} \quad \forall \boldsymbol{k}_1, \boldsymbol{k}_2 \in \mathbb{R}^3$$

with $\boldsymbol{k}_1 \neq \boldsymbol{b}_a + k_1 \mathbf{L}^\top \boldsymbol{H}$, $\boldsymbol{k}_2 \neq \boldsymbol{b}_\omega + k_2 \mathbf{L}^\top \boldsymbol{H}$ for any $k_1, k_2 \in \mathbb{R}$.

5.5.2 Singular input analysis of the body frame attitude error equations

This section deals with the singular input analysis of the LTV system in Eq. (5.29). By successively exponentiating matrix $\mathbf{A}_R$ in Eq. (5.29b) and taking into account that $[\boldsymbol{v}]_\times^3 = -\|\boldsymbol{v}\|^2 [\boldsymbol{v}]_\times$,

$$\mathbf{A}_R^{5+i} = \begin{cases} \propto \mathbf{A}_R^4 & \text{for, } i = 1, 3, 5, \dots \\ \propto \mathbf{A}_R^5 & \text{for, } i = 2, 4, 6, \dots \end{cases}$$

As a consequence, terms of the form $\mathbf{C}_{jR}\mathbf{A}_R^{5+i}$ for $i \geq 1$, $j = 1, 2$ are proportional to previous rows of the observability matrix, being redundant in terms of matrix rank. In addition note that the time derivatives of $\mathbf{A}_R$ share the same block structure and its k-th time derivative can be calculated as

$$\overset{(k)}{\mathbf{A}_R} = \begin{pmatrix} \mathbf{0}_3 & \mathbf{0}_3 & \mathbf{0}_3 & \mathbf{0}_3 & \mathbf{0}_3 \\ \mathbf{0}_3 & \mathbf{0}_3 & -\overset{(k)}{\mathbf{L}}[\boldsymbol{a}]_\times & -\overset{(k)}{\mathbf{L}} & \mathbf{0}_3 \\ \mathbf{0}_3 & \mathbf{0}_3 & \mathbf{0}_3 & \mathbf{0}_3 & \mathbf{0}_3 \\ \mathbf{0}_3 & \mathbf{0}_3 & \mathbf{0}_3 & \mathbf{0}_3 & \mathbf{0}_3 \\ \mathbf{0}_3 & \mathbf{0}_3 & \mathbf{0}_3 & \mathbf{0}_3 & \mathbf{0}_3 \end{pmatrix} \quad \forall k \geq 1$$

Considering the observability matrix related with $\mathbf{C}_{1R}$, and taking into account that $\dot{\mathbf{C}}_{1R} = \mathbf{0}$ and that $\mathbf{C}_{1R}\dot{\mathbf{A}}_R = \mathbf{0}$ the observability matrix corresponding to the measurement matrix $\mathbf{C}_{1R}$ can be written as

$$\mathbf{O}_{R_1} = \begin{pmatrix} \mathbf{C}_{R1} \\ \mathbf{C}_{r1}\mathbf{A}_L \\ \mathbf{C}_{L1}\mathbf{A}_L^2 \\ \mathbf{C}_{L1}\mathbf{A}_L^3 \\ \mathbf{C}_{L1}\mathbf{A}_L^4 \\ \mathbf{C}_{L1}\mathbf{A}_L^5 \end{pmatrix} = \begin{pmatrix} \mathbf{I}_3 & \mathbf{0}_3 & \mathbf{0}_3 & \mathbf{0}_3 & \mathbf{0}_3 \\ \mathbf{0}_3 & \mathbf{I}_3 & \mathbf{0}_3 & \mathbf{0}_3 & \mathbf{0}_3 \\ \mathbf{0}_3 & \mathbf{0}_3 & -\mathbf{L}[\boldsymbol{a}]_\times & -\mathbf{L} & \mathbf{0}_3 \\ \mathbf{0}_3 & \mathbf{0}_3 & \mathbf{L}[\boldsymbol{a}]_\times[\boldsymbol{\omega}]_\times & \mathbf{0}_3 & \mathbf{L}[\boldsymbol{a}]_\times \\ \mathbf{0}_3 & \mathbf{0}_3 & -\mathbf{L}[\boldsymbol{a}]_\times[\boldsymbol{\omega}]_\times^2 & \mathbf{0}_3 & -\mathbf{L}[\boldsymbol{a}]_\times[\boldsymbol{\omega}]_\times \\ \mathbf{0}_3 & \mathbf{0}_3 & \mathbf{L}[\boldsymbol{a}]_\times[\boldsymbol{\omega}]_\times^3 & \mathbf{0}_3 & \mathbf{L}[\boldsymbol{a}]_\times[\boldsymbol{\omega}]_\times^2 \end{pmatrix} \tag{5.41}$$

By taking into account that $\mathbf{C}_{R2}\mathbf{A}_R = \mathbf{0}$ the observability matrix for $\mathbf{C}_{R2}$ can be written as

$$\mathbf{O}_{R_2} = \begin{pmatrix} \mathbf{C}_{R2} \\ \dot{\mathbf{C}}_{R2} + \mathbf{C}_{R2}\mathbf{A}_R \\ \ddot{\mathbf{C}}_{R2} + 2\dot{\mathbf{C}}_{R2}\mathbf{A}_R \\ \dddot{\mathbf{C}}_{R2} + 3\ddot{\mathbf{C}}_{R2}\mathbf{A}_R + 3\dot{\mathbf{C}}_{R2}\mathbf{A}_R^2 + \mathbf{C}_{R2}\mathbf{A}_R^3 \\ \vdots \end{pmatrix} = \begin{pmatrix} \vdots \\ \sum_{l=0}^{i} \binom{i}{l} \overset{(i-l)}{\mathbf{C}}_{R2}\mathbf{A}_R^l \\ \vdots \end{pmatrix} \tag{5.42}$$

where k in the last equations indicates the (block) row index. By developing the matirix expressions it can be found that

$$\mathbf{O}_{R2} = \begin{pmatrix} \mathbf{0}_3 & \mathbf{0}_3 & \mathbf{D}_1 & \mathbf{0}_3 & \mathbf{0}_3 \\ \mathbf{0}_3 & \mathbf{0}_3 & \mathbf{D}_2 & \mathbf{0}_3 & \mathbf{E}_2 \\ \mathbf{0}_3 & \mathbf{0}_3 & \mathbf{D}_3 & \mathbf{0}_3 & \mathbf{E}_3 \\ \vdots & \vdots & \vdots & \vdots & \vdots \\ \mathbf{0}_3 & \mathbf{0}_3 & \mathbf{D}_{15} & \mathbf{0}_3 & \mathbf{E}_{15} \end{pmatrix}$$

where

$$\mathbf{D}_{i+1} = \sum_{l=0}^{i} (-1)^i \binom{i}{l} \left[[\boldsymbol{\omega}]_\times^{i-l} \mathbf{L}^\mathsf{T}\boldsymbol{H} \right]_\times [\boldsymbol{\omega}]_\times^l \quad \forall i \geq 0$$

$$\mathbf{E}_{i+1} = \sum_{l=1}^{i} (-1)^i \binom{i}{l} \left[[\boldsymbol{\omega}]_\times^{i-l} \mathbf{L}^\mathsf{T}\boldsymbol{H} \right]_\times [\boldsymbol{\omega}]_\times^{l-1} \quad \forall i \geq 1$$

It is worth noting that matrices $\mathbf{D}_i \, \forall i > 1$ share the vector $\mathbf{L}^\mathsf{T}\boldsymbol{H}$ as an element of its nullspace whatever the vector $\boldsymbol{\omega}$ is. However this is not the case for matrices $\boldsymbol{E}_i$ whose linear combination is full column rank. A nullspace analysis over $\mathbf{O}_R^\mathsf{T} = \mathbf{O}_{R_1}^\mathsf{T}\mathbf{O}_{R_2}^\mathsf{T}$ reveals that:

- For the case in which both $\boldsymbol{a} = \mathbf{0}$ and $\boldsymbol{\omega} = \mathbf{0}$, the observability matrix $\mathbf{O}_R$ reduces to

$$\mathbf{O}_R = \begin{pmatrix} \mathbf{I}_3 & \mathbf{0}_3 & \mathbf{0}_3 & \mathbf{0}_3 & \mathbf{0}_3 \\ \mathbf{0}_3 & \mathbf{I}_3 & \mathbf{0}_3 & \mathbf{0}_3 & \mathbf{0}_3 \\ \mathbf{0}_3 & \mathbf{0}_3 & \mathbf{0}_3 & -\mathbf{L} & \mathbf{0}_3 \\ \mathbf{0}_3 & \mathbf{0}_3 & [\mathbf{L}^\mathsf{T}\boldsymbol{H}]_\times & \mathbf{0}_3 & \mathbf{0}_3 \\ \mathbf{0}_3 & \mathbf{0}_3 & \mathbf{0}_3 & \mathbf{0}_3 & -[\mathbf{L}^\mathsf{T}\boldsymbol{H}]_\times \end{pmatrix}$$

Elements in the kernel of $\mathbf{O}_R$ have the form

$$\boldsymbol{n}_{R1} = \begin{pmatrix} \mathbf{0}_{6\times 1} \\ \mathbf{L}^\mathsf{T}\boldsymbol{H} \\ \mathbf{0}_{3\times 1} \\ \mathbf{L}^\mathsf{T}\boldsymbol{H} \end{pmatrix}$$

and the associated singular input can be described by

$$\boldsymbol{u}_{sR1} = \begin{pmatrix} b_a \\ b_\omega \end{pmatrix}$$

- In the case that the vehicle does not rotate, i.e., $\boldsymbol{\omega} = \mathbf{0}$ and the specific force is not null $\boldsymbol{a} \neq \mathbf{0}$, after eliminating null rows, matrix $\mathbf{O}_R$ reduces to

$$
\mathbf{O}_R = \begin{pmatrix}
\mathbf{I}_3 & \mathbf{0}_3 & \mathbf{0}_3 & \mathbf{0}_3 & \mathbf{0}_3 \\
\mathbf{0}_3 & \mathbf{I}_3 & \mathbf{0}_3 & \mathbf{0}_3 & \mathbf{0}_3 \\
\mathbf{0}_3 & \mathbf{0}_3 & -\mathbf{L}\left[\boldsymbol{a}\right]_\times & -\mathbf{L} & \mathbf{0}_3 \\
\mathbf{0}_3 & \mathbf{0}_3 & \mathbf{0}_3 & \mathbf{0}_3 & \mathbf{L}\left[\boldsymbol{a}\right]_\times \\
\mathbf{0}_3 & \mathbf{0}_3 & \left[\mathbf{L}^\top \boldsymbol{H}\right]_\times & \mathbf{0}_3 & \mathbf{0}_3 \\
\mathbf{0}_3 & \mathbf{0}_3 & \mathbf{0}_3 & \mathbf{0}_3 & -\left[\mathbf{L}^\top \boldsymbol{H}\right]_\times
\end{pmatrix}
$$

In that case the nullspace is spanned by vectors as

$$
\boldsymbol{n}_{R2} = \begin{pmatrix}
\mathbf{0}_{6\times 1} \\
\mathbf{L}^\top \boldsymbol{H} \\
-\left[a\right]_\times \mathbf{L}^\top \boldsymbol{H} \\
\mathbf{0}_3
\end{pmatrix}
$$

And the associated constant singular input is represented by

$$
\boldsymbol{u}_{sR2} = \begin{pmatrix} \boldsymbol{k} \\ \boldsymbol{b}_\omega \end{pmatrix} \forall \boldsymbol{k} \in \mathbb{R}^3, \boldsymbol{k} \neq \boldsymbol{b}_a
$$

- In the case that there are no external actions acting over the platform $\boldsymbol{a} = \mathbf{0}$ and the aircraft rotates freely, $\boldsymbol{\omega} \neq \mathbf{0}$, $\mathbf{O}_{R1}$ simplifies and the observability matrix is represented by

$$
\mathbf{O}_R = \begin{pmatrix}
\mathbf{I}_3 & \mathbf{0}_3 & \mathbf{0}_3 & \mathbf{0}_3 & \mathbf{0}_3 \\
\mathbf{0}_3 & \mathbf{I}_3 & \mathbf{0}_3 & \mathbf{0}_3 & \mathbf{0}_3 \\
\mathbf{0}_3 & \mathbf{0}_3 & \mathbf{0}_3 & -\mathbf{L} & \mathbf{0}_3 \\
\mathbf{0}_3 & \mathbf{0}_3 & \left[\mathbf{L}^\top \boldsymbol{H}\right]_\times & \mathbf{0}_3 & \mathbf{0}_3 \\
\mathbf{0}_3 & \mathbf{0}_3 & \mathbf{D}_2 & \mathbf{0}_3 & \mathbf{D}_3 \\
\mathbf{0}_3 & \mathbf{0}_3 & \mathbf{D}_3 & \mathbf{0}_3 & \mathbf{E}_3 \\
\vdots & \vdots & \vdots & \vdots & \vdots
\end{pmatrix}
$$

Since as said $\mathbf{D}_i \ \forall i \geq 1$ share the same nullsspace vector $\mathbf{L}^\top \boldsymbol{H}$, the nullspace of $\mathbf{O}_R$ is spanned by the vector

$$
\boldsymbol{n}_{R3} = \begin{pmatrix}
\mathbf{0}_{6\times 1} \\
\mathbf{L}^\top \boldsymbol{H} \\
\mathbf{0}_{6\times 1}
\end{pmatrix}
$$

The associates singular input in this case is given by

$$
\boldsymbol{u}_{sR3} = \begin{pmatrix} \boldsymbol{b}_a \\ \boldsymbol{k} \end{pmatrix} \forall \boldsymbol{k} \in \mathbb{R}^3, \boldsymbol{k} \neq \boldsymbol{b}_\omega
$$

- For the specific case in which $\boldsymbol{\omega}$ is constant and parallel to the magnetic field, i.e, $\boldsymbol{\omega} = \kappa \mathbf{L}^\top \boldsymbol{H}$ terms of the form $\left[[\boldsymbol{\omega}]_\times^p \mathbf{L}^\top \boldsymbol{H}\right]_\times \forall p > 0$ present in $\mathbf{D}_i$, $\mathbf{E}_i$, $i = 1, 2, ..15$ get null and $\mathbf{O}_R$ simplifies in

$$
\mathbf{O}_R = \begin{pmatrix}
\mathbf{I}_3 & \mathbf{0}_3 & \mathbf{0}_3 & \mathbf{0}_3 & \mathbf{0}_3 \\
\mathbf{0}_3 & \mathbf{I}_3 & \mathbf{0}_3 & \mathbf{0}_3 & \mathbf{0}_3 \\
\mathbf{0}_3 & \mathbf{0}_3 & -\mathbf{L}\left[\boldsymbol{a}\right]_\times & -\mathbf{L} & \mathbf{0}_3 \\
\mathbf{0}_3 & \mathbf{0}_3 & \mathbf{L}\left[\boldsymbol{a}\right]_\times\left[\mathbf{L}^\top \boldsymbol{H}\right]_\times & \mathbf{0}_3 & \mathbf{L}\left[\boldsymbol{a}\right]_\times \\
\mathbf{0}_3 & \mathbf{0}_3 & -\mathbf{L}\left[\boldsymbol{a}\right]_\times\left[\mathbf{L}^\top \boldsymbol{H}\right]_\times^2 & \mathbf{0}_3 & -\mathbf{L}\left[\boldsymbol{a}\right]_\times\left[\mathbf{L}^\top \boldsymbol{H}\right]_\times \\
\mathbf{0}_3 & \mathbf{0}_3 & \mathbf{L}\left[\boldsymbol{a}\right]_\times\left[\mathbf{L}^\top \boldsymbol{H}\right]_\times^3 & \mathbf{0}_3 & \mathbf{L}\left[\boldsymbol{a}\right]_\times\left[\mathbf{L}^\top \boldsymbol{H}\right]_\times^2 \\
\mathbf{0}_3 & \mathbf{0}_3 & \left[\mathbf{L}^\top \boldsymbol{H}\right]_\times & \mathbf{0}_3 & \mathbf{0}_3 \\
\mathbf{0}_3 & \mathbf{0}_3 & -\left[\mathbf{L}^\top \boldsymbol{H}\right]_\times^2 & \mathbf{0}_3 & -\left[\mathbf{L}^\top \boldsymbol{H}\right]_\times \\
\mathbf{0}_3 & \mathbf{0}_3 & \left[\mathbf{L}^\top \boldsymbol{H}\right]_\times^3 & \mathbf{0}_3 & \left[\mathbf{L}^\top \boldsymbol{H}\right]_\times^2
\end{pmatrix}
$$

Which shows that $\mathbf{O}_{R_1}$ has a non-empty nullspace spanned by elements of the proportional to

$$
\boldsymbol{n}_{R4} = \begin{pmatrix}
\mathbf{0}_{6\times 1} \\
\mathbf{L}^\top \boldsymbol{H} \\
-\left[\boldsymbol{a}\right]_\times \mathbf{L}^\top \boldsymbol{H} \\
\mathbf{0}_{3\times 1}
\end{pmatrix}
$$

Similarly as discussed for $\boldsymbol{n}_{L1}$, the vector spanning the nullspace represents a rotation about the direction of the magnetic field for the attitude and an increment of accelerometer bias that is orthogonal to the direction of the magnetic field and the specific force.

In contrast, the constant singular input compatible with this condition is given by

$$
\boldsymbol{u}_{sR4} = \begin{pmatrix} \boldsymbol{a}_m \\ \boldsymbol{\omega}_m \end{pmatrix} = \begin{pmatrix} \boldsymbol{k}_1 \\ \boldsymbol{b}_w + k_2 \mathbf{L}^\top \boldsymbol{H} \end{pmatrix} \quad \forall \boldsymbol{k}_1 \in \mathbb{R}^3, \boldsymbol{k}_1 \neq \boldsymbol{b}_a, k_2 \in \mathbb{R}
$$

Note that this case includes the case $\boldsymbol{\omega} = 0$ which implies a non-rotating aircraft.

- In the much more particular case in which vectors $\boldsymbol{a}$ and $\boldsymbol{\omega}$ are parallel and take the direction of the magnetic field, i.e., $\boldsymbol{a} = \kappa_1 \mathbf{L}^\top \boldsymbol{H}$ and $\boldsymbol{\omega} = \kappa_2 \mathbf{L}^\top \boldsymbol{H}$. Considering that redundant rows are not necessary in terms of rank, the nullspace of $\mathbf{O}_R$ is equivalent to that of $\mathbf{O}'_R$ given by

$$
\mathbf{O}_R = \begin{pmatrix}
\mathbf{I}_3 & \mathbf{0}_3 & \mathbf{0}_3 & \mathbf{0}_3 & \mathbf{0}_3 \\
\mathbf{0}_3 & \mathbf{I}_3 & \mathbf{0}_3 & \mathbf{0}_3 & \mathbf{0}_3 \\
\mathbf{0}_3 & \mathbf{0}_3 & -\left[\mathbf{L}^\top \boldsymbol{H}\right]_\times & -\mathbf{L} & \mathbf{0}_3 \\
\mathbf{0}_3 & \mathbf{0}_3 & \left[\mathbf{L}^\top \boldsymbol{H}\right]_\times^2 & \mathbf{0}_3 & \mathbf{L}\left[\mathbf{L}^\top \boldsymbol{H}\right]_\times \\
\mathbf{0}_3 & \mathbf{0}_3 & -\mathbf{L}\left[\mathbf{L}^\top \boldsymbol{H}\right]_\times^3 & \mathbf{0}_3 & -\mathbf{L}\left[\mathbf{L}^\top \boldsymbol{H}\right]_\times^2 \\
\mathbf{0}_3 & \mathbf{0}_3 & \left[\mathbf{L}^\top \boldsymbol{H}\right]_\times & \mathbf{0}_3 & \mathbf{0}_3 \\
\mathbf{0}_3 & \mathbf{0}_3 & -\left[\mathbf{L}^\top \boldsymbol{H}\right]_\times^2 & \mathbf{0}_3 & -\left[\mathbf{L}^\top \boldsymbol{H}\right]_\times \\
\mathbf{0}_3 & \mathbf{0}_3 & \left[\mathbf{L}^\top \boldsymbol{H}\right]_\times^3 & \mathbf{0}_3 & \left[\mathbf{L}^\top \boldsymbol{H}\right]_\times^2
\end{pmatrix}
$$

from where it can be observerd that block columns three and five of $\mathbf{O}_R$ share the same nullspace $\mathbf{L}^\top H$ and as a consequence the nullspace of $\mathbf{O}_R$ is represented by the vector

$$
\boldsymbol{n}_{R5} = \begin{pmatrix} \mathbf{0}_{6\times1} \\ \mathbf{L}^\top H \\ \mathbf{0}_{3\times1} \\ \mathbf{L}^\top H \end{pmatrix}
$$

In a similar way as discussed before for $\boldsymbol{n}_{L2}$, $\boldsymbol{n}_{R2}$ represents a possible drift in the values of the attitude and $\boldsymbol{b}_\omega$ in the direction of the magnetic field. In this case the singular input is identified by the vector

$$
\boldsymbol{u}_{sR5} = \begin{pmatrix} \boldsymbol{a}_m \\ \boldsymbol{\omega}_m \end{pmatrix} = \begin{pmatrix} \boldsymbol{b}_a + k_1 \mathbf{L}^\top H \\ \boldsymbol{b}_\omega + k_2 \mathbf{L}^\top H \end{pmatrix} \quad \forall k_1, k_2 \in \mathbb{R}
$$

- For generic non-null constant values of $\boldsymbol{a}$ and $\boldsymbol{\omega}$, respectively constant values of $\boldsymbol{a}_m \neq \boldsymbol{b}_a$, the rank analysis of $\mathbf{O}_R$ can be related with the rank study of the reduced matrix $\mathbf{O}'_R$ constructed from row elements of $\mathbf{O}_R$

$$
\mathbf{O}'_R = \begin{pmatrix}
\mathbf{I}_3 & \mathbf{0}_3 & \mathbf{0}_3 & \mathbf{0}_3 & \mathbf{0}_3 \\
\mathbf{0}_3 & \mathbf{I}_3 & \mathbf{0}_3 & \mathbf{0}_3 & \mathbf{0}_3 \\
\mathbf{0}_3 & \mathbf{0}_3 & -\mathbf{L}\left[a\right]_\times & -\mathbf{L} & \mathbf{0}_3 \\
\mathbf{0}_3 & \mathbf{0}_3 & \mathbf{L}\left[a\right]_\times\left[\omega\right]_\times & \mathbf{0}_3 & \mathbf{L}\left[a\right]_\times \\
\mathbf{0}_3 & \mathbf{0}_3 & \left[\mathbf{L}^\top H\right]_\times & \mathbf{0}_3 & \mathbf{0}_3 \\
\mathbf{0}_3 & \mathbf{0}_3 & -\left[\left[\omega\right]_\times \mathbf{L}^\top H\right]_\times - \left[\mathbf{L}^\top H\right]_\times\left[\omega\right]_\times & \mathbf{0}_3 & -\left[\mathbf{L}^\top H\right]_\times
\end{pmatrix}
$$

Let the partition of $\mathbf{O}'_R$ as

$$
\mathbf{O}'_R = \left(\mathbf{r}_1^\top, \mathbf{r}_2^\top, \mathbf{r}_3^\top, \mathbf{r}_4^\top, \mathbf{r}_5^\top, \mathbf{r}_6^\top\right)^\top
$$

with r_i representing the block row matrix and

$$
\boldsymbol{n}_{R6} = \left(\boldsymbol{n_1}^\top, \boldsymbol{n_2}^\top, \boldsymbol{n_3}^\top, \boldsymbol{n_4}^\top, \boldsymbol{n_5}^\top\right)^\top
$$

representing an element of the nullspace of $\mathbf{O}'_R$, then

$$
\mathbf{r}_i \boldsymbol{n}_{R6} = \mathbf{0} \ \forall i = 1, 2, ..., 5
$$

From a nullspace perspective, block rows $\mathbf{r}_1$ and $\mathbf{r}_2$, force any vector in the nullspace of $\mathbf{O}'_R$ to have null $\boldsymbol{n}_1$ and $\boldsymbol{n}_2$, i.e., $\boldsymbol{n}_1 = \mathbf{0}$ and $\boldsymbol{n}_2 = \mathbf{0}$. The fifth block row $\mathbf{r}_5$ suggests that components $\boldsymbol{n}_3$ of the null space vector have to be either zero or conform a vector parallel to $\mathbf{L}^\top H$, i.e,

$$
\mathbf{r}_5 \boldsymbol{n}_{R6} = \mathbf{D}_1 \boldsymbol{n}_3 = \mathbf{0} \Rightarrow \boldsymbol{n}_3 = \begin{cases} \mathbf{0} \\ \mathbf{L}^\top H \end{cases}
$$

In fact it can be seen that $\mathbf{L}^\top \boldsymbol{H}$ is in the nullspace of any $\mathbf{D}_i \ \forall i = 1, 2, ..16$. Using this, the last block row of $\mathbf{O}'_R$, $\mathbf{r}_6$, implies that $\boldsymbol{n}_5$ has to be again, either zero or conform a vector parallel to $\mathbf{L}^\top \boldsymbol{H}$

$$\mathbf{r}_6 \boldsymbol{n}_{R6} = \mathbf{D}_2 \boldsymbol{n}_3 + \mathbf{E}_2 \boldsymbol{n}_5 = 0 \Rightarrow \boldsymbol{n}_5 = \begin{cases} \mathbf{0} \\ \mathbf{L}^\top \boldsymbol{H} \end{cases}$$

It can be shown that the non-null values of $\boldsymbol{n}_3$ and $\boldsymbol{n}_5$ proposed are not compatible with the fourth block row i.e.,

$$\mathbf{L}\left[\boldsymbol{a}\right]_\times \left[\boldsymbol{\omega}\right]_\times \mathbf{L}^\top \boldsymbol{H} + \mathbf{L}\left[\boldsymbol{a}\right]_\times \mathbf{L}^\top \boldsymbol{H} \neq \mathbf{0}$$

thus leading to the conclusion that $\boldsymbol{n}_3$ and $\boldsymbol{n}_5$ have to be null. With that, using the third block row, it can be shown that $\boldsymbol{n}_4$ has to be also null, leading to an empty kernel for $\mathbf{O}'_R$. This implies that the matrix $\mathbf{O}'_R$ is full column rank. Furthermore, since $\mathbf{O}'_R$ is produced from rows of $\mathbf{O}_R$, $\mathbf{O}_R$ is also full column rank and as a consequence the system represented by Eq. (5.29) is WLO.

5.5.3 LTV singular input analysis: results summary

Results presented shown that under particular aircraft configurations the observability of the dynamic system is compromised.

Table 5.1 shows a condensed summary of the results obtained in the previous sections. It can be observed that for the particular values of $\boldsymbol{\omega}$ and $\boldsymbol{a}$ discussed the system has to have equivalent[1] elements in the kernel produced by the same singular inputs. Many of the analysed configurations are not likely to appear in practice, or usually controllers will not seek to hold those configurations in time, e.g., turning about the magnetic field direction while the external forces points in the same direction. From all of this singular inputs and associated system indistinguishable regions the case for which $\boldsymbol{\omega} = \mathbf{0}$ and $\boldsymbol{a} \neq \mathbf{0}$ is the most generic configuration. In fact, this configuration represents the aircraft in hover mode, a flight configuration central in many UAV misions.

The most stunning result is that the observability matrix derived for system Eq. (5.28) has not full rank whenever $\boldsymbol{\omega}$ and $\boldsymbol{a}$ are constant in contrast with the results for Eq. (5.29) which for generic constant values of $\boldsymbol{\omega}$ and $\boldsymbol{a}$ is demonstrated to be WLO. This inconsistency may have been produced by the incremental formulation. If it is the case, this is a problem that may compromise all the results. In order to verify them, the next section deals with the singular input analysis directly over the nonlinear system.

---

[1]Note that for the system accounting for α_L, $\boldsymbol{H}$, represents a rotation about the vector field direction, which is the same rotation represented by $\mathbf{L}^\top \boldsymbol{H}$ for the system accounting for α_R

Condition	System	Nullspace	Singular inputs
$\boldsymbol{a} = \boldsymbol{0}$ $\boldsymbol{\omega} = \boldsymbol{0}$	Eq. (5.28)	$\left(\boldsymbol{0}_{1\times6},\, \boldsymbol{H}^\top,\, \boldsymbol{0}_{1\times3},\, (\mathbf{L}^\top \boldsymbol{H})^\top\right)^\top$	$\left(\boldsymbol{b}_a^\top,\, \boldsymbol{b}_\omega^\top\right)^\top$
	Eq. (5.29)	$\left(\boldsymbol{0}_{1\times6},\, (\mathbf{L}^\top \boldsymbol{H})^\top,\, \boldsymbol{0}_{1\times3},\, (\mathbf{L}^\top \boldsymbol{H})^\top\right)^\top$	
$\boldsymbol{a} \neq \boldsymbol{0}$ $\boldsymbol{\omega} = \boldsymbol{0}$	Eq. (5.28)	$\left(\boldsymbol{0}_{1\times6},\, \boldsymbol{H}^\top,\, -([\boldsymbol{a}]_\times \mathbf{L}^\top \boldsymbol{H})^\top,\, \boldsymbol{0}_{1\times3}\right)^\top$	$\left(\boldsymbol{k}^\top,\, \boldsymbol{b}_\omega^\top\right)^\top$
	Eq. (5.29)	$\left(\boldsymbol{0}_{1\times6},\, (\mathbf{L}^\top \boldsymbol{H})^\top,\, -([\boldsymbol{a}]_\times \mathbf{L}^\top \boldsymbol{H})^\top,\, \boldsymbol{0}_{1\times3}\right)^\top$	
$\boldsymbol{a} = \boldsymbol{0}$ $\boldsymbol{\omega} \neq \boldsymbol{0}$	Eq. (5.28)	$\left(\boldsymbol{0}_{1\times6},\, \boldsymbol{H}^\top,\, \boldsymbol{0}_{1\times6}\right)^\top$	$\left(\boldsymbol{b}_a^\top,\, \boldsymbol{k}^\top\right)^\top$
	Eq. (5.29)	$\left(\boldsymbol{0}_{1\times6},\, (\mathbf{L}^\top \boldsymbol{H})^\top,\, \boldsymbol{0}_{1\times6}\right)^\top$	
$\boldsymbol{a} \neq \boldsymbol{0}$ $\boldsymbol{\omega} = \kappa \mathbf{L}^\top \boldsymbol{H}$	Eq. (5.28)	$\left(\boldsymbol{0}_{1\times6},\, \boldsymbol{H}^\top,\, (-[\boldsymbol{a}]_\times \mathbf{L}^\top \boldsymbol{H})^\top,\, \boldsymbol{0}_{1\times3}\right)$	$\begin{pmatrix} \boldsymbol{k}_1 \\ \boldsymbol{b}_\omega + k_2 \mathbf{L}^\top \boldsymbol{H} \end{pmatrix}$
	Eq. (5.29)	$\left(\boldsymbol{0}_{1\times6},\, (\mathbf{L}^\top \boldsymbol{H})^\top,\, (-[\boldsymbol{a}]_\times \mathbf{L}^\top \boldsymbol{H})^\top,\, \boldsymbol{0}_{1\times3}\right)^\top$	
$\boldsymbol{a} = \kappa_1 \mathbf{L}^\top \boldsymbol{H}$ $\boldsymbol{\omega} = \kappa_2 \mathbf{L}^\top \boldsymbol{H}$	Eq. (5.28)	$\left(\boldsymbol{0}_{1\times6},\, \boldsymbol{H}^\top,\, \boldsymbol{0}_{1\times3},\, (\mathbf{L}^\top \boldsymbol{H})^\top\right)^\top$	$\begin{pmatrix} \boldsymbol{b}_a + k_1 \mathbf{L}^\top \boldsymbol{H} \\ \boldsymbol{b}_\omega + k_2 \mathbf{L}^\top \boldsymbol{H} \end{pmatrix}$
	Eq. (5.29)	$\left(\boldsymbol{0}_{1\times6},\, (\mathbf{L}^\top \boldsymbol{H})^\top,\, \boldsymbol{0}_{1\times3},\, (\mathbf{L}^\top \boldsymbol{H})^\top\right)^\top$	
$\boldsymbol{a} =$ constant $\boldsymbol{\omega} =$ constant	Eq. (5.28)	$\left(\boldsymbol{0}_{1\times6},\, \boldsymbol{H}^\top,\, \boldsymbol{0}_{1\times3},\, (\mathbf{L}^\top \boldsymbol{H})^\top\right)^\top$	$\left(\boldsymbol{k}_1^\top,\, \boldsymbol{k}_2^\top\right)$
	Eq. (5.29)	-	-

TABLE 5.1: Singular input comparison for LTV dynamics

5.6 Singular inputs for the non-linear IMU driven dynamics

This section is devoted to the finding of the singular inputs of Eq. (5.12) that make the full state not estimable from the system input-output data. Again, constant inputs (null derivative signals) are going to be considered as argued in Section 5.5. Assuming constant inputs implies that time derivatives of input signal in Eq. (5.4) vanishes and reduces the observavility analysis to the study of the rank of

$$\mathcal{O}(\boldsymbol{x}, \boldsymbol{u}) = \begin{pmatrix} \vdots \\ \nabla_{\boldsymbol{x}} L_{\boldsymbol{f}}^k h_i(\boldsymbol{x}) \\ \vdots \end{pmatrix} \quad \text{for } i = 1, .., 7 \text{ and } k = 0, ..., m \tag{5.43}$$

with $\boldsymbol{f}(\boldsymbol{x}, \boldsymbol{u})$ representing the unique vector field obtained by considering $\boldsymbol{\omega}_m$ and $\boldsymbol{a}_m$ in Eq. (5.12a) constant. Note that this is the main difference with respect to what is done in Section 5.4.

In this case, the codistribution matrix $\mathcal{O}$ depends on the singular input vector. We will use this fact to find the singular inputs that make the system's state not fully recoverable. To this end, first the state dependent codistribution matrix is formulated. Then a set of singular inputs are identified for which the system state can not be recovered from input-output data. For these conditions the undistignuishable region is explicitly identified. Finally we use the same reasoning line to show that no singular inputs appear in the case of not considering the bias dynamics.

5.6.1 General form of the codistribution matrix for constant inputs

Let $\mathcal{O}_j$ contain the Lie derivatives in Eq. (5.43) for $\boldsymbol{h}_j$ with $j = \boldsymbol{\xi}, \boldsymbol{H}, \mathring{q}$

$$\mathcal{O}_j = \begin{pmatrix} \nabla_x \left(L_{\boldsymbol{f}}^0 \boldsymbol{h}_j \right) \\ \nabla_x \left(L_{\boldsymbol{f}}^1 \boldsymbol{h}_j \right) \\ \vdots \end{pmatrix} \tag{5.44}$$

and $\boldsymbol{f}$ be the dynamics in Eq. (5.12a). It is straightforward to derive

$$\mathcal{O}_\xi = \begin{pmatrix} \mathbf{I}_3 & \mathbf{0}_3 & \mathbf{0}_{3\times 4} & \mathbf{0}_3 & \mathbf{0}_3 \\ \mathbf{0}_3 & \mathbf{I}_3 & \mathbf{0}_{3\times 4} & \mathbf{0}_3 & \mathbf{0}_3 \\ \mathbf{0}_3 & \mathbf{0}_3 & \mathbf{A}_1 & -\mathbf{L} & \mathbf{0}_3 \\ \mathbf{0}_3 & \mathbf{0}_3 & \mathbf{A}_2 & \mathbf{B}_2 & \mathbf{C}_2 \\ \mathbf{0}_3 & \mathbf{0}_3 & \mathbf{A}_3 & \mathbf{B}_3 & \mathbf{C}_3 \\ \vdots & \vdots & \vdots & \vdots & \vdots \end{pmatrix} \tag{5.45}$$

being

$$\mathbf{A}_p = \begin{cases} \nabla_{\mathring{q}} \left(\mathbf{L} \left(\boldsymbol{a}_m - \boldsymbol{b}_a \right) \right) & \text{for } p = 1 \\ \nabla_{\mathring{q}} \left(\mathbf{A}_{p-1} \left(\dfrac{\boldsymbol{\Gamma}}{2} \left(\boldsymbol{\omega}_m - \boldsymbol{b}_\omega \right) \right) \right) & \text{for } p > 1 \end{cases} \tag{5.46a}$$

$$\mathbf{B}_p = \nabla_{\boldsymbol{b}_a} \left(\mathbf{A}_{p-1} \left(\frac{\Gamma}{2} \left(\boldsymbol{\omega}_m - \boldsymbol{b}_\omega \right) \right) \right) \quad \text{for } p > 1 \tag{5.46b}$$

$$\mathbf{C}_p = \nabla_{\boldsymbol{b}_\omega} \left(\mathbf{A}_{p-1} \left(\frac{\Gamma}{2} \left(\boldsymbol{\omega}_m - \boldsymbol{b}_\omega \right) \right) \right) \quad \text{for } p > 1 \tag{5.46c}$$

Noting that in general

$$\nabla_{\mathring{q}} \left(\mathbf{L} \boldsymbol{v} \right) \frac{\Gamma}{2} \boldsymbol{p} = \mathbf{L} \left(\boldsymbol{p} \times \boldsymbol{v} \right) \tag{5.47}$$

the previous matrices can be written as

$$\mathbf{A}_2 = \nabla_{\mathring{q}} \left(\mathbf{L} \left(\boldsymbol{\omega} \times \boldsymbol{a} \right) \right) \tag{5.48a}$$

$$\mathbf{A}_3 = \nabla_{\mathring{q}} \left(\mathbf{L} \left(\boldsymbol{\omega} \times \left(\boldsymbol{\omega} \times \boldsymbol{a} \right) \right) \right) \tag{5.48b}$$

$$\mathbf{A}_{2p} = - \left\| \boldsymbol{\omega} \right\|^2 \mathbf{A}_p \quad \forall p > 2 \tag{5.48c}$$

$$\mathbf{B}_p = -\mathbf{L} \left[\boldsymbol{\omega} \right]_\times^{p-1} \quad \forall p > 1 \tag{5.48d}$$

Expressing matrices $\mathbf{C}_p$ explicitly is not so simple, however the first of them can be written as

$$\mathbf{C}_2 = \mathbf{L} \left[\boldsymbol{a} \right]_\times$$
$$\mathbf{C}_3 = -\mathbf{L} \left(\left(\boldsymbol{a}^\top \boldsymbol{\omega} \right) \mathbf{I}_3 + \left(\boldsymbol{\omega} \boldsymbol{a}^\top \right) - 2 \left(\boldsymbol{a} \boldsymbol{\omega}^\top \right) \right)$$
$$\mathbf{C}_4 = -\mathbf{C}_2 \left(3 \left(\boldsymbol{\omega}^\top \boldsymbol{\omega} \right) \mathbf{I}_3 + 2 \left[\boldsymbol{\omega} \right]_\times^2 \right)$$

The covector matrix related to the magnetometer measurements is given by

$$\mathcal{O}_{\boldsymbol{H}} = \begin{pmatrix} \mathbf{0}_3 & \mathbf{0}_3 & \mathbf{D}_1 & \mathbf{0}_3 & \mathbf{0}_3 \\ \mathbf{0}_3 & \mathbf{0}_3 & \mathbf{D}_2 & \mathbf{0}_3 & \mathbf{E}_2 \\ \mathbf{0}_3 & \mathbf{0}_3 & \mathbf{D}_3 & \mathbf{0}_3 & \mathbf{E}_3 \\ \vdots & \vdots & \vdots & \vdots & \vdots \end{pmatrix} \tag{5.49}$$

being

$$\mathbf{D}_p = \begin{cases} \nabla_{\mathring{q}} \left(\mathbf{L}^\top \boldsymbol{H} \right) & \text{for } p = 1 \\ \nabla_{\mathring{q}} \left(\mathbf{D}_{p-1} \left(\frac{\Gamma}{2} \left(\boldsymbol{\omega}_m - \boldsymbol{b}_\omega \right) \right) \right) & \text{for } p > 1 \end{cases}$$

$$\mathbf{E}_p = \nabla_{\boldsymbol{b}_\omega} \left(\mathbf{D}_{p-1} \left(\frac{\Gamma}{2} \left(\boldsymbol{\omega}_m - \boldsymbol{b}_\omega \right) \right) \right) \quad \text{for } p > 1$$

Noting that

$$\nabla_{\mathring{q}} \left(\mathbf{L}^\top \boldsymbol{v} \right) \frac{\Gamma}{2} \boldsymbol{p} = \left[\mathbf{L}^\top \boldsymbol{v} \right]_\times \boldsymbol{p} \tag{5.50}$$

the $\mathbf{D}_p$ matrices can be generated recursively as

$$\mathbf{D}_{p+1} = (-1)^p \left[\boldsymbol{\omega} \right]_\times^p \mathbf{D}_p \tag{5.51}$$

for $p > 1$. The matrices $\mathbf{E}_p$, as the matrices $\mathbf{C}_p$ are not easy to express explicitly, however as has been done for $\mathbf{C}_p$, the first of them can be expressed as

$$\mathbf{E}_2 = -\left[\mathbf{L}^\top H\right]_\times$$
$$\mathbf{E}_3 = -\left(\left(H^\top \mathbf{L}\boldsymbol{\omega}\right)\mathbf{I}_3 + \left(\boldsymbol{\omega}H^\top \mathbf{L}\right) - 2\left(\mathbf{L}^\top H\boldsymbol{\omega}^\top\right)\right)$$
$$\mathbf{E}_4 = -\mathbf{E}_2\left(3\left(\boldsymbol{\omega}^\top \boldsymbol{\omega}\right)\mathbf{I}_3 + 2\left[\boldsymbol{\omega}\right]_\times^2\right)$$

Finally the covector matrix corresponding to the unit quaternion constraint can be expressed as

$$\mathcal{O}_{\mathring{q}} = \begin{pmatrix} \mathbf{0}_{1\times6} & \mathbf{F}_1 & \mathbf{0}_{1\times3} & \mathbf{0}_{1\times3} \\ \mathbf{0}_{1\times6} & \mathbf{F}_2 & \mathbf{0}_{1\times3} & \mathbf{G}_2 \\ \mathbf{0}_{1\times6} & \mathbf{F}_3 & \mathbf{0}_{1\times3} & \mathbf{G}_3 \\ \vdots & \vdots & \vdots & \vdots \end{pmatrix} \tag{5.52}$$

being

$$\mathbf{F}_p = \begin{cases} \nabla_{\mathring{q}}\left(q_0^2 + \boldsymbol{q}_v^\top \boldsymbol{q}_v\right) = \mathring{q}^\top & \text{for } p = 1 \\ \nabla_{\mathring{q}}\left(\mathbf{F}_{p-1}\left(\dfrac{\boldsymbol{\Gamma}}{2}\left(\boldsymbol{\omega}_m - \boldsymbol{b}_\omega\right)\right)\right) & \text{for } p > 1 \end{cases}$$

$$\mathbf{G}_p = \nabla_{\boldsymbol{b}_\omega}\left(\mathbf{F}_{p-1}\left(\dfrac{\boldsymbol{\Gamma}}{2}\left(\boldsymbol{\omega}_m - \boldsymbol{b}_\omega\right)\right)\right) \quad \text{for } p > 1$$

Given that $\mathring{q}^\top \boldsymbol{\Gamma} = \mathbf{0}$ by construction, $\mathbf{F}_p$ and $\mathbf{G}_p$ are null for $p > 1$. Then, the columnspace spanned by $\mathcal{O}_{\mathring{q}}$, named $\mathrm{col}\,(\mathcal{O}_{\mathring{q}})$ reduces to

$$\mathrm{col}\,(\mathcal{O}_{\mathring{q}}) = \mathrm{col}\left(\begin{pmatrix} \mathbf{0}_{1\times6} & \mathring{q}^\top & \mathbf{0}_{1\times3} & \mathbf{0}_{1\times3} \end{pmatrix}\right) \tag{5.53}$$

which can be shown to be a linear combination of the first three rows of $\mathcal{O}_{\boldsymbol{H}}$ i.e. noting that $\mathbf{R}^\top H \neq \mathbf{0} \ \forall\, \mathbf{R} \in SO(3)$

$$\left(\mathbf{L}^\top H\right)^\top \mathbf{D}_1 \propto \mathring{q}^\top$$

or which is equivalent,

$$\det\begin{pmatrix} \mathbf{D}_1 \\ \mathring{q}^\top \end{pmatrix} = 0$$

Hence, considering $\mathcal{O}_{\mathring{q}}$ in the observability analysis is redundant and, as a consequence, following the rank criterion, the system is WLO if there exist $\boldsymbol{u}$ such that the matrix

$$\mathcal{O}(\boldsymbol{x}, \boldsymbol{u}) = \begin{pmatrix} \mathcal{O}_\xi(\boldsymbol{x}, \boldsymbol{u})) \\ \mathcal{O}_{\boldsymbol{H}}(\boldsymbol{x}, \boldsymbol{u})) \end{pmatrix}, \tag{5.54}$$

is full rank $\forall\, \boldsymbol{x} \in \mathcal{M}$.

Finding all the points where the rank of $\mathcal{O}(\boldsymbol{x}, \boldsymbol{u})$ is not complete is a difficult task. However, a wide region of states where the rank of $\mathcal{O}$ fails to be maximum for a particular value of constant inputs is identified in the next section.

5.6.2   The role of angular speed in the observability

Theorem 5.6.1. *The vector*

$$\boldsymbol{u} = \begin{pmatrix} \boldsymbol{k}_1 \\ \boldsymbol{b}_\omega + k_2 \mathbf{L}^\top \boldsymbol{H} \end{pmatrix}$$

for fixed $\boldsymbol{k}_1 \neq \boldsymbol{b}_a$ and fixed $k_2 \in \mathbb{R}$, is a singular input for the system Eq. (5.13), under measurement equations Eq. (5.11).

Proof. The selected input relates with the aircraft angular speed and specific force by Eq. (4.2a) and Eq. (4.2b) with null $\boldsymbol{\eta}_a$ and null $\boldsymbol{\eta}_\omega$, which results in $\boldsymbol{\omega} = k_2 \mathbf{L}^\top \boldsymbol{H}$ and constant non null $\boldsymbol{a}$.

Consider the case in which the aircraft is not rotating i.e. $\boldsymbol{\omega} = k_2 \mathbf{L}^\top \boldsymbol{H}$ with $k_2 = 0$. By imposing this condition over $\mathcal{O}(\boldsymbol{x})$ it can be verified that matrices $\mathbf{A}_p$, $\mathbf{B}_p$ and $\mathbf{D}_p$ for $p > 1$ and matrices $\mathbf{C}_p$ and $\mathbf{E}_p$ for $p > 2$ become null. That reduces the covector matrix $\mathcal{O}$ to

$$\mathcal{O}_s = \begin{pmatrix} \mathbf{I}_3 & \mathbf{0}_3 & \mathbf{0}_{3\times4} & \mathbf{0}_3 & \mathbf{0}_3 \\ \mathbf{0}_3 & \mathbf{I}_3 & \mathbf{0}_{3\times4} & \mathbf{0}_3 & \mathbf{0}_3 \\ \mathbf{0}_3 & \mathbf{0}_3 & \mathbf{A}_1 & -\mathbf{L} & \mathbf{0}_3 \\ \mathbf{0}_3 & \mathbf{0}_3 & \mathbf{0}_{3\times4} & \mathbf{0}_3 & \mathbf{C}_2 \\ \mathbf{0}_3 & \mathbf{0}_3 & \mathbf{D}_1 & \mathbf{0}_3 & \mathbf{0}_3 \\ \mathbf{0}_3 & \mathbf{0}_3 & \mathbf{0}_{3\times4} & \mathbf{0}_3 & \mathbf{E}_2 \end{pmatrix} \tag{5.55}$$

It can be verified that $\operatorname{rank}(\mathcal{O}_s) = 15$. As a consequence, $\mathcal{O}_s$ has a non-empty kernel spanned by a unique symmetry

$$\boldsymbol{w}_s = \operatorname{kern}(\mathcal{O}_s) = \begin{pmatrix} \mathbf{0}_{6\times1} \\ \frac{1}{2}\boldsymbol{\Gamma}(\mathring{q})\mathbf{L}^\top \boldsymbol{H} \\ \left[\mathbf{L}^\top \boldsymbol{H}\right]_\times (\boldsymbol{a}_m - \boldsymbol{b}_a) \\ \mathbf{0}_{3\times1} \end{pmatrix} \tag{5.56}$$

When $k_2 \neq 0$, $\mathcal{O}$ does not simplify. However, it can still be demonstrated that Eq. (5.56) is a symmetry of the system by verifying that $\mathcal{O}\boldsymbol{w}_s = \mathbf{0}$. Given that $\mathcal{O}_s$ is a subpart of $\mathcal{O}$ it suffices to verify, that for any $p > 1$

$$\left(\mathbf{0}_{3\times6}\ \mathbf{A}_p\ \mathbf{B}_p\ \mathbf{C}_p\right)\boldsymbol{w}_s = \mathbf{0} \tag{5.57a}$$

$$\left(\mathbf{0}_{3\times6}\ \mathbf{D}_p\ \mathbf{0}_3\ \mathbf{E}_p\right)\boldsymbol{w}_s = \mathbf{0} \tag{5.57b}$$

with $\boldsymbol{w}_s$ the symmetry in Eq. (5.56). Eq. (5.57b) will always be satisfied since as shown in Eq. (5.51) all $\mathbf{D}_p$ share the same nullspace. Then, by introducing Eqs. (5.48a-5.48d) in Eq. (5.57a) and using Eq. (5.47) leads to

$$\mathbf{L}\left(\left[k_2\mathbf{L}^\top \boldsymbol{H}\right]_\times [\boldsymbol{\omega}]_\times^{p-1} \boldsymbol{a} - [\boldsymbol{\omega}]_\times^{p-1} \left[k_2\mathbf{L}^\top \boldsymbol{H}\right]_\times \boldsymbol{a}\right) = 0$$

for $p > 1$, which is null for any $\boldsymbol{\omega} = \kappa\mathbf{L}^\top \boldsymbol{H}$ with independence of the value of p. As a consequence, the covector matrix $\mathcal{O}$ is not full column rank, and the input-output map for this singular input fails to be invertible. □

The integration of the continuous symmetry in Eq. (5.56), leads to the indistinguishable region of $\boldsymbol{x}_0$ given by $\boldsymbol{x}_I$ and parameterized by the scalar τ as

$$\boldsymbol{x}_I(\boldsymbol{x}_0, \tau) = \int_0^\tau \boldsymbol{w}_h(\boldsymbol{x}(\boldsymbol{\gamma})) \mathrm{d}\gamma$$

whose solution is

$$\boldsymbol{x}_I(\tau, \boldsymbol{x}_0) = \left(\boldsymbol{\xi}_0^\top, \, \boldsymbol{v}_0^\top, \, \mathring{q}_I^\top, \, \boldsymbol{b}_{a_I}^\top, \, \boldsymbol{b}_{\omega_0}^\top \right)^\top \tag{5.58}$$

where

$$\mathring{q}_I = \mathring{q}_0 \mathring{q}_\tau = \mathring{q}_0 \begin{pmatrix} \cos(\tau) \\ \sin(\tau) \dfrac{\boldsymbol{H}}{\|\boldsymbol{H}\|} \end{pmatrix} \tag{5.59}$$

and

$$\boldsymbol{b}_{a_I} = \boldsymbol{a}_m + \mathbf{L}^\top(\mathring{q}_I) \mathbf{L}^\top(\mathring{q}_0)\, (\boldsymbol{g}) \tag{5.60}$$

The connected set of infinite states represented by Eq. (5.58) maps to the same system's output, i.e. the same sensor readings with identical derivatives. As a consequence, the true value of the state cannot be inferred without ambiguity. In particular, the state can be estimated up to an arbitrary rotation of the attitude about the magnetic field direction represented by Eq. (5.59). This rotation affects, in addition, the acceleration bias which, as shown in Eq. (5.60), adapts to fulfill the velocity dynamics in Eq. (5.12a) with $\dot{v} = 0$.

It is important to note that this singular input is part of many important flight modes, characteristic of Vertical Take-off and Landing (VTOL) UAVs. These include take-off and landing manoeuvres, constant speed movement and, especially, the hover condition. These conditions represent the most usual manoeuvres in the majority of missions of VTOL vehicles.

5.6.3 The role of specific forces in the observability

Theorem 5.6.2. *The vector*

$$\boldsymbol{u} = \begin{pmatrix} \boldsymbol{b}_a + k_1 \mathbf{L}^\top \boldsymbol{H} \\ \boldsymbol{k}_2 \end{pmatrix}$$

for fixed $k_1 \in \mathbb{R}$ and $\boldsymbol{k}_2 \neq \boldsymbol{b}_\omega$, $\boldsymbol{k}_2 \in \mathbb{R}^3$ is a singular input for the system Eq. (5.13), under measurement equations Eq. (5.11).

Proof. The input selected implies null external acceleration $\boldsymbol{a} = k_1 \mathbf{L}^\top \boldsymbol{H}$ and constant turn rate of the platform. The former relation, $\boldsymbol{a} = k_1 \mathbf{L}^\top \boldsymbol{H}$ implies null matrices $\mathbf{A}_i$, $\mathbf{B}_i$ and $\mathbf{C}_i$ for any i given Eq. (5.46a). As a consequence, after eliminating null rows, the codistribution matrix $\mathcal{O}$

reduces to

$$\mathcal{O} = \begin{pmatrix} \mathbf{I}_3 & \mathbf{0}_3 & \mathbf{0}_{3\times 4} & \mathbf{0}_3 & \mathbf{0}_3 \\ \mathbf{0}_3 & \mathbf{I}_3 & \mathbf{0}_{3\times 4} & \mathbf{0}_3 & \mathbf{0}_3 \\ \mathbf{0}_3 & \mathbf{0}_3 & \mathbf{A}_1 & -\mathbf{L} & \mathbf{0}_3 \\ \mathbf{0}_3 & \mathbf{0}_3 & \mathbf{D}_1 & \mathbf{0}_3 & \mathbf{0}_3 \\ \mathbf{0}_3 & \mathbf{0}_3 & \mathbf{D}_2 & \mathbf{0}_3 & \mathbf{E}_2 \\ \mathbf{0}_3 & \mathbf{0}_3 & \mathbf{D}_3 & \mathbf{0}_3 & \mathbf{E}_3 \\ \vdots & \vdots & \vdots & \vdots & \vdots \end{pmatrix}$$

Given that the nullspace of $\mathbf{D}_1$, represented by the vector

$$\boldsymbol{w}_3 = \text{null}\,(\mathbf{D}_1) = \frac{\boldsymbol{\Gamma}(\mathring{q})}{2}\mathbf{L}^\top\boldsymbol{H}$$

is shared for any $\mathbf{D}_p$, $p > 2$ (see Eq. (5.51)), and $\mathbf{L}$, $\mathbf{E}_3$ and obviously identity matrix are full row rank, the dimension of the columnspace of $\mathcal{O}$ is 9 and its nullspace is spanned by the symmetry

$$\boldsymbol{w}_s = \begin{pmatrix} \mathbf{0}_{6\times 1} \\ \frac{\boldsymbol{\Gamma}(\mathring{q})}{2}\mathbf{L}^\top\boldsymbol{H} \\ \mathbf{0}_{6\times 1} \end{pmatrix} \tag{5.61}$$

As a consequence, the state can not be obtained from the input-output map which fails to be invertible locally. $\qquad\square$

The integration of the symmetry leads to an indistinguishable region represented by a rotation obout the magnetic field direction affecting the attitude, i.e,

$$\boldsymbol{x}_I(\tau, \boldsymbol{x}_0) = \left(\boldsymbol{\xi}_0^\top,\ \boldsymbol{v}_0^\top,\ (\mathring{q}_0\mathring{q}_I)^\top,\ \boldsymbol{b}_{a_0}^\top,\ \boldsymbol{b}_{\omega_0}^\top\right)^\top \tag{5.62}$$

where

$$\mathring{q}_I = \begin{pmatrix} \cos(\tau) \\ \sin(\tau)\dfrac{\boldsymbol{H}}{\|\boldsymbol{H}\|} \end{pmatrix} \tag{5.63}$$

The ideal case in which the specific forces are null is interesting because it is related with what can be expected when the aircraft actuation is null during flight. However, in practice, external actions are never null even in the case of null actuation given that drag forces are always present for a moving platform. The case in which $\boldsymbol{a} = k_1\mathbf{L}^\top\boldsymbol{H}$ is very narrow, and unlikely to happen in normal aircraft missions. Note that the main source term contributing to $\boldsymbol{a}$ is the actuator force, whose main task is to control the aircraft. Then, the conflicting case $\boldsymbol{a} = k_1\mathbf{L}^\top\boldsymbol{H}$ with k_1 will be accomplished if $\boldsymbol{f}_{act}$ points in a direction near to $\mathbf{L}^\top\boldsymbol{H}$ which might only depend on the controlling or trajectory tracking purposes.

5.6.4 Singular input analysis for generic constant inputs

When system inputs do not take the particular values discussed previously the observability matrix has full row rank. This can be demonstrated analysing the nullspace of the reduced matrix

$$\mathcal{O}' = \begin{pmatrix} \mathbf{I}_3 & \mathbf{0}_3 & \mathbf{0}_{3\times4} & \mathbf{0}_3 & \mathbf{0}_3 \\ \mathbf{0}_3 & \mathbf{I}_3 & \mathbf{0}_{3\times4} & \mathbf{0}_3 & \mathbf{0}_3 \\ \mathbf{0}_3 & \mathbf{0}_3 & \mathbf{A}_1 & -\mathbf{L} & \mathbf{0}_3 \\ \mathbf{0}_3 & \mathbf{0}_3 & \mathbf{A}_2 & \mathbf{B}_2 & \mathbf{C}_2 \\ \mathbf{0}_3 & \mathbf{0}_3 & \mathbf{D}_1 & \mathbf{0}_3 & \mathbf{0}_3 \\ \mathbf{0}_3 & \mathbf{0}_3 & \mathbf{D}_3 & \mathbf{0}_3 & \mathbf{E}_3 \end{pmatrix} \tag{5.64}$$

Since any element in the nullspace of $\mathcal{O}$ has to be also in the nullspace of $\mathcal{O}'$, demonstrating that the nullspace of $\mathcal{O}'$ is empty implies that the nullspace of $\mathcal{O}$ is also empty.

Let

$$\boldsymbol{w}_s = \left(\boldsymbol{w}_1^\top, \boldsymbol{w}_2^\top, \boldsymbol{w}_3^\top, \boldsymbol{w}_4^\top, \boldsymbol{w}_5^\top, \right)^\top$$

be the a potential symmetry for the system, then for every block row of $\mathcal{O}'$, denoted by $\mathbf{r}_i \, i = 1, 2, ..., 6$ has to be orthogonal to the symmetry

$$\mathbf{r}_i \, \boldsymbol{w}_s = \mathbf{0}$$

It is clear that the orthogonality condition for $\mathbf{r}_1$, $\mathbf{r}_2$ can only be accomplished by choosing $\boldsymbol{w}_1 = \boldsymbol{w}_2 = \mathbf{0}$.

The relation

$$\mathbf{r}_5 \, \boldsymbol{w}_s = \mathbf{D}_1 \boldsymbol{w}_3 = 0$$

forces $\boldsymbol{w}_3$ be either $\mathbf{0}$ or $\frac{\Gamma}{2} \mathbf{L}^\top \boldsymbol{H}$. Eq. (5.51) shows that any vector in the nullspace of $\mathbf{D}_1$ is also a null vector of $\mathbf{D}_p$, then the product

$$\mathbf{r}_6 \boldsymbol{w}_s = \mathbf{D}_3 \boldsymbol{w}_3 + \mathbf{E}_3 \boldsymbol{w}_5 = \mathbf{E}_3 \boldsymbol{w}_5$$

Given that $\mathbf{E}_3$ is full rank it can be seen that $\boldsymbol{w}_5 = \mathbf{0}$.

Developing the product $\mathbf{r}_3$, $\boldsymbol{w}_s$ leads to

$$\mathbf{A}_1 \frac{\Gamma(\mathring{q})}{2} \mathbf{L}^\top \boldsymbol{H} - \mathbf{L} \boldsymbol{w}_4 = \mathbf{L} \left[\mathbf{L}^\top \boldsymbol{H} \right]_\times \boldsymbol{a} - \mathbf{L} \boldsymbol{w}_4 = \mathbf{0}$$

which lead to $\boldsymbol{w}_4 = \left[\mathbf{L}^\top \boldsymbol{H} \right]_\times \boldsymbol{a} = - \left[\boldsymbol{a} \right]_\times \mathbf{L}^\top \boldsymbol{H}$.

Finally, $\mathbf{r}_4 \, \boldsymbol{w}_s$ leads to

$$\mathbf{L} \left(\left[\mathbf{L}^\top \boldsymbol{H} \right]_\times \left[\boldsymbol{\omega} \right]_\times \boldsymbol{a} - \left[\boldsymbol{\omega} \right]_\times \left[\mathbf{L}^\top \boldsymbol{H} \right]_\times \boldsymbol{a} \right)$$

which is not zero in the general case that $\boldsymbol{a} \neq \mathbf{0}$ or $\boldsymbol{\omega} \neq \mathbf{L}^\top \boldsymbol{H}$. As a consequence $\boldsymbol{w}_3 = \mathbf{0}$ which forces all the vector $\boldsymbol{w}_s$ to be null indicating that the nullspace of $\mathcal{O}'$ and henceforth the

nullspace of $\mathcal{O}$ are empty. Since the nullity of $\mathcal{O}$ is zero its rank is maximum and equals the system dimension ($n = 16$) as a consequence the state is observable from the input-output map.

5.6.5   Singular input analysis without bias

Even though the literature is used to admit the sensor model in Eq. (4.2) to account for the internal dynamics of the IMU, system biases could be taken as constant in the case of having precise enough sensors (with stable readings). However, the estimation performance would be closely linked to the accomplishment of the sensor stability premise.

Consider the reduced state

$$\boldsymbol{x}_r = \left(\boldsymbol{\xi}^\top, \, \boldsymbol{v}^\top, \, \mathring{q}^\top \right)^\top \tag{5.65}$$

whose dynamics are defined by

$$\dot{\boldsymbol{x}}_r = \boldsymbol{f}(\boldsymbol{x}_r) = \begin{pmatrix} \boldsymbol{v} \\ \boldsymbol{g} + \mathbf{L}(\mathring{q}) \left(\boldsymbol{a}_m - \bar{\boldsymbol{b}}_a \right) \\ \frac{1}{2} \boldsymbol{\Gamma}(\mathring{q}) \left(\boldsymbol{\omega}_m - \bar{\boldsymbol{b}}_\omega \right) \end{pmatrix} \tag{5.66}$$

where $\bar{\boldsymbol{b}}_\omega$ and $\bar{\boldsymbol{b}}_a$ are fixed known quantities. The WLO of the reduced system can be verified from results in Section 5.4 and ensuring that the rank of the reduced observability matrix (composed by the two left column blocks of Eq. (5.30)) equals the dimension of the reduced estate, i.e., 10.

This section, introduced for the sake of completeness, is devoted to show that for the reduced dynamic system is not free of singularities. In the case that $\boldsymbol{u} = (\boldsymbol{a}_m^\top, \boldsymbol{\omega}_m^\top)$ is constant, the codistribution matrix is represented by

$$\mathcal{O}_r(\boldsymbol{x}_r, \boldsymbol{u}) = \begin{pmatrix} \mathbf{I}_3 & \mathbf{0}_3 & \mathbf{0}_{3\times4} \\ \mathbf{0}_3 & \mathbf{I}_3 & \mathbf{0}_{3\times4} \\ \mathbf{0}_3 & \mathbf{0}_3 & \mathbf{A}_1 \\ \mathbf{0}_3 & \mathbf{0}_3 & \mathbf{A}_2 \\ \vdots & \vdots & \vdots \\ \mathbf{0}_3 & \mathbf{0}_3 & \mathbf{D}_1 \\ \mathbf{0}_3 & \mathbf{0}_3 & \mathbf{D}_2 \\ \vdots & \vdots & \vdots \end{pmatrix}$$

which is full row rank provided that $(\mathbf{A}_1^\top \mathbf{D}_1^\top)^\top$ is full column rank which is produced whenever $\boldsymbol{a}_m \neq \mathbf{L}^\top \boldsymbol{H} + \bar{\boldsymbol{b}}_a$.

When $\boldsymbol{a} = k_1 \mathbf{L}^\top \boldsymbol{H}$ $\mathbf{A}_i = \mathbf{B}_i = \mathbf{C}_i = \mathbf{0}$ as can be seen in Eq. (5.46a). Since the nullspace of matrices $\mathbf{D}_i$ is represented by vectors multiples of $\frac{1}{2} \boldsymbol{\Gamma}(\mathring{q}) \mathbf{L}^\top \boldsymbol{H}$, the nullspace of $\mathcal{O}_r$ is spanned by the symmetries

$$\boldsymbol{w}_{sr} = \begin{pmatrix} \mathbf{0}_{6\times1} \\ = \frac{1}{2} \boldsymbol{\Gamma}(\mathring{q}) \mathbf{L}^\top \boldsymbol{H} \end{pmatrix} \tag{5.67}$$

This will also hold even in the case of considering the angular velocity bias and its dynamics. In that case, the codistribution matrix

$$\mathcal{O}_{r2}(\boldsymbol{x}_r, \boldsymbol{u}) = \begin{pmatrix} \mathbf{I}_3 & \mathbf{0}_3 & \mathbf{0}_{3\times4} & \mathbf{0}_3 \\ \mathbf{0}_3 & \mathbf{I}_3 & \mathbf{0}_{3\times4} & \mathbf{0}_3 \\ \mathbf{0}_3 & \mathbf{0}_3 & \mathbf{A}_1 & \mathbf{0}_3 \\ \mathbf{0}_3 & \mathbf{0}_3 & \mathbf{A}_2 & \mathbf{C}_2 \\ \mathbf{0}_3 & \mathbf{0}_3 & \mathbf{A}_3 & \mathbf{C}_3 \\ \vdots & \vdots & \vdots & \\ \mathbf{0}_3 & \mathbf{0}_3 & \mathbf{D}_1 & \mathbf{0}_3 \\ \mathbf{0}_3 & \mathbf{0}_3 & \mathbf{D}_2 & \mathbf{E}_2 \\ \mathbf{0}_3 & \mathbf{0}_3 & \mathbf{D}_3 & \mathbf{E}_3 \\ \vdots & \vdots & \vdots & \end{pmatrix}$$

is full column rank for generic values of $\boldsymbol{a}$, however, Eq. (5.67) is still a symmetry when $\boldsymbol{a} = \mathbf{L}^\top \boldsymbol{H}$.

This integration of this symmetry, produces and indistinguishable region composed by an additional rotation about the magnetic field direction as it was the case in Section 5.6.3.

As commented before, since the actuator direction, fixed in the body frame, represents the leading term in $\boldsymbol{a}$, it is very unlikely to have system trajectories visiting the undistinguishable region for long time periods.

5.7 Observability issues: results

In order to highlight and give sound to the presented findings, the results of applying an estimator to a controlled UAV described by Eq. (5.7) in hover flight is analysed. This simulation intends to highlight the unability to obtain good state estimations in the hover case.

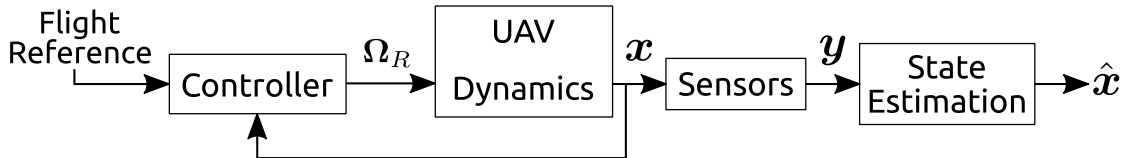A diagram of the simulated system is shown in Fig. 5.1.

FIGURE 5.1: Simulation diagram

Note that the controller is not in feedback with the estimator output data. Otherwise, in the case when the estimator failed to produce good estimations (when the system visited the indistinguishability region) the control actions would provide undesired motion and deviations from the hover condition. It is a non-realistic simulation for control, although it is legitimate in this case since only in simulation it is possible to know the true values of the biases.

Noise is present in the sensors through a realistic model calibrated from static measurements of a real quadrotor. The state estimation implemented is a Multiplicative Extended Kalman

Filter (MEKF) [77, 26] adapted to the dynamics in Eq. (5.9). It has been designed to receive
sensors outputs of the IMU, magnetometers and GPS asynchronously at rates of 100 Hz, 30 Hz
and 5 Hz respectively and supply estimates of the state at 100 Hz. The state reconstructed by
the estimator is depicted in Fig. 5.2 as well as the true values of the simulated states, Fig. 5.3,
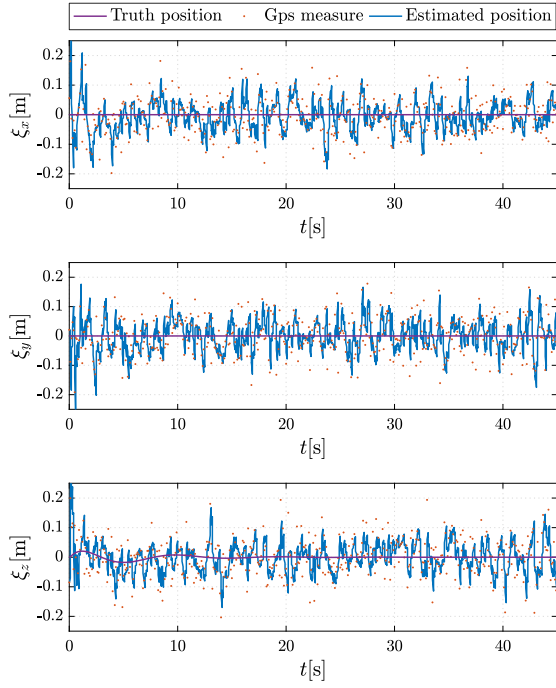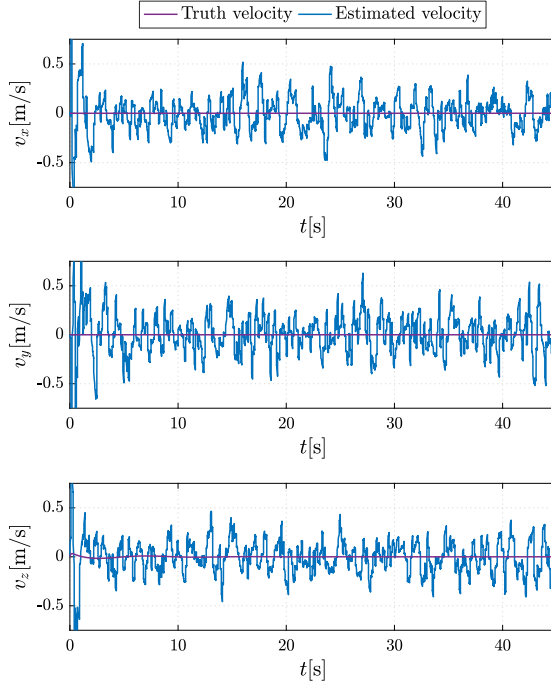Fig. 5.4, Fig. 5.5 and Fig. 5.6.
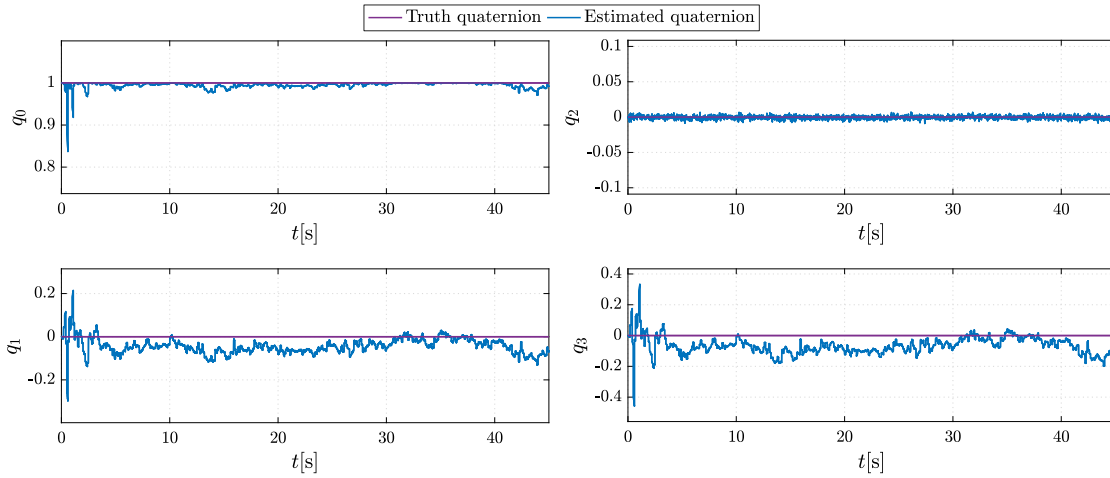

FIGURE 5.2: Position

FIGURE 5.3: Linear velocity

FIGURE 5.4: Attitude quaternion

From the results it is apparent that the position, the velocity and the gyroscope bias converge to
the true values. However, the accelerometer biases and the attitude quaternion do not. This is
the effect of the singular inputs. The state estimator cannot distinguish between the true value of
the attitude and the accelerometer bias and any other value inside the indistinguishable region.
As a consequence, the state drifts, evolving inside the indistinguishable region, and cannot be
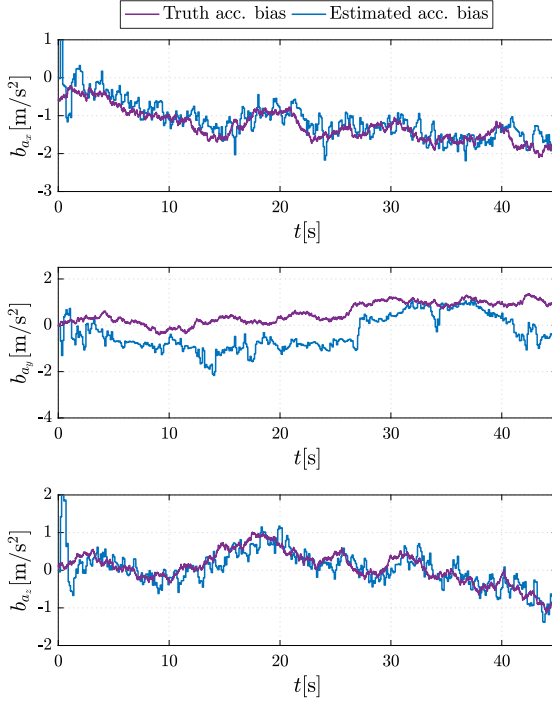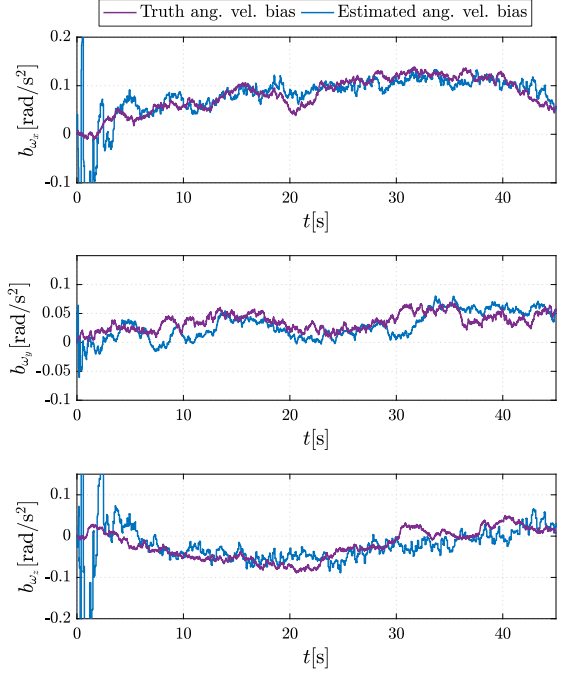
FIGURE 5.5: Accelerometer bias

FIGURE 5.6: Gyroscope bias

corrected. To better illustrate this effect, the incremental quaternion rotation between every estimated quaternion shown in Fig. 5.4 has been calculated as

$$\delta \mathring{q}_k = \mathring{q}_{k+1} \mathring{q}_k^{-1}.$$

From there, the direction about which the incremental rotation is made can be extracted by normalizing the vectorial part of the quaternion

$$\boldsymbol{e}_k = \frac{\delta \boldsymbol{q}_{v_k}}{\left\| \delta \boldsymbol{q}_{v_k} \right\|} \tag{5.68}$$

Fig. 5.7, shows an histogram of the values of $\boldsymbol{e}$ by axis against the normalized direction of the true magnetic field set in simulation as

$$\boldsymbol{H} = \left(0.546, \, 0.007, \, 0.838 \right)^{\top}.$$

It can be observed that while the noise introduces random rotations in almost any direction, the preference to rotate about $\boldsymbol{H}$ and hence to evolve inside the indistinguishable region prevails in the estimated system trajectory.

Finally Fig. 5.8 shows how the velocity equation in Eq. (5.12a) is fulfilled (achieving null value) in spite of the non converging values of the estimated $\boldsymbol{b}_{a_h}$ and $\mathring{q}_h$.
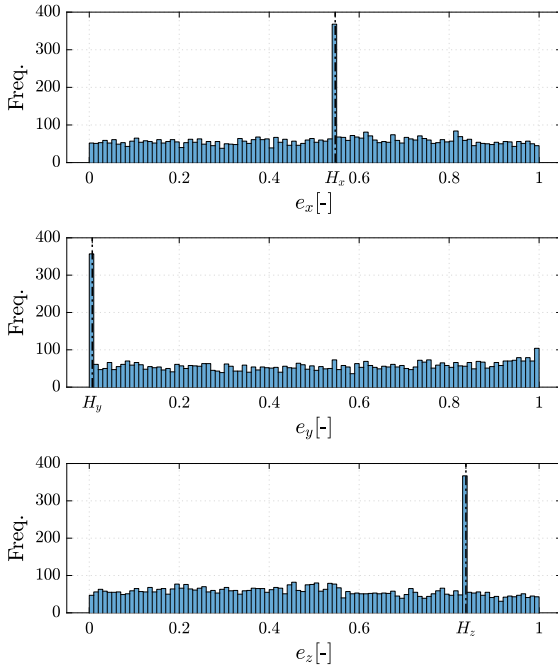
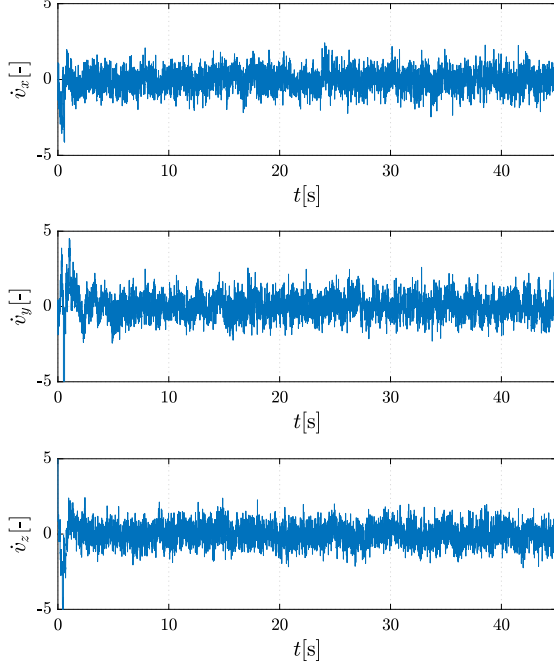FIGURE 5.7: Incremental rotation direction

FIGURE 5.8:   Acceleration for the estimated state

Comparing results with LTV analysis

The observability properties of the system in Eq. (5.12a), driven by IMU outputs and assuming magnetometer and GPS outputs as measurements, have been analyzed in the previous sections. A non-linear analysis of the non-linear system in Eq. (5.13) under measurement equations Eq. (5.11) showed that the system has singular inputs for which an important symmetry exists, Eq. (5.56). The integration of the symmetry leads to an indistinguishable region that compromises the state estimation whenever the aircraft is in hover.

Similar indistinguishable regions, as the one derived for the non-linear case, are shown in Section 5.5.1 and Section 5.5.2 when using the LTV system equations and analysis. However, as has been pointed out before and it is shown in Table 5.1, the LTV analysis presents an incongruence. The singular input analysis of Eq. (5.28) predicts estimation problems for constant angular velocity $\boldsymbol{\omega}$ and constant specific force $\boldsymbol{a}$. This results differ from which have been obtained in the singular input analyses of Eq. (5.29) under same conditions which coincides with what has been derived for the the non-linear case.

The results of applying an estimator to a controlled UAV are provided to verify the observability predictions derived from the non-linear and the LTV procedures. In this case the same simulation set up presented in the previous section (Fig. 5.1) with the same controller and state estimator parameters has been used. The only difference is that, in this case, noise at the output has been eliminated to enhance results readability.

The first simulation implements a hover flight. Results (Figs. 5.12, 5.13, 5.11) show that, as expected, the estimator is not capable to estimate correctly neither the acceleration bias nor the

attitude quaternion. In contrast, position (Fig. 5.9) and velocity(Fig. 5.10) estimates converge to the true values in less than 3 s. This is what was expected given the input analysis results.

The second scenario is near hover flight, but with the aircraft spinning with a constant yaw rate (i.e., yaw is linearly increasing). In this case, the LTV method associated to Eq. (5.28) still expects observability issues while the method considering Eq. (5.29) and the non-linear analysis predict the proper estimation of the state. Simulation results shown in Figs. (5.14-5.18) depicts the proper convergence of all the states to their true values.

The comparison of the LTV and non-linear observability analyses shows how the later does not suffer from parametrization induced problems when compared with the simpler LTV analysis. Given that the analysis needs to be done only once, complexity of the method is justified by providing a more accurate description of the observability issues on the platform.
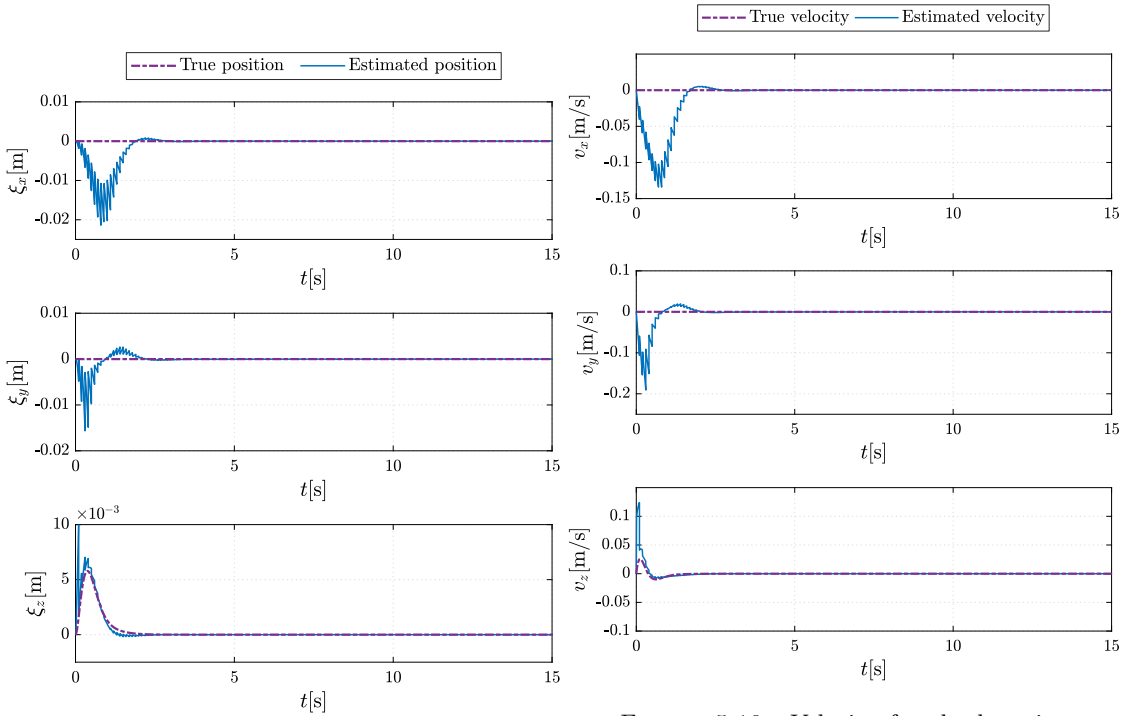

FIGURE 5.9: Position for the hovering case

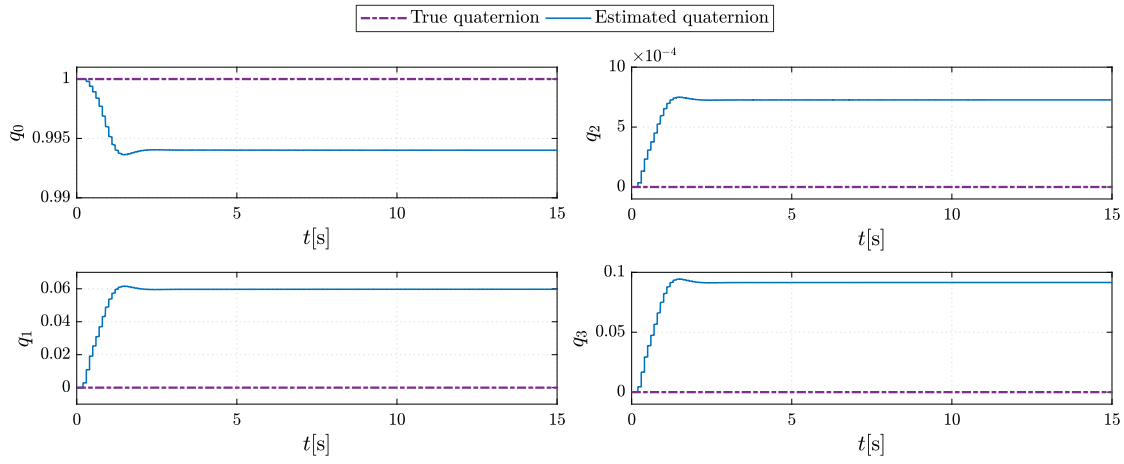FIGURE 5.10: Velocity for the hovering case

FIGURE 5.11: Attitude quaternion for the hovering case
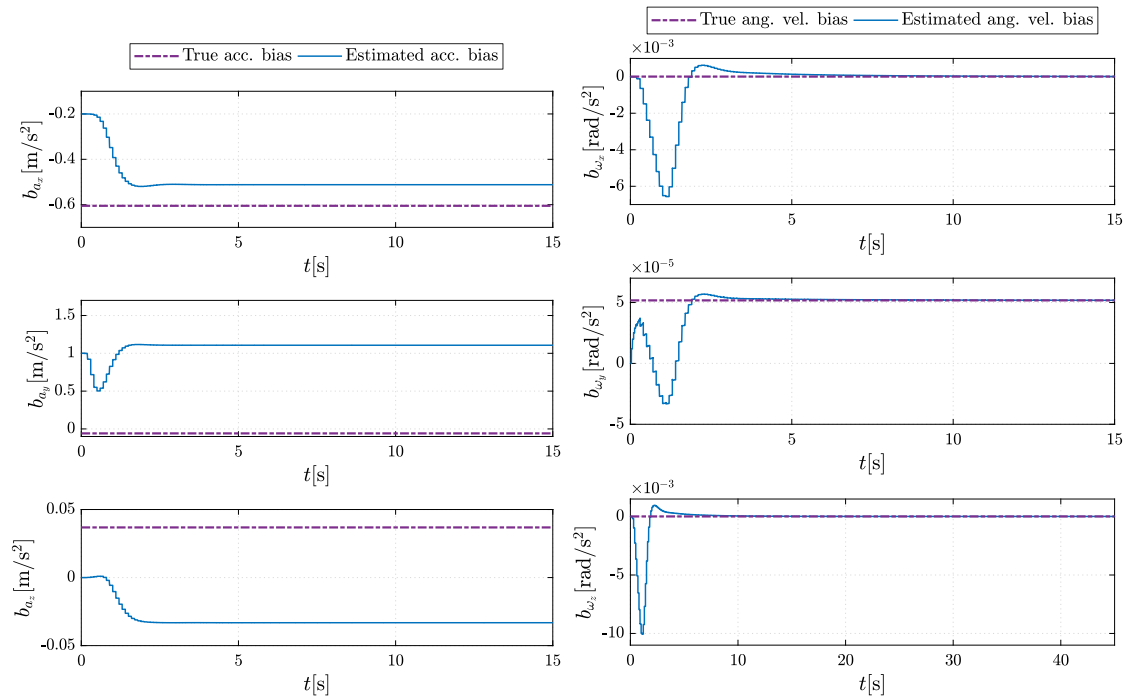

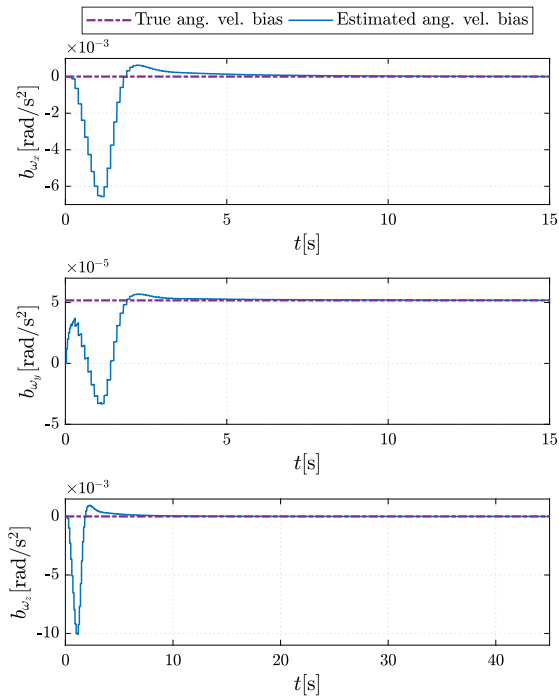FIGURE 5.12: Accelerometers bias for the
hovering case

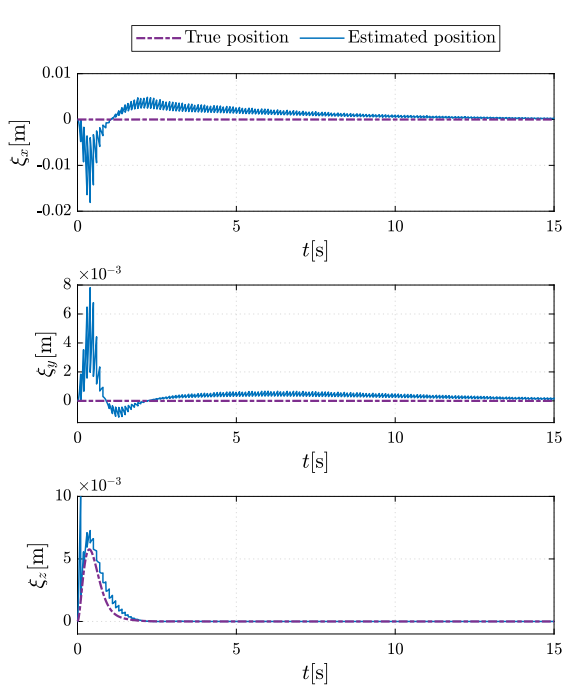FIGURE 5.13: Gyroscopes bias for the
hovering case

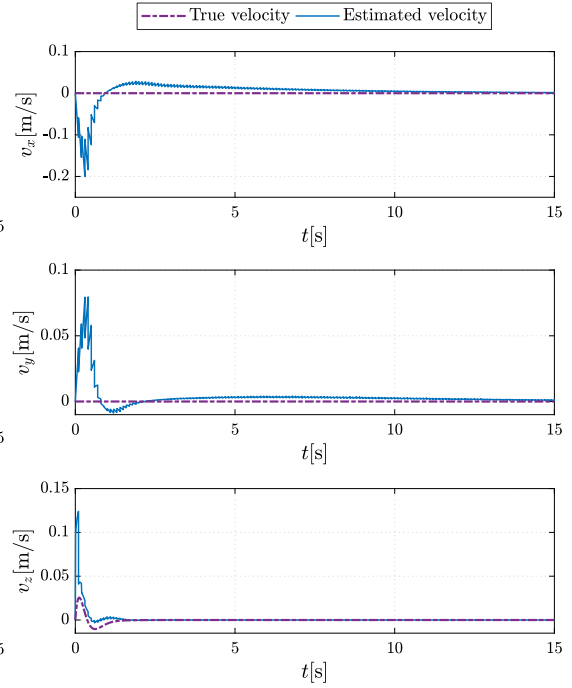FIGURE 5.14: Position for the yawing case

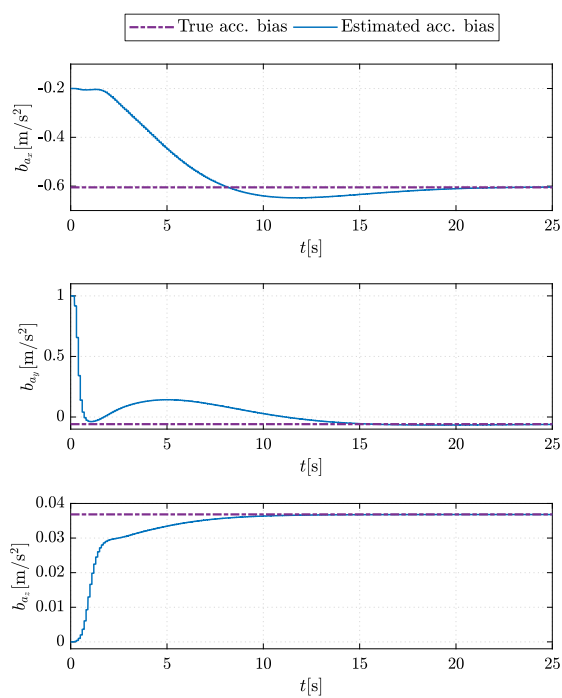FIGURE 5.15: Velocity for the yawing case

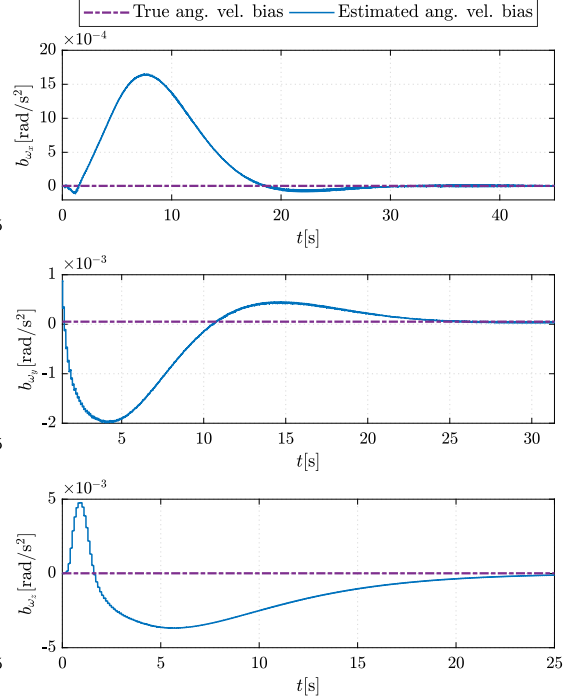FIGURE 5.16: Accelerometers bias for the yawing case

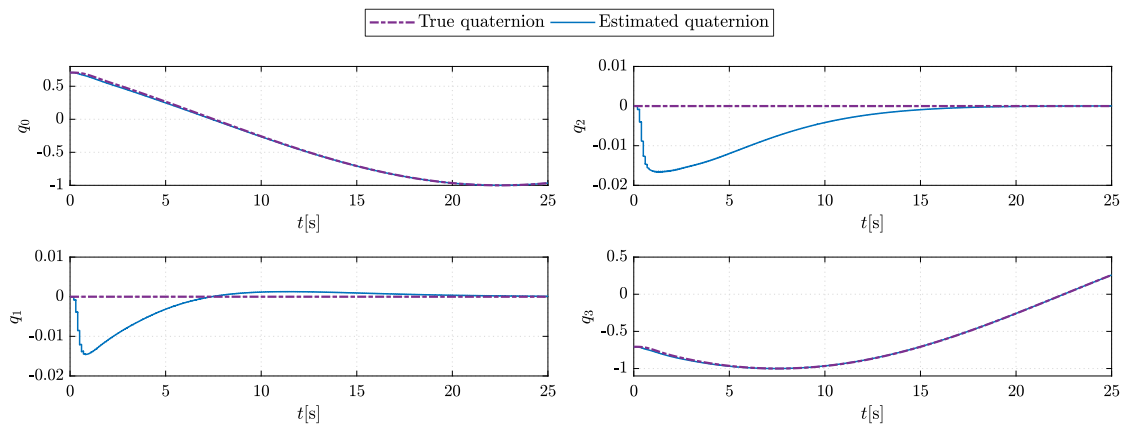FIGURE 5.17: Gyroscopes bias for the yawing case

FIGURE 5.18: Attitude quaternion for the yawing case

5.8 Conclusion

In this chapter the observability study of a body flying in a 3D space using GPS, IMU and magnetometer sensors has been contemplated. Linear and non-linear observability analyses have been presented. These analyses show that the system has singular configurations for the specific case of some constant inputs. When aplying these results to VTOL aircrafts it is possible to conclude that the observability is degraded in many important flight modes containing the hover condition. In these cases, attitude and accelerometer biases can not be uniquely determined since the estimation is free to evolve along a unidimensional path that relates every possible orientation to a different accelerometer bias. In particular, with the aircraft in hover, the estimated orientation is determined except for a rotation about the magnetic field direction, whereas the accelerometer bias adapts itself to compensate for the difference between the measured specific force and the gravity which is expressed in the body frame by means of the estimated orientation.

The non-linear observability analysis provided avoids the discrepancies that the linear analysis present depending on the model error equations in use. Since the goal of the observability study is to verify the possibility of implementing state estimation solutions, its anlaysis implies off-line calculations that only need to be run once. Hence, the unambiguity and insights provided by the non-linear formulation justify its additional complexity.

Chapter 6

State Estimation

State estimation is an important element in any automatic control system that is to be implemented in a flying vehicle. Autonomy of flying robots and in particular navigation of unmanned aerial vehicles needs of state estimation algorithms to provide complete knowledge of the aircraft state and at the same time remove noise of the measured variables. Even the simplest controller for attitude stabilization requires some kind of data fusion to obtain the pitch, roll and yaw angles.

The attitude determination problem has been deeply studied in the past for its importance in satellite and space missions. A good overview of filtering techniques and attitude determination methods, a central problem in this area is provided in [26].

State estimation of unmanned aircraft needs in addition the tracking of the linear velocity and position variables which are coupled with the attitude as shown in Chap. (3). State estimation with navigation purposes can be approximated using linear theory with a Luenberger observer or a Kalman filter when the aircraft is near hover. However, equations of motion for flying vehicles are non-linear and linear approximations may be too crude for many applications and specifically for those that need high manoeuvrability of the platform. Consequently, it is more usual to use nonlinear state observers, such as the Extended Kalman Filter (EKF) [35, 77], the Unscented Kalman Filter [49, 33], the sliding mode observer [12] and algorithms derived from them.

This chapter deals with the EKF, probably the most frequent state observer in the UAV domain. However few derivations considering the full navigation state exist and none of them have dealt with our specific sensor setup. In the Section 6.1 the discrete Kalman Filter (KF) and Extended Kalman Filter (EKF) basics are exposed. In Section 6.2 we derive the adaptation of the system dynamics and discuss filtering strategies to implement our particular EKF for which precise algorithmic expressions are given. We also discuss issues that are typically not reported in the literature, such as when to update or propagate in the estimator algorithm or which coordinate frame (body or world) should be used to represent each state variable. This leads to the formulation of four potentially different but equivalent discrete event-based filters. An initialisation routine to determine the initial attitude of the aircraft in a steady condition is presented and

the section concludes with flow diagram of the filter to be implemented. Section 6.2.7 shows the simulation results of the execution of the four filters and a small comparative of the results for a specific scenario were observability is guaranteed.

6.1   Kalman and Extended Kalman filters

The Kalman Filter used for state estimation is able to produce optimal (minimum variance) results for linear systems with linear measure equations in presence of white Gaussian noise, such as

$$\boldsymbol{x}_{k+1} = \boldsymbol{\Phi}\boldsymbol{x}_k + \mathbf{G}\boldsymbol{v}_k$$
$$\boldsymbol{z}_k = \mathbf{C}\boldsymbol{x}_k + \mathbf{F}\boldsymbol{w}_k$$

where, $\boldsymbol{x}_k$, $\boldsymbol{z}_k$, $\boldsymbol{v}_k$ and $\boldsymbol{w}_k$ represent the state, the measurement, the model error and the measurement noise at the discrete time instant k. The matrix $\boldsymbol{\Phi}$ is known as propagation matrix, whereas $\mathbf{C}$ is known as measurement matrix. Both describe the effect of the system state in the next time step. $\mathbf{B}$ and $\mathbf{D}$ represent the effect of uncertainty in the system outputs and does not have any special name in literature.

The idea under the Kalman filter is to track the evolution of the state and a measure of its uncertainty in time and fuse them with the also uncertain system observations. In the case that $\boldsymbol{v}_k$ and $\boldsymbol{w}_k$ are normal distributed, and time uncorrelated (white Gaussian processes), given the linearity of the model, it is guaranteed that the states can be defined as white Gaussian processes too. Since a Gaussian variable can be completely described by its first two static moments (mean and covariance), the process of filtering a random variable reduces to tracking the value of the two parameters that define the distribution.

Let $\hat{\boldsymbol{x}}_k$ represent the estimation of of the state vector $\boldsymbol{x}$ at the time instant k and let $\mathbf{P}_k$ describe the covariance of the estimation error $\boldsymbol{x}_k - \hat{\boldsymbol{x}}_k$. Let $\mathbf{Q}_k$ represent the covariance of $\mathbf{G}\boldsymbol{v}$ and $\mathbf{R}_k$ the covariance of $\mathbf{F}\boldsymbol{w}$. Let $\boldsymbol{x}^-$ and $\boldsymbol{x}^+$ identify the predicted and corrected estimation values respectively. Then, the Kalman filtering process can be decomposed in two steps:

- **Prediction or propagation:** The mean estimation of the system states are propagated through the mean nominal model. In this phase the covariance of the error grows continuously due to the model errors

$$\hat{\boldsymbol{x}}_{k+1}^- = \boldsymbol{\Phi}\hat{\boldsymbol{x}}_k^+$$
$$\mathbf{P}_{k+1}^- = \boldsymbol{\Phi}\mathbf{P}_k\boldsymbol{\Phi}^\top + \mathbf{Q}_k \tag{6.1}$$

- **Correction or update:** When a measurement is available, the state and the state error covariance are updated by means of a linear correction. The linear gain $\mathbf{K}$ is known as Kalman Gain and ensures minimum covariance of the estimation error after correction

$$\mathbf{K} = \mathbf{P}_{k+1}^{-}\mathbf{C}^{\top}\left(\mathbf{C}^{\top}\mathbf{P}_{k+1}^{-}\mathbf{C} + \mathbf{R}_k\right)^{-1}$$
$$\hat{\boldsymbol{x}}_{k+1}^{+} = \hat{\boldsymbol{x}}_{k+1}^{-} + \mathbf{K}\left(\boldsymbol{z}_{k+1} - \mathbf{C}\hat{\boldsymbol{x}}_{k+1}^{-}\right) \qquad (6.2)$$
$$\mathbf{P}_{k+1}^{+} = \left(\mathbf{I} - \mathbf{K}\mathbf{C}\right)\mathbf{P}_{k+1}^{-}$$

The optimal gain calculated above will change at every iteration based on the past value of the error estimation covariance. However since the system is guaranteed to converge to the optimal estimation, the gain matrix achieves an stationary value after some iterations. This constant value can be calculated beforehand and used as Kalman gain. This procedure still ensures the convergence to the optimal result and avoids calculating an inverse of an $p \times p$ matrix (being p the measurement dimension) at the expense of a accepting slower convergence.

In practice, real dynamic systems are not linear, measurement equations are not linear, and the disturbances involved do not behave as white gaussian noises. The Extended KF (EKF) is an extension of the traditional Kalman Filter that applies the same structure of Kalman filter to systems that aren't linear or are involved with non-gaussian noises or disturbances. In the filtering process, the EKF predicts incoming measurements and future states using the system non-linear equations while the second statistic moment is propagated through a linearized version of the system dynamics and measurement equations. It must be clear that the probability density function (pdf) of a random variable transformed by a non-linear function may not be characterizable by the same set of parameters than before the transformation. While the Kalman gain is still selected to minimize the size of the second statistic moment, this does not ensure minimum error on the estimation. As a consequence the results of applying the EKF are suboptimal in the sense that they would converge to the optimal ones as the nonlinearities of the system are relaxed and the probabilistic distribution of the errors and noises present in the system approach to the white-noise case.

For the general discrete non-linear system described by

$$\boldsymbol{x}_{k+1} = \boldsymbol{f}\left(\boldsymbol{x}_k, \boldsymbol{v}_k\right)$$
$$\boldsymbol{z}_k = \boldsymbol{h}\left(\boldsymbol{x}_k, \boldsymbol{w}_k\right)$$

the propagation and correction steps are defined by Algorithm. 2 and Algorithm. 3 respectively.

Algorithm 2: EKF propagation

Data: $\hat{\boldsymbol{x}}_{k-1}^{+}$, $\mathbf{P}_{k-1}$, $\boldsymbol{z}_k$, $\mathbf{Q}_k$
Result: $\hat{\boldsymbol{x}}_k^{-}$, $\mathbf{P}_k^{-}$

1. Linearize the process model on $\boldsymbol{x} = \hat{\boldsymbol{x}}_{k-1}^{+} \rightarrow \boldsymbol{\Phi} = \frac{\partial \boldsymbol{f}}{\partial \boldsymbol{x}}\big|_{\hat{\boldsymbol{x}}_{k-1}^{+}}$, $\mathbf{G} = \frac{\partial \boldsymbol{f}}{\partial \boldsymbol{v}}\big|_{\hat{\boldsymbol{x}}_{k-1}^{+}}$

2. Predict the covariance at the next time step $\mathbf{P}_k^{-} = \boldsymbol{\Phi}\mathbf{P}_{k-1}\boldsymbol{\Phi}^{\top} + \mathbf{G}\mathbf{Q}\mathbf{G}^{\top}$

3. Predict $\hat{\boldsymbol{x}}_k^{-}$ from $\hat{\boldsymbol{x}}_{k-1}^{+}$ and the process model $\boldsymbol{x}_{k+1}^{-} = \boldsymbol{f}\left(\boldsymbol{x}_k^{+}, \boldsymbol{0}\right)$

The jacobian of functions $\boldsymbol{f}$ and $\boldsymbol{h}$ present in both, propagation and correction algorithms, constitute the linear approximation of the system used for the covariance propagation, the Kalman gain calculation and state and covariance correction.

Algorithm 3: EKF correction

Data: $\hat{\boldsymbol{x}}_k^-$, $\mathbf{P}_k^-$, $\boldsymbol{z}_k$, $\mathbf{R}_k$
Result: $\hat{\boldsymbol{x}}_k^+$, $\mathbf{P}_k^+$

    1. Linearize the measurement model on $\boldsymbol{x} = \hat{\boldsymbol{x}}_k^- \to \mathbf{C} = \frac{\partial \boldsymbol{h}}{\partial \boldsymbol{x}}\big|_{\hat{\boldsymbol{x}}_k^-}$

    2. Calculate the suboptimal gain $\mathbf{K} = \mathbf{P}_k^- \mathbf{C}^\top (\mathbf{C}\mathbf{P}_k^- \mathbf{C}^\top + \mathbf{R})^{-1}$

    3. Update the covariance of the estimation error $\mathbf{P}_k^+ = (\mathbf{I} - \mathbf{K}\mathbf{C})\mathbf{P}_k^-$

    4. Estimate the sensor output $\hat{\boldsymbol{z}}$ from the measurement model at $\boldsymbol{x} = \hat{\boldsymbol{x}}_k^-$, $\hat{\boldsymbol{z}} = \boldsymbol{h}(\hat{\boldsymbol{x}}_k^-, \mathbf{0})$

    5. Update the state $\hat{\boldsymbol{x}}_k^+ = \hat{\boldsymbol{x}}_k^- + \mathbf{K}(\boldsymbol{z}_k - \hat{\boldsymbol{z}})$

6.2   Particularizing the EKF

The generalities of the last section are particularised here to generate a state estimator for our platform. The estimation problem can be reduced to estimating the state Eq. (2.75a) or Eq. (2.75b) whose dynamics are given by Eq. (3.10), Eq. (3.11) respectively under the measurements of GPS, IMU and magnetometer sensors. However, two important drawbacks difficult the implementation of the general filter shown in the last section. Firstly, the specific suite of sensors under consideration. Particularly the bias present in the IMU sensors make the use of its measurements invalid for state correction. IMU measures, can be used to drive the dynamic system instead of correcting it, by replacing angular velocities and the effect of external forces, at expenses of extending the state as shown in Chap. (5). While increasing the length of the state will in general increase the computational burden of the estimation algorithm, by considering IMU measurements in the propagation phase prevents the inversion of square matrix with dimension the length of the measurement vector (6×6 in this case) at a rate given by the IMU sampling rate (usually about $100\,\mathrm{Hz}$) speeding up the algorithm execution.

Secondly, the quaternion constraint $\|\mathring{q}\| = 1$ is not satisfied by default by the update of the filter. The consideration of that constraint makes the covariance matrix to be positive semi-definite (PSD) by construction [46]. This is a case difficult to deal with in both propagation and update stages. In the propagation step is difficult to guarantee the PSD condition of the covariance matrix after the propagation step due to the linear transformation. Singular covariances are conflicting in the update stages cause they can lead to non-symmetric or negative definite error covariance matrix after the update. As a consequence, quaternions should be avoided when using filters with linear correction updates. The solution is to use an incremental error state $\delta\boldsymbol{x}$ over the mean estimation of the true state $\boldsymbol{x}$ which uses a minimal representation for the attitude. In such a way, the variables contemplated by the EKF filter are $\delta\boldsymbol{x}$ and its associated covariance, which will not have singularity problems when using a minimal attitude parametrization. If that is the case, the true estate $\boldsymbol{x}$ can be related with the nominal $\hat{\boldsymbol{x}}$ and incremental one $\delta\boldsymbol{x}$ by

$$\boldsymbol{x} = \hat{\boldsymbol{x}} \oplus \delta\boldsymbol{x} \tag{6.3}$$

or

$$\boldsymbol{x} = \delta\boldsymbol{x} \oplus \hat{\boldsymbol{x}} \tag{6.4}$$

where the symbol $\oplus$ stands for composition. For the case that the error state relates with the true state by direct addition or subtraction over the nominal state, the composition is commutative and then, the two previous relations become equivalent. However, since the incremental attitude is naturally defined over the nominal attitude by multiplication (in contrast to the additive structure usually used), and attitude composition is not commutative, the nominal plus incremental error state decomposition leads to two possible sets of states as shown in Eq. (5.14). In view of the fact that the correction step only affects the incremental state, a new filter step has to be considered right after the correction in order to transfer the information from the incremental state to the nominal state and reset the incremental value to zero. This new stage was introduced under the name of reset step in [56].

6.2.1 Nominal and error state dynamics and measure equations

The incremental state formulation and its impact on the system dynamics have been already presented in Section 5.3.2 and Section 5.3.3, where the observability of the state in Eq. (2.75a) have been considered. In what follows, they will be reproduced for the sake of completeness and similar results will be provided by considering the alternative state in Eq. (2.75b). This leads to four different filter dynamics and measurement equations that will be derived.

The IMU driven state equivalent to Eq. (2.75a) is represented by

$$\boldsymbol{x}_{IMU_1} = \left(\boldsymbol{\xi}^{\top},\ {}^{w}\boldsymbol{v}^{\top},\ \mathring{q}^{\top},\ \boldsymbol{b}_a^{\top},\ \boldsymbol{b}_\omega^{\top}\right)^{\top}$$

with dynamics Eq. (5.9)

$$\dot{\boldsymbol{x}}_{IMU_1} = \begin{pmatrix} {}^{w}\boldsymbol{v} \\ \boldsymbol{g} + \mathbf{L}(\mathring{q})\left(\boldsymbol{a}_m - \boldsymbol{b}_a - \boldsymbol{\eta}_a\right) \\ \frac{1}{2}\boldsymbol{\Gamma}(\mathring{q})\left(\boldsymbol{\omega}_m - \boldsymbol{b}_\omega - \boldsymbol{\eta}_\omega\right) \\ \boldsymbol{\eta}_{b_a} \\ \boldsymbol{\eta}_{b_\omega} \end{pmatrix} \tag{6.5}$$

By defining the relation between the true attitude, the estimated attitude, and the attitude error (represented by twice the Gibbs vector) in the body $\boldsymbol{\alpha_R}$ or world $\boldsymbol{\alpha_L}$ frames using Eq. (5.16) results in

$$\mathring{q} = \frac{\hat{\mathring{q}}\begin{pmatrix} 2 \\ \boldsymbol{\alpha_R} \end{pmatrix}}{\sqrt{4 + \boldsymbol{\alpha}_R^{\top}\boldsymbol{\alpha}_R}} \tag{6.6}$$

or

$$\mathring{q} = \frac{\begin{pmatrix} 2 \\ \boldsymbol{\alpha_L} \end{pmatrix}\hat{\mathring{q}}}{\sqrt{4 + \boldsymbol{\alpha}_L^{\top}\boldsymbol{\alpha}_L}} \tag{6.7}$$

two possible error states

$$\delta\boldsymbol{x}_{L1} = \begin{pmatrix} \delta\boldsymbol{\xi} \\ \delta\boldsymbol{v} \\ \boldsymbol{\alpha}_L \\ \delta\boldsymbol{b}_a \\ \delta\boldsymbol{b}_\omega \end{pmatrix} = \begin{pmatrix} \boldsymbol{\xi} - \hat{\boldsymbol{\xi}} \\ {}^w\boldsymbol{v} - {}^w\hat{\boldsymbol{v}} \\ \boldsymbol{\alpha}_L \\ \boldsymbol{b}_a - \hat{\boldsymbol{b}}_a \\ \boldsymbol{b}_\omega - \hat{\boldsymbol{b}}_\omega \end{pmatrix} \tag{6.8}$$

$$\delta\boldsymbol{x}_{R1} = \begin{pmatrix} \delta\boldsymbol{\xi} \\ \delta\boldsymbol{v} \\ \boldsymbol{\alpha}_R \\ \delta\boldsymbol{b}_a \\ \delta\boldsymbol{b}_\omega \end{pmatrix} = \begin{pmatrix} \boldsymbol{\xi} - \hat{\boldsymbol{\xi}} \\ {}^w\boldsymbol{v} - {}^w\hat{\boldsymbol{v}} \\ \boldsymbol{\alpha}_R \\ \boldsymbol{b}_a - \hat{\boldsymbol{b}}_a \\ \boldsymbol{b}_\omega - \hat{\boldsymbol{b}}_\omega \end{pmatrix} \tag{6.9}$$

can be obtained.

These error states lead to two feasible and different dynamic systems Eq. (5.24) and Eq. (5.25)

$$\dot{\delta\boldsymbol{x}}_{L1} = \begin{pmatrix} \dot{\delta\boldsymbol{\xi}} \\ \dot{\delta\boldsymbol{v}} \\ \dot{\boldsymbol{\alpha}}_L \\ \dot{\delta\boldsymbol{b}}_a \\ \dot{\delta\boldsymbol{b}}_\omega \end{pmatrix} = \begin{pmatrix} \delta\boldsymbol{v} \\ \left(\mathbf{L}(\boldsymbol{\alpha}_L) - \mathbf{I}_3\right)\mathbf{L}(\hat{\mathring{q}})\left(\boldsymbol{a}_m - \hat{\boldsymbol{b}}_a\right) - \mathbf{L}(\boldsymbol{\alpha}_L)\mathbf{L}(\hat{\mathring{q}})\left(\delta\boldsymbol{b}_a + \boldsymbol{\eta}_a\right) \\ -\frac{1}{2}\left(2\mathbf{I}_3 + \frac{\boldsymbol{\alpha}_L\boldsymbol{\alpha}_L^\top}{2} + [\boldsymbol{\alpha}_L]_\times\right)\mathbf{L}(\hat{\mathring{q}})\left(\delta\boldsymbol{b}_\omega + \boldsymbol{\eta}_\omega\right) \\ \boldsymbol{\eta}_{b_a} \\ \boldsymbol{\eta}_{b_\omega} \end{pmatrix} \tag{6.10}$$

and

$$\dot{\delta\boldsymbol{x}}_{R1} = \begin{pmatrix} \dot{\delta\boldsymbol{\xi}} \\ \dot{\delta\boldsymbol{v}} \\ \dot{\boldsymbol{\alpha}}_R \\ \dot{\delta\boldsymbol{b}}_a \\ \dot{\delta\boldsymbol{b}}_\omega \end{pmatrix} = \begin{pmatrix} \delta\boldsymbol{v} \\ \mathbf{L}(\hat{\mathring{q}})\left(\mathbf{L}(\boldsymbol{\alpha}_R) - \mathbf{I}_3\right)\left(\boldsymbol{a}_m - \hat{\boldsymbol{b}}_a\right) - \mathbf{L}(\hat{\mathring{q}})\mathbf{L}(\boldsymbol{\alpha}_R)\left(\delta\boldsymbol{b}_a + \boldsymbol{\eta}_a\right) \\ -\left(\mathbf{I}_3 + \frac{\boldsymbol{\alpha}_R\boldsymbol{\alpha}_R^\top}{4}\right)\left(\delta\boldsymbol{b}_\omega + \boldsymbol{\eta}_\omega\right) + \frac{1}{2}\boldsymbol{\alpha}_R \times \left(2\boldsymbol{\omega}_m - 2\hat{\boldsymbol{b}}_\omega - \delta\boldsymbol{b}_\omega - \boldsymbol{\eta}_\omega\right) \\ \boldsymbol{\eta}_{b_a} \\ \boldsymbol{\eta}_{b_\omega} \end{pmatrix} \tag{6.11}$$

Note that by assuming $\boldsymbol{\alpha}_L \ll 1$ or $\boldsymbol{\alpha}_R \ll 1$ and neglecting second order terms Eq. (5.26) and Eq. (5.27) are obtained.

A similar procedure can be carried out by considering the second navigation state in Eq. (2.75b). The difference form the previous case is that now the velocity $\boldsymbol{v}$ is defined in the body frame

$$\boldsymbol{x}_{n_2} = \left(\boldsymbol{\xi}^\top,\ {}^b\boldsymbol{v}^\top,\ \mathring{q}^\top,\ \boldsymbol{\omega}^\top\right)^\top$$

The alternate IMU driven state is defined by

$$\dot{\boldsymbol{x}}_{IMU_2} = \begin{pmatrix} {}^b\boldsymbol{v} \\ \mathbf{L}^\top(\mathring{q}){}^w\boldsymbol{g} + \left(\boldsymbol{a}_m - \boldsymbol{b}_a - \boldsymbol{\eta}_a\right) - \left(\boldsymbol{\omega}_m - \boldsymbol{b}_\omega - \boldsymbol{\eta}_\omega\right) \times {}^b\boldsymbol{v} \\ \frac{1}{2}\boldsymbol{\Gamma}(\mathring{q})\left(\boldsymbol{\omega}_m - \boldsymbol{b}_\omega - \boldsymbol{\eta}_\omega\right) \\ \boldsymbol{\eta}_{b_a} \\ \boldsymbol{\eta}_{b_\omega} \end{pmatrix} \tag{6.12}$$

From here, again two different error representations are valid

$$\delta \boldsymbol{x}_{L2} = \begin{pmatrix} \delta \boldsymbol{\xi} \\ \delta \boldsymbol{v} \\ \boldsymbol{\alpha}_L \\ \delta \boldsymbol{b}_a \\ \delta \boldsymbol{b}_\omega \end{pmatrix} = \begin{pmatrix} \boldsymbol{\xi} - \hat{\boldsymbol{\xi}} \\ {}^b\boldsymbol{v} - {}^b\hat{\boldsymbol{v}} \\ \boldsymbol{\alpha}_L \\ \boldsymbol{b}_a - \hat{\boldsymbol{b}}_a \\ \boldsymbol{b}_\omega - \hat{\boldsymbol{b}}_\omega \end{pmatrix} \tag{6.13}$$

or equivalently

$$\delta \boldsymbol{x}_{R2} = \begin{pmatrix} \delta \boldsymbol{\xi} \\ \delta \boldsymbol{v} \\ \boldsymbol{\alpha}_R \\ \delta \boldsymbol{b}_a \\ \delta \boldsymbol{b}_\omega \end{pmatrix} = \begin{pmatrix} \boldsymbol{\xi} - \hat{\boldsymbol{\xi}} \\ {}^b\boldsymbol{v} - {}^b\hat{\boldsymbol{v}} \\ \boldsymbol{\alpha}_R \\ \boldsymbol{b}_a - \hat{\boldsymbol{b}}_a \\ \boldsymbol{b}_\omega - \hat{\boldsymbol{b}}_\omega \end{pmatrix} \tag{6.14}$$

whose dynamics are defined by

$$\delta \dot{\boldsymbol{x}}_{L2} = \begin{pmatrix} \dot{\delta \boldsymbol{\xi}} \\ \dot{\delta \boldsymbol{v}} \\ \dot{\boldsymbol{\alpha}}_L \\ \dot{\delta \boldsymbol{b}}_a \\ \dot{\delta \boldsymbol{b}}_\omega \end{pmatrix} = \begin{pmatrix} (\mathbf{L}(\boldsymbol{\alpha}_L) - \mathbf{I}_3)\, \mathbf{L}(\hat{\hat{q}})\, {}^b\hat{\boldsymbol{v}} + \mathbf{L}(\boldsymbol{\alpha}_L)\mathbf{L}(\hat{\hat{q}})\delta \boldsymbol{v} \\ \mathbf{L}^\top(\hat{\hat{q}})\left(\mathbf{L}^\top(\boldsymbol{\alpha}_L) - \mathbf{I}_3\right){}^w\boldsymbol{g} + -\delta \boldsymbol{b}_a - \boldsymbol{\eta}_a + (\delta \boldsymbol{b}_\omega + \boldsymbol{\eta}_\omega) \times \left({}^b\hat{\boldsymbol{v}} + \delta \boldsymbol{v}\right) - \left(\boldsymbol{\omega}_m - \hat{\boldsymbol{b}}_\omega\right) \times \delta \boldsymbol{v} \\ -\frac{1}{2}\left(2\mathbf{I}_3 + \frac{\boldsymbol{\alpha}_L \boldsymbol{\alpha}_L^\top}{2} + [\boldsymbol{\alpha}_L]_\times\right) \mathbf{L}(\hat{\hat{q}})\left(\boldsymbol{b}_\omega - \hat{\boldsymbol{b}}_\omega + \boldsymbol{\eta}_\omega\right) \\ \boldsymbol{\eta}_{b_a} \\ \boldsymbol{\eta}_{b_\omega} \end{pmatrix}$$

$$\tag{6.15}$$

and

$$\delta \dot{\boldsymbol{x}}_{R2} = \begin{pmatrix} \dot{\delta \boldsymbol{\xi}} \\ \dot{\delta \boldsymbol{v}} \\ \dot{\boldsymbol{\alpha}}_R \\ \dot{\delta \boldsymbol{b}}_a \\ \dot{\delta \boldsymbol{b}}_\omega \end{pmatrix} = \begin{pmatrix} \mathbf{L}(\hat{\hat{q}})\left(\mathbf{L}(\boldsymbol{\alpha}_R) - \mathbf{I}_3\right){}^b\hat{\boldsymbol{v}} + \mathbf{L}(\hat{\hat{q}})\mathbf{L}(\boldsymbol{\alpha}_R)\delta \boldsymbol{v} \\ \left(\mathbf{L}^\top(\boldsymbol{\alpha}_R) - \mathbf{I}_3\right)\mathbf{L}^\top(\hat{\hat{q}})\,{}^w\boldsymbol{g} - \delta \boldsymbol{b}_a - \boldsymbol{\eta}_a + (\delta \boldsymbol{b}_\omega + \boldsymbol{\eta}_\omega) \times \left({}^b\hat{\boldsymbol{v}} + \delta \boldsymbol{v}\right) - \left(\boldsymbol{\omega}_m - \hat{\boldsymbol{b}}_\omega\right) \times \delta \boldsymbol{v} \\ -\left(\mathbf{I}_3 + \frac{\boldsymbol{\alpha}_R \boldsymbol{\alpha}_R^\top}{4}\right)\left(\boldsymbol{b}_\omega - \hat{\boldsymbol{b}}_\omega + \boldsymbol{\eta}_\omega\right) + \frac{1}{2}\boldsymbol{\alpha}_R \times \left(2\boldsymbol{\omega}_m - \boldsymbol{b}_\omega - \hat{\boldsymbol{b}}_\omega - \boldsymbol{\eta}_\omega\right) \\ \boldsymbol{\eta}_{b_a} \\ \boldsymbol{\eta}_{b_\omega} \end{pmatrix}$$

$$\tag{6.16}$$

Using the decomposition of the true state as in Eq. (6.3) or Eq. (6.4) the measure equations for the magnetometer in Eq. (4.3) become

$$\boldsymbol{h}_H(\hat{\boldsymbol{x}}, \delta \boldsymbol{x}, \boldsymbol{\eta}_H) = \mathbf{L}(\hat{\hat{q}})^\top \mathbf{L}(\boldsymbol{\alpha}_L)^\top\, {}^w\boldsymbol{B} + \boldsymbol{\eta}_H \tag{6.17}$$

or

$$h_H(\hat{x}, \delta x, \eta_H) = \mathbf{L}(\alpha_R)^\top \mathbf{L}(\hat{\hat{q}})^{\top w} B + \eta_H \tag{6.18}$$

In the case of the GPS measurement Eq. (4.4), the same equation holds with independence of the attitude

$$h_\xi(\hat{x}, \delta x, \eta_\xi) = \hat{\xi} + \delta \xi + \eta_\xi \tag{6.19}$$

Depending on the navigation state chosen and the choice for the incremental attitude error, four different but a priori equivalent non-linear dynamic systems are obtained. The initial estimation problem is then converted to the estimation of the IMU driven state, the incremental state and its associated covariance under known dynamics that use IMU measurements to propagate the state and GPS and magnetometer observations to perform corrections.

6.2.2   Implementation

On the implementation side, the EKF need of:

- The integration of the continuous dynamic equations in the propagation step. The nonlinearities of the equations makes impossible, in many cases, to find closed solutions. When that is the case, approximations or numerical integration schemes are used.

- The derivation of discrete jacobians that allow to propagate the uncertainty in the state variables and fuse them with the measurement uncertainties. This can be done by numerical approximation or preferably, in the cases when it is possible, by means of symbolic derivation for further faster evaluation.

This section focuses on the specific derivation and implementation of the filter equations for propagation correction and reset steps of the filter concerning the state x_{IMU_1} and δx_{1_L}. The remaining three options will be presented compactly at the end of the section.

For convenience we will denote x_{IMU_1} as x, we usually will refer to its estimation, denoted by $\hat{x}$, as nominal state. In accordance, δx_{L1} will be denoted by δx and referred to as state error or incremental state. The process errors will be considered to be part of the vector

$$\eta_p = \left(\eta_a^\top, \eta_\omega^\top, \eta_{b_a}^\top, \eta_{b_\omega}^\top \right)^\top$$

and the inputs, a_m and ω_m will be grouped under

$$u = \left(a_m^\top, \omega_m^\top \right)^\top$$

The nominal state dynamics in Eq. (6.5) will be denoted by $f_x(x, u, \eta_p)$, or simply f_x and the dynamics of the error state in Eq. (6.10) as $f_{\delta x}(\delta x, \hat{x}, u, \eta_p)$, or in short, $f_{\delta x}$.

Propagation step

During the propagation step, both, the nominal state and error state are propagated by integrating their respective non-linear models. At the beginning of the generic time step k, the nominal state representing the best approximation to the true state available is $\hat{x}_{k-1}^+$ and the error state associated to it is considered as null (imposed as initial condition and later forced by the reset step).

The particular form of the flow $\boldsymbol{f}_{\delta\boldsymbol{x}}$ for a null initial value of the error state $\delta\boldsymbol{x} = \boldsymbol{0}$ results in

$$\dot{\delta\boldsymbol{x}}_{L1} = 0$$

and as a consequence the value of the error state will not be altered, remaining null at the end of the propagation step $\delta\boldsymbol{x}_k^- = \delta\boldsymbol{x}_{k+1}^+ = \boldsymbol{0}$

The estimation of the nominal state at time t_k, can be obtained by using the its value at time $k-1$, $\hat{\boldsymbol{x}}_{k-1}^+$, taking the input vector $\boldsymbol{u}$ as constant during the integration time and imposing a null mean value for the process noise $\boldsymbol{\eta}_p = \boldsymbol{0}$

$$\hat{\boldsymbol{x}}_{k+1}^- = \hat{\boldsymbol{x}}_k^+ + \int_{t_k}^{t_{k+1}} \boldsymbol{f}_{\boldsymbol{x}}\Big|_{\substack{\boldsymbol{x}=\hat{\boldsymbol{x}}_k^+ \\ \boldsymbol{\eta}_p=\boldsymbol{0}}} \mathrm{d}t \tag{6.20}$$

While the integral concerning the position and velocity states can be calculated by

$$\begin{pmatrix} \hat{\boldsymbol{\xi}}_{k+1} \\ \hat{\boldsymbol{v}}_{k+1} \end{pmatrix} = \begin{pmatrix} \hat{\boldsymbol{\xi}}_k \\ \hat{\boldsymbol{v}}_k \end{pmatrix} + \int_{t_k}^{t_{k+1}} \begin{pmatrix} {}^{w}\hat{\boldsymbol{v}} \\ \boldsymbol{g} + \mathbf{L}(\hat{\mathring{q}})\left(\boldsymbol{a}_m - \hat{\boldsymbol{b}}_a\right) \end{pmatrix} \mathrm{d}t \tag{6.21}$$

and it can be seen that the biases does not change its values in the integration interval

$$\begin{pmatrix} \hat{\boldsymbol{b}}_{a_{k+1}} \\ \hat{\boldsymbol{b}}_{\omega_{k+1}} \end{pmatrix} = \begin{pmatrix} \hat{\boldsymbol{b}}_{a_k} \\ \hat{\boldsymbol{b}}_{\omega_k} \end{pmatrix} \tag{6.22}$$

for the quaternion, the simple integration

$$\mathring{q}_{k+1}^- = \mathring{q}_k^+ + \int_{t_k}^{t_{k+1}} \frac{1}{2}\mathring{q}\mathring{\omega} \,\mathrm{d}t$$

may not produce a unit quaternion at the time instant t_{k+1} given the finite numerical precision. Note that since the quaternion product can be written as

$$\frac{1}{2}\mathring{q}\mathring{\omega} = \mathbf{M}(\mathring{\hat{\omega}})\mathring{q}$$

being

$$\mathbf{M}(\mathring{\hat{\omega}}) = \frac{1}{2}\begin{pmatrix} 0 & -\hat{\boldsymbol{\omega}}^\top \\ \hat{\boldsymbol{\omega}} & -[\hat{\boldsymbol{\omega}}]_\times \end{pmatrix}$$

taking $\hat{\boldsymbol{\omega}} = \boldsymbol{\omega}_{m_k} - \boldsymbol{b}_{\omega_k}$ as piece-wise constant between time measures, the solution of the differential equation is

$$\mathring{q}_{k+1}^- = \exp\left(\mathbf{M}\left(t_{k+1} - t_k\right)\right)\mathring{q}_k^+ = \exp\left(\mathbf{M}\Delta t\right)\mathring{q}_k^+ \tag{6.23}$$

it turns out that $\exp\left(\mathbf{M}\Delta t\right)$ for constant $\boldsymbol{\omega}$ can be exactly calculated resulting in

$$\exp\left(\mathbf{M}\Delta t\right) = \left(\cos\left(\tfrac{\|\hat{\boldsymbol{\omega}}\|}{2}\Delta t\right)\mathbf{I}_{4\times4} + \mathbf{M}\frac{\sin\left(\tfrac{\|\hat{\boldsymbol{\omega}}\|}{2}\Delta t\right)}{\|\hat{\boldsymbol{\omega}}\|}\right)$$

which is equivalent to compose the actual quaternion from the right as

$$\mathring{q}_{k+1}^- = \mathring{q}_k^+ \mathring{r} \tag{6.24}$$

with

$$\mathring{r} = \begin{pmatrix} \cos\left(\tfrac{\|\hat{\boldsymbol{\omega}}\|}{2}\Delta t\right) \\ \sin\left(\tfrac{\|\hat{\boldsymbol{\omega}}\|}{2}\Delta t\right)\frac{\hat{\boldsymbol{\omega}}}{\|\hat{\boldsymbol{\omega}}\|} \end{pmatrix} \tag{6.25}$$

A similar result can be achieved by interpreting $\boldsymbol{\omega}\Delta t$ as a rotation vector (see Section 2.3.4) and using Eq. (2.71) to generate the quaternion $\mathring{r}$.

In the EKF framework, the covariance of the error state is propagated using the discrete transition matrix and the discrete process model covariance matrix. Those matrices can be estimated from their continuous counterparts as

$$\boldsymbol{\Phi} = \boldsymbol{\Phi}(\Delta t) = \exp\left(\mathbf{A}\Delta t\right) \tag{6.26a}$$

$$\mathbf{Q}_k = \int_0^{\Delta t} \boldsymbol{\Phi}(s)\mathbf{G}\mathbf{Q}_c\mathbf{G}^\top\boldsymbol{\Phi}(s)^\top\mathrm{d}s \tag{6.26b}$$

with $\mathbf{A}$ and $\mathbf{G}$ representing the jacobian of the continuous dynamics $\boldsymbol{f}_{\delta\boldsymbol{x}}$ evaluated at $\boldsymbol{x} = \hat{\boldsymbol{x}}_k^+$, $\delta\boldsymbol{x}_k = \mathbf{0}$ and under the assumption of null mean process noise and constant inputs in the integration interval

$$\mathbf{A} = \frac{\partial\boldsymbol{f}_{\delta\boldsymbol{x}}}{\partial\delta\boldsymbol{x}}\Bigg|_{\substack{\delta\boldsymbol{x}=\mathbf{0}\\\hat{\boldsymbol{x}}=\hat{\boldsymbol{x}}_k^+\\\boldsymbol{\eta}_p=\mathbf{0}}} = \begin{pmatrix} \mathbf{0}_3 & \mathbf{I}_3 & \mathbf{0}_3 & \mathbf{0}_3 & \mathbf{0}_3 \\ \mathbf{0}_3 & \mathbf{0}_3 & -\left[\mathbf{L}(\hat{\mathring{q}}_k^+)\left(\boldsymbol{a}_m - \hat{\boldsymbol{b}}_{a_k}^+\right)\right]_\times & -\mathbf{L}(\hat{\mathring{q}}_k^+) & \mathbf{0}_3 \\ \mathbf{0}_3 & \mathbf{0}_3 & \mathbf{0}_3 & \mathbf{0}_3 & -\mathbf{L}(\hat{\mathring{q}}_k^+) \\ \mathbf{0}_3 & \mathbf{0}_3 & \mathbf{0}_3 & \mathbf{0}_3 & \mathbf{0}_3 \\ \mathbf{0}_3 & \mathbf{0}_3 & \mathbf{0}_3 & \mathbf{0}_3 & \mathbf{0}_3 \end{pmatrix} \tag{6.27}$$

$$\mathbf{G} = \frac{\partial\boldsymbol{f}_{\delta\boldsymbol{x}}}{\partial\boldsymbol{\eta}_p}\Bigg|_{\substack{\delta\boldsymbol{x}=\mathbf{0}\\\hat{\boldsymbol{x}}=\hat{\boldsymbol{x}}_k^+\\\boldsymbol{\eta}_p=\mathbf{0}}} = \begin{pmatrix} \mathbf{0}_3 & \mathbf{0}_3 & \mathbf{0}_3 & \mathbf{0}_3 \\ -\mathbf{L}(\hat{\mathring{q}}_k^+) & \mathbf{0}_3 & \mathbf{0}_3 & \mathbf{0}_3 \\ \mathbf{0}_3 & -\mathbf{L}(\hat{\mathring{q}}_k^+) & \mathbf{0}_3 & \mathbf{0}_3 \\ \mathbf{0}_3 & \mathbf{0}_3 & \mathbf{I}_3 & \mathbf{0}_3 \\ \mathbf{0}_3 & \mathbf{0}_3 & \mathbf{0}_3 & \mathbf{I}_3 \end{pmatrix} \tag{6.28}$$

Integrals in Eq. (6.26a) and Eq. (6.26b), are often numerically approximated by truncation of a series expansion and assuming $\mathbf{G}\mathbf{Q}_c\mathbf{G}^\top$ diagonal. In Section 6.2.4 we describe a numerical

method for their exact calculation under the assumption of constant $\mathbf{A}$ and $\mathbf{Q}_c$ and a closed form for the specific case of the IMU driven state under consideration in this section, $\boldsymbol{x}_{IMU_1}$.

The propagation step will be run any time that IMU measurements are available. Denoting by Δt the difference in time between the last propagation and the current one, the propagation step is summarised in Algorithm. 4

Algorithm 4: EKF propagation

Data: $\hat{\boldsymbol{x}}_{k-1}^+$, $\mathbf{P}_{k-1}^+$, $\boldsymbol{\omega}_m$, $\boldsymbol{a}_m$, Δt
Result: $\hat{\boldsymbol{x}}_k^-$, $\mathbf{P}_k^-$

1. Calculate the incremental quaternion using Eq. (6.25).

2. Propagate the mean state by using Eqs. (6.21,6.22 and 6.24) to obtain $\hat{\boldsymbol{x}}_k^-$

3. Evaluate the jacobians in Eqs. (6.27 and 6.28)

4. Obtain the discrete transition matrix and process noise using Eq. (6.26)

5. Predict the covariance at the current time step $\mathbf{P}_k^- = \boldsymbol{\Phi}\mathbf{P}_{k-1}^+\boldsymbol{\Phi}^\top + \mathbf{Q}_k$

Measurement equations and update step

Measurements from magnetometers and GPS will not generally coincide in time, therefore, different updates steps must be applied depending on the incoming measure. Processing the system measures separately is, in fact, beneficial since in the calculation of the Kalman gain, a large matrix (with size, the length of the measurement vector) has to be inverted. By splitting the correction step in two, the inversion of a 6x6 matrix is simplified to the inversion of two 3x3 matrices. If the measurements from the GPS and magnetometer were uncorrelated (which is not the general case) then the update process could be run once for every component of the measurement avoiding any matrix inversion.

From the implementation perspective, the update step is given by the evaluation of the Algorithm. 3 slightly adapted to deal with our specific case. When a new measurement of the GPS or the magnetometer is available, at instant k, the state of the filters must be propagated up to that instant using Algorithm. 4 along with the most recent values of $\boldsymbol{\omega}_m$ and $\boldsymbol{a}_m$ to obtain $\hat{\boldsymbol{x}}_k^-$ and $\mathbf{P}_k^-$ ($\delta\boldsymbol{x}_k^-$ must remain null). Then, the correction procedure, particularised for the type of measurement in queue, allows to obtain the corrected state $\delta\boldsymbol{x}_k^+$, and its associated covariance $\mathbf{P}_k^+$.

The state correction makes use of the real measurement and a synthetic measurement generated by the predicted state and the measurement equations, present in Eq. (6.17) and Eq. (6.19), to correct the incremental state and the jacobian of the measure equations to correct the covariance.

Both equations and jacobians evaluated at the generic state $\hat{\boldsymbol{x}} = \hat{\boldsymbol{x}}_k^-$, and $\delta\boldsymbol{x}_k^- = 0$ result in

$$\hat{\boldsymbol{z}} = \hat{\boldsymbol{h}}_{\boldsymbol{\xi}}(\hat{\boldsymbol{x}}, \delta\boldsymbol{x}, \boldsymbol{\eta}_{\boldsymbol{\xi}})\bigg|_{\substack{\boldsymbol{x}=\hat{\boldsymbol{x}}_{k+1}^- \\ \delta\boldsymbol{x}=\delta\boldsymbol{x}_{k+1}^-=\mathbf{0} \\ \boldsymbol{\eta}_{\boldsymbol{\xi}}=\mathbf{0}}} = \hat{\boldsymbol{\xi}}_k^- \tag{6.29a}$$

$$\mathbf{C}_{\boldsymbol{\xi}} = \frac{\partial\boldsymbol{h}_{\boldsymbol{\xi}}}{\partial\delta\boldsymbol{x}}\bigg|_{\substack{\boldsymbol{x}=\hat{\boldsymbol{x}}_{k+1}^- \\ \delta\boldsymbol{x}=\delta\boldsymbol{x}_{k+1}^-=\mathbf{0} \\ \boldsymbol{\eta}_H=\mathbf{0}}} = \begin{pmatrix} \mathbf{I}_3 & \mathbf{0}_{3\times12} \end{pmatrix} \tag{6.29b}$$

for the GPS measurements and

$$\hat{\boldsymbol{z}} = \boldsymbol{h}_H(\hat{\boldsymbol{x}}, \delta\boldsymbol{x}, \boldsymbol{\eta}_H)\bigg|_{\substack{\hat{\boldsymbol{x}}=\hat{\boldsymbol{x}}_k^- \\ \delta\boldsymbol{x}=\mathbf{0} \\ \boldsymbol{\eta}_H=\mathbf{0}}} = \mathbf{L}(\hat{\bar{q}}_k^-)^{\top}{}^w\boldsymbol{B} \tag{6.30a}$$

$$\mathbf{C}_H = \frac{\partial\boldsymbol{h}_H}{\partial\delta\boldsymbol{x}}\bigg|_{\substack{\boldsymbol{x}=\hat{\boldsymbol{x}}_{k+1}^- \\ \delta\boldsymbol{x}=\delta\boldsymbol{x}_{k+1}^-=\mathbf{0} \\ \boldsymbol{\eta}_H=\mathbf{0}}} = \begin{pmatrix} \mathbf{0}_{3\times6} & \mathbf{L}(\hat{\bar{q}}_k^-)\left[{}^w\boldsymbol{B}\right]_{\times} & \mathbf{0}_{3\times6} \end{pmatrix} \tag{6.30b}$$

for the magnetometer.

The error measurement covariance matrices $\mathbf{R}$ can be obtained by examining the sensor's output in stationary conditions during a long period of time.

$$\mathbf{R}_H = \mathrm{cov}(\boldsymbol{\eta}_H)$$

$$\mathbf{R}_{\boldsymbol{\xi}} = \mathrm{cov}(\boldsymbol{\eta}_{\boldsymbol{\xi}})$$

Specific values for this matrices are presented in Section 4.3.2.

The update algorithm can be then formulated as

Algorithm 5: EKF correction

Data: $\mathbf{P}_k^-$, $\boldsymbol{\omega}_m$, $\boldsymbol{a}_m$, $\boldsymbol{z}_k$, measurement type
Result: $\delta\boldsymbol{x}_k^+$, $\mathbf{P}_k^+$

1. Evaluate the measurement function and Jacobian in Eq. (6.29) or Eq. (6.30) depending of the measurement type to obtain $\hat{\boldsymbol{z}}$ and $\mathbf{C}$.

2. Calculate the suboptimal gain $\mathbf{K} = \mathbf{P}_k^-\mathbf{C}^{\top}(\mathbf{C}\mathbf{P}_k^-\mathbf{C}^{\top} + \mathbf{R})^{-1}$

3. Update the covariance of the estimation error $\mathbf{P}_k^+ = (\mathbf{I} - \mathbf{K}\mathbf{C})\mathbf{P}_k^-$

4. Update the state $\delta\boldsymbol{x}_k^+ = \mathbf{K}(\boldsymbol{z}_k - \hat{\boldsymbol{z}})$

Note that by admitting null incremental state after propagation, it does not need to be an input of Algorithm. 5, which is also reflected in line four of the algorithm.

Reset step

After the update, the incremental states are corrected and in general they will take non-zero values. In contrast, the nominal state is not affected by the correction. The reset step, run at the end of every correction step, transfers the information accumulated in the incremental state to the nominal state implementing Eq. (6.4) and resetting the incremental state to zero,

$$\hat{\boldsymbol{\xi}}_k^+ = \hat{\boldsymbol{\xi}}_k^- + \delta \boldsymbol{\xi}_k^+ \tag{6.31a}$$

$$\hat{\boldsymbol{v}}_k^+ = \hat{\boldsymbol{v}}_k^- + \delta \boldsymbol{v}_k^+ \tag{6.31b}$$

$$\hat{\mathring{q}}_k^+ = \frac{\left(\dfrac{2}{\hat{\boldsymbol{\alpha}}_L}\right) \hat{\mathring{q}}_k^-}{\left\| \left(\dfrac{2}{\hat{\boldsymbol{\alpha}}_L}\right) \hat{\mathring{q}}_k^- \right\|} \tag{6.31c}$$

$$\hat{\boldsymbol{b}}_{a_k}^+ = \hat{\boldsymbol{b}}_{a_k}^- + \delta \boldsymbol{b}_{a_k}^+ \tag{6.31d}$$

$$\hat{\boldsymbol{b}}_{\omega_k}^+ = \hat{\boldsymbol{b}}_{\omega_k}^- + \delta \boldsymbol{b}_{\omega_k}^+ \tag{6.31e}$$

Note that Eq. (6.31c) has been slightly modified from Eq. (6.7). Given that the denominator in Eq. (6.7) is just an scalar factor, Eq. (6.31c) serves the same purpose enforcing the unit-norm that otherwise can be lost due to numerical precision errors.

After the reset of the filter states, Eq. (4.2b) and Eq. (4.2a) can be used to correct the values of the $\boldsymbol{a}$ and $\boldsymbol{\omega}$ variables by accounting for the estimated bias as

$$\hat{\boldsymbol{a}} = \boldsymbol{a}_m - \hat{\boldsymbol{b}}_a \tag{6.32a}$$

$$\hat{\boldsymbol{\omega}} = \boldsymbol{\omega} - \hat{\boldsymbol{b}}_\omega \tag{6.32b}$$

The reset step is summarised in Algorithm. 6

Algorithm 6: EKF reset

Data: $\mathbf{P}_k^-$, $\boldsymbol{\omega}_m$, $\boldsymbol{a}_m$, $\boldsymbol{z}_k$, measurement type
Result: $\delta \boldsymbol{x}_k^+$, $\mathbf{P}_k^+$

1. Transfer information of the incremental state to the nominal state using Eq. (6.31).

2. Update the values of the estimated angular velocity and external force acceleration using Eq. (6.32).

3. Reset the incremental state to zero.

Note that the last step of the algorithm can be omitted, since algorithms Algorithm. 4 and Algorithm. 5 are already adapted to consider null value of the incremental step.

6.2.3   Summary and formulation for other filter realisations

The derivation of the filter equations carried out with the state variables $\boldsymbol{x}_{IMU_1}$ and $\delta\boldsymbol{x}_L$ can be similarly done with the remaining variables leading to four different filter formulations. Eq. (6.22) and Eq. (6.24) in the propagation, Eq. (6.30a), Eq. (6.29a) and Eq. (6.29b) in the correction and Eq. (6.31) with the exception of Eq. (6.31c) in the reset step, do not depend on the attitude and velocity parametrization chosen. The incremental state $\delta\boldsymbol{x}$ is also independent of the filter choice and does not modify its value during the propagation step as long as it is selected to be null at the beginning of the filtering process.

The values of the jacobian matrices $\mathbf{A}$ and $\mathbf{G}$ both depend on the attitude error and the velocity parametrizations chosen. Whereas the update equations of $\boldsymbol{h}_H$ and the jacobian $\mathbf{C}_H$ depend only on the quaternion error representation.

In Table 6.1, the equations describing $\dot{\hat{\boldsymbol{\xi}}}$, $\dot{\hat{\boldsymbol{v}}}$ and $\dot{\boldsymbol{\alpha}}$ are specified along with the values of $\mathbf{A}$, $\mathbf{G}$ and $\mathbf{C}_H$ that define the implementation of the four filters proposed.

	Filter 1	Filter 2	Filter 3	Filter 4
$\boldsymbol{v}$	$^w\boldsymbol{v}$	$^w\boldsymbol{v}$	$^b\boldsymbol{v}$	$^b\boldsymbol{v}$
$\delta\mathring{q}$	$\boldsymbol{\alpha}_L$	$\boldsymbol{\alpha}_R$	$\boldsymbol{\alpha}_L$	$\boldsymbol{\alpha}_R$
$\dot{\boldsymbol{\xi}}$	$^w\boldsymbol{v}$	$^w\boldsymbol{v}$	$\mathbf{L}(\hat{\mathring{q}})\,^b\hat{\boldsymbol{v}}$	$\mathbf{L}(\hat{\mathring{q}})\,^b\hat{\boldsymbol{v}}$
$\dot{\hat{\boldsymbol{v}}}$	$^w\boldsymbol{g} + \mathbf{L}(\hat{\mathring{q}})(\boldsymbol{a}_m - \hat{\boldsymbol{b}}_a)$	$^w\boldsymbol{g} + \mathbf{L}(\hat{\mathring{q}})(\boldsymbol{a}_m - \hat{\boldsymbol{b}}_a)$	$\mathbf{L}^\top(\hat{\mathring{q}})\,^w\boldsymbol{g} + \boldsymbol{a}_m - \hat{\boldsymbol{b}}_a - (\boldsymbol{\omega}_m - \hat{\boldsymbol{b}}_\omega) \times {}^b\hat{\boldsymbol{v}}$	$\mathbf{L}^\top(\hat{\mathring{q}})\,^w\boldsymbol{g} + \boldsymbol{a}_m - \hat{\boldsymbol{b}}_a - (\boldsymbol{\omega}_m - \hat{\boldsymbol{b}}_\omega) \times {}^b\hat{\boldsymbol{v}}$
$\dot{\boldsymbol{\alpha}}$	Eq. (5.21a)	Eq. (5.21b)	Eq. (5.21a)	Eq. (5.21b)
$\mathbf{A}$	Eq. (6.27)	$\begin{pmatrix} \mathbf{0}_3 & \mathbf{I}_3 & \mathbf{0}_3 & \mathbf{0}_3 & \mathbf{0}_3 \\ \mathbf{0}_3 & \mathbf{0}_3 & -\mathbf{L}(\hat{\mathring{q}})[\boldsymbol{a}_m - \hat{\boldsymbol{b}}_a]_\times & -\mathbf{L}(\hat{\mathring{q}}) & \mathbf{0}_3 \\ \mathbf{0}_3 & \mathbf{0}_3 & -[\boldsymbol{\omega}_m - \hat{\boldsymbol{b}}_\omega]_\times & \mathbf{0}_3 & -\mathbf{I}_3 \\ \mathbf{0}_3 & \mathbf{0}_3 & \mathbf{0}_3 & \mathbf{0}_3 & \mathbf{0}_3 \\ \mathbf{0}_3 & \mathbf{0}_3 & \mathbf{0}_3 & \mathbf{0}_3 & \mathbf{0}_3 \end{pmatrix}$	$\begin{pmatrix} \mathbf{0}_3 & \mathbf{L}(\hat{\mathring{q}}) & -[\mathbf{L}(\hat{\mathring{q}})\,^b\hat{\boldsymbol{v}}]_\times & \mathbf{0}_3 & \mathbf{0}_3 \\ \mathbf{0}_3 & -[\boldsymbol{\omega}_m - \hat{\boldsymbol{b}}_\omega]_\times & \mathbf{L}(\hat{\mathring{q}})^\top[^b\boldsymbol{g}]_\times & -\mathbf{I}_3 & -[^b\hat{\boldsymbol{v}}]_\times \\ \mathbf{0}_3 & \mathbf{0}_3 & \mathbf{0}_3 & \mathbf{0}_3 & -\mathbf{L}(\hat{\mathring{q}}) \\ \mathbf{0}_3 & \mathbf{0}_3 & \mathbf{0}_3 & \mathbf{0}_3 & \mathbf{0}_3 \\ \mathbf{0}_3 & \mathbf{0}_3 & \mathbf{0}_3 & \mathbf{0}_3 & \mathbf{0}_3 \end{pmatrix}$	$\begin{pmatrix} \mathbf{0}_3 & \mathbf{L}(\hat{\mathring{q}}) & -\mathbf{L}(\hat{\mathring{q}})[^b\hat{\boldsymbol{v}}]_\times & \mathbf{0}_3 & \mathbf{0}_3 \\ \mathbf{0}_3 & -[\boldsymbol{\omega}_m - \hat{\boldsymbol{b}}_\omega]_\times & \mathbf{L}(\hat{\mathring{q}})^\top[^b\boldsymbol{g}]_\times & -\mathbf{I}_3 & -[^b\hat{\boldsymbol{v}}]_\times \\ \mathbf{0}_3 & \mathbf{0}_3 & -[\boldsymbol{\omega}_m - \hat{\boldsymbol{b}}_\omega]_\times & \mathbf{0}_3 & -\mathbf{I}_3 \\ \mathbf{0}_3 & \mathbf{0}_3 & \mathbf{0}_3 & \mathbf{0}_3 & \mathbf{0}_3 \\ \mathbf{0}_3 & \mathbf{0}_3 & \mathbf{0}_3 & \mathbf{0}_3 & \mathbf{0}_3 \end{pmatrix}$
$\mathbf{G}$	Eq. (6.28)	$\begin{pmatrix} \mathbf{0}_3 & \mathbf{0}_3 & \mathbf{0}_3 & \mathbf{0}_3 \\ -\mathbf{L}(\hat{\mathring{q}}) & \mathbf{0}_3 & \mathbf{0}_3 & \mathbf{0}_3 \\ \mathbf{0}_3 & -\mathbf{I}_3 & \mathbf{0}_3 & \mathbf{0}_3 \\ \mathbf{0}_3 & \mathbf{0}_3 & \mathbf{I}_3 & \mathbf{0}_3 \\ \mathbf{0}_3 & \mathbf{0}_3 & \mathbf{0}_3 & \mathbf{I}_3 \end{pmatrix}$	$\begin{pmatrix} \mathbf{0}_3 & \mathbf{0}_3 & \mathbf{0}_3 & \mathbf{0}_3 \\ -\mathbf{I}_3 & -[^b\hat{\boldsymbol{v}}]_\times & \mathbf{0}_3 & \mathbf{0}_3 \\ \mathbf{0}_3 & -\mathbf{L}(\hat{\mathring{q}}) & \mathbf{0}_3 & \mathbf{0}_3 \\ \mathbf{0}_3 & \mathbf{0}_3 & \mathbf{I}_3 & \mathbf{0}_3 \\ \mathbf{0}_3 & \mathbf{0}_3 & \mathbf{0}_3 & \mathbf{I}_3 \end{pmatrix}$	$\begin{pmatrix} \mathbf{0}_3 & \mathbf{0}_3 & \mathbf{0}_3 & \mathbf{0}_3 \\ -\mathbf{I}_3 & -[^b\hat{\boldsymbol{v}}]_\times & \mathbf{0}_3 & \mathbf{0}_3 \\ \mathbf{0}_3 & -\mathbf{I}_3 & \mathbf{0}_3 & \mathbf{0}_3 \\ \mathbf{0}_3 & \mathbf{0}_3 & \mathbf{I}_3 & \mathbf{0}_3 \\ \mathbf{0}_3 & \mathbf{0}_3 & \mathbf{0}_3 & \mathbf{I}_3 \end{pmatrix}$
$\mathbf{C_H}$	Eq. (6.30b)	$\begin{pmatrix} \mathbf{0}_{3\times6} & [\mathbf{L}(\hat{\mathring{q}})^\top{}^w\boldsymbol{B}]_\times & \mathbf{0}_{3\times6} \end{pmatrix}$	Eq. (6.30b)	$\begin{pmatrix} \mathbf{0}_{3\times6} & [\mathbf{L}(\hat{\mathring{q}})^\top{}^w\boldsymbol{B}]_\times \end{pmatrix}$

TABLE 6.1: Different filter dynamic equations and jacobian matrices

6.2.4   Exact calculation of $\boldsymbol{\Phi}$ and $\mathbf{Q}_k$

In the filtering process, the propagation routine is called when a new IMU measurement arrives. IMU's are able to run at rates up to $\approx 1\,\text{kHz}$ and as a consequence it is important to optimize the code inside the propagation.

As presented in [89], the calculation of the transition matrix $\boldsymbol{\Phi}$ and the discrete covariance $\mathbf{Q}_k$ can be achieved in the case that $\mathbf{A}$ and $\mathbf{G}$ are constant by the calculation of a unique matrix exponential with twice the size of $\mathbf{A}$ as

$$\exp\left(\begin{bmatrix} -\mathbf{A} & \mathbf{GQ}_c\mathbf{G}^\top \\ \mathbf{0} & \mathbf{A}^\top \end{bmatrix}\Delta t\right) = \begin{bmatrix} \mathbf{F}_2 & \mathbf{M} \\ \mathbf{0}_3 & \boldsymbol{\Phi}^\top \end{bmatrix}$$

from where the dimension of the zero matrix $\mathbf{0}$ is equal to the dimension of $\mathbf{A}$, $\mathbf{F}_2$ is not used and $\mathbf{Q}_k = \boldsymbol{\Phi}\mathbf{M}$.

There exist many ways for computing efficiently the matrix exponential and python and MatLab both use implementations based on the article [66]. Those methods usually approximate the exponential by either using a truncation of a series expansion, calculating eigenvalues or using other kinds of approximations for the matrix exponential. However, for the specific case of the filter developed in depth in the previous sections, Filter 1, the matrix exponential can be exactly determined.

Closed form for Filter 1

The jacobian matrix $\mathbf{A}$ in Eq. (6.27) derived for the filter state $\delta\boldsymbol{x}_{L1}$ is a nillpotent matrix, i.e. its powers, $\mathbf{A}^k$, become null for a finite value of k. In this particular case, for $k > 3$.

As a consequence, the decomposition of the matrix exponential as an infinite Taylor series summation,

$$\boldsymbol{\Phi}(\Delta t) = \exp\left(\mathbf{A}\Delta t\right) = \sum_{j=0}^{\infty} \frac{(\mathbf{A}\Delta t)^j}{j!}$$

reduces to

$$\boldsymbol{\Phi}(\Delta t) = \exp\left(\mathbf{A}\Delta t\right) = \sum_{j=0}^{3} \frac{(\mathbf{A}\Delta t)^j}{j!}$$

when the term $\boldsymbol{a}_m - \boldsymbol{b}_a$ inside $\mathbf{A}$ is considered constant.

The transition matrix $\boldsymbol{\Phi}$ can be then written as

$$\boldsymbol{\Phi}(\Delta t) = \begin{pmatrix} \mathbf{I}_3 & \mathbf{I}_3\Delta t & \mathcal{S}\frac{\Delta t^2}{2} & \mathcal{R}\frac{\Delta t^2}{2} & \mathcal{S}\mathcal{R}\frac{\Delta t^3}{6} \\ \mathbf{0}_3 & \mathbf{I}_3 & \mathcal{S}\Delta t & \mathcal{R}\Delta t & \mathcal{S}\mathcal{R}\frac{\Delta t^2}{2} \\ \mathbf{0}_3 & \mathbf{0}_3 & \mathbf{I}_3 & \mathbf{0}_3 & \mathcal{R}\Delta t \\ & \mathbf{0}_{6\times9} & & & \mathbf{I}_6 \end{pmatrix} \tag{6.33}$$

being $\mathcal{R} = -\mathbf{L}(\hat{\bar{q}})$ and $\mathcal{S} = -\left[\mathbf{L}(\hat{\bar{q}})\left(\boldsymbol{a}_m - \hat{\boldsymbol{b}}_a\right)\right]_\times$.

By substituting Eq. (6.33) in Eq. (6.26b) and integrating, the next discrete error covariance matrix is obtained

$$
\mathbf{Q}_k = \begin{pmatrix}
t_5\mathcal{A}_1 + t_8\left(\mathcal{W}_3 + \mathcal{AB}_2\right) + t_{10}\mathcal{WB}_5 & t_2\mathcal{A}_1 + t_6\left(\mathcal{W}_3 + \mathcal{AB}_2\right) + t_9\mathcal{WB}_5 & t_7\mathcal{WB}_4 + t_3\mathcal{W}_2 & t_3\mathcal{AB}_1 & t_4\mathcal{WB}_3 \\
 & t_1\mathcal{A}_1 + t_5\left(\mathcal{W}_3 + \mathcal{AB}_2\right) + t_8\mathcal{WB}_5 & t_2\mathcal{W}_2 + t_6\mathcal{WB}_4 & t_2\mathcal{AB}_1 & t_3\mathcal{WB}_3 \\
 & & t_1\mathcal{W}_1 + t_5\mathcal{WB}_2 & \mathbf{0}_3 & t_2\mathcal{WB}_1 \\
 & SYM & & t_1\mathbf{R}_{b_a} & \mathbf{0}_3 \\
 & & & & t_1\mathbf{R}_{b_\omega}
\end{pmatrix}
$$

being

$$
\begin{aligned}
\mathcal{A}_1 &= \mathcal{R}\mathbf{R}_a\mathcal{R}^\top & \mathcal{W}_1 &= \mathcal{R}\mathbf{R}_\omega\mathcal{R}^\top & \mathcal{WB}_1 &= \mathcal{R}\mathbf{R}_{b_\omega} & \mathcal{WB}_4 &= \mathcal{SR}\mathbf{R}_{b_\omega}\mathcal{R}^\top \\
\mathcal{AB}_1 &= \mathcal{R}\mathbf{R}_{b_a} & \mathcal{W}_2 &= \mathcal{SR}\mathbf{R}_\omega\mathcal{R}^\top & \mathcal{WB}_2 &= \mathcal{R}\mathbf{R}_{b_\omega}\mathcal{R}^\top & \mathcal{WB}_5 &= \mathcal{SR}\mathbf{R}_{b_\omega}\mathcal{R}^\top\mathcal{S}^\top \\
\mathcal{AB}_2 &= \mathcal{R}\mathbf{R}_{b_a}\mathcal{R}^\top & \mathcal{W}_3 &= \mathcal{SR}\mathbf{R}_\omega\mathcal{R}^\top\mathcal{S}^\top & \mathcal{WB}_3 &= \mathcal{SR}\mathbf{R}_{b_\omega}
\end{aligned}
$$

and

$$
\begin{aligned}
t_1 &= \Delta t & t_2 &= \frac{\Delta t^2}{2} & t_3 &= \frac{\Delta t^3}{6} & t_4 &= \frac{\Delta t^4}{24} & t_5 &= \frac{\Delta t^3}{3} \\
t_6 &= \frac{\Delta t^4}{8} & t_7 &= \frac{\Delta t^5}{30} & t_8 &= \frac{\Delta t^5}{20} & t_9 &= \frac{\Delta t^6}{72} & t_{10} &= \frac{\Delta t^7}{252}
\end{aligned}
$$

This closed form, avoids the general calculation of the matrix exponential replacing it by a few matrix multiplications without any approximation.

Closed analytic forms for the transition matrix and discrete covariances can be also obtained for the remaining filters despite of having non-nillpotent $\mathbf{A}$ matrices. It is possible given the structure of $\mathbf{A}$ and properties of the skew-symmetric matrix powers. However the solution obtained is analytically complex and depends of multiple evaluation of trigonometric functions.

6.2.5 Initialising the filter

Initial values of the estimated states are needed to start the filtering process. Initial rough values for the position and angular velocity can be set from their respective sensor measurements by neglecting bias and errors $\boldsymbol{b_a} = \boldsymbol{b_\omega} = \boldsymbol{\eta}_p = \mathbf{0}$. Moreover by initialising the filter at a rest position (e.g., with the quadrotor steady on the ground), ${}^w\boldsymbol{v}$ or ${}^b\boldsymbol{v}$ can be set to zero. In this section a procedure similar to one the shown in [88] is presented to estimate the quaternion orientation that relates the world and body frames based on measurements of accelerometers and magnetometers. The method is based on the attitude parametrization in [86] which decomposes a generic rotation in a sequence of two rotations about a known vector and its perpendicular direction. Compared to [88], the present method calculates the quaternion in a clearer and simpler way, with less operations and without the need to impose the direction of gravity in the world frame to be vertical.

Quaternion orientation from 2 vectors

Let two different frames with coincident origin be denoted by $\{\mathcal{F}_1\}$ and $\{\mathcal{F}_2\}$. Let in addition the vectors $\boldsymbol{a}$ and $\boldsymbol{b}$ represent physical 3D quantities for which their coordinates are known in $\{\mathcal{F}_1\}$ and $\{\mathcal{F}_2\}$, i.e., the four three dimensional vectors $^{\mathcal{F}_1}\boldsymbol{a}$, $^{\mathcal{F}_1}\boldsymbol{b}$, $^{\mathcal{F}_2}\boldsymbol{a}$ and $^{\mathcal{F}_2}\boldsymbol{b}$ are known.
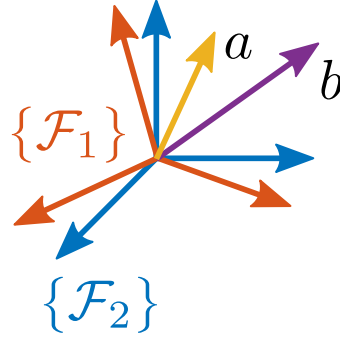
FIGURE 6.1: Two generic reference frames with different attitude and two vectors.

Let $\mathring{q}_0$ be the quaternion that represents the relative attitude between the frames such that

$$^{\mathcal{F}_1}\boldsymbol{a} = \mathbf{L}(\mathring{q}_0)^{\mathcal{F}_2}\boldsymbol{a} \tag{6.34a}$$

$$^{\mathcal{F}_1}\boldsymbol{b} = \mathbf{L}(\mathring{q}_0)^{\mathcal{F}_2}\boldsymbol{b} \tag{6.34b}$$

Finally, let the quaternion to be decomposed as

$$\mathring{q}_0 = \mathring{q}_\parallel \mathring{q}_\perp$$

where:

- $\mathring{q}_\perp$ represents a rotation from frame $\{\mathcal{F}_2\}$ to an intermediate frame $\{\mathcal{F}_i\}$ which shares the direction of $\boldsymbol{a}$ with the frame $\{\mathcal{F}_1\}$, but does not necessarily share the direction of $\boldsymbol{b}$. Then

$$^{\mathcal{F}_i}\boldsymbol{a} = \mathbf{L}(\mathring{q}_\perp)^{\mathcal{F}_2}\boldsymbol{a} = {}^{\mathcal{F}_1}\boldsymbol{a} \tag{6.35}$$

- $\mathring{q}_\parallel$ represents a rotation from the intermediate frame about the direction of $^{\mathcal{F}_1}\boldsymbol{a} = {}^{\mathcal{F}_i}\boldsymbol{a}$ that makes

$$^{\mathcal{F}_1}\boldsymbol{b} = \mathbf{L}(\mathring{q}_\parallel)^{\mathcal{F}_i}\boldsymbol{b} = \mathbf{L}(\mathring{q}_\parallel)\mathbf{L}(\mathring{q}_\perp)^{\mathcal{F}_2}\boldsymbol{b} \tag{6.36}$$

  Note that the rotation $\mathbf{L}(q_\parallel)$ will have no effect when applied over $^{\mathcal{F}_1}\boldsymbol{a}$ which implies that Eq. (6.35) and Eq. (6.36) are compatible.

By admitting the above proposals the problem of finding an initial attitude is reduced to finding $\mathring{q}_\parallel$ and $\mathring{q}_\perp$ which map both, $\boldsymbol{a}$ and $\boldsymbol{b}$ from frame $\{\mathcal{F}_2\}$ to $\{\mathcal{F}_1\}$ which after composition gives $\mathring{q}_0$.

The first rotation is defined to make ${}^{\mathcal{F}_1}\boldsymbol{a} = \mathbf{L}(q_\perp){}^{\mathcal{F}_2}\boldsymbol{a}$. The simpler and shorter rotation will be a rotation about the orthogonal direction of the plane that contains ${}^{\mathcal{F}_2}\boldsymbol{a}$ and ${}^{\mathcal{F}_1}\boldsymbol{a}$, i.e.,

$$\boldsymbol{u} = \frac{{}^{\mathcal{F}_2}\boldsymbol{a} \times {}^{\mathcal{F}_1}\boldsymbol{a}}{\|{}^{\mathcal{F}_2}\boldsymbol{a} \times {}^{\mathcal{F}_1}\boldsymbol{a}\|} \tag{6.37}$$

an angle $\theta \in [-\pi, \pi]$ given by

$$\theta = \arccos\left(\frac{{}^{\mathcal{F}_2}\boldsymbol{a}^\top {}^{\mathcal{F}_1}\boldsymbol{a}}{\|{}^{\mathcal{F}_2}\boldsymbol{a}\| \, \|{}^{\mathcal{F}_1}\boldsymbol{a}\|}\right) \tag{6.38}$$

Such rotation can be directly encoded in a quaternion by

$$\mathring{q}_\perp = \begin{pmatrix} \cos(\theta/2) \\ \sin(\theta/2)\,\boldsymbol{u} \end{pmatrix} \tag{6.39}$$

which needs the computation of a dot product, a cross product, three vector norms and three trigonometric computations.

Even not being indispensable, the same quaternion can be constructed in a more straightforward way without the use of trigonometric functions and substituting the three vector norms by two quaternion norms as formulated in Algorithm. 7:

Algorithm 7: Quaternion from two vectors

Data: ${}^{\mathcal{F}_1}\boldsymbol{a}, {}^{\mathcal{F}_2}\boldsymbol{a}$
Result: $\mathring{q}_\perp$

1. Calculate the auxiliar non-unit quaternion

$$\mathring{q}_{temp} = \begin{pmatrix} {}^{\mathcal{F}_2}\boldsymbol{a}^\top {}^{\mathcal{F}_1}\boldsymbol{a} \\ {}^{\mathcal{F}_2}\boldsymbol{a} \times {}^{\mathcal{F}_1}\boldsymbol{a} \end{pmatrix} \tag{6.40}$$

   and its norm $\|\mathring{q}_{temp}\|$.

2. Replace the scalar component of the quaternion by

$$\mathring{q}_{temp_0} = \mathring{q}_{temp_0} + \|\mathring{q}_{temp}\| \tag{6.41}$$

3. Normalize the resulting quaternion as

$$\mathring{q}_\perp = \frac{\mathring{q}_{temp}}{\|\mathring{q}_{temp}\|} \tag{6.42}$$

Note that the quaternion in Eq. (6.40) could be written as

$$\mathring{q}_{temp} = \|{}^{\mathcal{F}_2}\boldsymbol{a}\| \, \|{}^{\mathcal{F}_1}\boldsymbol{a}\| \begin{pmatrix} \cos(\theta) \\ \sin(\theta)\,\boldsymbol{u} \end{pmatrix}$$

whose norm is $\left\|{}^{\mathcal{F}_2}\boldsymbol{a}\right\|\left\|{}^{\mathcal{F}_1}\boldsymbol{a}\right\|$. After Eq. (6.41) the norm transforms to

$$\|\mathring{q}_{temp}\| = 2\left\|{}^{\mathcal{F}_2}\boldsymbol{a}\right\|\left\|{}^{\mathcal{F}_1}\boldsymbol{a}\right\|\sqrt{\frac{1+\cos(\theta)}{2}}$$

Finally, given that for $\theta \in [-\pi, \pi]$

$$\sqrt{\frac{1+\cos(\theta)}{2}} = \cos\left(\frac{\theta}{2}\right)$$

and by considering the double angle trigonometric relation, $\sin(\theta) = 2\cos(\theta/2)\sin(\theta/2)$ Eq. (6.42) produces

$$\mathring{q}_\perp = \begin{pmatrix} \dfrac{\cos(\theta)+1}{2\sqrt{\frac{\cos(\theta)+1}{2}}} \\ \dfrac{\sin(\theta)}{2\sqrt{\frac{\cos(\theta)+1}{2}}}\boldsymbol{u} \end{pmatrix} = \begin{pmatrix} \cos\left(\frac{\theta}{2}\right) \\ \sin\left(\frac{\theta}{2}\right)\boldsymbol{u} \end{pmatrix}$$

The quaternion $\mathring{q}_\parallel$ represents a rotation about the line of ${}^{\mathcal{F}_1}\boldsymbol{a}$ that finally makes vectors in $\{\mathcal{F}_i\}$ to meet $\{\mathcal{F}_1\}$. The quaternion that performs this rotation can be found by following the procedure in Algorithm. 7 by substituting inputs ${}^{\mathcal{F}_1}\boldsymbol{a}$ and ${}^{\mathcal{F}_2}\boldsymbol{a}$ by $\boldsymbol{b}'$ and $\boldsymbol{b}''$ being

$$\boldsymbol{b}' = {}^{\mathcal{F}_1}\boldsymbol{b} \times {}^{\mathcal{F}_1}\boldsymbol{a} \tag{6.43}$$

and

$$\boldsymbol{b}'' = {}^{\mathcal{F}_i}\boldsymbol{b} \times {}^{\mathcal{F}_1}\boldsymbol{a} = \mathbf{L}(\mathring{q}_\perp){}^{\mathcal{F}_2}\boldsymbol{b} \times {}^{\mathcal{F}_1}\boldsymbol{a} \tag{6.44}$$

The initialisation process shown is reversible in the sense that the same exact result can be obtained by exchanging $\boldsymbol{a}$ and $\boldsymbol{b}$ but having different intermediate quaternions.

The initial orientation of the aircraft can be obtained by replacing the vectors ${}^{\mathcal{F}_1}\boldsymbol{a}$, ${}^{\mathcal{F}_1}\boldsymbol{b}$, ${}^{\mathcal{F}_1}\boldsymbol{a}$ and ${}^{\mathcal{F}_2}\boldsymbol{b}$ by ${}^w\boldsymbol{g}$, ${}^w\boldsymbol{H}$, ${}^b\boldsymbol{a}$ and ${}^b\boldsymbol{H}$, under force equilibrium (gravity compensated, i.e. steady in the ground). However, in practice, misalignment between accelerometers and magnetometers sensors as well as uncertainty in the components of ${}^w\boldsymbol{H}$ and in a more limited sense ${}^w\boldsymbol{g}$, make the presented procedure not fully reversible. When the relative disposition between vectors $\boldsymbol{a}$ and $\boldsymbol{b}$ is not the same for every frame, the described methodology, recreates the quaternion $\mathring{q}_0$ that aligns the vector $\boldsymbol{a}$ in both frames and minimize the angle between the representations of $\boldsymbol{b}$, i.e.,

$$\mathring{q}_0 = \arg\min_{\mathring{q}} \left({}^w\boldsymbol{H}^\top\mathbf{L}(\mathring{q}){}^b\boldsymbol{H}\right)^2$$
$$\text{s.t.}\,{}^w\boldsymbol{g}^\top - \mathbf{L}(\mathring{q}){}^b\boldsymbol{a} = 0$$

Moreover, once calculated $\mathring{q}_0$ this process allows to produce new estimations of the local gravity and magnetic field vectors as $\boldsymbol{g}^{w\prime} = \mathbf{L}(\mathring{q}_0){}^b\boldsymbol{a}$ and ${}^w\boldsymbol{B}' = \mathbf{L}(\mathring{q}_0)\left({}^b\boldsymbol{B}\right)$. Given that the new $\boldsymbol{g}^{w\prime}$, ${}^w\boldsymbol{B}'$ make sensor readings coherent with the model, its use replacing the nominal ones will diminish the effect of the miss-alignment and sensitivity calibration enhancing the estimation in the filtering process.

6.2.6 Filter execution flow

As has been exposed before, the initial continuous-discrete filter (continuous dynamics and discrete measurements) have been converted at a discrete discrete event-triggered filter after considering the IMU state and its incremental form. Fig. 6.2, shows the diagram flow that describes the implementation of the Filter 1, detailed in the previous section.
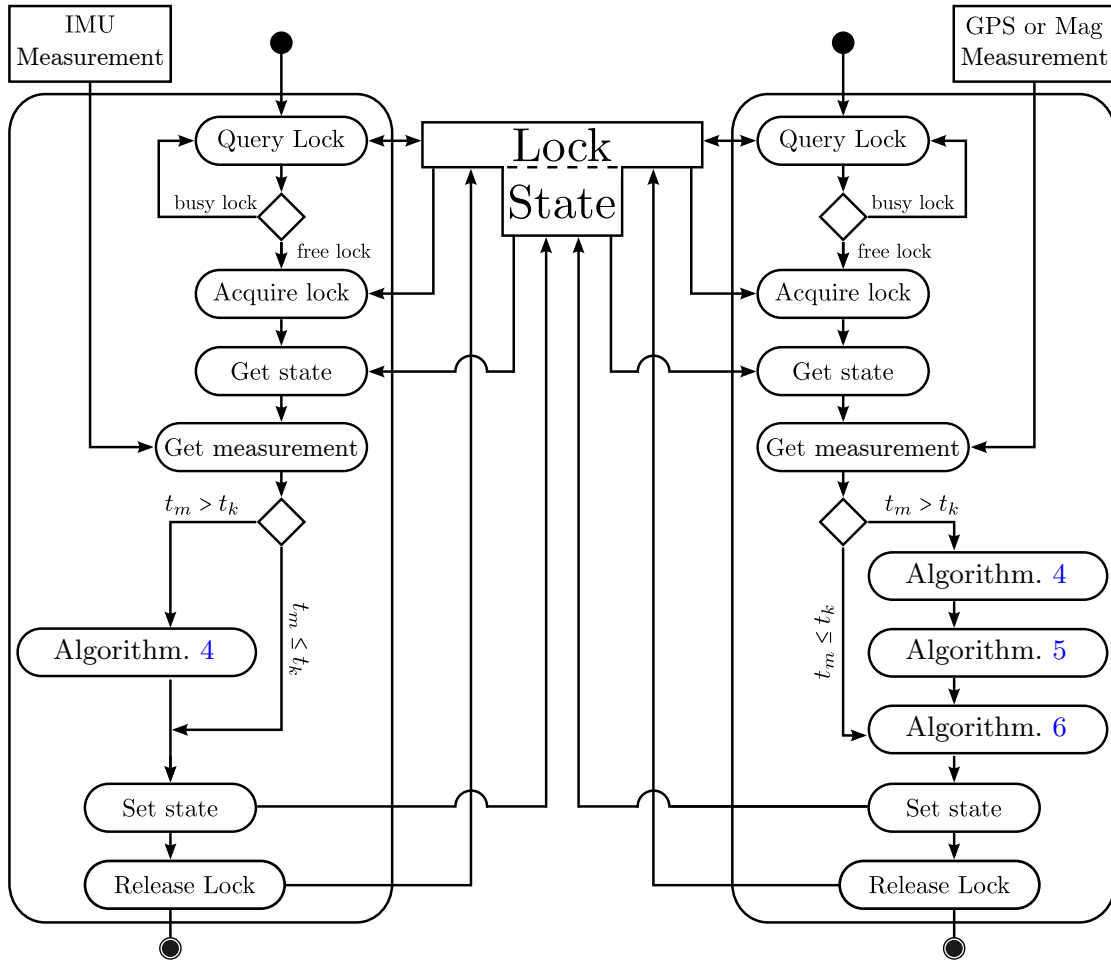

FIGURE 6.2: Flow diagram for the state filtering process of the Filter 1.

A lock has been added to guarantee single thread access to the state in the presence of multiple events occurring simultaneously in time. The event based filtering updates the time whenever a new measurement is available. Given the serial communication with the platform it is unlikely to have delayed measurements, so a simple discard strategy is applied over sensor outputs if the measurement corresponds to a time instant in the past. This strategy is also supported by the high rate associated to the sensor measurements.
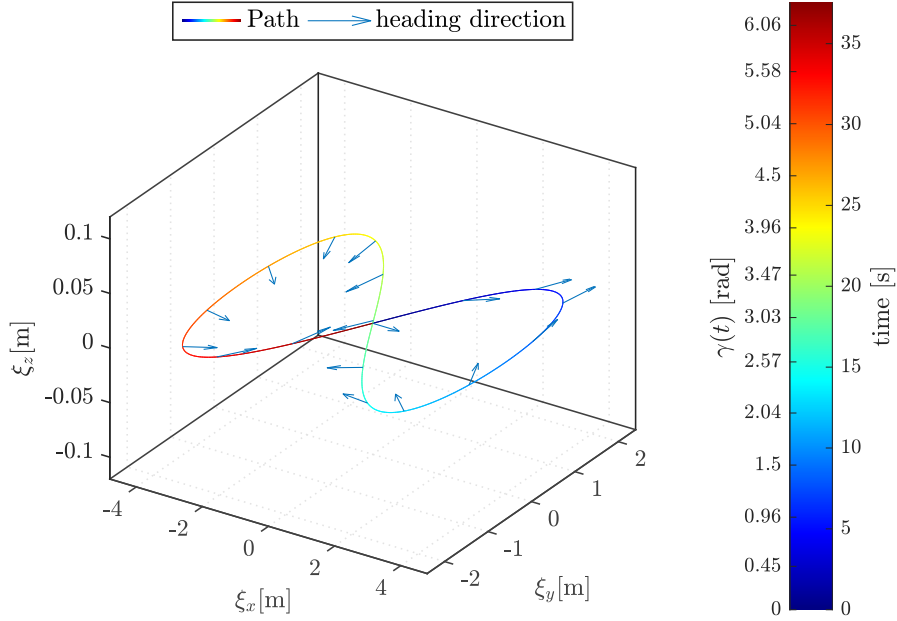
FIGURE 6.3: First loop path trajectory commanded to the aircraft

6.2.7   Results

In order to show the operation of the filters, the simulation framework shown in Fig. 5.1, have been considered again.   The controller is given by a PID for the attitude in cascade with a PD position controller with gravity compensation. The reference trajectory is an eight-shaped trajectory with constant height, constant path velocity and linearly increasing heading angle represented by the lemniscata equation

$$x(t) = a\sin(\gamma(t))$$
$$y(t) = a\cos(\gamma(t))\sin(\gamma(t))$$
$$z(t) = 0$$
$$\psi = \omega_p t$$
$$\dot{\lambda}(t) = \frac{v_p}{a\sqrt{2 + \cos^2(\gamma(t)) - 2\cos^2(\gamma(t))\sin^2(\gamma(t))}}$$

with $a = 4\,\mathrm{m}$ defining the path span, $v_p = 1\,\mathrm{m\,s^{-1}}$ the path velocity and $\omega_p = \frac{2\pi}{30}\,\mathrm{rad\,s^{-1}}$ the angular heading velocity.

The resulting path is shown in Eq. (6.3), and has been intentionally selected to avoid the constant appearance of singular inputs described in Section 5.6.

Initial conditions for the simulation have been set to guarantee null initial yaw angle and null initial position and velocity. The true north magnetic field direction vector has been chosen to be

$${}^w\boldsymbol{H} = (569.0, 6.5, 822.3)^\top \tag{6.45}$$

The calibrated sensor models (equal per axis gain and fixed bias corrected) presented in Section 4.2 have been used to reproduce asynchronous and noisy sensor outputs during the simulation. Initial value for the accelerometer and gyroscope bias have been set higher than the usual, to help visualize the filter bias convergence

$$\boldsymbol{b}_{a_0} = (0.19,\, 0.071,\, -0.29)^\top \quad \boldsymbol{b}_{\omega_0} = (-0.097,\, 0.077,\, 0.80)^\top$$

respectively.

The run of the four filters has been made after the initialization described in Section 6.2.5, and assuming the same sensor models than in simulation. The initial error covariance matrix have been chosen large enough to account for the uncertainty of the initial estimates. In particular, it have been chosen as

$$\mathbf{P}_0 = \text{blkdiag}\left(\mathbf{P}_{\boldsymbol{\xi}_0}, \mathbf{P}_{\boldsymbol{v}_0}, \mathbf{P}_{\boldsymbol{\alpha}_0}, \mathbf{P}_{\boldsymbol{b}_{a0}}, \mathbf{P}_{\boldsymbol{b}_{\omega0}}\right)$$

being

$$\mathbf{P}_{\boldsymbol{\xi}_0} = \text{diag}\,(1,\, 1,\, 1) \tag{6.46a}$$

$$\mathbf{P}_{\boldsymbol{v}_0} = \text{diag}\,(0.3,\, 0.3,\, 0.3) \tag{6.46b}$$

$$\mathbf{P}_{\boldsymbol{b}_{a_0}} = \text{diag}\,(0.05,\, 0.05,\, 0.05) \tag{6.46c}$$

$$\mathbf{P}_{\boldsymbol{b}_{\omega_0}} = \text{diag}\,(0.05,\, 0.05,\, 0.05) \tag{6.46d}$$

$$\mathbf{P}_{\boldsymbol{\alpha}_0} = 10^{-4} \begin{pmatrix} 5.1781 & 0.0407 & 7.5490 \\ 0.0407 & 5.1791 & 0.1684 \\ 7.5490 & 0.1684 & 13.7766 \end{pmatrix} \tag{6.46e}$$

The first four matrix error covariances shown have been selected to ensure that with a 95% of probability the initial position, velocity, accelerometer bias and gyroscope bias errors will be contained in a ball of $3\,\text{m}$, $1.65\,\text{ms}^{-1}$, $0.22\,\text{ms}^{-2}$ and $0.22\,\text{rad s}^{-1}$ of radius respectively. The initial covariance of the attitude error has been derived by running the initialization algorithm over a synthetic test of 1000 random vector realizations for the magnetic field and the gravity assuming an error covariance in $^w\boldsymbol{H}$ as defined by Eq. (4.26) and the error distribution for $\boldsymbol{a} = {}^w\boldsymbol{g}$ given by the initial covariance error in Eq. (6.46c). The resulting quaternions have been transformed to twice the Gibbs vector as in Eq. (5.15) and matrix $\mathbf{P}_{\boldsymbol{\alpha}_0}$, Eq. (6.46e), represents its covariance. The covariance ensures that with a 95% of probability the initial attitude will be determined within an error inferior to $13\,\text{deg}$ about any direction.

Figs. (6.4-6.12) show the output of the Filter1 compared with the true state. Filters outputs are generated from simulated data and model sensors and true values are obtained from the simulated state. The plots that contain magnitudes directly related with the incremental state by addition or subtraction such that the estimated position (Fig. 6.4), velocity (Fig. 6.5), the accelerometer bias (Fig. 6.8) and the gyroscope bias (Fig. 6.9), incorporate information of the confidence intervals calculated from the diagonal elements of covariance matrix. Finally, Fig. 6.4, Fig. 6.10, Fig. 6.11 and Fig. 6.12 also show the value of the simulated sensors. The filter convergence to

the true values is attained within the first two seconds of simulation for the position, attitude and gyroscope bias and convergence of the velocity and accelerometer bias is achieved in the next three seconds.
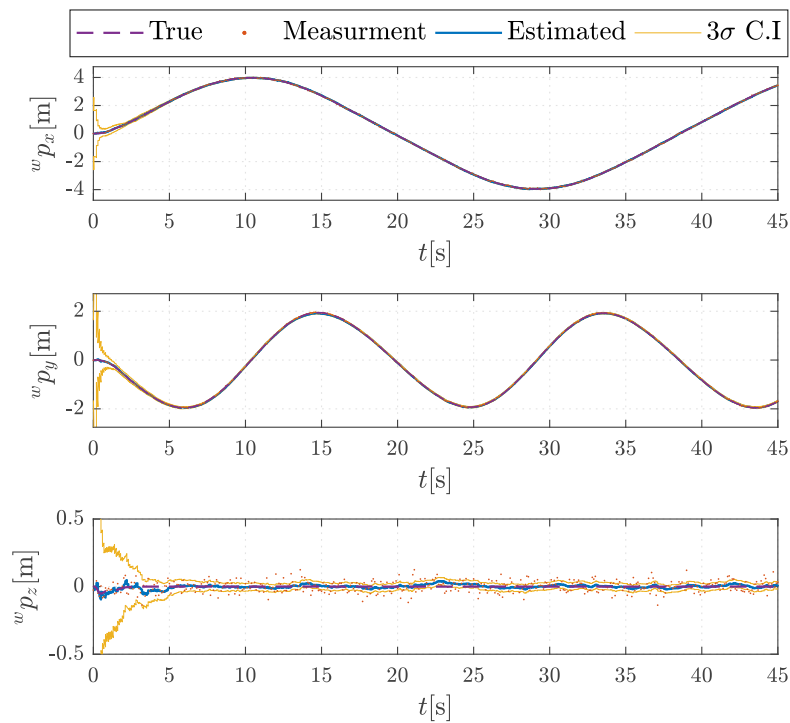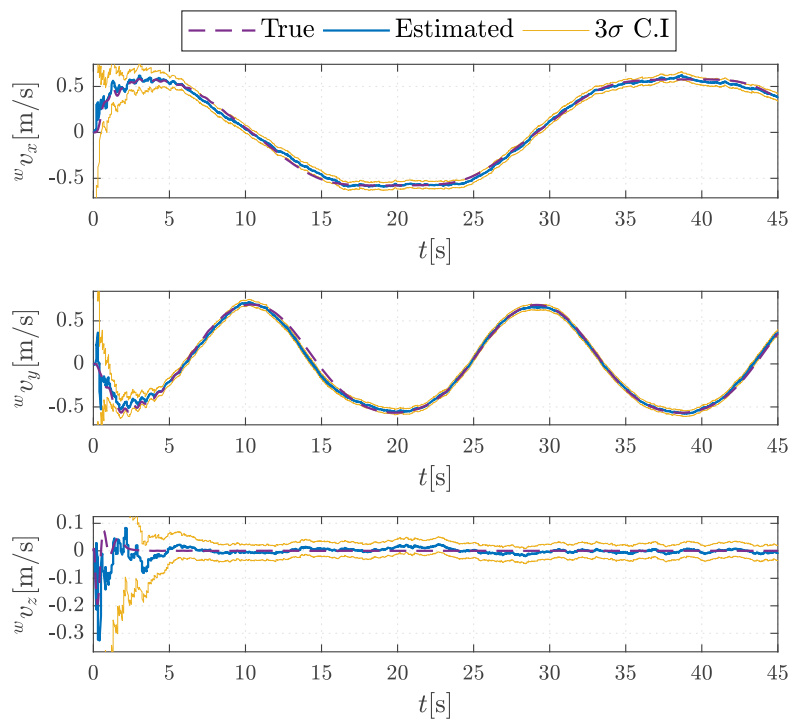

FIGURE 6.4: Aircraft position.
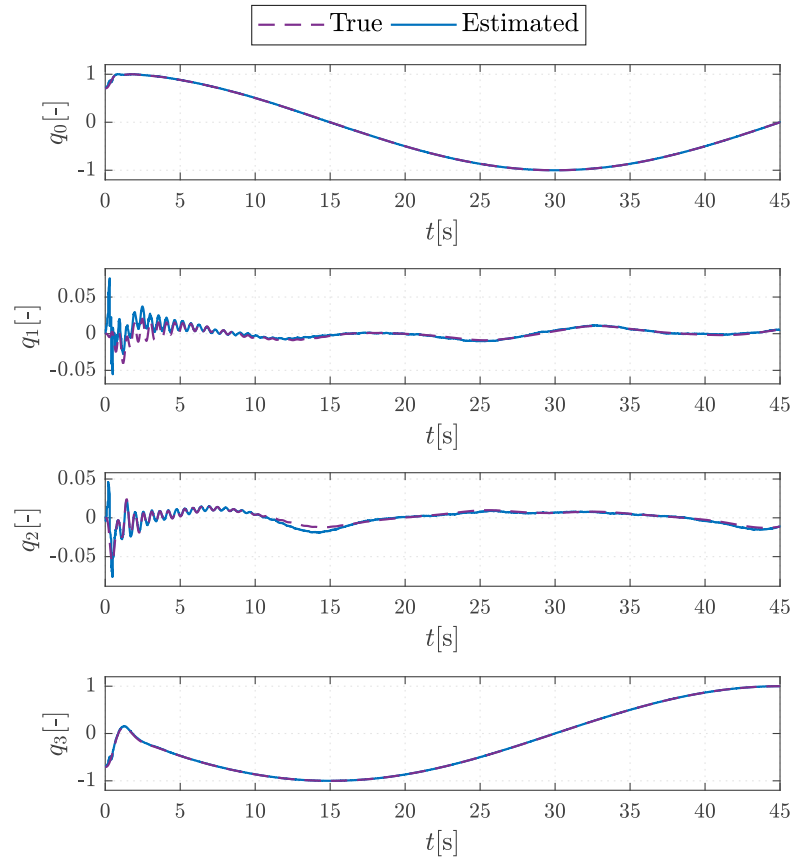

FIGURE 6.5: Aircraft velocity.
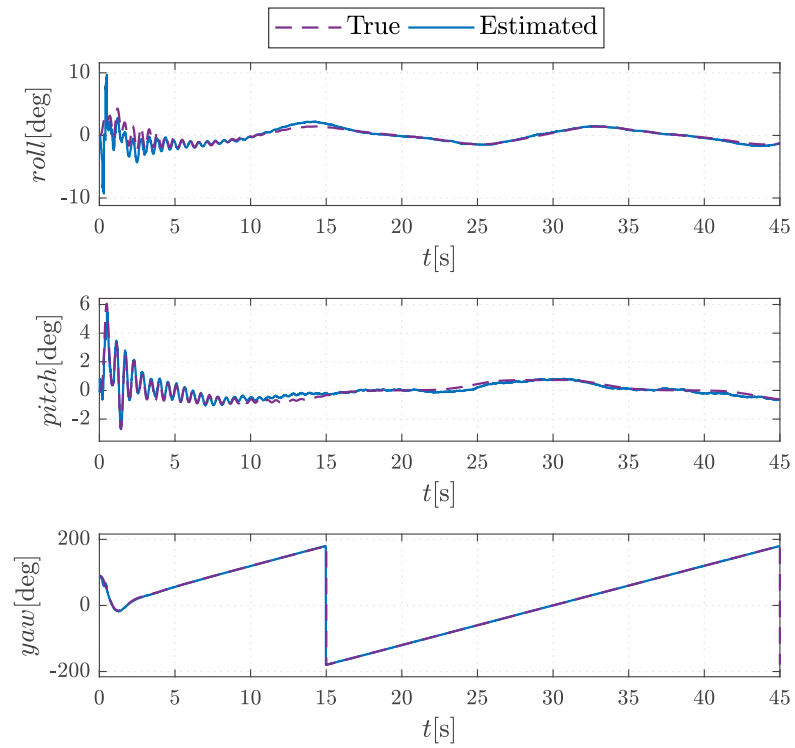
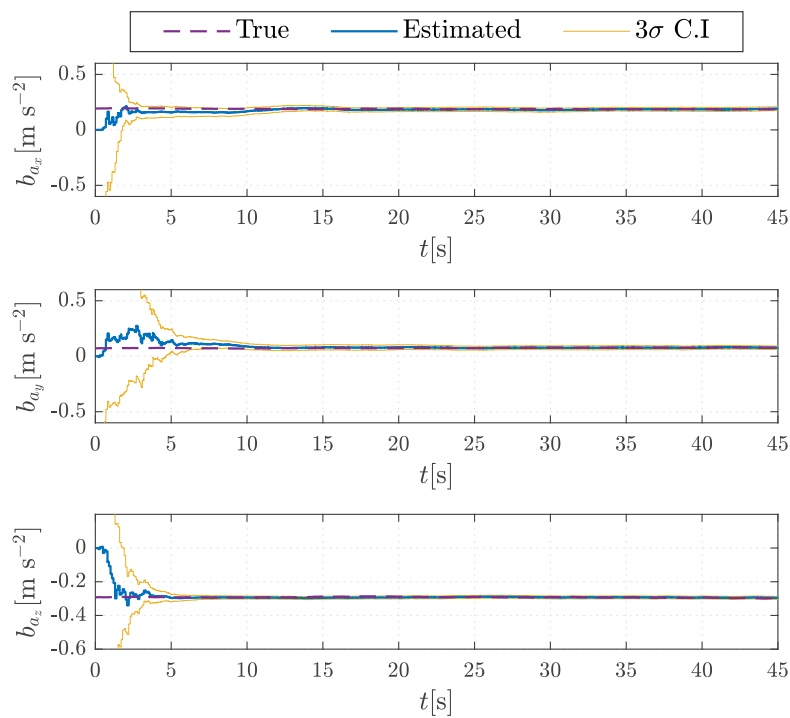FIGURE 6.6: Aircraft attitude quaternion.

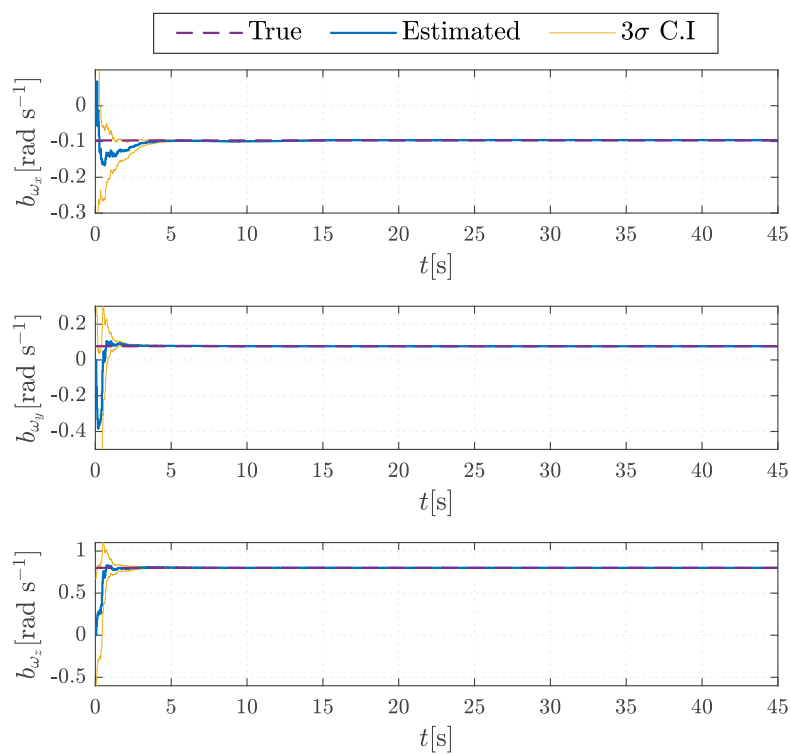FIGURE 6.7: Aircraft Euler angles.

FIGURE 6.8: Aircraft accelerometer bias.
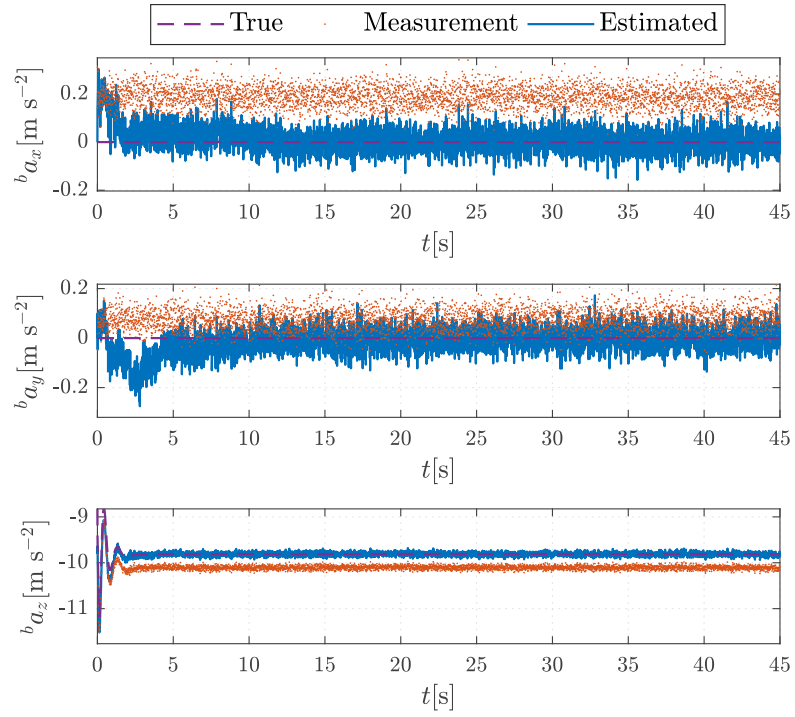

FIGURE 6.9: Aircraft gyroscope bias.

FIGURE 6.10: Aircraft external forces acceleration.
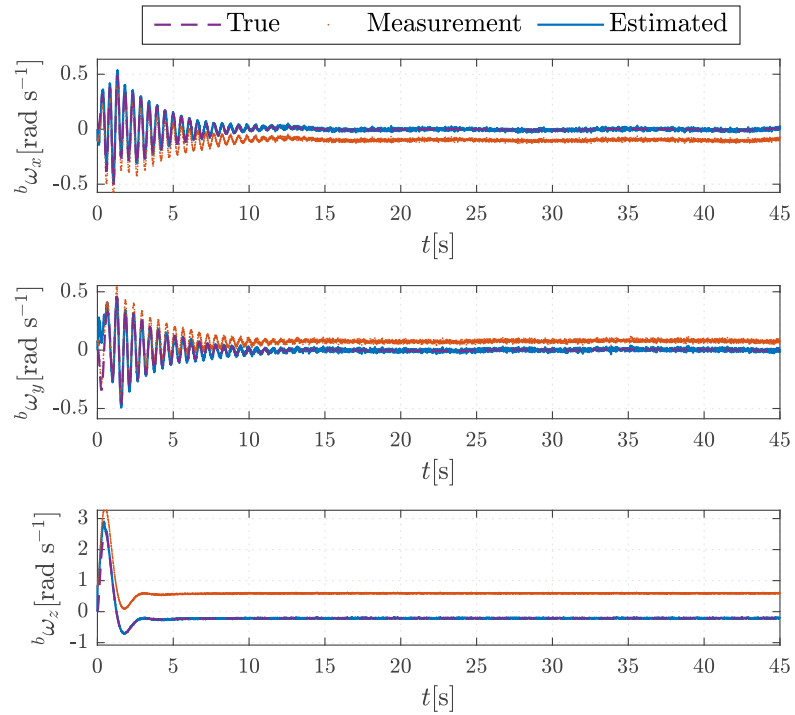
FIGURE 6.11: Aircraft angular velocity.
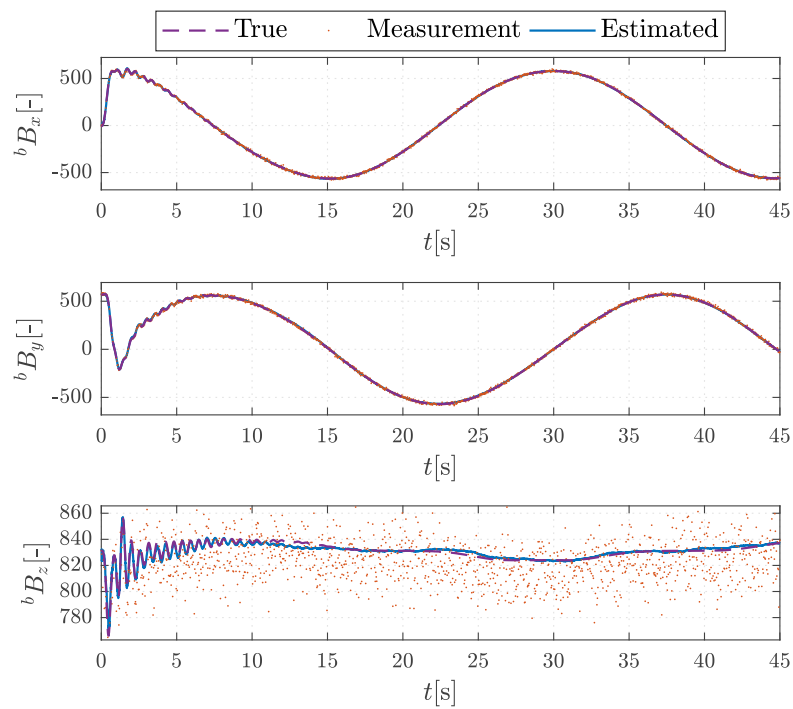
FIGURE 6.12: In-body magnetic field direction.

Results of the four filter implementations are given in the error plots Figs.(6.13-6.20). Duplicate velocity plots are shown in order to consider the different velocity choices between filters. The same has been done to show the attitude error, however in this case it was just a choice since the same error could be used from the known quaternion at the output of the four filters. As it can be seen, with independence of the filter, the errors and error covariances shown are very similar, demonstrating the equivalence of the four filters. Table 6.2 show the accumulated estimation error calculated as

$$E_j = \sqrt{\frac{1}{T} \int_0^T \boldsymbol{e}_j^\top \boldsymbol{e}_j \, \mathrm{d}t}$$

with j representing either position, velocity, attitude, accelerometer bias or gyroscope bias, $\boldsymbol{e}$ representing the estimation error of that variable and T the simulation time.
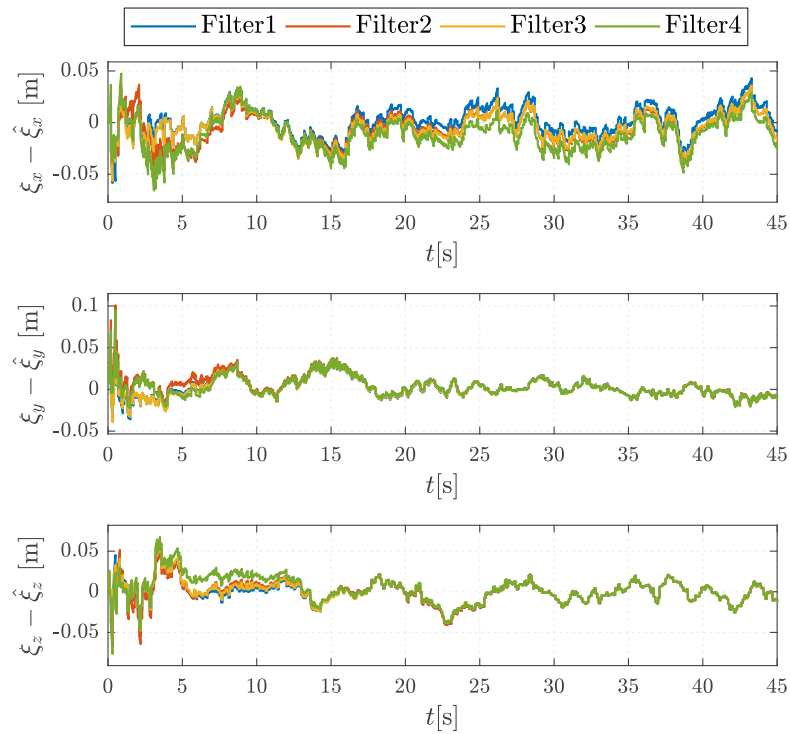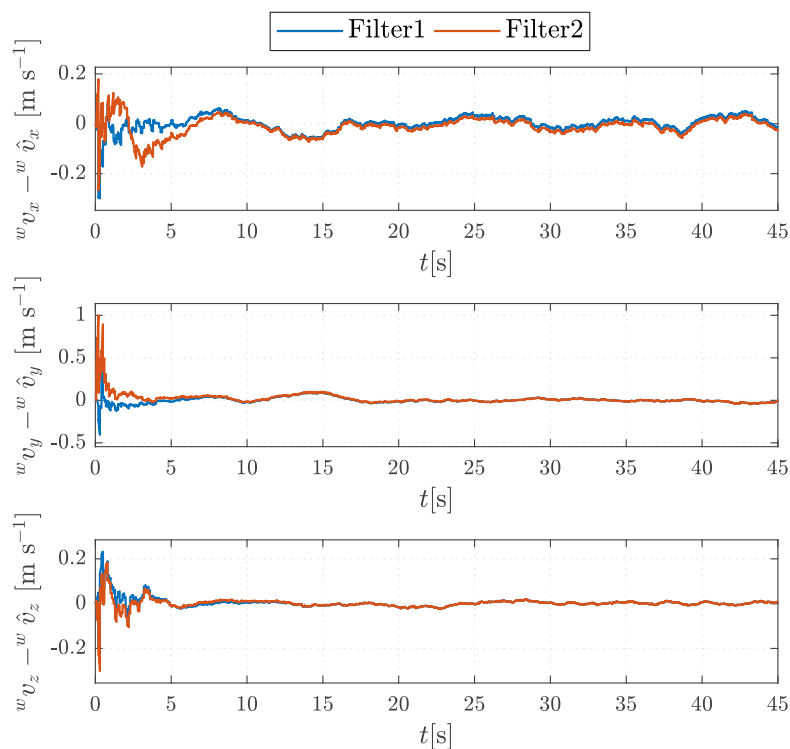

FIGURE 6.13: Aircraft position estimation error.

FIGURE 6.14: Aircraft velocity estimation error for filters 1 and 2.
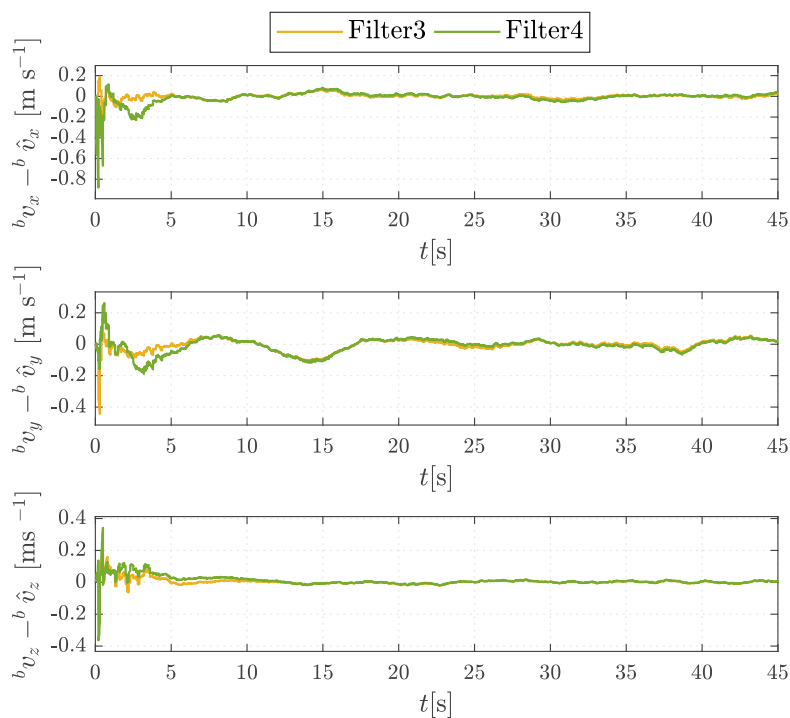

FIGURE 6.15: Aircraft velocity estimation error for filters 3 and 4.
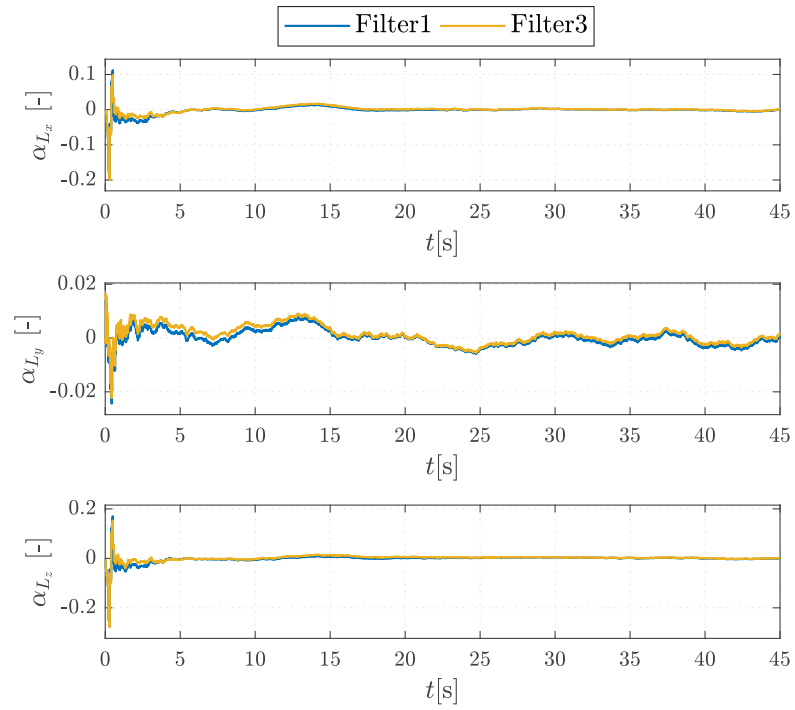
FIGURE 6.16: Aircraft attitude estimation error for filters 1 and 3.
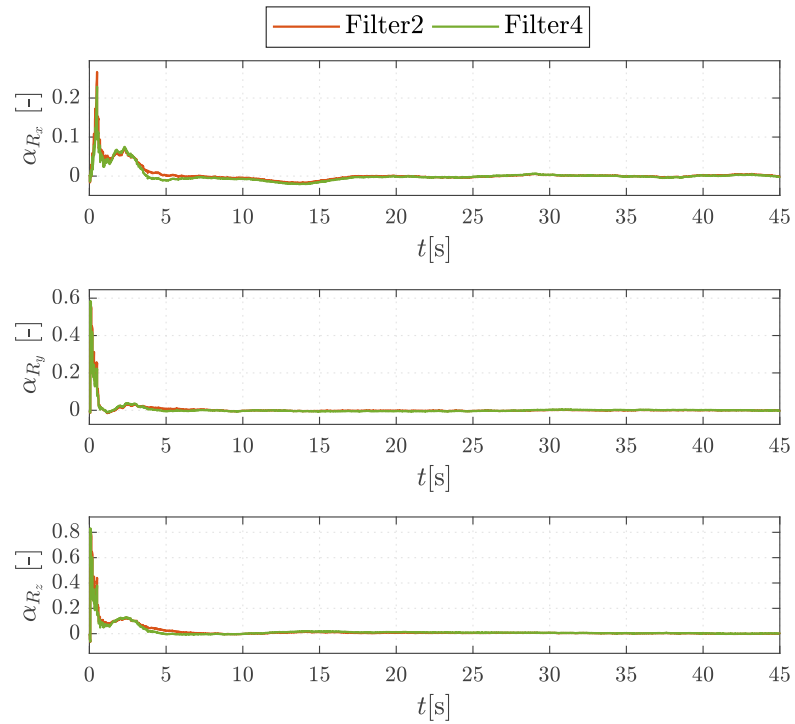

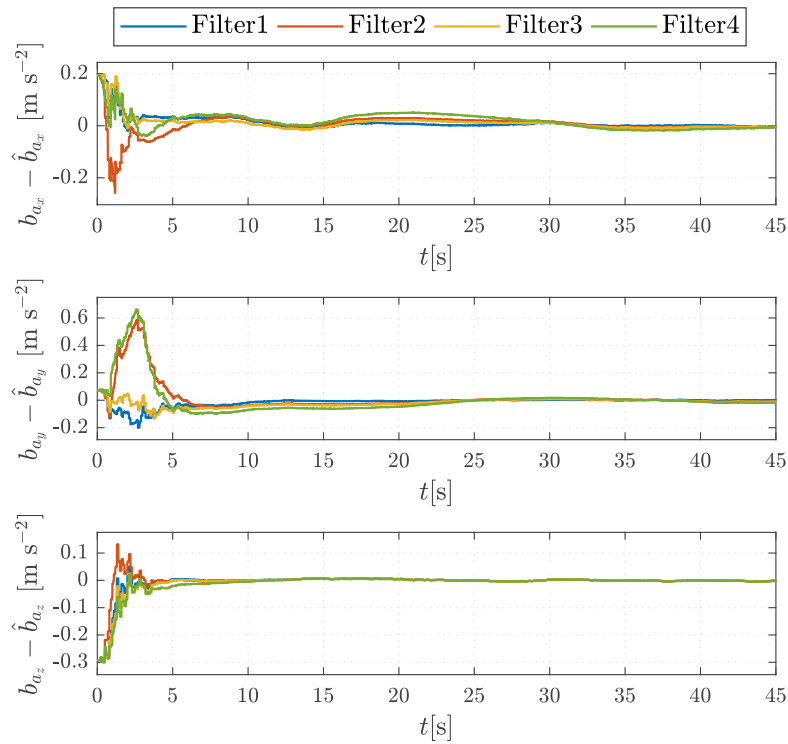FIGURE 6.17: Aircraft attitude estimation error for filters 2 and 4.

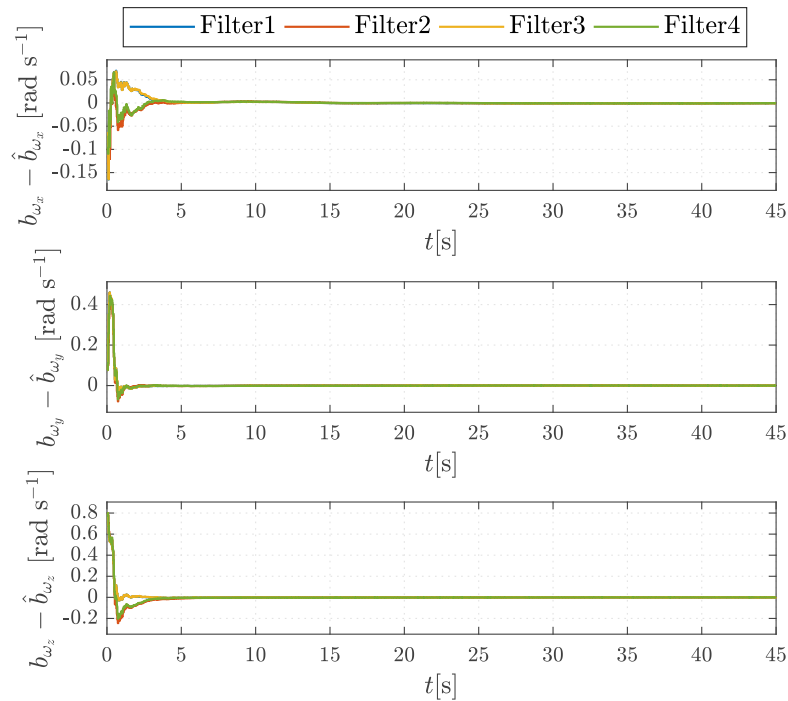FIGURE 6.18: Accelerometer's bias estimation error.

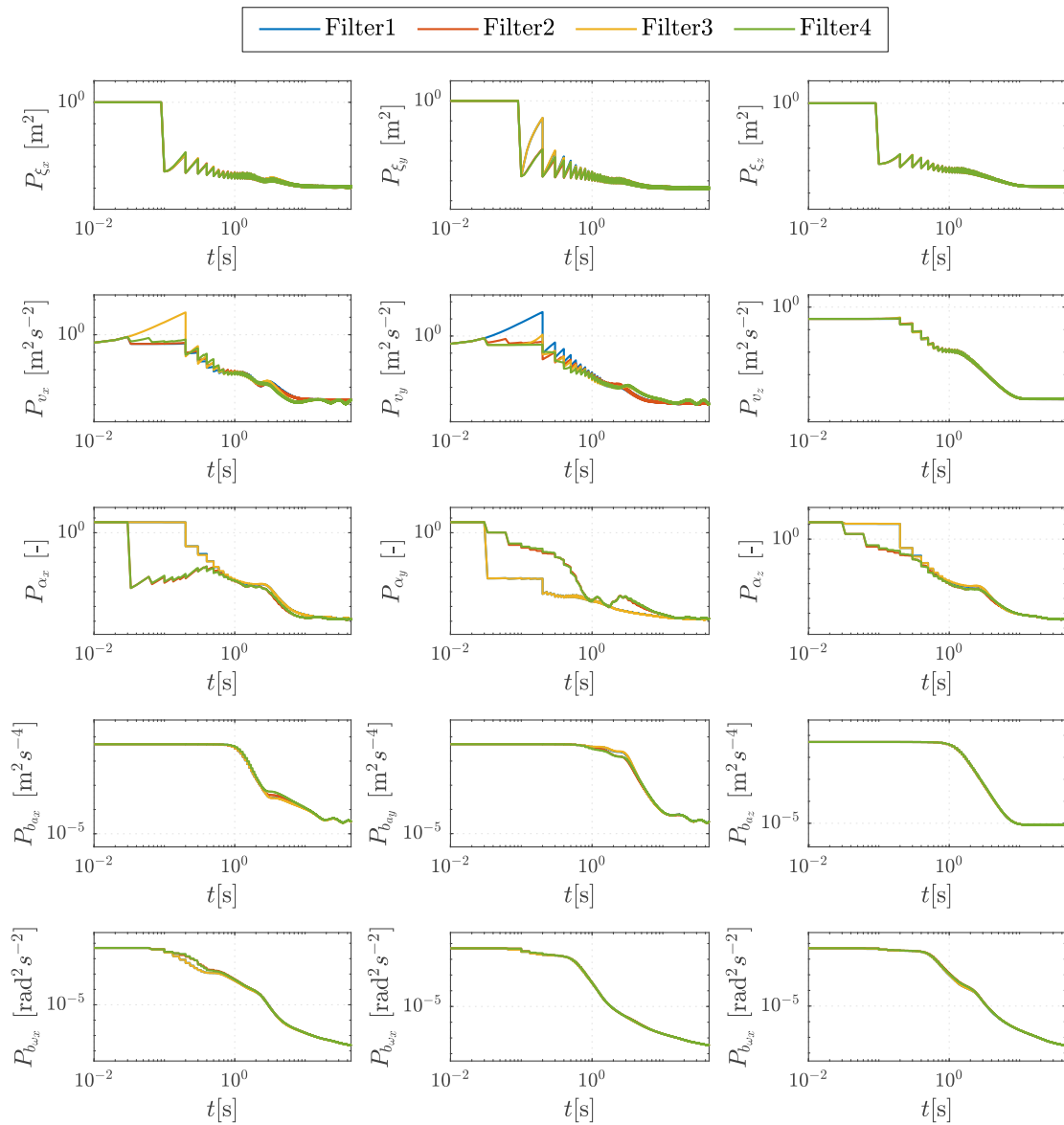FIGURE 6.19: Gyroscope's bias estimation error.

FIGURE 6.20: Log-log plots of the diagonal entries of the estimation error covariance matrix.

	Filter 1	Filter 2	Filter 3	Filter 4	
$E_{\boldsymbol{\xi}} \cdot 10^{-2}$ [m]	2.2950	2.4512	2.2997	2.7899	Best score
$E_{\boldsymbol{v}} \cdot 10^{-2}$ [m s^{-1}]	5.5595	8.1739	5.2793	8.4373	
$E_{\boldsymbol{\alpha}} \cdot 10^{-2}$ [-]	2.1756	6.6454	2.0598	5.9785	
$E_{\boldsymbol{b}_a} \cdot 10^{-2}$ [m s^{-2}]	6.3480	11.8204	6.3342	13.8326	
$E_{\boldsymbol{b}_\omega} \cdot 10^{-2}$ [rad s^{-1}]	7.0337	7.3714	6.9390	7.2826	Worst score

TABLE 6.2: Accumulated estimation error for the 4 filter implementations

6.3   Dealing with observability issues

Biases are slow varying, and this is the reason why many people takes them as constant. In Chap. (5) it has been shown that taking biases as constant eliminates the most conflicting indistinguishable region that appears around the hover configuration. This is not a bad idea when good estimates of the initial values of biases are available and the system running time is short enough not to have the real value of the bias deviated too much from its assumed constant estimation. However, if any of the previous conditions is not fulfilled, the system state estimates can diverge from the true values. An engineering approach to the problem is to inflate the covariance of the state process noise to account for the uncertainty associated to the considered bias value in the reduced states. This solution comes with the drawback of having to tune the covariance by trial-and-error [96].

A way of dealing with this problem is by using the Schmidt Kalman Filter (SKF, also known as Consider Kalman Filter CKF) [78, 96]. This filter allows a separation of the full state between traditional states and "considered" states, i.e., those states whose value is going to be considered as if they were known parameters. With such a partition in mind, an optimization problem can be solved to find the optimal filter gain that minimizes the a posteriori error covariance under the constraint of not updating the considered states. This procedure leads to a modified gain, which is suboptimal in the sense that does not minimize the full state error covariance. In contrast, the new filter does not modify the considered states values nor the associated covariances in the correction step, but it takes into account the effect of the uncertainty of the considered states in the remaining state. This is useful because, at this point the considered states can be dropped from the filter, and just the short version of the states and its associated equations need to be taken into account. The Schmidt Kalman filter has also demonstrated to be effective in the case that the considered states have low observability as for example when considering camera offsets or gravity coefficients [96, 98].

Observability results of Chap. (5) demonstrated that flying in some configurations cause observability degradation in the sense that the state can not be fully recovered from input-output information. By studying the kernel of the observability matrix it has been demonstrated that the system has one degree of freedom represented by the extra parameter in the indistinguishable region in Eq. (5.58) that relates the system attitude and the accelerometer biases. Note that, this degree of freedom could be eliminated by having a sensor measuring one of the states involved in the indistinguishable region or, what is shown to be equivalent [84], by imposing an additional constraint involving one of those states. By default, the Schmidt Kalmand Filter (SKF), will

implement the optimal solution of the problem under the constraint of constant value on the considered states eliminating the extra degree of freedom. However, the observability analysis suggests that there is no need to impose all the bias values to be constant. On the contrary, by fixing one of them the state turns out to be recoverable from input-output data.

Estimation examples have been provided in this chapter and at the end of Chap. (5) depicting estimation performance under favourable and unfavourable flight conditions. In particular, results in Chap. (5) are appealing since they demonstrate that the traditional EKF, tends to provide incorrect estimations when the system is inside an indistinguishable region. In what follows, we present a filter based in the Schmidt Kalman Filter, that exploits information from the symmetries and indistinguishable regions derived in Chap. (5) to restrict the evolution of the solution in some undesirable directions.

6.3.1   The Schmidt Kalman filter update

Let the values of $\boldsymbol{x}^-$ and $\mathbf{P}^-$ be known at the time instant when a new noise corrupted measurement related with the state by the linear (or linearized) measurement model

$$\boldsymbol{y} = \mathbf{C}\boldsymbol{x} + \boldsymbol{\eta}$$

is available. Then a linear update can be produced by

$$\hat{\boldsymbol{x}}^+ = \hat{\boldsymbol{x}}^- + \mathbf{K}\left(\boldsymbol{y} - \mathbf{C}\hat{\boldsymbol{x}}^-\right)$$

Denoting by $\boldsymbol{e}^- = \boldsymbol{x} - \hat{\boldsymbol{x}}^-$ the a priori error, and using the measurement model, the a posteriori error can be calculated as

$$\boldsymbol{e}^+ = \boldsymbol{x} - \hat{\boldsymbol{x}}^+ = (\mathbf{I} - \mathbf{K}\mathbf{C})\,\boldsymbol{e}^- + \mathbf{K}\boldsymbol{\eta}$$

And the a posteriori error covariance as

$$\mathbf{P}^+ = E\left((\mathbf{x} - \mathbf{x}^+)(\mathbf{x} - \mathbf{x}^+)^\top\right) = \mathbf{P}^- - \mathbf{K}\mathbf{C}\mathbf{P}^- - \mathbf{P} - \mathbf{C}^\top\mathbf{K}^\top + \mathbf{K}\mathbf{W}^{-1}\mathbf{K}^\top \tag{6.47}$$

being

$$\mathbf{W} = \left(\mathbf{C}\mathbf{P}^-\mathbf{C}^\top + \mathbf{R}\right)$$

Note that at this point no assumptions have been made for the gain. Thus Eq. (6.47) is valid for any choice of $\mathbf{K}$. The Kalman filter selects the gain $\mathbf{K}$ that minimizes the trace of the a posteriori error covariance matrix. i.e.

$$\mathbf{K}_{opt} = \underset{\mathbf{K}}{\operatorname{argmin}} \quad \operatorname{trace}(\mathbf{P}^+)$$

which leads to the the optimal gain

$$\mathbf{K}_{opt} = \mathbf{P}^-\mathbf{C}^\top\mathbf{W}^{-1} \tag{6.48}$$

and updates for the state and error covariance in Algorithm. 5.

Let now the state partition be,

$$\boldsymbol{x}^\top = (\boldsymbol{x}_s, \boldsymbol{x}_p)$$

where $\boldsymbol{x}_s$ represents the states that are going to be updated and $\boldsymbol{x}_p$ represents the states that are not going to be updated, but whose uncertainty is expected to impact the estimation of $\boldsymbol{x}_s$.

This partition extends to the system measurement matrix as

$$\mathbf{C} = \begin{pmatrix} \mathbf{C}_s & \mathbf{C}_p \end{pmatrix}$$

and the Kalman gain matrix

$$\mathbf{K} = \begin{pmatrix} \mathbf{K}_s \\ \mathbf{K}_p \end{pmatrix}$$

and allows the formulation of the a posteriori error covariance matrix as

$$\mathbf{P}^+ = \begin{pmatrix} \mathbf{P}_{ss}^+ & \mathbf{P}_{sp}^+ \\ \mathbf{P}_{ps}^+ & \mathbf{P}_{pp}^+ \end{pmatrix} \tag{6.49}$$

being

$$\mathbf{P}_{ss}^+ = \mathbf{P}_{ss}^- - \mathbf{K}_s \mathbf{C} \begin{pmatrix} \mathbf{P}_{ss}^- \\ \mathbf{P}_{ps}^- \end{pmatrix} - \begin{pmatrix} \mathbf{P}_{ss}^- \\ \mathbf{P}_{ps}^- \end{pmatrix}^\top \mathbf{C}^\top \mathbf{K}_s^\top + \mathbf{K}_s \mathbf{W} \mathbf{K}_s^\top$$

$$\mathbf{P}_{sp}^+ = \mathbf{P}_{sp}^- - \mathbf{K}_s \mathbf{C} \begin{pmatrix} \mathbf{P}_{sp}^- \\ \mathbf{P}_{pp}^- \end{pmatrix} - \begin{pmatrix} \mathbf{P}_{ss}^- \\ \mathbf{P}_{ps}^- \end{pmatrix}^\top \mathbf{C}^\top \mathbf{K}_p^\top + \mathbf{K}_s \mathbf{W} \mathbf{K}_p^\top$$

$$\mathbf{P}_{ps}^+ = \left(\mathbf{P}_{ps}^+ \right)^\top$$

$$\mathbf{P}_{pp}^+ = \mathbf{P}_{pp}^- - \mathbf{K}_p \mathbf{C} \begin{pmatrix} \mathbf{P}_{sp}^- \\ \mathbf{P}_{pp}^- \end{pmatrix} - \begin{pmatrix} \mathbf{P}_{sp}^- \\ \mathbf{P}_{pp}^- \end{pmatrix}^\top \mathbf{C}^\top \mathbf{K}_p^\top + \mathbf{K}_p \mathbf{W} \mathbf{K}_p^\top$$

Under this partition, the optimization problem to compute the gain is

$$\left(\mathbf{K}_{s_{opt}}, \mathbf{K}_{p_{opt}} \right) = \underset{\mathbf{K}_s, \mathbf{K}_p}{\operatorname{argmin}} \quad \operatorname{trace}(\mathbf{P}^+) = \operatorname{trace}(\mathbf{P}_{ss}^+) + \operatorname{trace}\left(\mathbf{P}_{pp}^+\right) \tag{6.50}$$

Since $\mathbf{K}_s$ is only present in the $\mathbf{P}_{ss}^+$ equation and it is not contained in $\mathbf{P}_{pp}^+$ and the same is true for the case of $\mathbf{K}_p$ and $\mathbf{P}_{pp}^+$ and $\mathbf{P}_{ss}^+$ respectively, the optimization problem could be split in two

$$\mathbf{K}_{s_{opt}} = \underset{\mathbf{K}_s}{\operatorname{argmin}} \quad \operatorname{trace}(\mathbf{P}_{ss}^+) = \begin{pmatrix} \mathbf{P}_{ss}^- & \mathbf{P}_{sp}^- \end{pmatrix} \mathbf{C}^\top \mathbf{W}^{-1} \tag{6.51}$$

$$\mathbf{K}_{p_{opt}} = \underset{\mathbf{K}_p}{\operatorname{argmin}} \quad \operatorname{trace}\left(\mathbf{P}_{pp}^+\right) = \begin{pmatrix} \mathbf{P}_{ps}^- & \mathbf{P}_{pp}^- \end{pmatrix} \mathbf{C}^\top \mathbf{W}^{-1} \tag{6.52}$$

which represents the same solution of Eq. (6.48) with the difference of having two separated parts.

By substituting the optimal gain $\mathbf{K}_s = \mathbf{K}_{s_{opt}}$ but letting $\mathbf{K}_p$ undefined in Eq. (6.49), the off-diagonal elements of the error covariance matrix can be written without considering $\mathbf{K}_p$ as

$$
\begin{aligned}
\mathbf{P}_{sp}^+ = & \ \mathbf{P}_{sp}^- - \mathbf{K}_{s_{opt}} \mathbf{C} \begin{pmatrix} \mathbf{P}_{sp}^- \\ \mathbf{P}_{pp}^- \end{pmatrix} - \begin{pmatrix} \mathbf{P}_{ss}^- \\ \mathbf{P}_{ps}^- \end{pmatrix}^\top \mathbf{C}^\top \mathbf{K}_p^\top + \begin{pmatrix} \mathbf{P}_{ss}^- & \mathbf{P}_{sp}^- \end{pmatrix} \mathbf{C}^\top \mathbf{K}_p^\top = \\
& \ \mathbf{P}_{sp}^- - \mathbf{K}_{s_{opt}} \mathbf{C} \begin{pmatrix} \mathbf{P}_{sp}^- \\ \mathbf{P}_{pp}^- \end{pmatrix}
\end{aligned}
\tag{6.53}
$$

and $\mathbf{P}_{ps}^+ = \left(\mathbf{P}_{ps}^+\right)^\top$. This leads to the error covariance matrix

$$
\mathbf{P}^+ = \begin{pmatrix} \mathbf{P}_{ss}^- - \mathbf{K}_{s_{opt}} \mathbf{W} \mathbf{K}_{s_{opt}}^\top & \mathbf{P}_{sp}^- - \mathbf{K}_{s_{opt}} \mathbf{C} \begin{pmatrix} \mathbf{P}_{sp}^- \\ \mathbf{P}_{pp}^- \end{pmatrix} \\ \mathbf{P}_{ps}^- - \begin{pmatrix} \mathbf{P}_{sp}^- \\ \mathbf{P}_{pp}^- \end{pmatrix}^\top \mathbf{C}^\top \mathbf{K}_{s_{opt}}^\top & \mathbf{P}_{pp}^- - \mathbf{K}_p \mathbf{C} \begin{pmatrix} \mathbf{P}_{sp}^- \\ \mathbf{P}_{pp}^- \end{pmatrix} - \begin{pmatrix} \mathbf{P}_{sp}^- \\ \mathbf{P}_{pp}^- \end{pmatrix}^\top \mathbf{C}^\top \mathbf{K}_p^\top + \mathbf{K}_p \mathbf{W} \mathbf{K}_p^\top \end{pmatrix}
$$

In the case of also imposing $\mathbf{K}_s = \mathbf{K}_{s_{opt}}$, the error covariance matrix in Algorithm. 5 is recovered. It can be written, in partitioned form, as

$$
\mathbf{P}_{opt}^+ = \begin{pmatrix} \mathbf{P}_{ss}^- - \mathbf{K}_{s_{opt}} \mathbf{W} \mathbf{K}_{s_{opt}}^\top & \mathbf{P}_{sp}^- - \mathbf{K}_{s_{opt}} \mathbf{C} \begin{pmatrix} \mathbf{P}_{sp}^- \\ \mathbf{P}_{pp}^- \end{pmatrix} \\ \mathbf{P}_{ps}^- - \begin{pmatrix} \mathbf{P}_{sp}^- \\ \mathbf{P}_{pp}^- \end{pmatrix}^\top \mathbf{C}^\top \mathbf{K}_{s_{opt}}^\top & \mathbf{P}_{pp}^- - \mathbf{K}_{p_{opt}} \mathbf{W} \mathbf{K}_{p_{opt}}^\top \end{pmatrix}
$$

In the case of the Schmidt Kalman filter, the value of $\mathbf{K}_p$ is forced to be null if the constraint of not updating the state $\boldsymbol{x}_p$ for any measurement $\boldsymbol{y}$ and with independence of the previous state estimate $\hat{\boldsymbol{x}}^-$ is considered. Since Eq. (6.51) does not depend on $\mathbf{K}_p$, the solution of Eq. (6.48) leads to a suboptimal gain

$$
\mathbf{K}_{SKF} = \begin{pmatrix} \mathbf{K}_{s_{SKF}} \\ \mathbf{0} \end{pmatrix} = \begin{pmatrix} \mathbf{K}_{s_{opt}} \\ \mathbf{0} \end{pmatrix} = \begin{pmatrix} \mathbf{P}_{ss}^- \mathbf{C}_s^\top + \mathbf{P}_{sp}^- \mathbf{C}_p^\top \\ \mathbf{0} \end{pmatrix} \mathbf{W}^{-1}
\tag{6.54}
$$

By substituting the result in Eq. (6.54) into Eq. (6.49), the a posteriori covariance turns up to be

$$
\mathbf{P}_{SKF}^+ = \begin{pmatrix} \mathbf{P}_{ss}^- - \mathbf{K}_{s_{SKF}} \mathbf{W} \mathbf{K}_{s_{SKF}}^\top & \mathbf{P}_{sp}^- - \mathbf{K}_{s_{SKF}} \mathbf{C} \begin{pmatrix} \mathbf{P}_{sp}^- \\ \mathbf{P}_{pp}^- \end{pmatrix} \\ \mathbf{P}_{ps}^- - \begin{pmatrix} \mathbf{P}_{sp}^- \\ \mathbf{P}_{pp}^- \end{pmatrix}^\top \mathbf{C}^\top \mathbf{K}_{s_{SKF}}^\top & \mathbf{P}_{pp}^- \end{pmatrix}
\tag{6.55}
$$

The choice of the filter gain $\mathbf{K}$ in Eq. (6.54) guarantees not updating the states $\boldsymbol{x}_p$ while at the same time considers the effect of their associated uncertainty in the $\boldsymbol{x}_s$ states through the cross covariance terms. In the traditional SKF, the state of the system can be at this point reduced by directly not considering the $\boldsymbol{x}_p$ states anymore.

Initially, the SKF was intended to deal with the problems associated with slow varying parameters with observability issues, which is indeed our problem if we consider $\boldsymbol{x}_s$ to represent the navigation state, i.e., $\boldsymbol{x}_s = \left(\boldsymbol{\xi}^\top, \boldsymbol{v}^\top, \boldsymbol{\alpha}^\top\right)^\top$ and $\boldsymbol{x}_p = \left(\boldsymbol{b}_a^\top, \boldsymbol{b}_\omega^\top\right)^\top$. Note however, that not updating the values of the bias terms while using the SKF tends to increase the uncertainty associated to the estimation of the remaining states. Thus, ideally we would like to use the SKF update at the time that some of the states are not observable while using the full EKF in the case that full observability of the system's states is guaranteed. This means that in practice the state cannot be reduced and that a smooth transition between different observers has to be provided. Noting that the SKF a posteriori covariance matrix in Eq. (6.54) can be produced from the optimal Kalman Filter covariance error by

$$\mathbf{P}_{SKF}^+ = \mathbf{P}_{opt}^+ + \begin{pmatrix} \mathbf{0} & \mathbf{0} \\ \mathbf{0} & +\mathbf{K}_{p_{opt}}\mathbf{W}\mathbf{K}_{p_{opt}}^\top \end{pmatrix} \tag{6.56}$$

and that the SKF update for $\boldsymbol{x}_p$ can just be forced to take the values of the a priori estimation in the update as

$$\hat{\boldsymbol{x}}_{SKF}^+ = \begin{pmatrix} \hat{\boldsymbol{x}}_{s_{opt}}^+ \\ \hat{\boldsymbol{x}}^- \end{pmatrix}$$

the SKF can always be obtained by the KF outputs, thus guaranteeing an easy transition between both estimators when needed.

6.3.2   Update strategy

As commented in the previous sections, the observability results in Chap. (5) reveal a non-empty kernel for the observability codistribution matrix spanned by a unique symmetry in many different flight configurations. Among them, the most conflicting one is related with flying in hover mode.

Traditionally, the SKF was used on systems with low observable states by holding the value of all the conflicting states. However, the indistinguishable region in Eq. (5.58), reproduced here for convenience,

$$\boldsymbol{x}_I(\tau, \boldsymbol{x}_0) = \left(\boldsymbol{\xi}_0^\top, \boldsymbol{v}_0^\top, \mathring{q}_I^\top, \boldsymbol{b}_{a_I}^\top, \boldsymbol{b}_{\omega_0}^\top\right)^\top \tag{6.57}$$

being

$$\mathring{q}_I = \mathring{q}_0\mathring{q}_\tau = \mathring{q}_0 \begin{pmatrix} \cos(\tau) \\ \sin(\tau)\dfrac{\boldsymbol{H}}{\|\boldsymbol{H}\|} \end{pmatrix} \tag{6.58}$$

and

$$\boldsymbol{b}_{a_I} = \boldsymbol{a}_m + \mathbf{L}^\top(\mathring{q}_\tau)\mathbf{L}^\top(\mathring{q}_0)\left(\boldsymbol{g}\right) \tag{6.59}$$

has only one degree of freedom, given by τ in Eq. (6.57), that represents the magnitude of a drift rotation of the platform about the magnetic field direction.

Note that taking

$$\boldsymbol{b}_{a_0} = \mathbf{L}^\top(\mathring{q}_0)\left(\boldsymbol{g}\right)$$
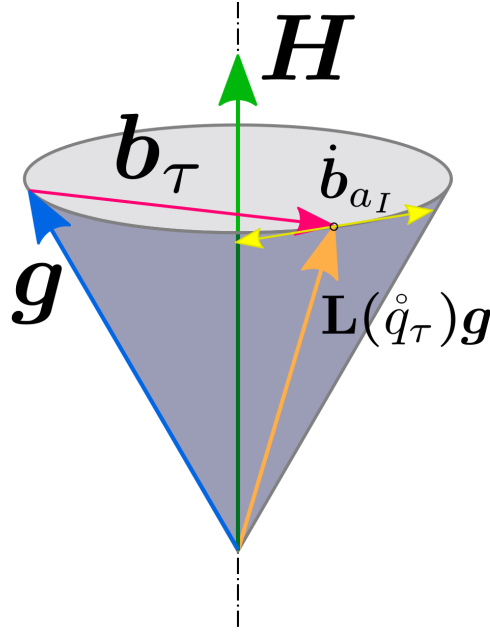
FIGURE 6.21: Bias and attitude drifts effects in hover related singular input conditions

which corresponds to the nominal value of the bias in a hover condition $\dot{v} = 0$ and denoting $^b\boldsymbol{g} = \mathbf{L}^\top(\mathring{q}_0)\,^w\boldsymbol{g}$, the bias drift $\boldsymbol{b}_\tau = \boldsymbol{b}_{a_I} - \boldsymbol{b}_{a_0}$ can be written as

$$\boldsymbol{b}_\tau = \left(\mathbf{R}^\top(\mathring{q}_\tau) - \mathbf{I}_3\right){}^b\boldsymbol{g}$$

The drift of the bias can be interpreted as an incremental bias, $\boldsymbol{b}_\tau$, that lies in the base of a cone whose axis has the same direction as the magnetic field and whose generatrix is represented by the gravity vector[1] as depicted in Fig. 6.21 The instantaneous bias drift is represented by the symmetry in Eq. (5.56) associated to the accelerometer bias, i.e,

$$\frac{\partial \boldsymbol{b}_{a_I}}{\partial \boldsymbol{\tau}} = \beta \left[\mathbf{R}^\top \boldsymbol{H}\right]_\times (\boldsymbol{a}_m - \boldsymbol{b}_a)$$

where β represents the angular velocity related to the rotated angle $\boldsymbol{\tau}$. Given that in hover,

$$\boldsymbol{a}_m - \boldsymbol{b}_a = \mathbf{R}^\top \boldsymbol{g}$$

this drift is, by construction, perpendicular to the magnetic field direction and perpendicular to the gravity vector rotated by the orientation drift

$$\frac{\partial \boldsymbol{b}_{a_I}}{\partial \boldsymbol{\tau}} \parallel \mathbf{R}^\top(\mathring{q}_I)\,(\boldsymbol{H} \times \boldsymbol{g}) \tag{6.60}$$

With the aim of preventing errors in the EKF estimation when visiting the described indistinguishable region, we present an SKF correction step based on only fixing one component of

---

[1]Equations are formulated with vectors in the body frame, however from a geometrical point of view the relative position of those vectors does not change under a frame transformation. Thus, the results can be generalised for vectors $\boldsymbol{g}$ and $\boldsymbol{H}$ in any frame.

the accelerometer bias vector. The suggested approach forces the vector component of the accelerometer bias, related with the maximum absolute value component of the vector resulting from Eq. (6.60), to remain constant during the correction step. In that way, if $\boldsymbol{b}_{a_\tau}$ is forced to be take a constant value in one of the equations of Eq. (6.59), this equation will allow to determine the value of $\boldsymbol{\tau}$ removing the extra degree of freedom and avoiding the estimation drift inside the indistinguishable region.

A similar result could arise if instead of the accelerometer bias, one of the components of the attitude is fixed. However, note that the time scale of the biases dynamics is usually slower than the attitude one. Therefore, fixing components of the biases is usually safer than fixing any attitude component.

This SKF estimation strategy will modify the EKF update described in Algorithm. 5. Algorithm. 8 provides a pseudocode of this process.

Algorithm 8: SKF correction

Data: $\mathbf{P}_k^-$, $\boldsymbol{\omega}_m$, $\boldsymbol{a}_m$, $\boldsymbol{z}_k$, measurement type
Result: $\delta\boldsymbol{x}_k^+$, $\mathbf{P}_k^+$

1. Evaluate the cross product in Eq. (6.60) and search for the vector entry with minimum absolute value i.

2. Store the a priori accelerometer bias in the vector position i and its associated covariance $b_{a_{hold}} = b_{a_i}^-$, $P_{a_{hold}} = P_{a_{i,i}}^-$

3. Evaluate the measurement function and Jacobian in Eq. (6.29) or Eq. (6.30) depending of the measurement type to obtain $\hat{\boldsymbol{z}}$ and $\mathbf{C}$.

4. Calculate the suboptimal gain $\mathbf{K} = \mathbf{P}_k^- \mathbf{C}^\top (\mathbf{C}\mathbf{P}_k^- \mathbf{C}^\top + \mathbf{R})^{-1}$

5. Update the covariance of the estimation error $\mathbf{P}_k^+ = (\mathbf{I} - \mathbf{KC})\mathbf{P}_k^-$

6. Update the state $\delta\boldsymbol{x}_k^+ = \mathbf{K}(\boldsymbol{z}_k - \hat{\boldsymbol{z}})$

7. Set the stored values in the a posteriori state and covariance estimations $b_{a_i}^+ = b_{a_{hold}}$ and $P_{a_{i,i}}^+ = P_{a_{hold}}$

This alternative correction strategy can be activated anytime that the system configuration coincides with a hover state. Although this is a simple condition to visualize, noise in the sensors and possible biases make this hover test dificult in practice. Given that the SKF is a suboptimal filter, here it is proposed to maintain the SKF correction stage activated during any flight condition. In this way, when the aircraft visits the indistinguishable region, the SKF will protect the estimations from drifting whereas in non singular input conditions, it will behave suboptimally. Notice that under conditions $\boldsymbol{\omega} \neq \alpha\mathbf{L}^\top\boldsymbol{H}$, the state is by definition recoverable and given that the aircraft is rotating, $\mathbf{L}^\top(\mathring{q}_0)\boldsymbol{g}$ will change forcing an alternation in the component of the bias to fix.
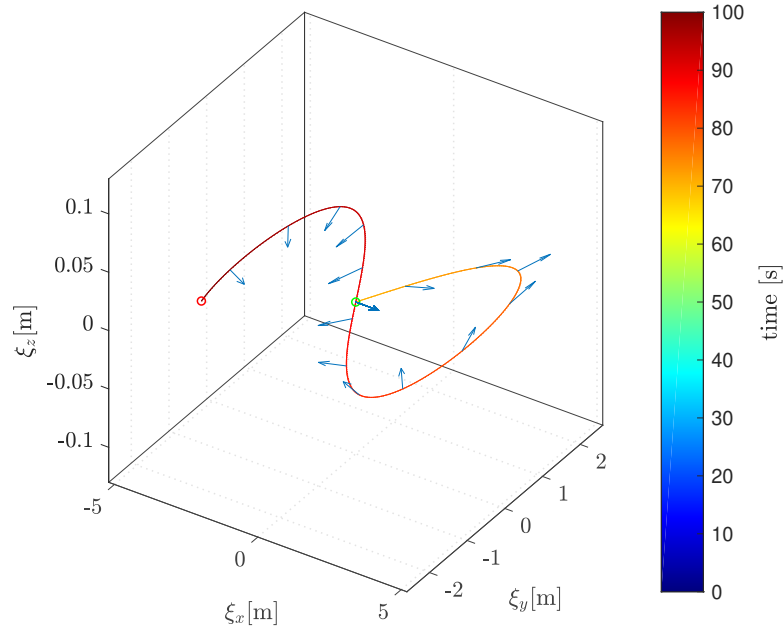
FIGURE 6.22: Uncalibrated scenario path. Hover until $t = 70\,\text{s}$ followed by an 8-shaped trajectory until $t = 100\,\text{s}$

6.3.3   Results

In order to demonstrate the benefits that the presented SKF strategy provides, we have compared filtering results generated by the EKF and SKF estimators in two simulation scenarios whose structure is represented by Fig. 5.1. Both simulation scenarios share the controller parameters, the mass properties, the magnetic and gravity directions, the sensors sampling rate and the GPS and magnetometer parameters presented in Chap. (4). However, they differ in the parameters defining accelerometers and gyroscope sensors covariances. The first scenario uses an IMU with intentionally higher sensor covariance, while the second scenario uses the sensor calibrated parameters in Chap. (4). For this reason we will refer to the first scenario as uncalibrated scenario whereas the second scenario will be called calibrated scenario.

Both scenarios share a similar commanded trajectory, which will be composed by a hover flight during an initial time window followed by a segment of the eight shaped path shown in Fig. 6.3. Both trajectories share the geometry but differ in the time spent in hover and performing the path segment with motion. The trajectory of the uncalibrated scenario can be seen in Fig. 6.22.

Both filters rely on the Filter 1 dynamics shown in Table 6.1 and its implementation discussed in Section 6.2. As a remainder, both sensors differ in the update step, the EKF implements the update in Algorithm. 5 while the SKF implements the slightly modified version described in Algorithm. 8. The execution of the filters share the same initialization procedure of Section 6.2.5 with $\boldsymbol{g} = {}^{w}\boldsymbol{g} = (0, 0, 9.81)^{\top}$, $\boldsymbol{H}$ in Eq. (6.45) and the initial value of the error covariance in Eq. (6.46).

Uncalibrated scenario

In order to analyse the performance of the SKF when the full state of the system is not recoverable from input-output data, this scenario considers 70 s of the trajectory in hover and 30 s performing the 8-shaped trajectory. In addition, this scenario is characterized by having values of the IMU error covariance of

$$\mathbf{Q}_a = 4 \cdot 10^{-3}\mathbf{I}_3 \qquad\qquad \mathbf{Q}_{ba} = 3.8 \cdot 10^{-2}\mathbf{I}_3$$
$$\mathbf{Q}_\omega = 1.1 \cdot 10^{-3}\mathbf{I}_3 \qquad\qquad \mathbf{Q}_{b\omega} = 2 \cdot 10^{-3}\mathbf{I}_3$$

and initial values for the bias in simulation

$$\boldsymbol{b}_{a_0} = (-0.61,\, -0.06,\, 0.04)^\top \quad \boldsymbol{b}_{\omega_0} = (0.063,\, 0.0518,\, -0.010)^\top$$

respectively.

Figs. (6.23-6.34) show the estimation results of both filters. As expected, during hover, both filters approximate correctly the position, the velocity and the gyroscope bias and have problems recovering some components of the state related with the attitude and the accelerometer bias. By calculating the cross product in Eq. (6.60) assuming null attitude drift

$$\mathbf{R}(\mathring{q}_I)^\top \left(\boldsymbol{H} \times \boldsymbol{g}\right) = \boldsymbol{H} \times \boldsymbol{g} = (63.7,\, -5576.2,\, 0)^\top$$

it can be seen that the bias drift is affecting mostly the second component of the estimated accelerometer bias, b_{a_y}. It can be appreciated in Fig. 6.31 where inconsistent results are obtained near $t = 60$ s because the estimate falls outside the confidence interval. The SKF approach, fixes automatically b_{a_y} during the hover condition as can be seen in Fig. 6.32. By enforcing the constant value of the estimation through the update, since in the propagation biases are not modified, the estimation takes a constant value until the eight-shaped trajectory starts. The covariance grows continuously as a result of the successive propagation steps and its value is not modified in the correction step.

By comparing Fig. 6.31 with Fig. 6.32, it can be observed that the SKF provides improved estimations of the remaining bias states. Similar effects can be interpreted by looking at the attitude, either by using the quaternions in Fig. 6.27 and Fig. 6.28 or the Euler angles in Fig. 6.29 and Fig. 6.30, the estimation of the orientation is also improved when using the SKF.

When the 8-shaped trajectory starts, both systems converge to the true values. However, it can be appreciated in Fig. 6.25, that the gross error accumulated by the EKF during the hover manoeuvre affects the initial transient estimation of the velocity providing more error than the SKF. The effects of alternating the fixed component of the bias during the 8-shaped trajectory are visible in the alternated periods of covariance increasing and decreasing that affects components b_{a_x} and b_{a_y} of the SKF.

Despite being theoretically worse during the guaranteed estimation periods, the SKF behaves well and no special difference is observed when compared with the EKF results.
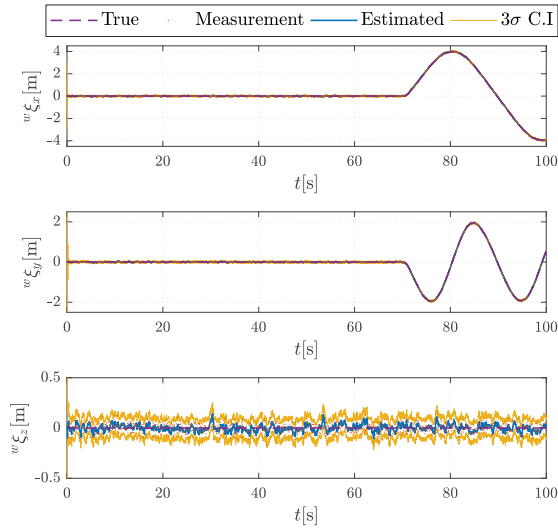
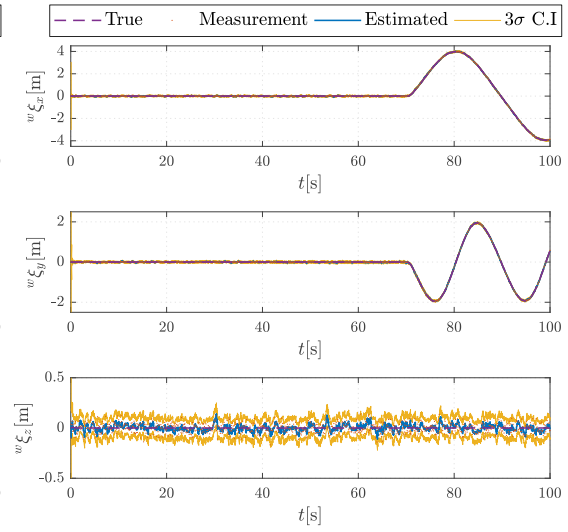FIGURE 6.23: EKF position estimation in the uncalibrated scenario

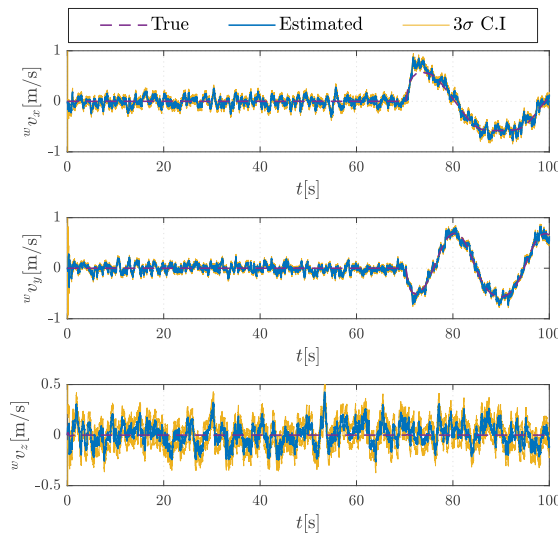FIGURE 6.24: SKF position estimation in the uncalibrated scenario

FIGURE 6.25: EKF velocity estimation in the uncalibrated scenario
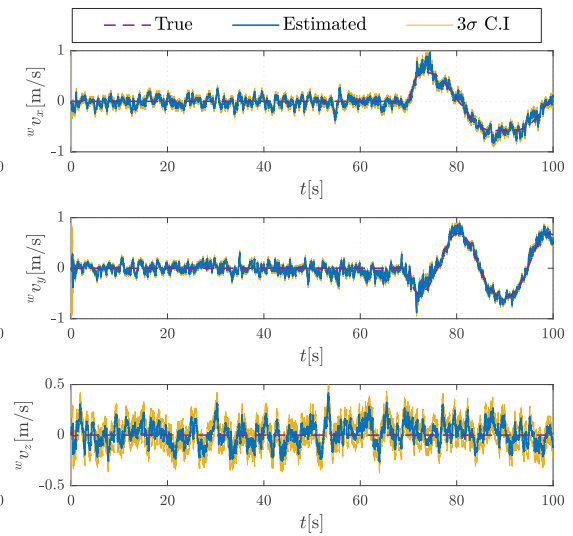
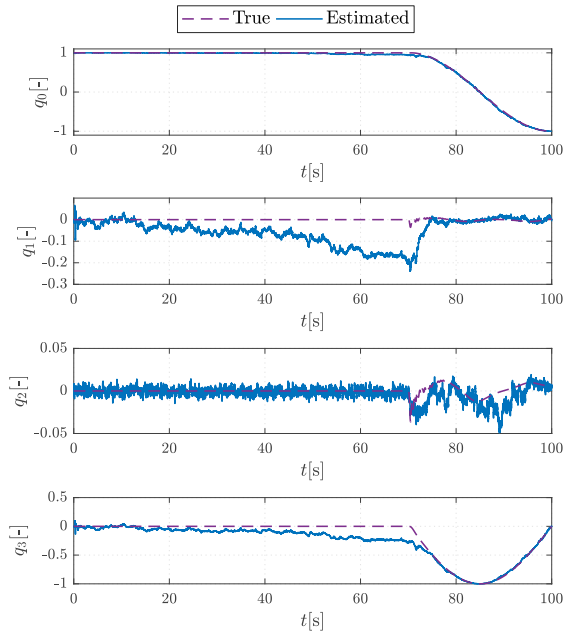FIGURE 6.26: SKF velocity estimation in the uncalibrated scenario

FIGURE 6.27: EKF quaternion estimation
in the uncalibrated scenario

FIGURE 6.28: SKF quaternion estimation
in the uncalibrated scenario

FIGURE 6.29: EKF Euler angles estima-
tion in the uncalibrated scenario

FIGURE 6.30: SKF Euler angles estima-
tion in the uncalibrated scenario
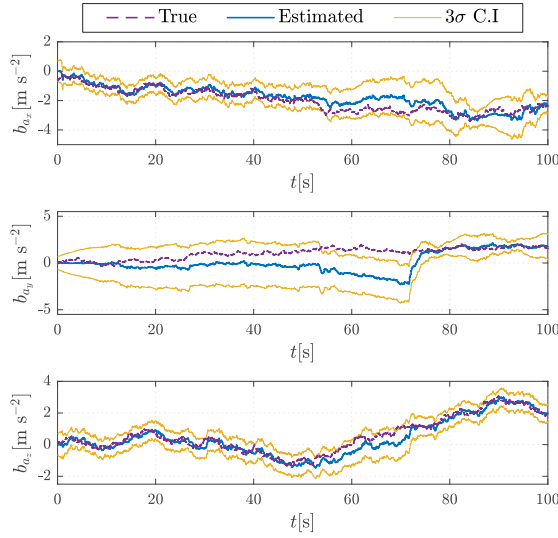
FIGURE 6.31: EKF accelerometer bias estimation in the uncalibrated scenario
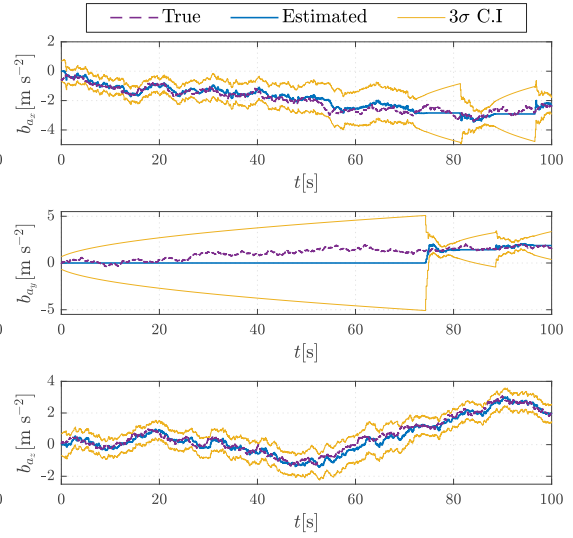
FIGURE 6.32: SKF accelerometer bias estimation in the uncalibrated scenario
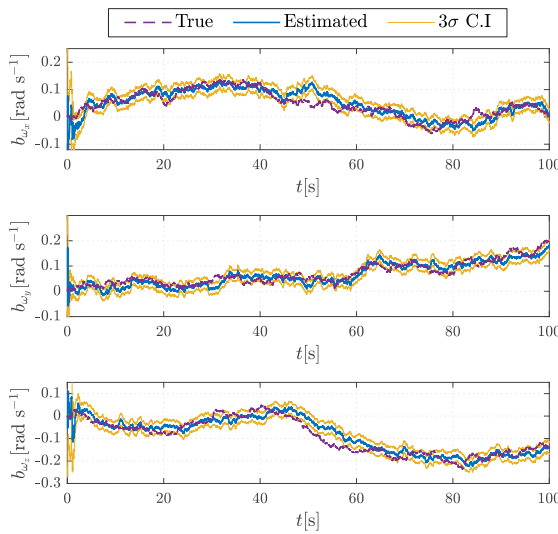
FIGURE 6.33: EKF gyroscope bias estimation in the uncalibrated scenario

FIGURE 6.34: SKF gyroscope bias estimation in the uncalibrated scenario

Calibrated scenario

In this simulation, IMU sensors take its calibrated values presented in Chap. (4). Compared with the previous scenario, these values are smaller and as a consequence lower variance on the sensor biases and their covariances will be expected. The simulation time in hover has been reduced to 50 s and the 8-shaped incremented accordingly. Initial simulation biases have been set to

$$\boldsymbol{b}_{a_0} = (0.19,\, 0.071,\, -0.294)^\top \quad \boldsymbol{b}_{\omega_0} = (-0.097,\, 0.0767,\, 0.802)^\top$$

respectively.

Estimation results are presented in Figs. 6.35-6.46. Again, positions, velocities and gyroscope biases are estimated by both filters with a very similar result. In contrast, it can be seen that the SKF outperforms the EKF solution related to the accelerometer bias and attitude. Specifically, the EKF estimation of b_{a_y} moves away from the true value diminishing at the same time the covariance and affecting the attitude estimation. In the same situation the SKF holds constant the component of b_{a_y}, while accumulates uncertainty on its covariance. The effect of this accumulation is present in the plot. However it is not appreciated because of the low values found in the sensor calibration phase.
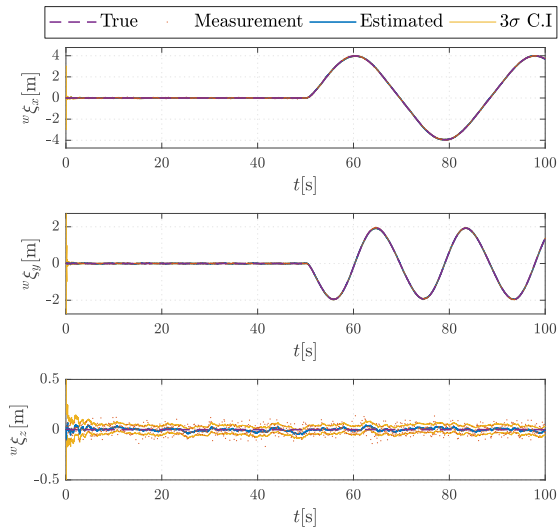
FIGURE 6.35: EKF position estimation in
the calibrated scenario
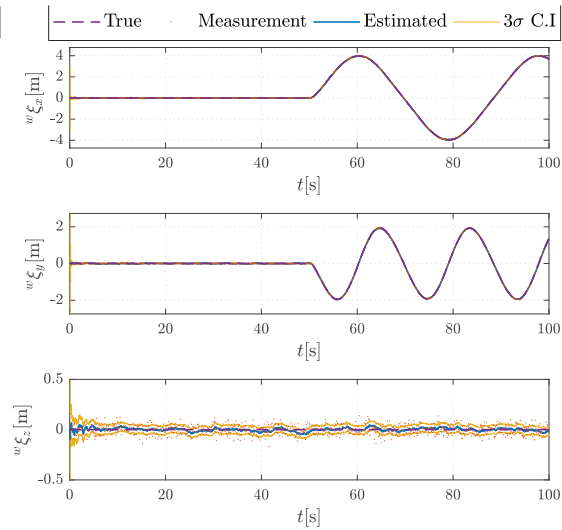
FIGURE 6.36: SKF position estimation in
the calibrated scenario
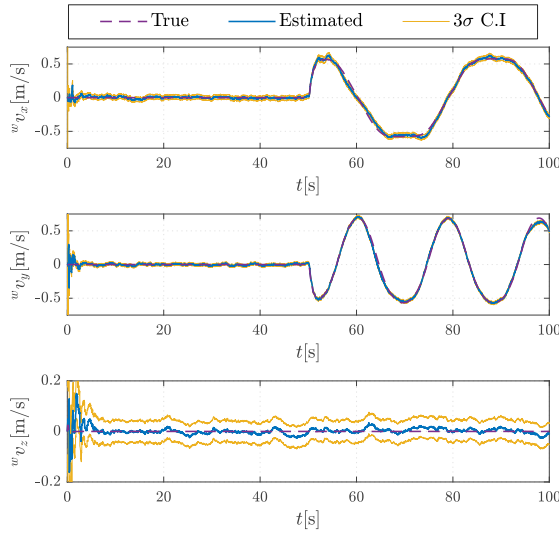
FIGURE 6.37: EKF velocity estimation in the calibrated scenario
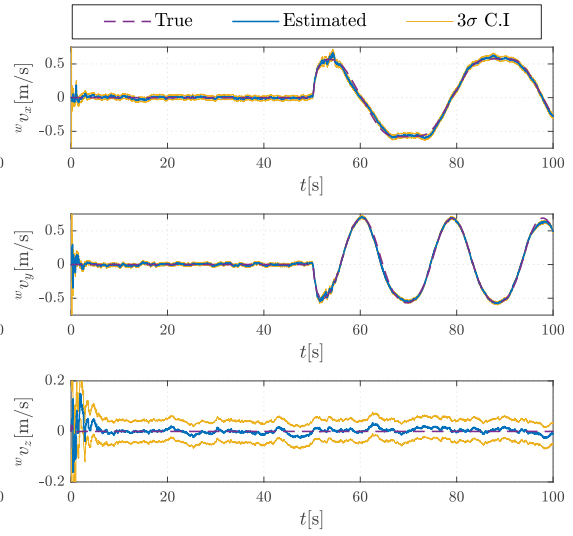
FIGURE 6.38: SKF velocity estimation in the calibrated scenario
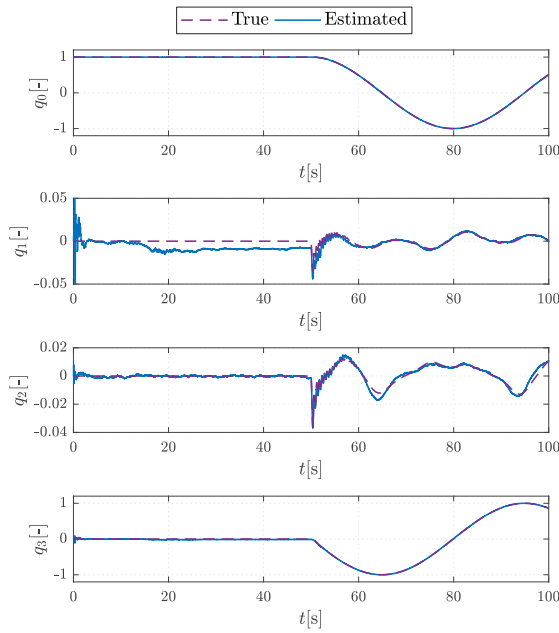
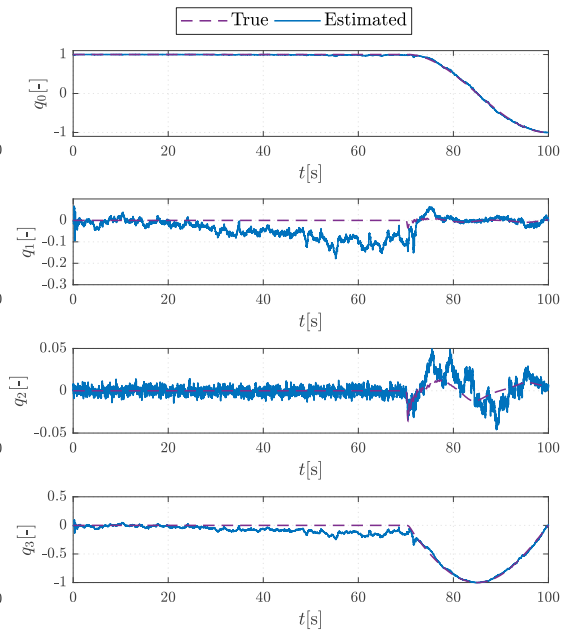FIGURE 6.39: EKF quaternion estimation in the calibrated scenario
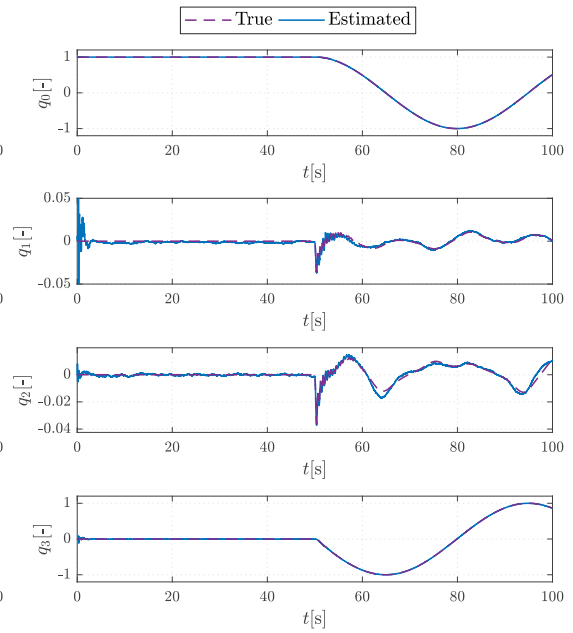
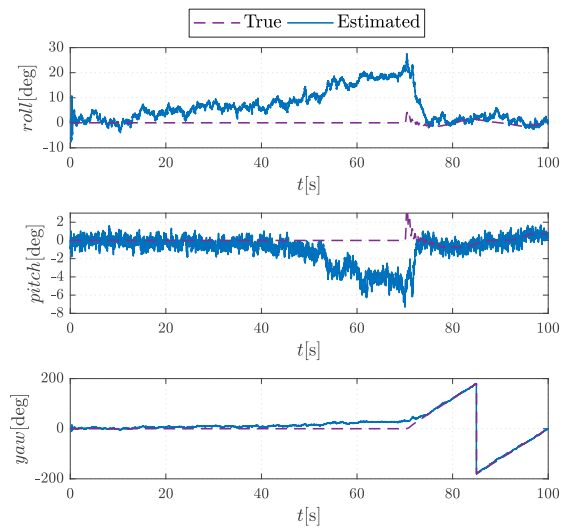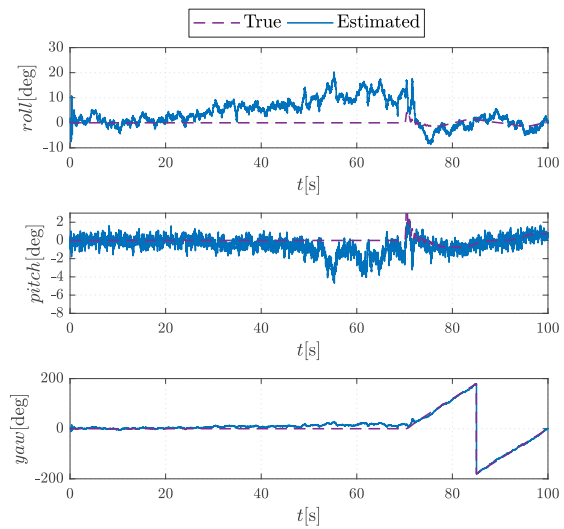FIGURE 6.40: SKF quaternion estimation in the calibrated scenario
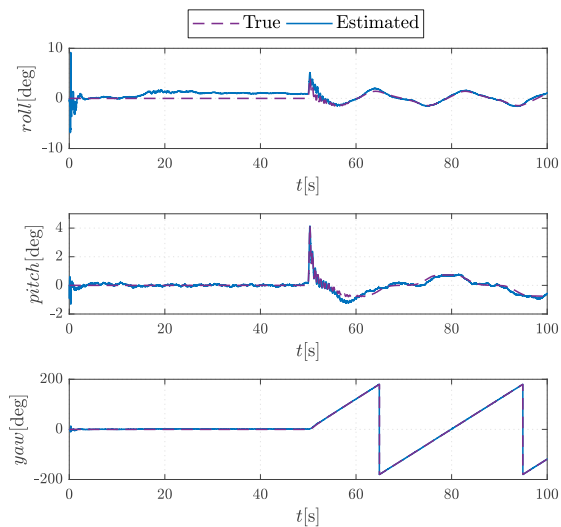
FIGURE 6.41: EKF Euler angles estimation in the calibrated scenario
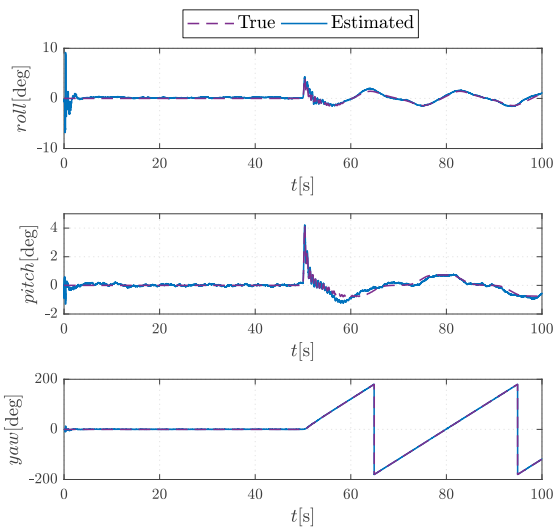
FIGURE 6.42: SKF Euler angles estimation in the calibrated scenario
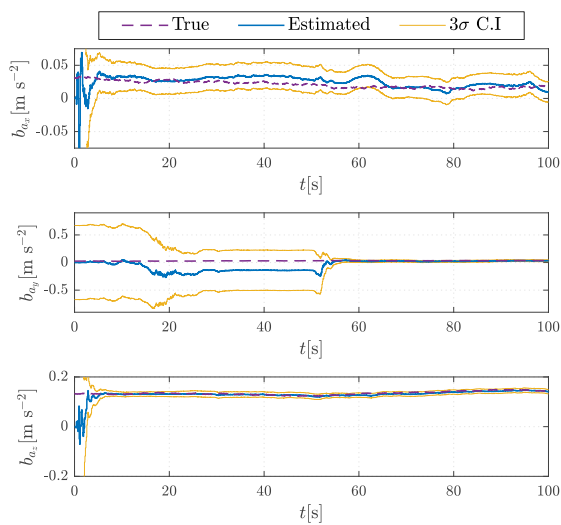
FIGURE 6.43: EKF accelerometer bias estimation in the calibrated scenario
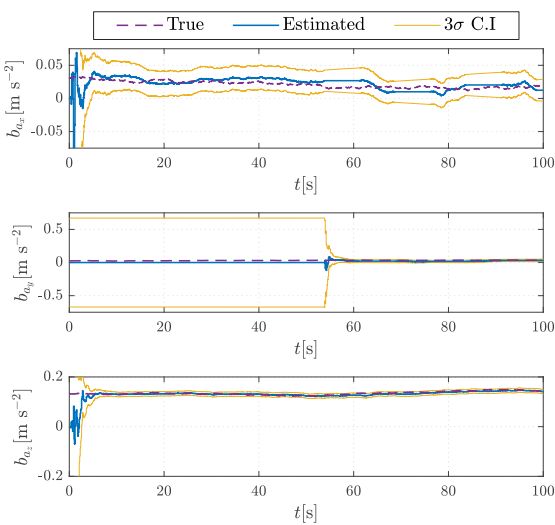
FIGURE 6.44: SKF accelerometer bias estimation in the calibrated scenario

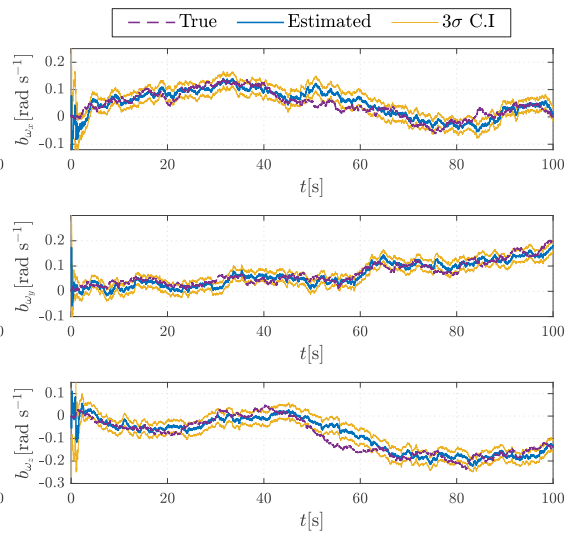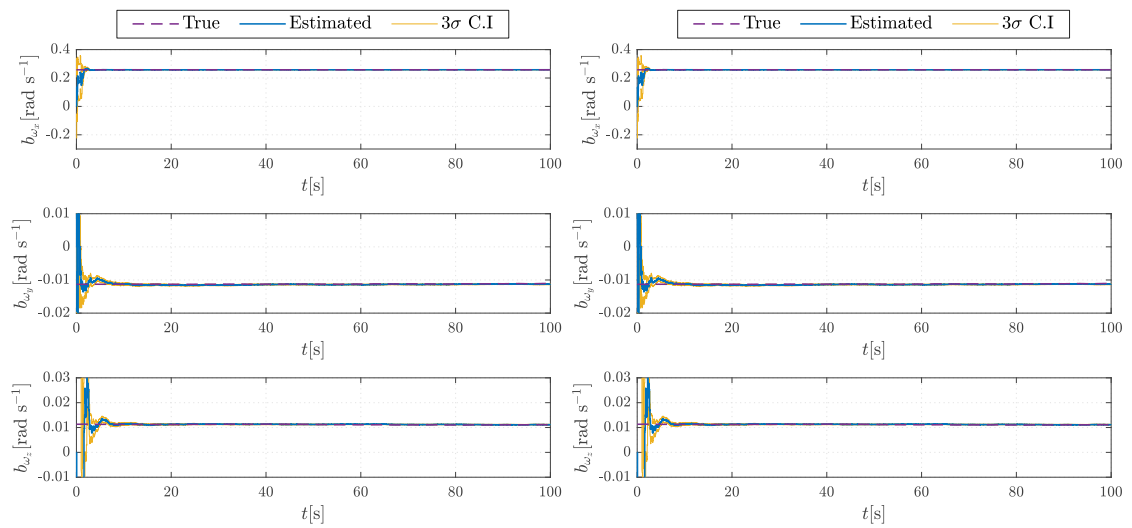FIGURE 6.45: EKF gyroscope bias estimation in the calibrated scenario

FIGURE 6.46: SKF gyroscope bias estimation in the calibrated scenario

6.4   Conclusion

The first part of the the chapter presents four different EKF derivations for the aircraft dynamics based in different but equivalent aircraft dynamics. Among the different alternatives, those considering attitude composition by the left presented better accuracy (Filter 1 and Filter 3 in Table 6.1 and Table 6.2). Moreover, the dynamics considered in Filter 1 allows for the derivation of a closed form filter that avoids the use of iterative calculation routines in favour of more direct ones.

The SKF based filter, described in the second part of the chapter, constitutes a filter alternative that avoids the drifting of the solution present in the traditional EKF when the full state of the system is not recoverable from input-output data. The SKF procedure, here presented, supported by the indistinguishable region equations derived in previous chapters does not need to fix all the biases as is usually suggested in the literature but only one of them. In particular, the SKF identifies a direction in space where the accelerometer biases are more prone to drift, it analyses which component of the estimation bias vector will be mostly affected and does not allow to change its value in the filter update step. From an implementation perspective, the SKF needs only adding two simple actions in the update step of the EKF.

The results show how both filters perform. The proper behaviour of the SKF compared with the EKF is verified inside and outside of the indistinguishable region. In the former, the SKF solution is shown to provide more coherent and precise results when compared with the EKF. In the later, it is shown that in practice the SKF sub-optimal solution resembles quite well the optimal one and the effects of freezing the covariances alternate among the estimated accelerometer bias components as the aircraft rotates.

Part III

External Disturbance Estimation

Chapter 7

External Disturbances Estimation in UAVs

7.1 Introduction

Disturbances and model uncertainty are usually undesirable characteristics that are always present in real systems and their models. Controllers work to ideally ensure stability and maximize performance (tracking or regulation). However, the presence of these disturbances degrade the effectiveness of nominal controllers and may even destabilize the system. One way of dealing with those perturbations is to consider the disturbance rejection performance as an additional objective in the controller design which lead to the concepts of $\mathcal{H}_\infty$ [91, 3] or the input-to-state stability (ISS) [5, 6]. The result of the controller synthesis problem is, in that case, a compromise between tracking and robust performance. An alternative way which has been studied extensively for a number of years is the design of disturbance observers. The idea that when a disturbance estimation is available, a control action can be taken to compensate for the influence of the disturbance, has given birth to disturbance-observer-based control (DOBC), which has been reviewed extensively in [23]. Since the 1960s, several techniques have been proposed to obtain the disturbance estimation, such as unknown input observers [40], perturbation observers [45], equivalent input disturbance-based estimators [79], extended state observers [47], nonlinear disturbance observers [21, 22] and fuzzy Takagi-Sugeno filters [24]. There are applications of the cited observers in areas like chemistry and aerospace, while they are extensively used in industrial mechanical systems like manipulators [83].

Dealing with disturbances and unmodelled dynamics is a crucial and critical issue in the control of unmanned aerial vehicles (UAVs). In some environments, controlling UAVs is a very challenging task, since any controller that does not take into account the disturbances may lead to undesired behaviours ranging from performance degradation to instability. For this reason, there has been some interest in applying DOBC to UAVs. For example, in [75, 76], the non-linear equations of motion expressed in world and body frames with the generalised momentum as state serve as basis

to reconstruct the disturbance. In these works, algebraic equations involving the disturbance and the unknown derivatives of the state are derived and the disturbance estimation is obtained by feeding the integral of the algebraic equations to a second order filter. In [97] a non-linear disturbance observer is derived. It is based on the Newton-Euler non-linear equations of motion using velocities and accelerations as states. The angular magnitudes are expressed in the body reference frame and the translational magnitudes are given in the world frame. Stability of the estimator is demonstrated in the case of constant external disturbances (null derivative) and in the absence of noise. The estimator there is a simplified version of the observer in [83] which, although it does not use the UAV equations of motion, shows a similar development with the consideration of non-constant disturbances as time polynomial varying signals. Note that the effectiveness of the above works has been demonstrated either by using indoor sensors, which provide very precise measurements of position and velocity, or by considering noise-free simulation scenarios. At the same time, they share the hypothesis that the disturbance is slow varying.

In the particular case under study, we propose to use the momentum dynamic equations (linear and spin) expressed in the world reference frame as a model of the system. In Addition, the UAV model is extended by incorporating a high order disturbance model, as proposed by [42, 31, 83]. This way of expressing the system presents the advantage of producing a completely linear model with potential high order dynamics which allows the inclusion of information about the nature of disturbances at a desired derivative order.

In the current chapter, the observers in [83] and [76] are adapted to our system and derived considering the outputs of the state estimators of Chap. (6) and actuator actions as inputs. An additional Kalman Observer is also derived and analysed. It takes advantage of the linearity of the system to bring optimal properties to the estimation. The Kalman observer differs from the other two filters in that it is formulated directly in discrete time, which favours its implementation in digital platforms. Besides, it also takes explicitly into account noise and model errors. A comparison of the three estimators is provided to highlight their limitations and estimation behaviour.

The structure of this chapter is as follows: Firstly, Section 7.2 introduces the high order dynamic model. In Section 7.3 we take advantage of this fact to obtain simplified versions of some wrench observers derived in the literature for similar systems and formulate two additional observers based on Kalman theory. A comparison of the four filter performance over ideal and noisy scenarios is also presented there.

7.2   High Order Dynamic Equations

Let the vector

$$^{w}\boldsymbol{p} = \begin{pmatrix} m\,{}^{w}\boldsymbol{v} \\ {}^{w}\mathbf{J}\,{}^{w}\boldsymbol{\omega} \end{pmatrix} \in \mathbb{R}^{6} \tag{7.1}$$

represent the lumped linear and spin momenta in the world frame $\{\mathcal{B}\}$, where the vector ${}^{w}\boldsymbol{v} \in \mathbb{R}^{3}$ defines the relative velocity of the origin of the body frame $\{\mathcal{B}\}$ with respect to the origin of the

world frame, expressed in world coordinates; ${}^{w}\boldsymbol{\omega} \in \mathbb{R}^3$ represents the relative angular velocity of the body frame with respect to the world frame, also in world coordinates; $m \in \mathbb{R}$ denotes the body mass and ${}^{w}\mathbf{J} \in \mathbb{R}^3$ is the inertia of the body as seen from the inertial frame. Let, in addition, $\mathring{q}$ be the quaternion that represents the aircraft attitude such that, as in Chap. (2)

$$ {}^{w}\boldsymbol{r} = \mathbf{L}(\mathring{q})\,{}^{b}\boldsymbol{r} \tag{7.2} $$

where ${}^{w}\boldsymbol{r}$ and ${}^{b}\boldsymbol{r}$ are different representations of a generic vector $\boldsymbol{r} \in \mathbb{R}^3$ expressed in the frames $\{W\}$ and $\{B\}$ respectively, and $\mathbf{L}(\mathring{q}) \in SO(3)$ the rotation matrix given by Eq. (2.35). By knowing the orientation, the system inertia ${}^{w}\mathbf{J}$ can be related with the constant inertia of the body ${}^{b}\mathbf{J}$ by ${}^{w}\mathbf{J}(\mathring{q}) = \mathbf{L}(\mathring{q})\,{}^{b}\mathbf{J}\mathbf{L}(\mathring{q})^{\top}$.

The rate of change of the momenta vector in the inertial frame can be simply described by

$$ {}^{w}\dot{\boldsymbol{p}} = \begin{pmatrix} m\,{}^{w}\boldsymbol{g} + \mathbf{L}(\mathring{q})\,{}^{b}\boldsymbol{f}_a + {}^{w}\boldsymbol{f}_e \\ \mathbf{L}(\mathring{q})\,{}^{b}\boldsymbol{\tau}_a + {}^{w}\boldsymbol{\tau}_e \end{pmatrix} \tag{7.3} $$

where ${}^{w}\boldsymbol{g} \in \mathbb{R}^3$ is the gravity's acceleration vector, known in $\{W\}$; ${}^{b}\boldsymbol{f}_a \in \mathbb{R}^3$ and ${}^{b}\boldsymbol{\tau}_a \in \mathbb{R}^3$ are the actuator force and torque vectors actions over the system's center of mass, which are naturally described in the body frame and, finally, ${}^{w}\boldsymbol{f}_e \in \mathbb{R}^3$ and ${}^{w}\boldsymbol{\tau}_e \in \mathbb{R}^3$ are the unknown external forces and torques acting on the platform also over the center of mass.

Eq. (7.3) can be written in a compact way as

$$ {}^{w}\dot{\boldsymbol{p}} = \left(m\boldsymbol{g}' + \mathbf{L}'(\mathring{q})\boldsymbol{w}_a + \boldsymbol{d} \right) \tag{7.4} $$

where

$$ \boldsymbol{g}' = \left({}^{w}\boldsymbol{g}^{\top}, 0, 0, 0 \right)^{\top} \tag{7.5} $$

is the extended gravity vector,

$$ \mathbf{L}'(\mathring{q}) = \begin{pmatrix} \mathbf{L}(\mathring{q}) & \mathbf{0} \\ \mathbf{0} & \mathbf{L}(\mathring{q}) \end{pmatrix} \tag{7.6} $$

is an augmented rotation matrix,

$$ \boldsymbol{w}_a^{\top} = \left({}^{b}\boldsymbol{f}_a^{\top}, {}^{b}\boldsymbol{\tau}_a^{\top} \right) \tag{7.7} $$

is the actuator wrench, and

$$ \boldsymbol{d} = \Delta\boldsymbol{w}_a + \Delta\boldsymbol{g}' + \begin{pmatrix} {}^{w}\boldsymbol{f}_e \\ {}^{w}\boldsymbol{\tau}_e \end{pmatrix} \tag{7.8} $$

is a vector representing the disturbances acting on the system, which accounts for the effect of the external wrench but also the effect of unmodelled dynamics, represented by $\Delta\boldsymbol{w}_a$ and $\Delta\boldsymbol{g}'$.

The main goal of Eq. (7.3) is to serve as a model for disturbance estimation. Therefore, there is no need to extend the model in the upward direction to relate the momenta integrals with the position and attitude, magnitudes that will be provided by the state estimator as shown in Chap. (6). At this point it will be assumed that $\mathring{q}$, ${}^{w}\boldsymbol{v}$, ${}^{b}\boldsymbol{\omega}$ and the unbiased measures from

accelerometers represented by

$$^b\boldsymbol{a} = \frac{^b\boldsymbol{f}_a + \mathbf{L}^\top {}^w\boldsymbol{f}_{ext}}{m}$$

are provided at regular instants of time by the output of the estimator derived in Chap. (6).

Under this hypothesis, Eq. (7.3) is a simple integrator system driven by external inputs, whose dynamics must match with the measures of $^w\boldsymbol{v}$, $^b\boldsymbol{\omega}$ and $^b\boldsymbol{a}$.

Note that the linearity of the system has been achieved by the proper choice of state and reference frame and is not a product of a linearization neither an approximation of the non-linear counterparts.

7.2.1   Disturbance model

The dynamics of $\boldsymbol{d}$ is generally unknown and this is the main reason why works like [75] and [97] suppose that $\dot{\boldsymbol{d}} = 0$. However, this constraint could slow down the estimation output in the case of fast varying dynamics. In order to alleviate this drawback, it could be assumed that the disturbance $\boldsymbol{d}$ is a continuous function driven by an unknown time varying exogenous input $\boldsymbol{\eta}(t)$ at its r-th derivative

$$\overset{(r)}{\boldsymbol{d}} = \boldsymbol{\eta}(t) \tag{7.9}$$

as suggested in [42], and later used in [83].

In this case, it is interesting to consider an augmented version of the disturbance vector, given by

$$\boldsymbol{d}_v = \left(\boldsymbol{d}^\top, \dot{\boldsymbol{d}}^\top, \cdots, \overset{(r-1)}{\boldsymbol{d}^\top}\right)^\top \tag{7.10}$$

with the dynamics of $\boldsymbol{d}_v$ described by

$$\dot{\boldsymbol{d}}_v = \mathbf{F}\boldsymbol{d}_v + \mathbf{G}\boldsymbol{\eta} \tag{7.11}$$

where $\mathbf{F} \in \mathbb{R}^{6r \times 6r}$ is given by

$$\mathbf{F} = \left(\begin{array}{c|c} \mathbf{0}_{6r \times 6} & \begin{array}{c} \mathbf{I}_{6(r-1)} \\ \hline \mathbf{0}_{6 \times 6(r-1)} \end{array} \end{array}\right) \tag{7.12}$$

and $\mathbf{G} \in \mathbb{R}^{6r \times 6}$ is defined as

$$\mathbf{G} = \left(\begin{array}{c} \mathbf{0}_{6(r-1) \times 6} \\ \hline \mathbf{I}_6 \end{array}\right) \tag{7.13}$$

The disturbance vector $\boldsymbol{d}$ can be recovered anytime from $\boldsymbol{d}_v$ as $\boldsymbol{d} = \mathbf{H}\boldsymbol{d}_v$, where $\mathbf{H} \in \mathbb{R}^{6 \times 6r}$ is another selection matrix defined by

$$\mathbf{H} = \left(\mathbf{I}_6, \mathbf{0}_{6 \times 6(r-1)}\right) \tag{7.14}$$

7.2.2 Extended model considering disturbances

The augmented dynamic model with state $\boldsymbol{x} = \left({}^{w}\boldsymbol{p}^{\top}, \, \boldsymbol{d}_v^{\top} \right)^{\top}$ and dynamics given by Eq. (7.4) and Eq. (7.11) can be summarized as

$$\dot{\boldsymbol{x}} = \begin{pmatrix} {}^{w}\dot{\boldsymbol{p}} \\ \dot{\boldsymbol{d}}_v \end{pmatrix} = \begin{pmatrix} m\boldsymbol{g}' + \mathbf{L}'(\mathring{q})\boldsymbol{w}_a + \mathbf{H}\boldsymbol{d}_v \\ \mathbf{F}\boldsymbol{d}_v + \mathbf{G}\boldsymbol{\eta} \end{pmatrix} \tag{7.15}$$

Let $\mathring{q}$ and $\boldsymbol{w}_a$ be known and let $\boldsymbol{\eta} = \boldsymbol{\eta}(t)$ represent an unknown input, then the dynamics in Eq. (7.15) are linear and can be rewritten as

$$\dot{\boldsymbol{x}} = \mathbf{A}\boldsymbol{x} + \mathbf{B}\boldsymbol{u} + \mathbf{W}_1\boldsymbol{\eta} \tag{7.16}$$

where

$$\mathbf{A} = \left(\begin{array}{c|c} \mathbf{0}_{6(r+1)\times 6} & \dfrac{\mathbf{H}}{\mathbf{F}} \end{array} \right), \tag{7.17}$$

$$\mathbf{B} = \begin{pmatrix} \mathbf{I}_6 \\ \mathbf{0}_{6r\times 6} \end{pmatrix} \tag{7.18}$$

$$\mathbf{W}_1 = \begin{pmatrix} \mathbf{0}_{6\times 6} \\ \mathbf{G} \end{pmatrix} \tag{7.19}$$

and

$$\boldsymbol{u} = m\boldsymbol{g}' + \mathbf{L}'(\mathring{q})\boldsymbol{w}_a \tag{7.20}$$

A discrete version of the model in Eq. (7.15) can be formulated as

$$\boldsymbol{x}_{k+1} = \varPhi_d \boldsymbol{x}_k + \mathbf{W}'\eta_k + \mathbf{B}_d \boldsymbol{u}_k, \tag{7.21}$$

where

$$\varPhi_d = \mathrm{expm}\left(\mathbf{A}\left(t_{k+1} - t_k \right) \right)$$

$$\mathbf{B}_d = \mathbf{M}\begin{pmatrix} \mathbf{I}_{6\times 6} \\ \mathbf{0}_{6r\times 6} \end{pmatrix}$$

$$\mathbf{M} = \int_{t_k}^{t_{k+1}} \mathrm{expm}\left(\varPhi_c(t_{k+1} - \tau) \right) \, \mathrm{d}\tau$$

$\boldsymbol{u}_k = m\boldsymbol{g}' + \mathbf{L}'\boldsymbol{w}_{a_k}$ is assumed constant during the integration,

$$\mathbf{W}' = \left(\begin{array}{c|c} \mathbf{0}_{6(r+1)\times 6r} & \dfrac{\mathbf{0}_{6r\times 6}}{\mathbf{I}_{6\times 6}} \end{array} \right),$$

and $\boldsymbol{\eta}_k$ is the discrete counterpart of $\boldsymbol{\eta}(t)$.

Remark 1: Φ_k, $\mathbf{M}$ and hence $\mathbf{B}_d$ are constant provided that the sampling period represented by $\Delta t = t_{k+1} - t_k$ is also constant. Moreover, given the structure of $\mathbf{A}$, $\mathbf{A}^i = \mathbf{0}$ for $i > r$, then Φ_k and $\mathbf{M}$ can be calculated as a finite sum of matrices

$$\Phi_k = \mathrm{expm}\left(\Phi_c \Delta t\right) = \sum_{i=0}^{\infty} \frac{\left(\Phi_c \Delta t\right)^i}{i!} = \sum_{i=0}^{r} \frac{\left(\Phi_c \Delta t\right)^i}{i!},$$

$$\mathbf{M} = \int_0^{\Delta t} \mathrm{expm}\left(\Phi_c \tau\right) \mathrm{d}\tau = \sum_{i=0}^{\infty} \frac{\Phi_c^i \Delta t^{i+1}}{i+1!} = \sum_{i=0}^{r} \frac{\Phi_c^i \Delta t^{i+1}}{i+1!}.$$

7.3   Ext. Disturbances estimation using Linear and Spin Momenta

This section describes four disturbance observers that will be compared subsequently. The first two are drawn from the literature but adapted to the dynamics considered in Section 7.2, while the remaining ones are Kalman based observers.

7.3.1   Momentum Based External Forces Estimator revisited

A Momentum Based External Forces Estimator (MBEFE) is presented in [75] and [76]. This estimator assumes that the derivative of the disturbance is null and consequently the derivatives of the estimation are not taken into account.

The disturbance, $\boldsymbol{d}$, is isolated from Eq. (7.4) as

$$\boldsymbol{d} = {}^w\dot{\boldsymbol{p}} - m\boldsymbol{g}' - \mathbf{L}'\boldsymbol{w}_a.$$

Since this signal is affected by noise and ${}^w\dot{\boldsymbol{p}}$ is not known, the authors propose to filter $\boldsymbol{d}$ using a second order filter.

This way, the estimation of the disturbance becomes

$$\ddot{\hat{\boldsymbol{d}}} + \mathbf{K}_1 \dot{\hat{\boldsymbol{d}}} + \mathbf{K}_2 \hat{\boldsymbol{d}} = \mathbf{K}_2 \left({}^w\dot{\boldsymbol{p}} - m\boldsymbol{g}' - \mathbf{L}'\boldsymbol{w}_a\right)$$

which, by integrating twice in time and replacing $\int_0^t {}^w\dot{\boldsymbol{p}}\mathrm{d}\tau$ by ${}^w\boldsymbol{p}$ leads to

$$\hat{\boldsymbol{d}} = -\int_0^t \left[\mathbf{K}_1 \hat{\boldsymbol{d}} - \mathbf{K}_2 \left({}^w\boldsymbol{p} - \int_0^t \left[m\boldsymbol{g}' + \mathbf{L}'\boldsymbol{w}_a + \hat{\boldsymbol{d}}\right] \mathrm{d}\tau'\right)\right]\mathrm{d}\tau. \tag{7.22}$$

Remark 2: Gain matrices $\mathbf{K}_1$ and $\mathbf{K}_2$ shape the dynamic response of the estimator and must be chosen to make the filter stable. In case they are chosen diagonal

$$\mathbf{K}_{1_{i,i}} = 2\zeta_i \omega_{n,i},$$
$$\mathbf{K}_{2_{i,i}} = \omega_{n,i}^2,$$

where $\omega_{n,i}$ and ζ_i represent the natural frequency and damping factor, respectively, of the $i-th$ DOF of the estimator dynamics.

7.3.2 High Order non-linear Disturbance Observer revisited in momentum form

The High Order non-linear Disturbance Observer (HODO) is presented in [83]. The derivations and conclusion presented in this section follow the lines of the original work adapted to the system in Eq. (7.15).

Let e be the error between the real disturbance d_v and its estimated counterpart $\hat{d}_v$

$$e = d_v - \hat{d}_v. \tag{7.23}$$

The error dynamics can be described using Eq. (7.11) as

$$\dot{e} = \dot{d}_v - \dot{\hat{d}}_v = \mathbf{A}d_v + \mathbf{W}\eta(t) - \dot{\hat{d}}_v. \tag{7.24}$$

By choosing

$$\dot{\hat{d}}_v = \mathbf{K}\left({}^w\dot{p} - mg' - \mathbf{L}'w_a\right) + \left(\mathbf{A} - \mathbf{K}\mathbf{H}\right)\hat{d}_v, \tag{7.25}$$

which implies that

$$\hat{d}_v = \mathbf{K}^w p + \int_0^t \left[\left(\mathbf{A} - \mathbf{K}\mathbf{H}\right)\hat{d}_v - \mathbf{K}\left(mg' + \mathbf{L}'w_a\right)\right]\mathrm{d}\tau, \tag{7.26}$$

the error dynamics becomes

$$\dot{e} = \left(\mathbf{A} - \mathbf{K}\mathbf{H}\right)e + \mathbf{W}\eta, \tag{7.27}$$

where $\mathbf{K} \in \mathbb{R}^{6r \times 6}$ is a gain matrix to be defined. Selecting it such that $\left(\mathbf{A} - \mathbf{K}\mathbf{H}\right)$ is negative definite, the system in Eq. (7.27) is bounded-input-bounded-output (BIBO) stable which means that the error on the disturbance estimation will be bounded as long as the model error represented by $\eta(t)$ is bounded.

Remark 3: The design of $\mathbf{K}$ may not seem trivial. However, given the constant and simple structures of $\mathbf{A}$ and $\mathbf{H}$, $\mathbf{K}$ can be designed by pole placement using a similar approach as the one shown in [83].

7.3.3 Kalman High-order Observer

In this section two different Kalman High-order Observers (KHO) for the system in Eq. (7.21) are derived. The estimators of the previous sections use measurements of velocities, attitude and actuator wrenches and do not allow to consider extra information coming from the accelerometers. However, the Kalman Observer allows by its nature to reconcile measures from multiple sensors even if they are related or redundant. The two filters derived here differ in the measures taken into account in the estimation. The first one, named KHO1, uses the same set of

inputs as the filters in previous sections and the second one, named KHO2, uses, in addition, the accelerometers measurements.

From the model in Eq. (7.21), a linear Kalman observer can be formulated as a two stage algorithm that estimates the disturbance and the momentum simultaneously. Let $\boldsymbol{x}_k^-$ be the best estimate of the state at time instant t_k, assuming that all the measures up to t_{k-1} are known, and $\boldsymbol{x}_k^+$ represent the best estimate of the state at time instant t_k when a new measurement $\boldsymbol{y}_k$ has entered the system. The matrix $\mathbf{P}_k$ represents the covariance of state error, i.e. $\mathbf{P}_k^- = E((\hat{\boldsymbol{x}}_k^- - \boldsymbol{x}_k)(\hat{\boldsymbol{x}}_k^- - \boldsymbol{x}_k)^\top)$ while $\mathbf{P}_k^+ = E((\hat{\boldsymbol{x}}_k^+ - \boldsymbol{x}_k)(\hat{\boldsymbol{x}}_k^+ - \boldsymbol{x}_k)^\top)$

The linear Kalman filtering algorithm that produces the estimations of $\boldsymbol{x}_k^+$ and $\mathbf{P}_k^+$ is represented by the concatenation of Eq. (6.1) and Eq. (6.2), reproduced here for clarity purposes,

$$\hat{\boldsymbol{x}}_k^- = \Phi_k \hat{\boldsymbol{x}}_{k-1}^+ + \mathbf{B}_d \boldsymbol{u}_k, \tag{7.28}$$

$$\boldsymbol{P}_k^- = \Phi_k \mathbf{P}_{k-1}^+ \Phi_k^\top + \mathbf{Q}_k, \tag{7.29}$$

$$\mathbf{K} = \mathbf{P}_k^- \mathbf{C}^\top \left(\mathbf{C} \mathbf{P}_k^- \mathbf{C} + \mathbf{R}\right)^{-1}, \tag{7.30}$$

$$\hat{\boldsymbol{y}}_k = \mathbf{C} \hat{\boldsymbol{x}}_k^- + \mathbf{D} \boldsymbol{w}_{a_k}, \tag{7.31}$$

$$\hat{\boldsymbol{x}}_k^+ = \hat{\boldsymbol{x}}_k^- + \mathbf{K}(\boldsymbol{y}_k - \hat{\boldsymbol{y}}_k), \tag{7.32}$$

$$\mathbf{P}_k^+ = (\mathbf{I} - \mathbf{K}\mathbf{C})\mathbf{P}_k^-. \tag{7.33}$$

is run once a new measure is available at time instant k.

Matrix $\mathbf{Q}_k = \mathbf{W}'\mathbf{Q}(\mathbf{W}')^\top$ in Eq. (7.29) is a positive definite matrix representing the covariance of the model error, assumed here as $\boldsymbol{\eta}_k \sim \mathcal{N}(\mathbf{0}, \mathbf{Q})$.

While the propagation equations Eq. (7.28) and Eq. (7.29) are common for both Kalman filters, the sensor model in Eq. (7.31) differs. Matrix $\mathbf{R}$ represents the covariance of the measurement errors and is defined differently for each implementation in the next two subsections.

KHO1

The first Kalman observer uses the same information as the MBEFE and HODO filters. The measurement model is defined as

$$\boldsymbol{y} = \begin{pmatrix} {}^w\boldsymbol{v} \\ {}^b\boldsymbol{\omega} \end{pmatrix} + \boldsymbol{v}_k = \mathbf{C}\boldsymbol{x}_k + \boldsymbol{v}_k,$$

where

$$\mathbf{C} = \left(\mathrm{blkdiag}(\tfrac{1}{m}\mathbf{I}_3, \, {}^b\mathbf{J}^{-1}\mathbf{L}^\top) \quad \mathbf{0}_{6\times 6(r-1)}\right)$$

while $\mathbf{D}$ in Eq. (7.31) is null.

$\boldsymbol{v}_k \in \mathbb{R}^6 \sim \mathcal{N}(0, \mathbf{R})$ is the sensor noise vector which is assumed normally distributed with covariance $\mathbf{R}$.
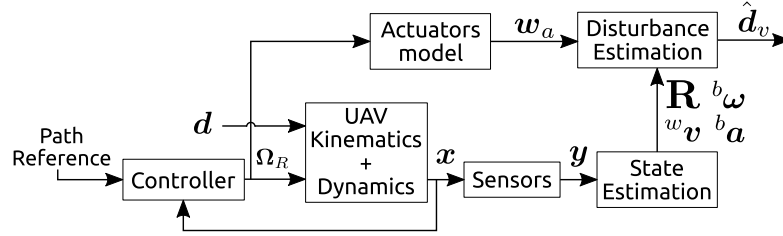
FIGURE 7.1: Simulation setup

KHO2

The second Kalman observer considers also the accelerometer readings. The measurement model is then given by

$$\boldsymbol{y} = \begin{pmatrix} {}^{w}\boldsymbol{v} \\ {}^{b}\boldsymbol{\omega} \\ \frac{1}{m}\left(\mathbf{L}^{\top}\boldsymbol{d} + \boldsymbol{f}_a\right) \end{pmatrix} + \boldsymbol{v}_k = \mathbf{C}\boldsymbol{x}_k + \mathbf{D}\boldsymbol{w}_{a_k} + \boldsymbol{v}_k,$$

where

$$\mathbf{C} = \begin{pmatrix} \text{blkdiag}(\frac{1}{m}\mathbf{I}_3,\ {}^{b}\mathbf{J}^{-1}\mathbf{L}^{\top},\ \frac{1}{m}\mathbf{L}^{\top}) & \mathbf{0}_{9\times 6(r-1)-3} \end{pmatrix}$$

and

$$\mathbf{D} = \frac{1}{m}\left(\begin{array}{c|c} \mathbf{0}_{6\times 3} & \\ \hline \mathbf{I}_{3\times 3} & \mathbf{0}_{9\times 3} \end{array}\right).$$

$\boldsymbol{v}_k \in \mathbb{R}^9 \sim \mathcal{N}(0, \mathbf{R})$ is again the sensor noise vector, assumed as before normally distributed with covariance $\mathbf{R}$.

7.3.4   Case studies

The simulation setup of Fig. 7.1 has been used to test and compare the derived estimators.

A quadrotor with $m = 1.023\,\text{kg}$ and ${}^{b}\mathbf{J} = \text{diag}\,(9.5, 9.5, 18.6)\,10^{-3}\,\text{kgm}^2$ is controlled to perform a hovering flight during all the simulation time with a simple cascade controller composed by a gravity compensated PD for trajectory control and a PID for attitude control. The inputs of the dynamic model are the desired angular velocities of the four rotors Ω_R along with the disturbance $\boldsymbol{d}$. The system measurements are provided by the usual sensor suite in the thesis, an IMU that measures the angular velocity of the aircraft and the acceleration of external forces, a tri-axial magnetometer that outputs the Earth's magnetic field direction and a GPS sensor that outputs the position in the world frame. As mentioned before, this information feeds the state estimator presented in Chap. (6) to produce estimates of the attitude quaternion, $\mathring{q}$, and linear velocity, ${}^{w}\boldsymbol{v}$, while it also corrects and alleviates the noise in the IMU's outputs ${}^{b}\boldsymbol{\omega}$ and ${}^{b}\boldsymbol{a}$. Moreover, the actuator wrench $\boldsymbol{w}_a$ is reconstructed by using the simple model in Eq. (4.30) and parameters in Eq. (4.31). Discrepancies between the reconstructed model and the simulated one may exist because in this case the motor dynamics are not considered, however it is expected that this error will be estimated in $\boldsymbol{d}$ as pointed out before in Eq. (7.8). Inputs for the disturbance

estimators are updated at $100\,\mathrm{Hz}$ and they are held constant between updates for the continuous disturbance estimators.

Ideal scenario

This scenario tests the disturbance estimators with noise-free inputs when the force shown in Fig. 7.2 acts over the system in the world x direction. The initial value of the estimation has been set to zero while the initial value for the state error covariances in the case of Kalman observers have been set high enough to smooth out the possible initial errors.
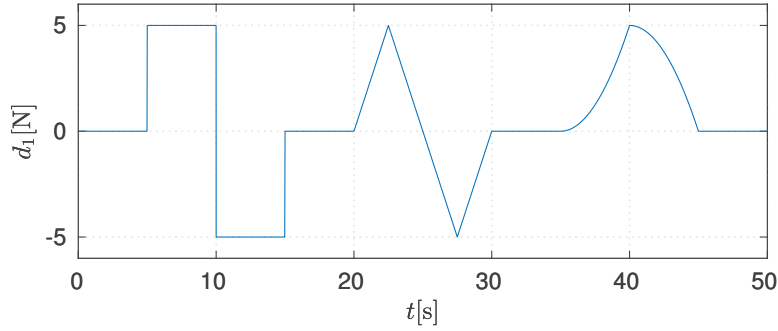
FIGURE 7.2: Disturbance applied to the quadrotor. First part is a succession of constant signals (from $t = 5$ to $t = 15$). The second one is a triangular signal (from $t = 20$ to $t = 30$ and the third part is a quadratic signal (from $t = 35$ to $t = 35$)

Fig. 7.3 shows the disturbance estimation and the estimation errors for the described observers. In this scenario the parameters have been tuned to show the fundamental limitations of each observer as follows: for HODO and MBEFE gains are high enough to rapidly accommodate the system dynamics; for KHO1 and KHO2, the measurement error covariances $\mathbf{R}$ are small enough to reflect the absence of noise in the inputs and the model covariances $\mathbf{Q}$ are high enough to consider possible errors in the model. They have been selected as shown in Table 7.1

Filter	Parameters		
MBEFE	$\mathbf{K}_1 = 10\mathbf{I}_6$	$\mathbf{K}_2 = 20\mathbf{I}_6$	
HODO	$\mathbf{K} = \left(45\mathbf{I}_6,\, 675\mathbf{I}_6,\, 3375\mathbf{I}_6\right)^{\top}$	$r = 3$	
KHO1	$\mathbf{Q}_1 = 0.1\mathbf{I}_6$	$\mathbf{R}_1 = 1\cdot 10^{-6}\mathbf{I}_6$	$r = 3$
KHO2	$\mathbf{Q}_2 = 0.1\mathbf{I}_6$	$\mathbf{R}_2 = 1\cdot 10^{-6}\mathbf{I}_9$	$r = 3$

TABLE 7.1: Filter parameters for the ideal scenario

It can be observed that even in the ideal case the MBEFE observer fails to recover the behaviour of the disturbance. This error cannot be alleviated by improving the tuning since it is a limitation of the force model (null derivative) implicit in the estimator. The HODO and the KHO observers are able to reconstruct the signal properly, only showing discrepancies in the abrupt changes (high frequency content) not represented by the 3-rd null derivative model chosen.
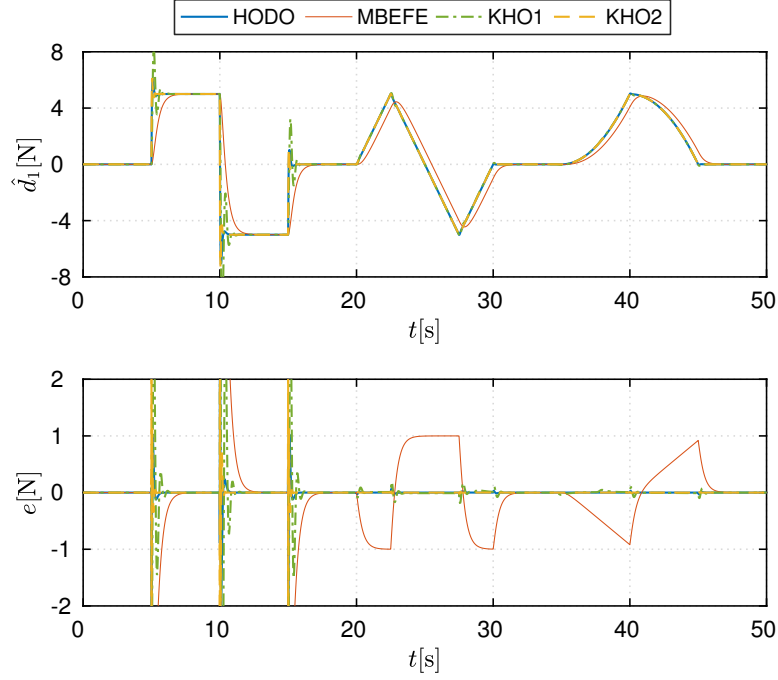
FIGURE 7.3: Disturbance estimation and errors for the proposed observers

TABLE 7.2: Accumulated Error E for the estimation in the ideal scenario

Ideal Case	E [N]
MBEFE	1.06
HODO	0.20
KHO1	0.52
KHO2	0.18

The accumulated estimation error for each filter, calculated as

$$E = \sqrt{\frac{1}{T} \int_0^T e^2 \mathrm{d}t} \tag{7.34}$$

is shown in Table 7.2. It can be observed that KHO2 performs better than KHO1 with equivalent parameters. This behaviour has been observed in the rest of experiments.

Realistic scenario

In order to test the presented estimators under a more realistic disturbance scenario, the results in section IV.B of [75] where a quadrotor with additional payload flies in hover in front of a fan have been used. An approximation of their reconstructed wrench presented in Fig. 7.4 has been taken as disturbance input to the system depicted in Fig. 7.1. Moreover, the sensor models have been calibrated to mimic the actual sensors of a real quadrotor before state estimation. As a consequence, the inputs to the disturbance observer $\mathring{q}$, $^w\boldsymbol{v}$, $^b\boldsymbol{\omega}$ and $^b\boldsymbol{a}$ are perturbed by noise, thus affecting the estimation performance.
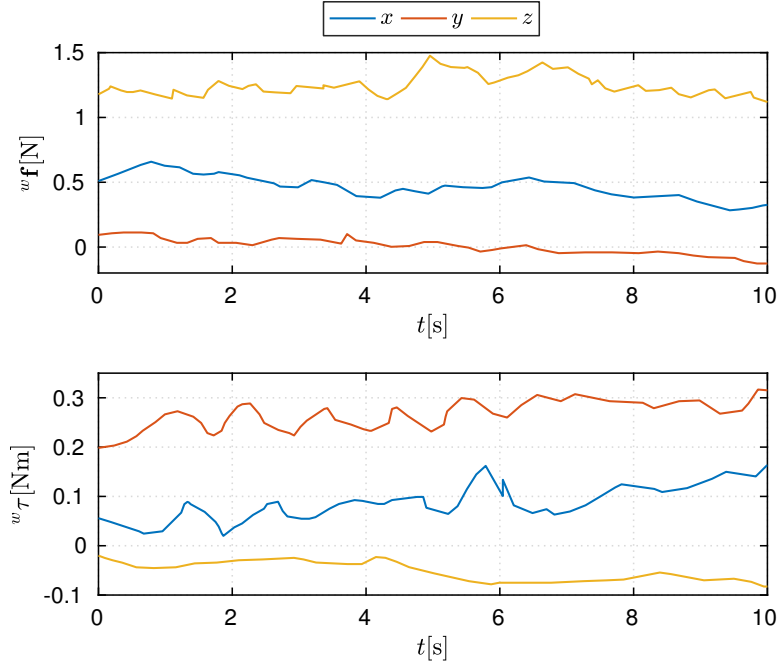
FIGURE 7.4: Disturbance applied over the system

For the sake of clarity, considering the similar structures of the KHO1 and KHO2 and the better performance of KHO2, this section does not show the results of KHO1.

Since the performance of the observers varies with the tuning of their parameters, the gains have been chosen to minimize the mean squared error while keeping sensible tracking performance. The values of these parameters are shown in Table 7.3

Filter	Parameters		
MBEFE	$\mathbf{K}_1 = 2.5\mathbf{I}_6$	$\mathbf{K}_2 = 10\mathbf{I}_6$	
HODO	$\mathbf{K} = \left(5.8\mathbf{I}_6, 11.4\mathbf{I}_6, 7.4\mathbf{I}_6\right)^\top$		$r = 3$
KHO2	$\mathbf{Q}_2 = 1 \cdot 10^{-6}\mathbf{I}_6$ $\mathbf{R}_2 = 4 \cdot 10^{-4}\text{blkdiag}\left(\mathbf{I}_3, 0.07\mathbf{I}_3, 0.1\mathbf{I}_3\right)$		$r = 3$

TABLE 7.3: Filter parameters for the noisy scenario

Figs. 7.5 and 7.6 show the time evolution of the estimation errors for every component of the force and torque respectively. In addition, the accumulated estimation errors calculated as in Eq. (7.34) are presented in Table 7.4.

The MBEFE is able to reject noise easily while it is still unable to follow correctly the proposed disturbances. Regarding the HODO, it has been observed that noise perturbs the output of the estimation and, while selecting less demanding tuning parameters would filter better the noise, it would also make the estimation performance poorer. The KHO2 presents the best results among the three estimators. The main benefit of the Kalman observer is that it can adapt its gain given $\mathbf{R}$ and $\mathbf{Q}$. In the case that $\mathbf{R}$ and $\mathbf{Q}$ match the covariances of noise and error model
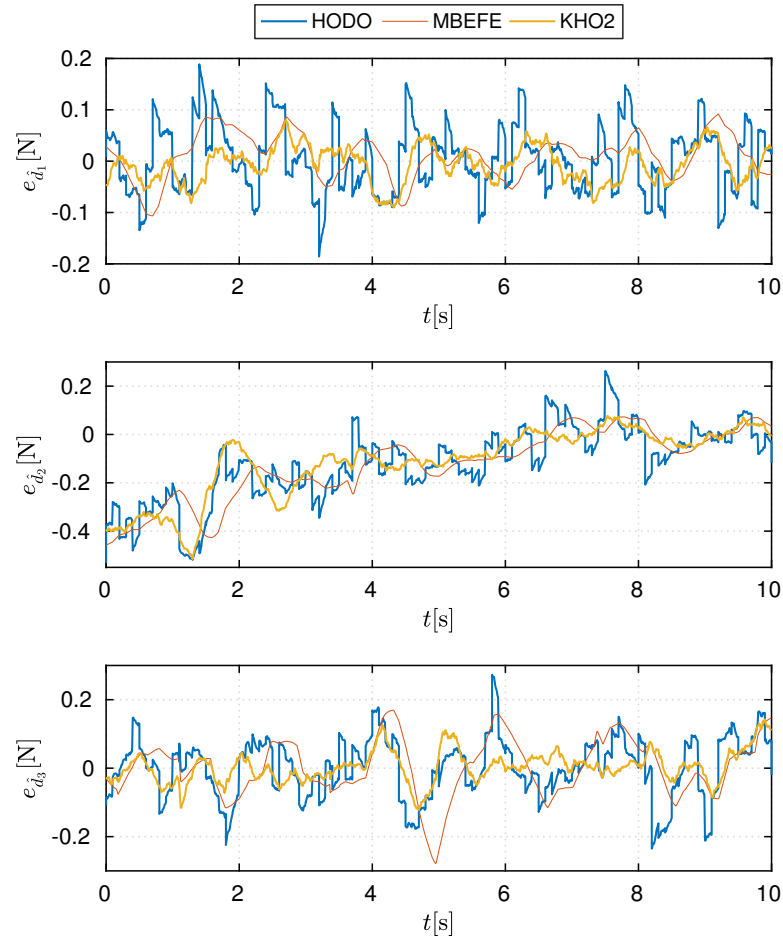
FIGURE 7.5: Force estimation errors in the realistic scenario

TABLE 7.4: Accumulated Error E for the estimation in a realistic scenario

Non-ideal Case	HODO	MBEFE	KHO2
$E_{\hat{d}_1}[\text{N}]$	0.0669	0.0439	0.0360
$E_{\hat{d}_2}[\text{N}]$	0.1911	0.1886	0.1788
$E_{\hat{d}_3}[\text{N}]$	0.0868	0.0835	0.0456
$E_{\hat{d}_4}[\text{Nm}]$	0.0154	0.0275	0.0121
$E_{\hat{d}_5}[\text{Nm}]$	0.0129	0.0206	0.0112
$E_{\hat{d}_6}[\text{Nm}]$	0.0062	0.0093	0.0057
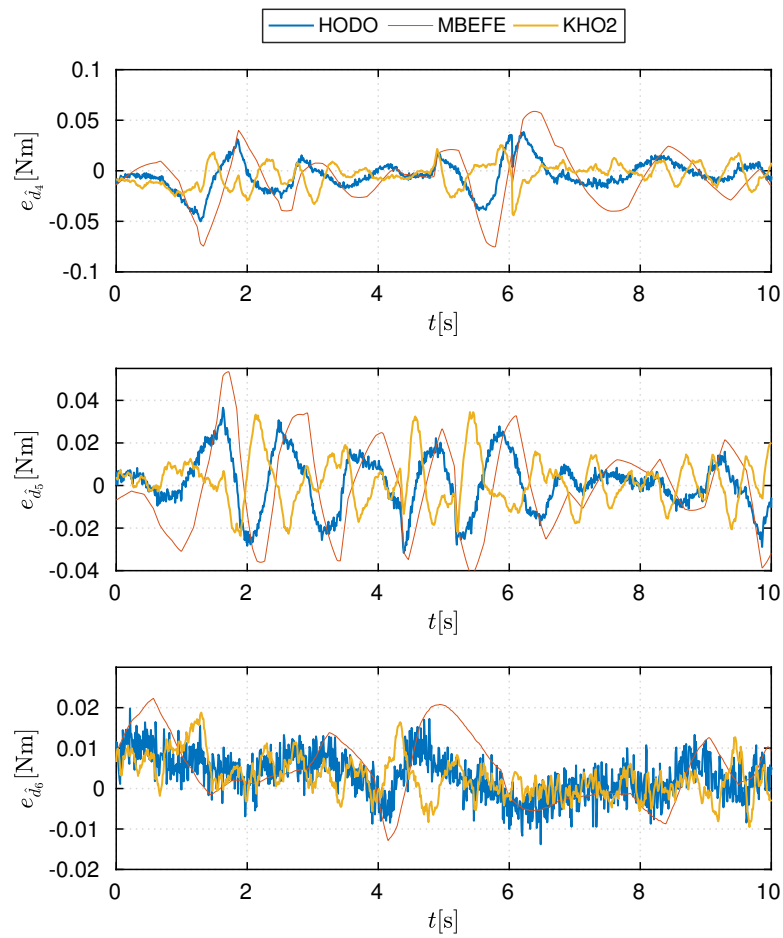
FIGURE 7.6: Torque estimation errors in the realistic scenario

perfectly, the estimation is guaranteed to be optimal. In contrast, by selecting different $\mathbf{R}$ and $\mathbf{Q}$ (which is the case) the estimation is expected to be suboptimal. However, in the experience of the authors, even with a poor selection of the covariance matrices the KHO2 produces better estimations of the disturbance than the other observers.

7.4 Conclusion

In this chapter a linear model for external disturbance estimation is provided. The linearity of the model enables the simplification of some wrench observers derived in the literature and allows to formulate two new observers based on Kalman theory. Simulation results show the superiority of the Kalman observers. This approach outperforms traditional ones because the Kalman methods are able to reconcile data and take into account multiple redundant or related inputs while other observers do not. Moreover, the tuning of the Kalman observers is related to noise and model descriptions and although this fact has not been used here, the authors have experienced more robustness of the tracking performance when tuning the Kalman observers than when fine-tuning the other type of observers.

Chapter 8

Quadratic Bounded Observers. Application to UAVs External Disturbances Estimation

This chapter is mainly focused in the design of a special kind of quadratically bounded state observer and its application to the disturbance estimation.

Roughly speaking, quadratic boundedness (QB) refers to guaranteeing the boundedness of all the state trajectories of a system by means of a quadratic Lyapunov function. This concept was introduced first for nonlinear systems in [16], and later extended to nominally linear systems in [17]. Since then, several results have exploited this concept for the purpose of state estimation. For instance, [7] has used QB to deal with stability and design of receding-horizon estimators. On the other hand, [8] has applied QB to the design of state estimators for discrete-time linear systems with polytopic uncertainties, and this work has been extended further by [99], where state disturbances and measurement noise have been considered independently. Notably, QB has been invoked to solve problems related to output feedback stabilization [28, 29, 30, 69, 68], fault tolerant control [94] and fault estimation [19, 18, 95]. Recently, further extensions of the QB concept have been investigated, see e.g. the extended nonquadratic boundedness introduced by [100].

The quadratically bounded state observers derived here take into account the existence of a trade-off between the convergence rate and the ultimate (steady-state) error bounding ellipsoid. In order to handle both objectives, a scalarised objective function with one design parameter is built, such that the design problem is made convex. The obtained design procedure ensures an optimal trade-off between transient and asymptotic behaviours, in the same spirit as [8], but differing from it in two important aspects. First, instead of minimizing the ultimate upper bound of the error, the volume of the ellipsoid to which the error belongs is minimized, which leads to minimal error solutions. Considering the volume of the solution as an objective to minimize is an idea that has not been presented in the literature before. Second, while the whole state

estimation is guaranteed to converge to the real state, the proposed design method allows the user to select a part of the state, whose associated estimation error is minimized, which gives tighter solutions for the considered part of the state. These facts make the proposed approach different from other techniques developed for observer design, such as the ones based on $\mathcal{H}_\infty$ optimization [91, 3] or the input-to-state stability (ISS) concept [5, 6] which do not minimize explicitly the volume of the steady state ellipsoid's error.

Finally it is shown how the proposed approach can be effectively applied to the problem of estimating the disturbances in UAVs, by using the high-order model introduced in Section 7.2. The possibility of choosing only a part of the state whose associated error wants to be minimized is exploited here to produce minimum volume error disturbance and fast convergence estimators. The considered example exhibits the effect of the decision variable in the design and the simulation results demonstrate the performance of the observer for different choices of the design parameter estimating a disturbance.

Information of this chapter is organized in two differentiated sections covering the design of QB observers (Section 8.1) and the disturbance estimator design and its application (Section 8.3) respectively.

8.1   Optimal Quadratic Boundedness Observer

Consider the dynamic system defined as [1]

$$
\begin{cases}
\dot{\boldsymbol{x}} = \mathbf{A}\boldsymbol{x} + \mathbf{B}\boldsymbol{u} + \mathbf{W}_1\boldsymbol{\eta}_1 \\
\boldsymbol{y} = \mathbf{C}\boldsymbol{x} + \mathbf{D}\boldsymbol{u} + \mathbf{W}_2\boldsymbol{\eta}_2 \\
\boldsymbol{z} = \mathbf{E}_1\boldsymbol{x}
\end{cases}
\tag{8.1}
$$

where $\boldsymbol{x} = \boldsymbol{x}(t) \in \mathbb{R}^n$ represents the state, $\boldsymbol{u} = \boldsymbol{u}(t) \in \mathbb{R}^m$ represents the input, $\boldsymbol{y} = \boldsymbol{y}(t) \in \mathbb{R}^p$ represents the output, $\boldsymbol{\eta}_1 = \boldsymbol{\eta}_1(t) \in \mathbb{R}^{l_1}$ represents the disturbances affecting the dynamic model, $\boldsymbol{\eta}_2 = \boldsymbol{\eta}_2(t) \in \mathbb{R}^{l_2}$ represents the measurement noise and $\boldsymbol{z} = \boldsymbol{z}(t) \in \mathbb{R}^q$ represents a subset of the state vector. Moreover, the matrices $\mathbf{A} \in \mathbb{R}^{n \times n}$, $\mathbf{B} \in \mathbb{R}^{n \times m}$, $\mathbf{W}_1 \in \mathbb{R}^{n \times l_1}$, $\mathbf{C} \in \mathbb{R}^{p \times n}$, $\mathbf{D} \in \mathbb{R}^{p \times m}$, $\mathbf{W}_2 \in \mathbb{R}^{p \times l_2}$ and $\mathbf{E}_1 \in \mathbb{R}^{q \times n}$ are constants with $\mathbf{E}_1$ representing a part of a permutation matrix.

Let the vector containing the disturbance and noise terms, denoted as $\bar{\boldsymbol{\eta}} = (\boldsymbol{\eta}_1^\top, \boldsymbol{\eta}_2^\top)^\top$, be bounded by the ellipsoid $\epsilon_{\mathbf{Q}}(\bar{\boldsymbol{\eta}})$, i.e.,

$$
\bar{\boldsymbol{\eta}}^\top \mathbf{Q} \bar{\boldsymbol{\eta}} \le 1
\tag{8.2}
$$

and let the estimation of the state $\boldsymbol{x}$ be represented by $\hat{\boldsymbol{x}}$ and the error associated to the state estimation be denoted as $\boldsymbol{e} = \boldsymbol{x} - \hat{\boldsymbol{x}}$. In addition, let the error of estimation of $\boldsymbol{z}$ be defined as $\boldsymbol{e}_z = \mathbf{E}_1 \boldsymbol{e}$.

The main goal of this section is to design a linear observer for the state, which provides some guarantees on the ultimate bounds and transient behaviour of the signal $\boldsymbol{e}_z$.

---

[1]Throughout the section, the dependence of signals on time is omitted to ease the notation.

To this end, let the dynamics of $\boldsymbol{x}$ be rewritten as

$$\dot{\boldsymbol{x}} = \mathbf{A}\boldsymbol{x} + \mathbf{B}\boldsymbol{u} + \mathbf{W}_1\boldsymbol{\eta}_1 + \mathbf{K}\boldsymbol{y} - \mathbf{K}\boldsymbol{y} \tag{8.3}$$

which leads to

$$\dot{\boldsymbol{x}} = (\mathbf{A} + \mathbf{KC})\,\boldsymbol{x} + \mathbf{B}\boldsymbol{u} + \mathbf{KD}\boldsymbol{u} + \mathbf{W}_1\boldsymbol{\eta}_1 + \mathbf{KW}_2\boldsymbol{\eta}_2 - \mathbf{K}\boldsymbol{y} \tag{8.4}$$

By defining the estimation dynamics as

$$\dot{\hat{\boldsymbol{x}}} = (\mathbf{A} + \mathbf{KC})\,\hat{\boldsymbol{x}} + (\mathbf{B} + \mathbf{KD})\,\boldsymbol{u} - \mathbf{K}\boldsymbol{y}, \tag{8.5}$$

the dynamics of the estimation error are described by

$$\dot{\boldsymbol{e}} = (\mathbf{A} + \mathbf{KC})\,\boldsymbol{e} + \mathbf{W}_1\boldsymbol{\eta}_1 + \mathbf{KW}_2\boldsymbol{\eta}_2 \tag{8.6}$$

Definition 8.1.1. The system in Eq. (8.6), under conditions in Eq. (8.2) is quadratically bounded for a given symmetric matrix $\mathbf{P} > 0$, if the derivative of the quadratic Lyapunov function $V = \boldsymbol{e}^{\top}\mathbf{P}\boldsymbol{e}$ given by

$$\dot{V} = 2\boldsymbol{e}^{\top}\mathbf{P}\dot{\boldsymbol{e}} \tag{8.7}$$

is guaranteed to be negative for values of $V > 1$, i.e.,

$$V = \boldsymbol{e}^{\top}\mathbf{P}\boldsymbol{e} > 1 \Rightarrow \dot{V} = 2\boldsymbol{e}^{\top}\mathbf{P}\dot{\boldsymbol{e}} < 0 \quad \forall\,\bar{\boldsymbol{\eta}} \in \epsilon_{\mathbf{Q}} \tag{8.8}$$

The quadratic boundedness conditions stated above can be formulated as a feasibility problem.

Proposition 8.1.1. The dynamic system Eq. (8.6) with Eq. (8.2) is quadratically bounded with a Lyapunov matrix $\mathbf{P}$ if there exists a symmetric matrix $\mathbf{P} > 0$, a matrix $\mathbf{K}$ and a scalar $\alpha > 0$ for which

$$\begin{bmatrix} \mathbf{\Psi} + \alpha\mathbf{P} & \mathbf{PW}_1 & \mathbf{YW}_2 \\ \mathbf{W}_1^{\top}\mathbf{P} & & \\ \mathbf{W}_2^{\top}\mathbf{Y}^{\top} & & -\alpha\mathbf{Q} \end{bmatrix} \leq 0 \tag{8.9}$$

being

$$\mathbf{\Psi} = \mathbf{A}^{\top}\mathbf{P} + \mathbf{PA} + \mathbf{YC} + \mathbf{C}^{\top}\mathbf{Y}^{\top} \tag{8.10}$$

and

$$\mathbf{Y} = \mathbf{PK} \tag{8.11}$$

Proof. The time rate of change of the quadratic Lyapunov function $V(\boldsymbol{e}) = \boldsymbol{e}^{\top}\mathbf{P}\boldsymbol{e}$ along the solutions of Eq. (8.6) is given by

$$\begin{aligned} \dot{V}(e, \boldsymbol{\eta}_1, \boldsymbol{\eta}_2) \;&= \boldsymbol{e}^{\top}\mathbf{P}\dot{\boldsymbol{e}} + \dot{\boldsymbol{e}}^{\top}\mathbf{P}\boldsymbol{e} = \boldsymbol{e}^{\top}\mathbf{P}\left((\mathbf{A} + \mathbf{KC})\,\boldsymbol{e} + \mathbf{W}_1\boldsymbol{\eta}_1 + \mathbf{KW}_2\boldsymbol{\eta}_2\right) + \\ &\quad \left(\boldsymbol{e}^{\top}(\mathbf{A} + \mathbf{KC})^{\top} + \boldsymbol{\eta}_1^{\top}\mathbf{W}_1^{\top} + \boldsymbol{\eta}_2^{\top}\mathbf{W}_2^{\top}\mathbf{K}^{\top}\right)\mathbf{P}\boldsymbol{e} \\ &= \boldsymbol{e}^{\top}\left(\mathbf{A}^{\top}\mathbf{P} + \mathbf{PA} + \mathbf{PKC} + \mathbf{C}^{\top}\mathbf{K}^{\top}\mathbf{P}\right)\boldsymbol{e} + \\ &\quad \boldsymbol{\eta}_1^{\top}\mathbf{W}_1^{\top}\mathbf{P}\boldsymbol{e} + \boldsymbol{e}^{\top}\mathbf{PW}_1\boldsymbol{\eta}_1 + \boldsymbol{\eta}_2^{\top}\mathbf{W}_2^{\top}\mathbf{K}^{\top}\mathbf{P}\boldsymbol{e} + \boldsymbol{e}^{\top}\mathbf{PKW}_2\boldsymbol{\eta}_2 \end{aligned} \tag{8.12}$$

Given the unknown nature of $\boldsymbol{\eta}_1$ and $\boldsymbol{\eta}_2$, it is not guaranteed that $\dot{V}$ is negative definite. However, note that the condition in Eq. (8.2), bounds the values of $\boldsymbol{\eta}_1$ and $\boldsymbol{\eta}_2$, making $\dot{V} < 0$ for sufficient large values of $\boldsymbol{e}$ and any choice of $\mathbf{K}$ that makes $\mathbf{A} + \mathbf{KC} < 0$.

Defining $\bar{\boldsymbol{x}} = \left(\boldsymbol{e}^\top, \bar{\boldsymbol{\eta}}\right)^\top$ and making the change of variables $\mathbf{Y} = \mathbf{PK}$, the last equation can be rewritten in a quadratic form as

$$
\dot{V}(\bar{\boldsymbol{x}}) = \bar{\boldsymbol{x}}^\top
\begin{bmatrix}
\boldsymbol{\Psi} & \mathbf{PW}_1 & \mathbf{YW}_2 \\
\mathbf{W}_1^\top \mathbf{P} & \mathbf{0} & \mathbf{0} \\
\mathbf{W}_2^\top \mathbf{Y}^\top & \mathbf{0} & \mathbf{0}
\end{bmatrix}
\bar{\boldsymbol{x}}
\tag{8.13}
$$

which is negative semi-definite in the case that

$$
\begin{bmatrix}
\boldsymbol{\Psi} & \mathbf{PW}_1 & \mathbf{YW}_2 \\
\mathbf{W}_1^\top \mathbf{P} & \mathbf{0} & \mathbf{0} \\
\mathbf{W}_2^\top \mathbf{Y}^\top & \mathbf{0} & \mathbf{0}
\end{bmatrix}
\leq 0
\tag{8.14}
$$

On the other hand, considering the condition $V = \boldsymbol{e}^\top \mathbf{P} \boldsymbol{e} > 1$ and Eq. (8.2), the inequality

$$
\boldsymbol{e}^\top \mathbf{P} \boldsymbol{e} > \bar{\boldsymbol{\eta}}^\top \mathbf{Q} \bar{\boldsymbol{\eta}},
\tag{8.15}
$$

can be established or, equivalently,

$$
\bar{\boldsymbol{x}}^\top
\begin{bmatrix}
-\mathbf{P} & \mathbf{0} \\
\mathbf{0} & \mathbf{Q}
\end{bmatrix}
\bar{\boldsymbol{x}} < 0
\tag{8.16}
$$

which implies that the symmetric matrix

$$
\begin{bmatrix}
-\mathbf{P} & \mathbf{0} \\
\mathbf{0} & \mathbf{Q}
\end{bmatrix}
< 0.
\tag{8.17}
$$

By applying the S-procedure over the inequalities Eq. (8.14) and Eq. (8.17), Eq. (8.9) is obtained.
$\square$

Proposition 8.1.2. The quadratic boundedness in Eq. (8.9) implies exponential convergence of the error $\boldsymbol{e}$ to the interior of $\epsilon_{\mathbf{P}}(\boldsymbol{e})$ with decay rate driven by α provided that $\bar{\boldsymbol{\eta}}$ fulfills Eq. (8.2).

Proof. Pre and post-multiplying Eq. (8.9) by $\bar{\boldsymbol{x}}^\top$ and $\bar{\boldsymbol{x}}$, respectively, leads to

$$
\dot{V}(\boldsymbol{e}) + \alpha V(\boldsymbol{e}) - \alpha \bar{\boldsymbol{\eta}}^\top \mathbf{Q} \bar{\boldsymbol{\eta}} \leq 0
\tag{8.18}
$$

By using Eq. (8.2), it is clear that

$$
\dot{V}(\boldsymbol{e}) \leq \alpha \bar{\boldsymbol{\eta}}^\top \mathbf{Q} \bar{\boldsymbol{\eta}} - \alpha V(\boldsymbol{e}) \leq \alpha \left(1 - V(\boldsymbol{e})\right)
\tag{8.19}
$$

which makes $\dot{V}(\boldsymbol{e}) < 0$ for $\boldsymbol{e}^\top \mathbf{P} \boldsymbol{e} > 1$.

By integrating the case scenario in which $\dot{V}'(\boldsymbol{e}) = \alpha\left(1 - V'(\boldsymbol{e})\right)$, it can be seen that

$$V(\boldsymbol{e}) \le 1 + (V_0 - 1)\exp\left(-\alpha t\right) \tag{8.20}$$

with $V_0 = V(t_0) = \boldsymbol{e}(t_0)^\top \mathbf{P}\boldsymbol{e}(t_0)$ representing the unknown value of $V(t)$ at the initial time instant t_0. $\forall t > t_0$ the solutions of $V(\boldsymbol{e}(t))$ are ultimately bounded by $V = 1$, the errors $\boldsymbol{e}$ are guaranteed to converge to $\epsilon_{\mathbf{P}}(\boldsymbol{e})$ whenever $V_0 > 1$ and will remain inside $\epsilon_{\mathbf{P}}(\boldsymbol{e})$ as soon as they reach it or as long as $V_0 < 1$. Moreover, the value α modulates the decay rate: the higher α, the higher the convergence rate. $\qquad\square$

As a consequence of the convergence guarantee of $\boldsymbol{e}$ to $\epsilon_{\mathbf{P}}(\boldsymbol{e})$, the estimation error $\boldsymbol{e}_z$ is guaranteed to converge to the interior of the ellipsoid $\epsilon_{\mathbf{P}_z}(\boldsymbol{e}_z)$, where $\epsilon_{\mathbf{P}_z}(\boldsymbol{e}_z)$ is the resulting ellipsoid after projecting $\epsilon_{\mathbf{P}}(\boldsymbol{e})$ over the vector space generated by the rows of $\mathbf{E}_1$, $\langle \mathbf{E}_1 \rangle$ and

$$\mathbf{P}_z = \mathbf{E}_1 \mathbf{P} \mathbf{E}_1^\top - \mathbf{E}_1 \mathbf{P} \mathbf{E}_2^\top \left(\mathbf{E}_2 \mathbf{P} \mathbf{E}_2^\top\right)^{-1} \mathbf{E}_2 \mathbf{P} \mathbf{E}_1^\top \tag{8.21}$$

with $\mathbf{E}_2$ representing any orthogonal complement of $\mathbf{E}_1$, i.e., $\mathbf{E}_1 \mathbf{E}_2^\top = \mathbf{0}$. An exhaustive derivation is provided in the Ap. E.

8.2 State observer design

From the statements presented above, given a fixed measure of the ellipsoid containing the terms $\bar{\boldsymbol{\eta}}$, it can be established that the estimation error $\boldsymbol{e}_z$ will depend on:

- The size of $\epsilon_{\mathbf{P_z}}(\boldsymbol{e}_z)$, which represents a measure of the ultimate error bounds and can be measured through the volume of the ellipsoid

$$\text{Vol}\left(\epsilon_{\mathbf{P}_z}\right) = \frac{B_q}{\sqrt{\det\left(\mathbf{P}_z\right)}}, \tag{8.22}$$

  where B_q represents the volume of the unit-ball of dimension q (the dimension of the row space of $\mathbf{E}_1$).

- The convergence rate represented by α, which defines the behaviour of the transient response.

Ideally, the chosen observer gain $\mathbf{K}$ must try to maximize α while minimizing $\text{Vol}\left(\epsilon_{\mathbf{P}_z}\right)$. However, both objectives are not independent but are subject to the satisfaction of the constraint Eq. (8.9). Indeed, there does not necessarily exist a solution of the problem which optimizes α and $\text{Vol}\left(\epsilon_{\mathbf{P}_z}\right)$ at the same time.

Following the spirit of [8], but re-scaling the objectives as suggested in [65], a parametrized mixed objective function that fuses both objectives can be defined as

$$J_\mu(\alpha, \mathbf{P}_z) = \mu J_1 + (1 - \mu) J_2 \tag{8.23}$$

where μ has been introduced as a design parameter that defines the trade-off between J_1 and J_2, defined as

$$J_1 = \left(\frac{\mathrm{Vol}(\epsilon_{\mathbf{P}_z}) - \mathrm{Vol}(\epsilon_{\mathbf{P}_z})^\star}{\mathrm{Vol}(\epsilon_{\mathbf{P}_z})^\dagger - \mathrm{Vol}(\epsilon_{\mathbf{P}_z})^\star} \right) \tag{8.24}$$

and

$$J_2 = \left(\frac{\alpha - \alpha^\star}{\alpha^\dagger - \alpha^\star} \right). \tag{8.25}$$

The introduction of J_i, $i = 1, 2$ scales the values of the individual objectives. $J_i \in [0, 1]$ assigns the value of 0 to the complete achievement of the objective, i.e., $\alpha = \alpha^\star$, $\mathrm{Vol}(\epsilon_{\mathbf{P}_z}) = \mathrm{Vol}(\epsilon_{\mathbf{P}_z})^\star$ and the value of 1 to the nadir (worst) values $\alpha = \alpha^\dagger$, $\mathrm{Vol}(\epsilon_{\mathbf{P}_z}) = \mathrm{Vol}(\epsilon_{\mathbf{P}_z})^\dagger$.

The optimal quadratic bounded state observer which minimizes Eq. (8.23), can be designed by solving the optimization problem

$$\min_{\alpha > 0, \mathbf{P} > 0, \mathbf{Y}} \quad J_\mu(\alpha, \mathbf{P}_z)$$
$$\text{subject to} \quad Eq. \ (8.9) \tag{8.26}$$

for a fixed value of μ. In general the solution of Eq. (8.26) is not straightforward. However, an alternative optimization problem, which shares the same solution, can be achieved in two steps:

1. The constraint in Eq. (8.9) is not linear due to the product of unknowns α and $\mathbf{P}$. Nevertheless, it can be interpreted as an LMI for constant values of α. Thus, an equivalent problem to Eq. (8.26) can be obtained by splitting it in two nested optimization problems, one efficiently solvable by SDP solvers inside a second one with a single optimization variable

$$\min_{\alpha > 0} \quad J_\mu(\alpha, \mathrm{Vol}(\epsilon_{\mathbf{P}_z}^+)) \tag{8.27}$$

with $\epsilon_{\mathbf{P}_z}^+$ representing the ellipsoid whose associated quadratic matrix $\mathbf{P}_z^+$ is obtained by using Eq. (8.21) with $\mathbf{P} = \mathbf{P}^+$, that solves the optimization problem for fixed values of α and μ

$$(\mathbf{P}^+, \mathbf{Y}^+) = \operatorname*{argmin}_{\mathbf{P} > 0, \mathbf{Y}} \quad J_\mu(\alpha, \mathrm{Vol}(\epsilon_{\mathbf{P}_z}))$$
$$\text{subject to} \quad Eq. \ (8.9) \tag{8.28}$$

2. For fixed values of α and μ, J_2 is a constant and μB_q acts as a scaling parameter. Given that the square root function present in Eq. (8.22) is monotonically increasing, solving Eq. (8.28) is equivalent to maximizing the alternative objective function $J'(\mathbf{P}_z) = \det(\mathbf{P}_z)$ subject to Eq. (8.9).

Although the determinant of $\mathbf{P}_z$ can be rendered convex, since $\mathbf{P}_z$ is positive definite by construction, its relation to the original unknown $\mathbf{P}$ cannot due to the product on the right

hand side of Eq. (8.21). This drawback can be overcome by considering a new matrix $\mathbf{X} \geq 0$ and the constraint

$$\mathbf{X} \leq \mathbf{P}_z. \tag{8.29}$$

Eq. (8.29) can be expressed as an LMI on $\mathbf{P}$ by considering it as the Schur complement of $\mathbf{P}'_{22}$ in $\mathbf{P}'$, with

$$\mathbf{P}' = \begin{bmatrix} \mathbf{P}'_{11} & \mathbf{P}'_{12} \\ \mathbf{P}'_{21} & \mathbf{P}'_{22} \end{bmatrix} = \begin{bmatrix} \mathbf{E}_1\mathbf{P}\mathbf{E}_1^\top - \mathbf{X} & \mathbf{E}_1\mathbf{P}\mathbf{E}_2^\top \\ \mathbf{E}_2\mathbf{P}\mathbf{E}_1^\top & \mathbf{E}_2\mathbf{P}\mathbf{E}_2^\top \end{bmatrix} > 0. \tag{8.30}$$

Given that $\mathbf{E} = (\mathbf{E}_1^\top\,\mathbf{E}_2^\top)^\top$ is a full rank matrix representing a permutation, the transformation

$$\mathbf{E}^\top\mathbf{P}'\mathbf{E} \geq 0, \tag{8.31}$$

leads to the simpler matrix inequality independent of $\mathbf{E}_2$

$$\mathbf{P} - \mathbf{E}_1^\top\mathbf{X}\mathbf{E}_1 \geq 0 \tag{8.32}$$

The previous condition implies the existence of an ellipsoid $\epsilon_{\mathbf{X}}(\boldsymbol{e}_z)$ that encloses $\epsilon_{\mathbf{P}_z}(\boldsymbol{e}_z)$. Minimizing the volume of $\epsilon_{\mathbf{X}}(\boldsymbol{e}_z)$, i.e., maximizing the determinant of the matrix $\mathbf{X}$ will make $\epsilon_{\mathbf{X}}(\boldsymbol{e}_z)$ converge to the minimum volume $\epsilon_{\mathbf{P}_z}(\boldsymbol{e}_z)$ as long as no additional conditions over $\mathbf{X}$ are applied.

As a result of the above, Eq. (8.28) can be substituted by the convex optimization problem

$$
\begin{aligned}
(\mathbf{X}^+, \mathbf{P}^+, \mathbf{Y}^+) = &\operatorname*{argmax}_{\mathbf{X}>0,\mathbf{P}>0,\mathbf{Y}} \quad \det(\mathbf{X}) \\
\text{subject to} \quad & \quad Eq.\ (8.9) \\
& \quad Eq.\ (8.32)
\end{aligned} \tag{8.33}
$$

which guarantees that $\epsilon_{\mathbf{X}}^+ = \epsilon_{\mathbf{P}_z}^+$. Note that since μ is not present in Eq. (8.33), the optimal values $\mathbf{X}^+ = \mathbf{X}^+(\alpha)$, $\mathbf{P}^+ = \mathbf{P}^+(\alpha)$ and $\mathbf{Y}^+ = \mathbf{Y}^+(\alpha)$ will only depend on the chosen value α.

Taking into account the previous comments, the optimal quadratic bounded observer represented by $\mathbf{K}^\star = (\mathbf{P}^\star)^{-1}\mathbf{Y}^\star$ is given by the solution of the optimization problem in Eq. (8.27) with $\epsilon_{\mathbf{X}}^+ = \epsilon_{\mathbf{P}_z}^+$ and $\mathbf{X}^+$ being the solution of Eq. (8.33).

8.3 UAV optimal quadratic boundedness observer

In this section, we use the design procedure presented in Section 8.1 to generate an observer for the disturbance of an UAV which dynamics are represented by Eq. (7.16) under measurement equations represented by those in Section 7.3.3 i.e.

$$\boldsymbol{y} = \begin{pmatrix} {}^w\boldsymbol{v} \\ {}^b\boldsymbol{\omega} \\ \frac{1}{m}\left(\mathbf{L}^\top\boldsymbol{d} + \boldsymbol{f}_a\right) \end{pmatrix} + \boldsymbol{v}_k = \mathbf{C}\boldsymbol{x}_k + \mathbf{D}\boldsymbol{u}_k + \mathbf{W}_2\boldsymbol{v}_k,$$

where

$$\mathbf{C} = \left(\text{blkdiag}(\tfrac{1}{m}\mathbf{I}_3,\; {}^b\mathbf{J}^{-1}\mathbf{L}^\top,\; \tfrac{1}{m}\mathbf{L}^\top)\quad \mathbf{0}_{9\times 6(r-1)-3}\right),$$

$$\mathbf{D} = \frac{1}{m}\left(\begin{array}{c|c} \mathbf{0}_{6\times 3} & \\ \hline \mathbf{I}_{3\times 3} & \mathbf{0}_{9\times 3}\end{array}\right),$$

$$\mathbf{W}_2 = \mathbf{I}_9,$$

and $\boldsymbol{u}_k = \boldsymbol{w}_{a_k}$

To demonstrate the estimation performance, we use the simulation setup presented in Section 7.3.4 and Fig. 7.1 when the system is affected by the disturbance force acting on the world x direction in Fig. 7.2. Outputs of the state estimation process produce estimates of the vector $\boldsymbol{y}$ for which the measurement errors have been identified to be inside an ellipsoid $\epsilon_{\mathbf{Q}_2}(\boldsymbol{\eta}_2)$ with

$$\mathbf{Q}_2 = \begin{pmatrix} 1.5 & -0.3 & 0.3 & 8.3 & -3.2 & -3.1 & -0.2 & -0.02 & -0.1 \\ & 0.7 & -0.1 & -10.5 & 9.3 & -6.2 & 0.04 & -0.03 & -0.01 \\ & & 0.9 & 3.30 & 3.7 & -3.9 & 0.02 & -0.02 & -0.09 \\ & & & 2903 & 111.7 & -277.8 & -2.4 & -0.6 & -0.2 \\ & & & & 4281 & 242.1 & 0.6 & 2.5 & -1.5 \\ & & & & & 951.2 & -1.6 & 1.6 & 1.05 \\ & \text{SYM} & & & & & 0.2 & -0.01 & -0.01 \\ & & & & & & & 0.1 & -0.01 \\ & & & & & & & & 0.1 \end{pmatrix} \tag{8.34}$$

As before, the wrench is generated by the model in Eq. (4.30) and parameters in Eq. (4.31) and any error model is expected to be collected under the disturbance $\boldsymbol{d}$.

The value ofthe disturbance model order has been set to $r = 3$ while $\mathbf{Q}_1 = 10^6 \mathbf{I}_6$ has been selected big enough to make $\epsilon_{\mathbf{Q}_1}(\boldsymbol{\eta}_1)$ sufficiently small enough while taking into account possible numerical errors on the simulation. As consequence, the matrix

$$\mathbf{Q} = \frac{1}{2}\begin{pmatrix} \mathbf{Q}_1 & \mathbf{0} \\ \mathbf{0} & \mathbf{Q}_2 \end{pmatrix} \tag{8.35}$$

defines the model and measurement errors ellipsoid.

Since in this case the ultimate goal is to estimate only the disturbances $\boldsymbol{d}$ whereas the exact values of the remaining state are irrelevant, $\mathbf{E}_1$ has been chosen as

$$\mathbf{E}_1 = (\mathbf{0}_{6\times 6}, \mathbf{H}) \tag{8.36}$$

By using the previous data, the optimization problem in Eq. (8.33) has been solved for values of $\alpha \in [0, 20]$. The optimal volume of the produced ellipsoids $\epsilon_{\mathbf{X}}^+(\alpha)$ is shown in Fig. 8.1.

The results of the objective function for several values of μ along with the optimal value as a function of α can be found on Fig. 8.2. Finally, the optimal values of the unnormalized objectives
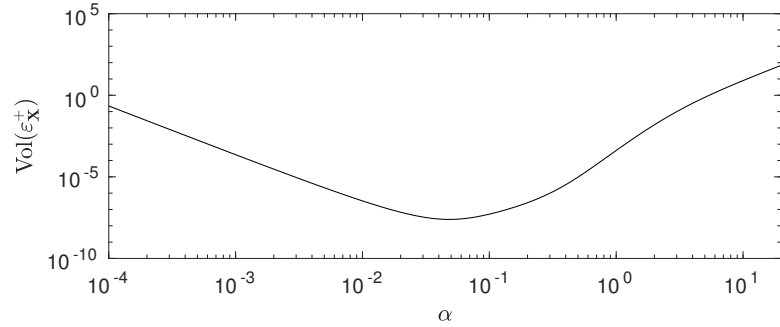
FIGURE 8.1: Minimum value of $\mathrm{Vol}(\epsilon_{\mathbf{X}}^{+})$ as a function of α.
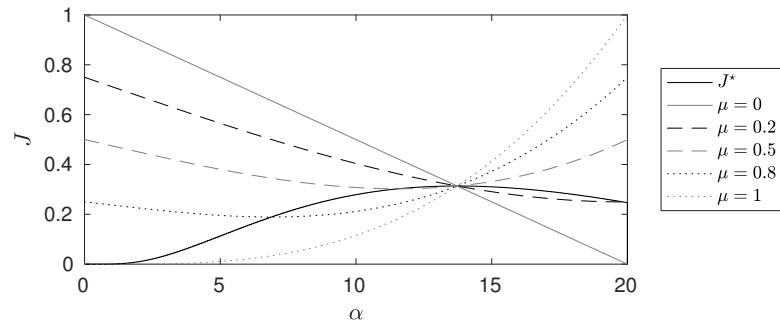
FIGURE 8.2: Values of the objective function as a function of α for fixed μ and optimal value of the objective function as a function of α.

$\alpha^{\star}$ and $\mathrm{Vol}(\epsilon_{\mathbf{X}}^{+})$ as a function of the design parameter μ are shown in Fig. 8.3.

The results of the estimation disturbance for the values of the decision variable $\mu = 0.2$ and $\mu = 0.95$ are shown in Fig. 8.4. Note that the estimation of the disturbance is not straightforward since in the piecewise transitions the signal derivatives are by definition unbounded. However, even in this case, the filter design guarantees the error stability and, by comparing the two outputs, it can be appreciated that when the hypothesis of the filter (in this case $\dddot{d} \in \epsilon_{\mathbf{Q}_1}(\boldsymbol{\eta}_1)$) is fulfilled the estimation corresponding to higher μ is slower than the one with lower value of μ, while it converges to a smaller region in the neighbourhood of the true signal, as it can also be observed in Fig. 8.3.
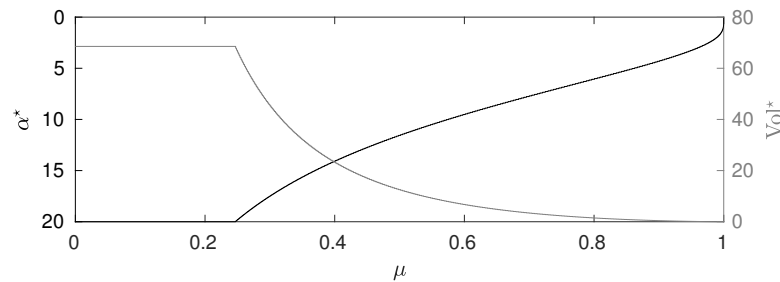
FIGURE 8.3: Optimal values of the convergence rate and ultimate bounding volume as a function of the design parameter.
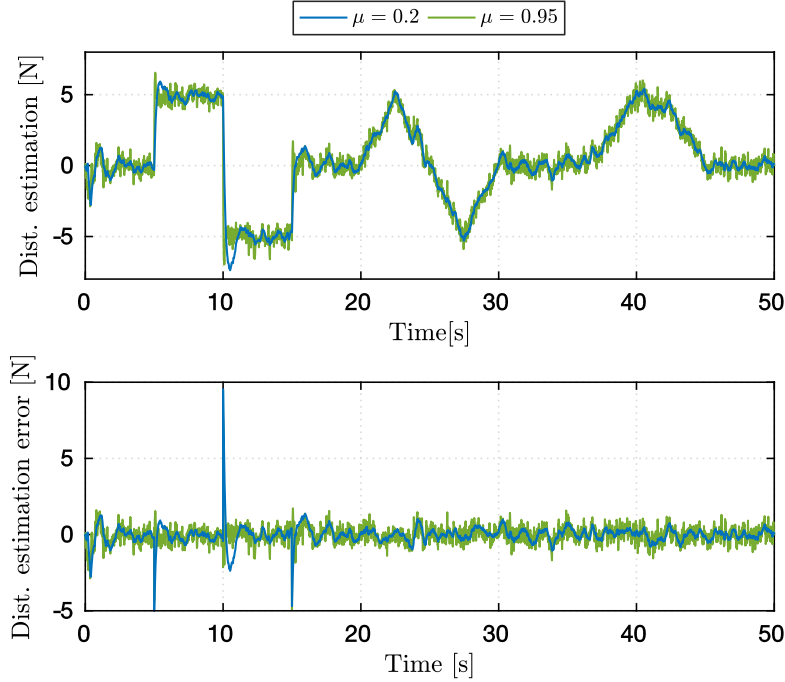
FIGURE 8.4: Disturbance estimation and errors for the proposed observers

8.4   Conclusion

Under the QB methodology the disturbance estimator tuning reduces to the specification of the sensor and model error ellipsoids, the degree, r, of the $r-th$ derivative to expand the disturbance model and the choice of μ. For a given disturbance, and experimental platform, r and the error ellipsoids may be determined and as consequence the only variable left is the design parameter μ. The choice of μ can be made in a meaningful way by giving priority to one of the objectives, i.e, low values of μ prioritize the convergence rate while high values will favour the minimum volume objective. Furthermore, even not having any criterion on the value of μ the derived estimator will still be stable.

Relations exist between the derived QB disturbance observer and the HODO disturbance estimator in Chap. (7). In essence both filters provide linear corrections to the estimation by means of a constant gain determined in advance. Under this viewpoint, the QB estimators can be generated by using the QB obtained gain in the same HODO filter and vice versa. Differences arise then, on how the filter gain is chosen and the guarantees associated to the particular choice. In particular, the QB procedure guarantees stability and a trade-off between the minimum volume error ellipsoid and the decay rate scheduled by the design parameter μ under ellipsoid bounding of the model and sensor errors. In contrast, any other stable gain selected for the HODO only guarantees a bounded estimation of the disturbance.

Part IV

Concluding Remaks

Chapter 9

Concluding Remarks

Navigating under physical interaction or the continuous effect of disturbances requires a state estimation solution that takes into account the effect of these phenomena.

This thesis approaches this problem in the case of considering a limited but standard sensor suite given by an IMU, a GPS and a 3axial magnetometer. To this end models of the aircraft dynamics, sensors and characteristics of the specific system are provided in the first part of this dissertation.

The ability of the considered sensor suite to allow the reconstruction of the state is assessed by performing linear and non-linear observability analyses over the system. These studies reveal the existence of singular observability conditions associated to a state space region inside which the state cannot be uniquely identified.

The traditional Extended Kalman filter formulation is then adapted to our system and several formulations are obtained and compared in the case of non-singular operations. Implementation efficiency and accuracy is discussed for each method. In order to circumvent the singular observability problems a Schmidt Kalman Filter is provided. The proposed SKF slightly modifies the presented EKF structure to take into account the nature of the indistinguishable regions. This solution does not suffer from state drifts inside the indistinguishable region and is demonstrated to provide more coherent and precise results in singular conditions while still providing similar performance in non-singular ones.

A disturbance model and several disturbance estimation methods based on the assumption of full state availability (provided, for example, by the state estimators of the previous chapters) has been developed. The linearity of the wrench (force, torque) – twist (linear and angular velocities) relation under a proper coordinate selection is exploited to construct disturbance models. These models are then used to derive linear filters that provide estimations of the external disturbances acting over the aircraft. Filters from the literature are modified and simplified to contemplate the proposed model and compared with new Kalman based filters that exploit linearity to obtain optimal estimations.

The design of Quadratic Bounded linear estimators that take into account bounds on the model uncertainty and measurement noise to provide estimations that consider explicitly a trade off between convergence velocity and minimum error solutions is presented and discussed. Finally, the QB formulation is applied to derive a disturbance observer for the UAV for which the effect on performance of the design parameter is evaluated.

In summary, this thesis contributes in three main fields related to the perception of UAVs. The provided advances regarding state observability and state estimation are generally applicable to any kind of VTOL UAVs equipped with the considered sensor suite. The disturbance estimation contribution extends the traditional perception capabilities of any UAV aircraft equipped with a state estimator solution providing information about the interaction with the environment by means of wrench like effects.

9.1   Summary and contributions

Chapters 2 and 3:

These chapters discuss the proper selection of state parametrizations regarding possible reference frames and many attitude choices, Chap. (2), and the alternative derivations for the system dynamics, Chap. (3). Despite the basic level of the derivations presented there, it is worth noting that the discussions provided are usually not present in the literature, where the various alternatives seem to have been obviated.

Chapter 4:

Chap. (4) is devoted to the description of platform specifics, starting from sensor models and their calibration and finishing with hardware description and actuation principles.

A method is proposed to identify the ellipsoid parameters that allow calibrating three axial sensors ensuring convergence in case of considering noise. Although this is not an utmost contribution to the field, this method is proposed here for the first time, to the best of the author's knowledge.

Chapter 5:

The observability analysis of the system under the consideration of the basic navigation sensor suite composed by an IMU, a GPS and a magnetometer had not been considered before. This chapter shows that a system given by the vehicle dynamics and measure equations is guaranteed to be observable under the observability strict definition. At the same time, it is shown that there exist particular flight conditions associated to singular inputs and system symmetries for which the system state can not be inferred from input output information. These conflicting conditions can be derived from either using an LTV analysis approach, which needs the linealization of the system or by a non-linear approach. It can be appreciated that LTV methods are not free of problems, since the results provided may not match for different parametrizations of the state. In contrast, the nonlinear approach presented, although more complex, is free of that problem. The most relevant result comes from noting that the hover condition, one of the most usual

flight configurations in VTOL UAV missions, has an associated singular input and system symmetry and as a consequence the state can not be discerned without ambiguity. For this flight condition, the indistinguishable region which describes the connected set of possible state solutions of the estimation problem is derived. This problem is confirmed in simulation and its effects over noise and ideal scenarios are reported.

Chapter 6:

This chapter presents EKF based estimators for the system under study. Four different, a priori equivalent, dynamic models considering different velocity realizations and different ways of composing attitude are explored here. For each of them, their associated discrete time event-based estimators are derived and precise algorithmic expressions that describe their implementation are presented. In particular, motivated by the idempotence property of the linearized dynamics corresponding to one of the models under study, the closed form (not relying in numerical solutions) of one of the filters is completely derived. The filters equations along with a non-straightforward but efficient initialization procedure and a description of the initialization parameters allow to compare simulation results of the estimation procedure for the four filters.

This chapter includes also the derivation of a filter that improves the EKF estimations in conflicting observability scenarios. The proposed filter is based on the SKF formulation along with the observability results in the previous chapter. The formulated filter identifies a direction in space where the accelerometer biases are more prone to drift, analyses which component of the estimation bias vector will be more affected and freezes its value in the filter update step. From an implementation perspective, the SKF can be integrated by simple adding two actions in the update step of the EKF. Results presented over two different scenarios show how both filters perform, verify the proper behaviour of the SKF in the indistinguishable region and its good performance in normal observability conditions.

Chapter 7:

Contributions of this chapter have impact in modelling and disturbance estimation areas. Regarding modelling, we present in this chapter an extended linear model which contains system navigation dynamics along with a linear high order model for the disturbance. The linearity of the system navigation dynamics is not the product of a linearization but the result of a proper selection of the system state which is represented by the system linear and spin momenta in the world frame. The high order model used to describe the disturbance dynamics represents a generalization of the null derivative condition used in many works in the literature, however this choice allow to estimate fast varying disturbances and also consider explicitly uncertainty in the systems.

The presented model is used to reformulate disturbance estimators already present in the literature. In order to take advantage of the linearity of the model two disturbance Kalman filters estimators are proposed and its performance is compared with the previous one. The inherent optimality under the Kalman filters and its ability to accommodate redundant measurements makes this estimators outperform. In practice, for any specific situation any filter could be specifically tuned to provide good results but more robustness of the

tracking performance has been experienced when tuning the Kalman observers than when fine-tuning the other type of observers.

Chapter 8:

The main contributions of Chap. (8) are related with the design of state observers for linear systems under quadratic bounded model and measurement uncertainties and its application to disturbance estimation.

The first part of the chapter describes the design of quadratically bounded observers. This design procedure takes into account the existence of a trade-off between the convergence rate and the volume of the ultimate (steady-state) error bounding ellipsoid. In order to handle these conflicting objectives, a scalarised objective function with one design parameter is built, such that the design problem is made convex. The main contributions of the presented methodology are twofold. First, instead of minimizing the ultimate upper bound of the error, the volume of the ellipsoid to which the error belongs is minimized, which gives minimum error solutions. Second, while the whole state estimation is guaranteed to converge to the real state, the proposed design method allows the user to select a part of the state, whose associated estimation error is minimized, which gives tighter solutions for the considered part of the state.

The later contribution described allows the use of the QB observers as a disturbance observers when used along with the high order model derived in previous chapters. An example is provided to show the effect of the decision variable in the design and the simulation results depict the performance of the observer for different choices of the design parameter estimating a disturbance.

9.2   Next steps and future lines of research

Practical implementation:

Many of the thesis results have been generated to solve a practical application. Even though there exist some parts of the chapters that clearly push the contents of the thesis in that direction as the calibrations in Chap. (4) or the efficient and event-based filter derivations in Chap. (5), there has not been time to test everything on a real platform. Then, the natural next steps have to do with

- On-line testing the estimation algorithms
- Revise the derivation of the the continuous disturbance estimation algorithms considering low level implementation aspects as the discretization, computational burden and/or execution times.
- Working in the integration of both state estimation and disturbance estimation running in the platform at the same time.
- Publishing code. In particular, state estimation algorithms presented here have been carefully coded an implemented as standalone libraries which will be open to the community soon.

GPS model:

In Chap. (4) it is considered that the GPS sensor provides measurements of the cartesian position in a local frame. It has been shown in appendix Ap. D that what really is happening is that the sensor provides measurements of latitude, longitude and altitude and that these measurements can always be converted to the local frame through a non-linear mapping. In the neighbourhood of the origin point of the local frame (up to $\approx 5\,\mathrm{km}$) this mapping is almost linear and a direct relation can be made between real measurements and the world frame position as well as between the measurement noise (assumed gaussian) in the latitude, longitude and altitude coordinates and the noise associated to x, y and z positions. Notice that we have made the assumption that the covariance of the position error was constant but this will not hold if the jacobian associated to the non-linear transformation changes. This condition gets worse as the aircraft operates farther form the origin of the local frame. This can be solved by considering the conversion between ECEF frame and the local frame as part of the measurement equation. This consideration will not affect the observability results since the jacobian of the non-linear transformation in Eq. (D.4) has guaranteed full row rank (its determinant is equal to 1 for any λ_0 φ_0). It will affect the filter equations in Chap. (6), but the EKF derivation could be modified to accommodate the non-linear model.

System symmetries and singular inputs:

The aim of Chap. (5) was to demonstrate that the possibility of determining the state of the UAV platform equipped with an specific sensor suite in specific flight configurations was degraded. Those results arise when examining the conditions for which a codistribution matrix of the system had not maximum row rank. The solutions for which the rank was deficient were found in many cases by simple observation of a common nullspace along every block row of the matrix, i.e., solutions provided for the problem of

$$\begin{pmatrix} \mathbf{A} + \mathbf{B} \\ \mathbf{C} \end{pmatrix} \boldsymbol{v} = 0$$

were found such that $\mathbf{A}\boldsymbol{v} = 0$, $\mathbf{B}\boldsymbol{v} = 0$ and $\mathbf{C}\boldsymbol{v} = 0$, which is equivalent to find

$$\mathrm{null}\begin{pmatrix} \mathbf{A} \\ \mathbf{B} \\ \mathbf{C} \end{pmatrix}$$

Since

$$\mathrm{null}\begin{pmatrix} \mathbf{A} \\ \mathbf{B} \\ \mathbf{C} \end{pmatrix} \subseteq \mathrm{null}\begin{pmatrix} \mathbf{A} + \mathbf{B} \\ \mathbf{C} \end{pmatrix}$$

solutions for which $(\mathbf{A} + \mathbf{B})\,\boldsymbol{v} = 0$ but $\mathbf{A}\boldsymbol{v} \neq 0$ $\mathbf{B}\boldsymbol{v} \neq 0$ were missed. Even though we expect those solutions to be marginal, their implications will scale depending of the times that the aircraft visits this specific region.

In a similar way, the analysis has been restricted to constant values of angular velocity and specific forces. By allowing them to change in time, many more indistinguishable regions might appear.

Attitude parametrization in the incremental error models:

Incremental error models in Chap. (5) and Chap. (6) are derived from the non-linear equations of motion and use minimal attitude representations to parametrize locally the aircraft attitude change. In such a way, singularity points inherent in the minimal representations can be held far from the interest point and singular covariance problems associated to the model error covariance matrix when considering non-minimal attitude parametrizations (quaternions or the rotation matrix) and its contraints simply disappear. It has been shown how those incremental models could be derived by considering the composition of the incremental attitude with the nominal one, either by the left or by the right. In the Chap. (5) we saw how those representations do not lead to the same singular input analysis results. In particular, the composition by the left showed a wider observability region, not present in the other incremental model neither in the non-linear one. Moreover, in Chap. (6) both representation led to different (a priori equivalent) system dynamics that led to different filter equations.

As a future line of research it could be interesting to study the incremental attitude representation

$$\mathring{q} = \mathring{\hat{q}}^x \delta \mathring{q} \mathring{\hat{q}}^{1-x}$$

with $0 \leq x \leq 1$ representing a fraction of the total rotated angle and $\mathring{\hat{q}}^x$ representing its associated rotation quaternion such that

$$\mathring{\hat{q}} = \mathring{\hat{q}}^x \mathring{\hat{q}}^{1-x}$$

which considers the two extreme cases ($x = 0$ leads to the left composition and the case $x = 1$ leads to the right one) but also many more, in order check if it is able to shed light about why both singular input analysis results do not coincide or even if it brings benefits to the singular input analysis or estimation.

Exploiting the initialisation procedure

In the literature, attitude estimators exist which use information of the aircraft angular rate and vector observations (usually magnetic field and accelerometers as if they were free of bias, noise and as if accelerometers sensed gravity) to provide filtered attitude and filtered bias free angular velocity quantities [52, 50]. Those procedures usually work by estimating the attitude from angular velocity integration and by estimating the same quantity through an optimization problem for later fusing them in a filter.

The initialization algorithm proposed in Chap. (6.2.5) may replace the minimization algorithms providing the exact solution in a deterministic way instead of providing an approximation using iterative methods.

Fine improving of the state estimator

In the derivation of the filtering equations for the state estimator of Chap. (6), the assumption of constant specific force, angular velocity and attitude is made to propagate the system nominal state and error covariance, i.e., the state is known at a given time t_k, and it is used to provide estimations at time t_{k+1} by means of Eq. (6.20). This constant assumption approximates the results better the smaller the time interval $t_{k+1} - t_k$ is. This aspect can be improved by considering:

- Higher order approximations to the angular velocity and specific force between IMU updates. When a new IMU measurement arrives, the present implementation propagates the state and error covariance using the last available estimations of the angular velocity and acceleration. However, notice that by having the bias estimated, a new estimation of these quantities can be reconstructed in the present time with the new IMU measurements and in particular the mean of both estimations can be used as an estimation of the mean value of those quantities.

- Since attitude is related with the integral of the angular velocity, constant attitude can only be achieved under zero angular velocity. The change of attitude along the integral of a trajectory can be taken into account in a simple way for constant angular velocities by expressing the rotation by means of the rotation vector parametrization in Section 2.3.4.

Observability under no observable conditions

The state estimator presented solves partially the problem of the solution drift in case of being in singular input conditions. As briefly commented in the dissertation, an ideal estimation would implement the extended Kalman filter during estimation favourable flight conditions and the proposed filter only in the instants that estimation is degraded. This mixed filter implementation has been set aside because the lack of a reliable switching mechanism that identifies if the aircraft is or is not in singular input conditions. The study of the viability of this switching mechanism based in sensor measurements, covariance expected behaviour or any other criteria may be considered in further works.

Next step in estimating disturbances

The high order model introduced in Eq. (7.2) has been used to derive disturbance estimators in Chap. (7) and Chap. (8). In the cases of the KHO or the QB disturbance estimators (Section 7.3.3 and Section 8.3 respectively) the filters have taken profit of the information regarding the disturbance uncertainty in its design phase. In the dissertation, only information of the disturbance bounds at the last derivative considered have been used. However, both methods could conciliate additional information over the bounds of the disturbance at other levels of the model (not only the last derivative) to enhance results.

Part V

Appendices

Appendix A

Skew-symmetric matrices

A skew symmetric matrix can be constructed from a 3-dimensional vector as

$$
[\boldsymbol{x}]_\times = \begin{pmatrix} 0 & -x_3 & x_2 \\ x_3 & 0 & -x_1 \\ -x_2 & x_1 & 0 \end{pmatrix}
$$

Skew symmetric matrices arise naturally to express the cross product of 3-dimensional vectors as a matrix-vector product

$$
\boldsymbol{v} \times \boldsymbol{u} = [\boldsymbol{v}]_\times \boldsymbol{u} = -[\boldsymbol{u}]_\times \boldsymbol{v}
$$

Matrix exponentiation of a skew-symmetric has the property of

$$
\begin{cases} [\boldsymbol{x}]_\times^{2n+1} = (-1)^n \|\boldsymbol{x}\|^{2n} [\boldsymbol{x}]_\times \\ [\boldsymbol{x}]_\times^{2(n+1)} = (-1)^n \|\boldsymbol{x}\|^{2n} [\boldsymbol{x}]_\times^2 \end{cases} \quad \text{for } n = 1, 2, 3, \dots
$$

Appendix B

Lagrange equations

The equations of motion for a rigid body floating in space can be derived from energetic metrics by using the lagrangian formulation.

Let

$$T = \frac{1}{2}\dot{q}^\top \mathbf{M}\dot{q} = \frac{1}{2}\sum_{i=1}^{N}\sum_{j=1}^{N} M_{ij}\dot{q}_i\dot{q}_j \tag{B.1}$$

represent the kinetic energy and

$$U = -mgz_w \tag{B.2}$$

represent the potential energy of a rigid body with respect to an inertial frame.

Let the Lagrangian function be defined as $L = T - U$. Therefore the motion equations of the system can be derived from

$$\frac{\mathrm{d}}{\mathrm{d}t}\left(\frac{\partial L}{\partial \dot{q}_i}\right) - \frac{\partial L}{\partial q_i} = W_i \tag{B.3}$$

Or equivalently

$$\frac{\mathrm{d}}{\mathrm{d}t}\left(\frac{\partial T}{\partial \dot{q}_i}\right) - \frac{\partial T}{\partial q_i} + \frac{\partial U}{\partial q_i} = W_i \tag{B.4}$$

where it has been imposed that $\frac{\partial U}{\partial \dot{q}_i} = 0$.

$$\frac{\mathrm{d}}{\mathrm{d}t}\left(\boxed{\frac{\partial T}{\partial \dot{q}_i}}\right) - \frac{\partial T}{\partial q_i} + \frac{\partial U}{\partial q_i} = W_i$$

$$\frac{\partial T}{\partial \dot{q}_i} = \frac{1}{2}\sum_{k=1}^{N} M_{kj}\dot{q}_k + \frac{1}{2}\sum_{j=1}^{N} M_{kj}\dot{q}_j. \tag{B.5}$$

Since the inertia matrix $\mathbf{M}$ is symmetric, the previous equation simplifies in

$$\frac{\partial T}{\partial \dot{q}_i} = \sum_{j=1}^{N} M_{ij}\dot{q}_j. \tag{B.6}$$

$$\boxed{\frac{\mathrm{d}}{\mathrm{d}t}\left(\frac{\partial T}{\partial \dot{q}_i}\right)} - \frac{\partial T}{\partial q_i} + \frac{\partial U}{\partial q_i} = W_i$$

$$\frac{\mathrm{d}}{\mathrm{d}t}\left(\frac{\partial T}{\partial \dot{q}_i}\right) = \frac{\mathrm{d}}{\mathrm{d}t}\left(\sum_{j=1}^{N} M_{ij}\dot{q}_j\right) = \sum_{j=1}^{N} M_{ij}\ddot{q}_j + \sum_{j=1}^{N} \frac{\partial M_{ij}}{\partial t}\dot{q}_j = \sum_{j=1}^{N} M_{ij}\ddot{q}_j + \sum_{j=1}^{N}\sum_{k=1}^{N} \frac{\partial M_{ij}}{\partial q_k}\dot{q}_j\dot{q}_k \qquad \text{(B.7)}$$

$$\frac{\mathrm{d}}{\mathrm{d}t}\left(\frac{\partial T}{\partial \dot{q}_i}\right) - \boxed{\frac{\partial T}{\partial q_i}} + \frac{\partial U}{\partial q_i} = W_i$$

$$\frac{\partial T}{\partial q_i} = \frac{1}{2}\sum_{k=1}^{N}\sum_{j=1}^{N} \frac{\partial M_{kj}}{\partial q_i}\dot{q}_k\dot{q}_j \qquad \text{(B.8)}$$

$$\frac{\mathrm{d}}{\mathrm{d}t}\left(\frac{\partial T}{\partial \dot{q}_i}\right) - \frac{\partial T}{\partial q_i} + \boxed{\frac{\partial U}{\partial q_i}} = W_i$$

$$\frac{\partial U}{\partial q_i} = -mg\boldsymbol{r}(\boldsymbol{\vartheta}) = \boldsymbol{g}(\vartheta) \qquad \text{(B.9)}$$

where $\boldsymbol{r}(\boldsymbol{\vartheta})$ relates the position of the center of mass on the chosen inertial frame with the altitude on the inertial world frame.

Putting all together

$$\mathbf{M}(\boldsymbol{q})\ddot{\boldsymbol{q}} + \mathbf{C}(\boldsymbol{q},\dot{\boldsymbol{q}})\,\dot{\boldsymbol{q}} + \boldsymbol{g}(\vartheta) = \boldsymbol{W} \qquad \text{(B.10)}$$

where

$$\mathbf{C}(\boldsymbol{q},\dot{\boldsymbol{q}})\,\dot{\boldsymbol{q}} = \sum_{j=1}^{N} \frac{\partial M_{ij}}{\partial t}\dot{q}_j - \frac{1}{2}\sum_{k=1}^{N}\sum_{j=1}^{N} \frac{\partial M_{kj}}{\partial q_i}\dot{q}_k\dot{q}_j \qquad \text{(B.11)}$$

Appendix C

Proper choice of C for Legendre representation

This section intends to show that $\mathbf{C}\left(\boldsymbol{q}, \dot{\boldsymbol{q}}\right)$ in the product $\mathbf{C}\left(\boldsymbol{q}, \dot{\boldsymbol{q}}\right)\dot{\boldsymbol{q}}$ can be chosen in such a way that $\dot{\mathbf{M}} = \mathbf{C}^{\mathsf{T}} + \mathbf{C}$.

$$\mathbf{C}\left(\boldsymbol{q}, \dot{\boldsymbol{q}}\right)\dot{\boldsymbol{q}} = \sum_{j=1}^{N} \frac{\partial M_{ij}}{\partial t}\dot{q}_j - \frac{1}{2}\sum_{k=1}^{N}\sum_{j=1}^{N} \frac{\partial M_{kj}}{\partial q_i}\dot{q}_k\dot{q}_j \tag{C.1}$$

The term $\frac{\partial M_{ij}}{\partial t}$ can be rewritten as

$$\frac{\partial M_{ij}}{\partial t} = \sum_{k=1}^{N} \frac{\partial M_{ij}}{\partial q_k}\dot{q}_k \tag{C.2}$$

or equivalently

$$\frac{\partial M_{ij}}{\partial t} = \frac{1}{2}\frac{\partial M_{ij}}{\partial t} + \frac{1}{2}\sum_{k=1}^{N} \frac{\partial M_{ij}}{\partial q_k}\dot{q}_k \tag{C.3}$$

This leads to

$$\begin{aligned}\mathbf{C}\left(\boldsymbol{q}, \dot{\boldsymbol{q}}\right)\dot{\boldsymbol{q}} = {} & \sum_{j=1}^{N}\sum_{k=1}^{N} \frac{\partial M_{ij}}{\partial q_k}\dot{q}_k\dot{q}_j - \frac{1}{2}\sum_{k=1}^{N}\sum_{j=1}^{N} \frac{\partial M_{kj}}{\partial q_i}\dot{q}_k\dot{q}_j = \\ & \frac{1}{2}\sum_{j=1}^{N} \frac{\partial M_{ij}}{\partial t}\dot{q}_j + \frac{1}{2}\sum_{j=1}^{N}\sum_{k=1}^{N}\left(\frac{\partial M_{ij}}{\partial q_k} - \frac{\partial M_{kj}}{\partial q_i}\right)\dot{q}_j\dot{q}_k\end{aligned} \tag{C.4}$$

Since the index j and k inside the summation can be interchanged without affecting the operation

$$\mathbf{C}\left(\boldsymbol{q}, \dot{\boldsymbol{q}}\right)\dot{\boldsymbol{q}} = \frac{1}{2}\sum_{j=1}^{N} \frac{\partial M_{ij}}{\partial t}\dot{q}_j + \frac{1}{2}\sum_{j=1}^{N}\sum_{k=1}^{N}\left(\frac{\partial M_{ik}}{\partial q_j} - \frac{\partial M_{kj}}{\partial q_i}\right)\dot{q}_j\dot{q}_k, \tag{C.5}$$

and thus $\mathbf{C}(\boldsymbol{q}, \dot{\boldsymbol{q}})$ can be selected as

$$\mathbf{C}\left(\boldsymbol{q}, \dot{\boldsymbol{q}}\right) = \frac{1}{2}\frac{\partial M_{ij}}{\partial t} + \frac{1}{2}\sum_{k=1}^{N}\left(\frac{\partial M_{ik}}{\partial q_j} - \frac{\partial M_{kj}}{\partial q_i}\right)\dot{q}_k, \tag{C.6}$$

or equivalently

$$\mathbf{C} = \frac{1}{2}\dot{\mathbf{M}} + \frac{1}{2}\mathbf{S} \tag{C.7}$$

Since the generalised inertia matrix $\mathbf{M}$ is symmetric, the matrix

$$\mathbf{S} = \sum_{k=1}^{N}\left(\frac{\partial M_{ik}}{\partial q_j} - \frac{\partial M_{kj}}{\partial q_i}\right)\dot{q}_k \tag{C.8}$$

is skew symmetric, that is, for the $i = j$ $S_{i}j = 0$ and for $i \neq j$ $S_{ij} = -S_{ji}$.

As a consequence

$$\mathbf{C}^{\top} + \mathbf{C} = \frac{1}{2}\dot{\mathbf{M}}^{\top} + \frac{1}{2}\dot{\mathbf{M}} + \frac{1}{2}\mathbf{S}^{\top} + \frac{1}{2}\mathbf{S} = \dot{\mathbf{M}} \tag{C.9}$$

Appendix D

GPS geoidal measurements to local reference frame

The GPS sensor demodulates satellite signals to provide measurements of the receiver's latitude, longitude and altitude. This physical quantities are referred to a reference frame named WGS84, which defines an orthogonal reference frame with origin at the Earth center of mass (considering oceans and atmosphere), whose $\boldsymbol{z}$ vector points to the direction of the IERS reference pole [67] and defines the direction of rotation of the mean ellipsoid, the $\boldsymbol{x}$ vector is contained in plane perpendicular to $\boldsymbol{z}$ pointing to the IERS reference meridian and $\boldsymbol{y}$ can be obtained by the cross product of $\boldsymbol{z} \times \boldsymbol{x}$ [27]. Once the frame is defined, a model for the earth ellipsoid can be easily formulated. The WGS84 geoid model is a revolution ellipsoid about the $\boldsymbol{z}$ axis with semi-major axis length

$$a = 6378137.0 \, \text{m} \tag{D.1}$$

and flattening

$$f = \frac{1}{298.257223563} \tag{D.2}$$

with additional parameters defining the earth angular velocity, and gravitational constants and coefficients. The value of the model parameters is constantly checked and updated if needed. For the case of the semi-major axis length a, it has been determined through recent measurements that it may be inaccurate for a few decimeters. The low impact of these decimeters in most applications have motivated to leave the original value for this parameter unchanged.

Given the geoid parameters in Eq. (D.1) and Eq. (D.2) and knowing the latitude (φ), longitude (λ) and altitude (h) contained in the vector $\boldsymbol{\Phi} = (\varphi, \lambda, h)^{\top}$ of a point, its cartesian position in the WGS84 frame can be recovered by the non-linear transformation

$$\begin{pmatrix} x \\ y \\ z \end{pmatrix} = \boldsymbol{f}_{WGS84}(\boldsymbol{\Phi}) = \begin{pmatrix} \left(\frac{a}{\sqrt{1-e^2 \sin^2(\varphi)}} + h \right) \cos(\varphi) \cos(\lambda) \\ \left(\frac{a}{\sqrt{1-e^2 \sin^2(\varphi)}} + h \right) \cos(\varphi) \sin(\lambda) \\ \left(\frac{a(1-e^2)}{\sqrt{1-e^2 \sin^2(\varphi)}} + h \right) \sin(\varphi) \end{pmatrix} \tag{D.3}$$

where e^2 is known as the first eccentricity squared and is related with the flattening as

$$e^2 = (2f - f^2) = 6.69437999014 \cdot 10^{-3}$$

Let $\mathbf{\Phi}_0 = (\varphi_0, \lambda_0, h_0)^\top$ represent the origin of a NED reference frame. Points in the WGS84 reference frame can be expressed in the NED frame by accounting for the relative orientation between frames and the distance to its origins Eq. (D.3). The orientation of the NED frame with respect to the WGS84 can be achieved after a rotation of λ_0 about the WGS84 $\boldsymbol{z}$ direction followed by a rotation of $-\left(\varphi_0 + \frac{\pi}{2}\right)$ about the $\boldsymbol{y}$ resultant axis. This leads to the next rotation matrix

$$^{NED}\mathbf{L}_{WGS84} = \begin{pmatrix} -\cos(\lambda_0)\sin(\varphi_0) & -\sin(\lambda_0)\sin(\varphi_0) & \cos(\varphi_0) \\ -\sin(\lambda_0) & \cos(\lambda_0) & 0 \\ -\cos(\lambda_0)\cos(\varphi_0) & -\sin(\lambda_0)\cos(\varphi_0) & -\sin(\varphi_0) \end{pmatrix} \tag{D.4}$$

By using this rotation matrix, the center of the WGS84 reference frame can be expressed in the NED frame as

$$^{NED}\boldsymbol{o}_{WGS84} = -\,^{NED}\mathbf{L}_{WGS84}\boldsymbol{f}_{WGS84}(\Phi_0)$$

With the origin and orientation between WGS84 and NED frames already defined, any point defined b y$\mathbf{\Phi}$ can be defined in the NED frame by

$$^{NED}\boldsymbol{\xi}(\mathbf{\Phi}) = \,^{NED}\mathbf{L}_{WGS84}\boldsymbol{f}_{WGS84}(\mathbf{\Phi}) + \,^{NED}\boldsymbol{o}_{WGS84} = \,^{NED}\mathbf{L}_{WGS84}\left(\boldsymbol{f}_{WGS84}(\mathbf{\Phi}) - \boldsymbol{f}_{WGS84}(\mathbf{\Phi}_0)\right)$$
$$\tag{D.5}$$

This transformation can be adapted to any other local reference frame such as ENU or NWU by simply changing the transformation matrix to reflect the different attitudes, e.g,

$$^{ENU}\mathbf{L}_{WGS84} = \begin{pmatrix} -\sin(\lambda_0) & \cos(\lambda_0) & 0 \\ -\cos(\lambda_0)\sin(\varphi_0) & -\sin(\lambda_0)\sin(\varphi_0) & \cos(\varphi_0) \\ \cos(\lambda_0)\cos(\varphi_0) & \sin(\lambda_0)\cos(\varphi_0) & \sin(\varphi_0) \end{pmatrix}$$

or

$$^{NWU}\mathbf{L}_{WGS84} = \begin{pmatrix} -\cos(\lambda_0)\sin(\varphi_0) & -\sin(\lambda_0)\sin(\varphi_0) & \cos(\varphi_0) \\ \sin(\lambda_0) & -\cos(\lambda_0) & 0 \\ \cos(\lambda_0)\cos(\varphi_0) & \sin(\lambda_0)\cos(\varphi_0) & \sin(\varphi_0) \end{pmatrix}$$

The non-linear transformation in Eq. (D.5) is used to convert readings of the GPS sensor to a local frame defined by $\mathbf{\Phi}_0$. The linearization of the transformation around the point $\mathbf{\Phi}_0$ is independent of the latitude and is given by the diagonal jacobian matrix

$$\mathbf{J} = \begin{pmatrix} \dfrac{a(1-e^2)}{(1-e^2\sin^2(\varphi_0))^{\frac{3}{2}}} + h_0 & 0 & 0 \\ 0 & \cos(\varphi_0)\left(\dfrac{a}{\sqrt{1-e^2\sin^2(\varphi_0)}} + h_0\right) & 0 \\ 0 & 0 & -1 \end{pmatrix}$$

which for the approximate coordinates of a point in Terrassa, Spain, $\varphi_0 = 41.5610803\,\text{deg}$, $\lambda_0 = 2.0209686\,\text{deg}$, $h_0 = 3.46813m$, takes the value of

$$\mathbf{J} = \begin{pmatrix} 1.11071 \cdot 10^5 & 0 & 0 \\ 0 & 8.34222 \cdot 10^4 & 0 \\ 0 & 0 & -1 \end{pmatrix} \tag{D.6}$$

when considering latitude and altitude in degrees. The diagonal structure of the jacobian holds up to an approximate distance of $5\,\text{km}$ from the reference point, which means that in short distances latitude and longitude act as x and y positions up to a scale factor.

Appendix E

Ellipsoid projection over a subspace

This section is devoted to finding the projection of the ellipsoid defined by

$$\epsilon_{\mathbf{P}}(\boldsymbol{x}) \coloneqq \boldsymbol{x}^\top \mathbf{P} \boldsymbol{x} \le 1 \tag{E.1}$$

with $\boldsymbol{x} \in \mathbb{R}^n$ and $\mathbf{P} > 0$, over the subspace to which the vector $\boldsymbol{z}_1$ belongs, being $\boldsymbol{z}_1 \in \mathbb{R}^m$, $m < n$ a part of the vector $\boldsymbol{x}$, i.e., $\boldsymbol{z} = \mathbf{E}_1 \boldsymbol{x}$ with $\mathbf{E}_1 \in \mathbb{R}^{m \times n}$ representing a distribution matrix. This problem is equivalent to finding the ellipsoidal projection of $\epsilon_{\mathbf{P}}(\boldsymbol{x})$ over the subspace spanned by the rows of $\mathbf{E}_1$, denoted by $\langle \mathbf{E}_1 \rangle$.

Consider also $\mathbf{E}_2 \in \mathbb{R}^l$ with $l = m - n$ to be any orthogonal complement of $\mathbf{E}_1$, i.e., $\langle \mathbf{E}_2 \rangle$ is orthogonal to $\langle \mathbf{E}_1 \rangle^\perp$ and $\boldsymbol{z}_2 = \mathbf{E}_2 \boldsymbol{x}$. Then, the next relation can be written

$$\boldsymbol{z} = \mathbf{E} \boldsymbol{x} \tag{E.2}$$

with

$$\mathbf{E} = \begin{bmatrix} \mathbf{E}_1 \\ \mathbf{E}_2 \end{bmatrix} \tag{E.3}$$

and $\boldsymbol{z} = (\boldsymbol{z}_1^\top, \boldsymbol{z}_2^\top)^\top$

Moreover, since the matrix $\mathbf{E}$ represents an orthonormal basis of $\mathbb{R}^n$, its inverse $\mathbf{E}^{-1} = \mathbf{E}^\top$ and, as a consequence

$$\boldsymbol{x} = \mathbf{E}^\top \boldsymbol{z} = \begin{bmatrix} \mathbf{E}_1^\top & \mathbf{E}_2^\top \end{bmatrix} \boldsymbol{z} = \mathbf{E}_1^\top \boldsymbol{z}_1 + \mathbf{E}_2^\top \boldsymbol{z}_2 \tag{E.4}$$

The projection of the boundary of the ellipsoid in Eq. (E.1) represented by $\partial \epsilon_{\mathbf{P}}(\boldsymbol{x})$ over $\langle \mathbf{E}_1 \rangle$ will describe the boundary of the target ellipsoid $\epsilon_{\mathbf{P}_z}(\boldsymbol{z}_1)$ represented as $\partial \epsilon_{\mathbf{P}_z}(\boldsymbol{z}_1)$. Let the scalar

function $S = \boldsymbol{x}^\top \mathbf{P} \boldsymbol{x} - 1$, then,

$$\partial \epsilon_{\mathbf{P_z}}(\boldsymbol{z}_1) := (\boldsymbol{x} \mid S = 0, \nabla_{\boldsymbol{x}}(S) \in \langle \mathbf{E}_1 \rangle)$$

or, equivalently

$$\partial \epsilon_{\mathbf{P_z}}(\boldsymbol{z}_1) := (\boldsymbol{x} \mid S = 0, \mathbf{E}_2 \nabla_{\boldsymbol{x}}(S) = \mathbf{0}) \tag{E.5}$$

The second condition on the right hand side of Eq. (E.5) implies that

$$\mathbf{E}_2 \mathbf{P} \boldsymbol{x} = 0 \tag{E.6}$$

By substituting Eq. (E.4) into the previous relation, a mapping between $\boldsymbol{z}_1$ and $\boldsymbol{z}_2$ can be found for points on the boundary as

$$\boldsymbol{z}_2 = -\left(\mathbf{E}_2 \mathbf{P} \mathbf{E}_2^\top\right)^{-1} \mathbf{E}_2 \mathbf{P} \mathbf{E}_1^\top \boldsymbol{z}_1$$

The previous result, along with Eq. (E.4), can be substituted in $\boldsymbol{x}^\top \mathbf{P} \boldsymbol{x} = 1$, leading to

$$\partial \epsilon_{\mathbf{P_z}}(\boldsymbol{z}_1) := \left(\boldsymbol{z}_1 \mid \boldsymbol{z}_1^\top \mathbf{P}_z \boldsymbol{z}_1 = 1\right)$$

with

$$\mathbf{P}_z = \mathbf{E}_1 \mathbf{P} \mathbf{E}_1^\top - \mathbf{E}_1 \mathbf{P} \mathbf{E}_2^\top \left(\mathbf{E}_2 \mathbf{P} \mathbf{E}_2^\top\right)^{-1} \mathbf{E}_2 \mathbf{P} \mathbf{E}_1^\top$$

Since $\epsilon_{\mathbf{P_z}}(\boldsymbol{z}_1)$ must contain the origin just as $\epsilon_{\mathbf{P}}(\boldsymbol{x})$ did, $\epsilon_{\mathbf{P_z}}(\boldsymbol{z}_1)$ will be defined by

$$\epsilon_{\mathbf{P_z}}(\boldsymbol{z}_1) := \left(\boldsymbol{z}_1 \mid \boldsymbol{z}_1^\top \mathbf{P}_z \boldsymbol{z}_1 \le 1\right)$$

References

[1] ROS asctec_mav_framework. https://github.com/ethz-asl/asctec_mav_framework, . Accessed: 2018-08-26.

[2] ETHZ asctec_hl_firmware. https://github.com/ethz-asl/asctec_mav_framework/tree/master/asctec_hl_interface, . Accessed: 2018-08-26.

[3] Masoud Abbaszadeh and Horacio J. Marquez. LMI optimization approach to robust H_∞ observer design and static output feedback stabilization for discrete-time nonlinear uncertain systems. *International Journal of Robust and Nonlinear Control*, 19(3):313–340, 2009. doi: 10.1002/rnc.1310.

[4] Abdulgany Reda Abdulghany. Generalization of parallel axis theorem for rotational inertia. *American Journal of Physics*, 85(10):791–795, 2017. doi: 10.1119/1.4994835.

[5] Angelo Alessandri. Observer design for nonlinear systems by using input-to-state stability. In *43rd Conference on Decision and control (CDC)*, volume 4, pages 3892–3897. IEEE, 2004. doi: 10.1109/ACC.2013.6579850.

[6] Angelo Alessandri. Design of time-varying state observers for nonlinear systems by using input-to-state stability. In *American Control Conference (ACC)*, pages 280–285. IEEE, 2013. doi: 10.1109/ACC.2013.6579850.

[7] Angelo Alessandri, Marco Baglietto, and Giorgio Battistelli. On estimation error bounds for receding-horizon filters using quadratic boundedness. *IEEE Transactions on Automatic Control*, 49(8):1350–1355, 2004. doi: 10.1109/TAC.2004.832652.

[8] Angelo Alessandri, Marco Baglietto, and Giorgio Battistelli. Design of state estimators for uncertain linear systems using quadratic boundedness. *Automatica*, 42(3):497–502, 2006. doi: 10.1016/j.automatica.2005.10.013.

[9] Ascending Technologies. AscTec Autopilot diagram. http://wiki.asctec.de/display/AR/AscTec+AutoPilot. Accessed: 2018-10-13.

[10] Federico Augugliaro, Sergei Lupashin, Michael Hamer, Cason Male, Markus Hehn, Mark W. Mueller, Jean Sebastian Willman, Fabio Gramazio, Matthias Kohler, and Raffaello D'Andrea. The Flight Assembled Architecture Installation: Cooperative Contruction with Flying Machines. *Control Systems Magazine*, (August), 2014. doi: 10.1109/MCS.2014.2320359.

[11] Moses Bangura and Robert Mahony. Real-time model predictive control for quadrotors. In *Preprints of the 19th World Congress The International Federation of Automatic Control, Cape Town, South Africa*, Agust 2014. doi: 10.3182/20140824-6-ZA-1003.00203.

[12] Abdelaziz Benallegue, Abdellah Mokhtari, and Leonid Fridman. High-order sliding-mode observer for a quadrotor uav. *International Journal of Robust and Nonlinear Control*, 18 (4-5):427–440, 2008. ISSN 1099-1239. doi: 10.1002/rnc.1225.

[13] Gildas Besançon, editor. *Nonlinear Observers and Applications*, volume 363. Springer, 2007. ISBN 354073502X. doi: 10.1007/978-3-540-73503-8_3.

[14] Samir Bouabdallah, Pierpaolo Murrieri, and Roland Siegwart. Design and control of an indoor micro quadrotor. In *International Conference on Robotics and Automation ICRA*, volume 5, pages 4393–4398. IEEE, 2004. doi: 10.1109/ROBOT.2004.1302409.

[15] John B. Brandt, Robert W. Deters, Gavin K. Ananda, and Michael S. Selig. UIUC Propeller Database, University of Illinois at Urbana-Champaign. `http://m-selig.ae.illinois.edu/props/propDB.html`. Accessed: 2018-08-22.

[16] Mark L. Brockman and Martin Corless. Quadratic boundedness of nonlinear dynamical systems. In *34th Conference on Decision and Control (CDC)*, volume 1, pages 504–509. IEEE, 1995.

[17] Mark L. Brockman and Martin Corless. Quadratic boundedness of nominally linear systems. *International Journal of Control*, 71(6):1105–1117, 1998.

[18] Mariusz Buciakowski, Marcin Witczak, Marcin Mrugalski, and Didier Theilliol. A quadratic boundedness approach to robust DC motor fault estimation. *Control Engineering Practice*, 66:181–194, 2017. doi: 10.1016/j.conengprac.2017.06.014.

[19] Mariusz Buciakowski, Marcin Witczak, Puig Vicenç, Damiano Rotondo, Fatiha Nejjari, and Józef Korbicz. A bounded-error approach to simultaneous state and actuator fault estimation for a class of nonlinear systems. *Journal of Process Control*, 52:14–25, 2017. doi: 10.1016/j.jprocont.2017.01.002.

[20] Chi-Tsong Chen. *Linear System Theory and Design*. Oxford University Press, Inc., 3rd edition, 1998. ISBN 0195117778.

[21] Wen-Hua Chen. Disturbance observer based control for nonlinear systems. *IEEE/ASME Transactions on Mechatronics*, 9(4):706–710, 2004. doi: 10.1109/TMECH.2004.839034.

[22] Wen-Hua Chen, Donald J. Ballance, Peter J. Gawthrop, and John O'Reilly. A nonlinear disturbance observer for robotic manipulators. *Transactions on Industrial Electronics*, 47 (4):932–938, 2000. doi: 10.1109/41.857974.

[23] Wen-Hua Chen, Jun Yang, Lei Guo, and Shihua Li. Disturbance-observer-based control and related methods - an overview. *IEEE Transactions on Industrial Electronics*, 63(2): 1083–1095, 2016. doi: 10.1109/TIE.2015.2478397.

[24] Ali Chibani, Mohammed Chadli, Peng Shi, and Naceur Benhadj Braiek. Fuzzy fault detection filter design for T-S fuzzy systems in the finite-frequency domain. *IEEE Transactions on Fuzzy Systems*, 25(5):1051–1061, 2017. doi: 10.1109/TFUZZ.2016.2593921.

[25] John L. Crassidis. Sigma-point kalman filtering for integrated gps and inertial navigation. *IEEE Transactions on Aerospace and Electronic Systems*, 42(2):750–756, 2006. doi: 10. 1109/TAES.2006.1642588.

[26] John L. Crassidis, F. Landis Markley, and Yang Cheng. Survey of nonlinear attitude estimation methods. *Journal of guidance, control, and dynamics*, 30(1):12–28, 2007. doi: 10.2514/1.22452.

[27] USA Departament of Defense. World Geodetic System 1984. Its Definition and Relationships with Local Geodetic Systems. Technical report, National Geospatial Intelligence Agency (NGA), July 2014. Version 1.0.0.

[28] Baocang Ding. Quadratic boundedness via dynamic output feedback for constrained nonlinear systems in Takagi–Sugeno's form. *Automatica*, 45(9):2093–2098, 2009. doi: 10.1016/j.automatica.2009.05.017.

[29] Baocang Ding. New formulation of dynamic output feedback robust model predictive control with guaranteed quadratic boundedness. *Asian Journal of Control*, 15(1):302–309, 2013. doi: 10.1002/asjc.496.

[30] Baocang Ding and Hongguang Pan. Output feedback robust MPC for LPV system with polytopic model parametric uncertainty and bounded disturbance. *International Journal of Control*, 89(8):1554–1571, 2016. doi: 10.1080/00207179.2016.1138144.

[31] Ashwini A. Godbole, Jaywant P. Kolhe, and Sanjay E. Talole. Performance analysis of generalized extended state observer in tackling sinusoidal disturbances. *Transactions on Control Systems Technology*, 21(6):2212–2223, 2013. doi: 10.1109/TCST.2012.2231512.

[32] Ernest .W. Griffith and K.S.P. Kumar. On the observability of nonlinear systems: I. *Journal of Mathematical Analysis and Applications*, 35(1):135 – 147, 1971. ISSN 0022-247X. doi: 10.1016/0022-247X(71)90241-1.

[33] Ruijie He, Sam Prentice, and Nicholas Roy. Planning in information space for a quadrotor helicopter in a GPS-denied environment. In *International Conference on Robotics and Automation (ICRA)*, pages 1814–1820. IEEE, May 2008. doi: 10.1109/ROBOT.2008. 4543471.

[34] Robert Hermann and Arthur Krener. Nonlinear controllability and observability. *IEEE Transactions on automatic control*, 22(5):728–740, 1977. doi: 10.1109/TAC.1977.1101601.

[35] Frank Hoffmann, Niklas Goddemeier, and Torsten Bertram. Attitude estimation and control of a quadrocopter. In *International Conference on Intelligent Robots and Systems (ICRA)*, pages 1072–1077. IEEE, Oct 2010.

[36] Sinpyo Hong, Man Hyung Lee, Ho-Hwan Chun, Sun-Hong Kwon, and Jason L. Speyer. Observability of error States in GPS/INS integration. *IEEE Transactions on Vehicular Technology*, 54(2):731–743, March 2005. ISSN 0018-9545. doi: 10.1109/TVT.2004.841540.

[37] Charles R. Horn, Roger A.and Johnson. *Matrix analysis*. Cambridge university press, 1990. ISBN 978-0-521-83940-2. doi: 10.1017/9781139020411.

[38] Alberto Isidori. *Nonlinear Control Systems*. Springer-Verlag London, third edition, 1995. ISBN 978-1-4471-3909-6. doi: 10.1007/978-1-84628-615-5.

[39] Antonio E. Jimenez-Cano, J. Martin, Guillermo Heredia, Anibal Ollero, and R. Cano. Control of an aerial robot with multi-link arm for assembly tasks. In *International Conference on Robotics and Automation (ICRA)*, pages 4916–4921. IEEE, May 2013. doi: 10.1109/ICRA.2013.6631279.

[40] C. Johnson. Accomodation of external disturbances in linear regulator and servomechanism problems. *IEEE Transactions on Automatic Control*, 16(6):635–644, 1971. doi: 10.1109/TAC.1971.1099830.

[41] Jonathan Kelly and Gaurav S. Sukhatme. Visual-inertial sensor fusion: Localization, mapping and sensor-to-sensor self-calibration. *The International Journal of Robotics Research*, 30(1):56–79, 2011. doi: 10.1177/0278364910382802.

[42] Kyung-Soo Kim, Keun-Ho Rew, and Soohyun Kim. Disturbance observer for estimating higher order disturbances in time series expansion. *IEEE Transactions on Automatic Control*, 55(8):1905–1911, 2010. doi: 10.1109/TAC.2010.2049522.

[43] Konstantin Kondak, Markus Bernard, Nicolas Meyer, and Günter Hommel. Autonomously Flying VTOL-Robots: Modelling and Control. In *International Conference on Robotics and Automation (ICRA)*, number April, pages 10–14. IEEE, 2007. ISBN 1424406021. doi: 10.1109/ROBOT.2007.363074.

[44] Shauying R. Kou, David L. Elliott, and Tzyh Jong Tarn. Observability of nonlinear systems. *Information and Control*, 22(1):89 – 99, 1973. ISSN 0019-9958. doi: 10.1016/S0019-9958(73)90508-1.

[45] SangJoo Kwon and Wan K. Chung. A discrete-time design and analysis of perturbation observer for motion control applications. *Transactions on Control Systems Technology*, 11 (3):399–407, 2003. doi: 10.1109/TCST.2003.810398.

[46] Ern J. Lefferts, F. Landis Markley, and Malcolm D. Shuster. Kalman filtering for spacecraft attitude estimation. *Journal of Guidance, Control, and Dynamics*, 5(5):417–429, 1982. doi: 10.2514/3.56190.

[47] Shihua Li, Jun Yang, Wen-Hua Chen, and Xisong Chen. Generalized extended state observer based control for systems with mismatched uncertainties. *IEEE Transactions on Industrial Electronics*, 59(12):4792–4802, 2012. doi: 10.1109/TIE.2011.2182011.

[48] Quentin Lindsey, Daniel Mellinger, and Vijay Kumar. Construction with quadrotor teams. *Autonomous Robots*, 33(3):323–336, June 2012. ISSN 0929-5593. doi: 10.1007/s10514-012-9305-0.

[49] Giuseppe Loianno, Michael Watterson, and Vijay Kumar. Visual inertial odometry for quadrotors on se(3). In *International Conference on Robotics and Automation (ICRA)*, pages 1544–1551. IEEE, May 2016. doi: 10.1109/ICRA.2016.7487292.

[50] Sebastian O.H. Madgwick, Andrew J. L. Harrison, and Ravi Vaidyanathan. Estimation of IMU and MARG orientation using a gradient descent algorithm. In *International Conference on Rehabilitation Robotics*, pages 1–7. IEEE, June 2011. doi: 10.1109/ICORR.2011.5975346.

[51] Venkatesh Madyastha, Vishal Ravindra, Srinath Mallikarjunan, and Anup Goyal. Extended Kalman filter vs. error state Kalman filter for aircraft attitude estimation. In *Guidance, Navigation, and Control Conference*, pages 1–23. AIAA, August 2011. doi: 10.2514/6.2011-6615.

[52] Robert Mahony, Tarek Hamel, and Jean-Michel Pflimlin. Nonlinear complementary filters on the special orthogonal group. *Transactions on automatic control*, 53(5):1203–1218, 2008. doi: 10.1109/TAC.2008.923738.

[53] Robert Mahony, Vijay Kumar, and Peter Corke. Multirotor aerial vehicles: Modeling, estimation, and control of quadrotor. *Robotics & amp amp Automation Magazine*, (19): 20–32, 2012. doi: 10.1109/MRA.2012.2206474.

[54] Lorenzo Marconi and Roberto Naldi. Control of aerial robots: Hybrid force and position feedback for a ducted fan. *IEEE Control Systems Magazine*, 32(4):43–65, Aug 2012. doi: 10.1109/MCS.2012.2194841.

[55] Lorenzo Marconi, Roberto Naldi, and Luca Gentili. Modelling and control of a flying robot interacting with the environment. *Automatica*, 47(12):2571–2583, December 2011. ISSN 00051098. doi: 10.1016/j.automatica.2011.09.020.

[56] F. Landis Markley. Attitude error representations for Kalman filtering. *Journal of guidance, control, and dynamics*, 26(2):311–317, 2003. doi: 10.2514/2.5048.

[57] F. Landis Markley. Unit Quaternion from Rotation Matrix. *Journal of Guidance, Control, and Dynamics*, 31(2):440–442, 2008. ISSN 0731-5090. doi: 10.2514/1.31730.

[58] Hehn Markus and Raffaello D'Andrea. Quadrocopter Trajectory Generation and Control. In *IFAC World Congress*, pages 1485–1491, Milano, Italy, August 2011. doi: 10.3182/20110828-6-IT-1002.03178.

[59] Agostino Martinelli. State estimation based on the concept of continuous symmetry and observability analysis: The case of calibration. *IEEE Transactions on Robotics*, 27(2): 239–255, 2011. doi: 10.1109/TRO.2011.2109210.

[60] Matthew McCrink and James W. Gregory. Blade element momentum modeling of low-re small uas electric propulsion systems. In *33rd Applied Aerodynamics Conference*, volume 3296. AIAA, 2015. doi: 10.2514/6.2015-3296.

[61] Daniel Mellinger and Vijay Kumar. Minimum snap trajectory generation and control for quadrotors. *International Conference on Robotics and Automation (ICRA)*, pages 2520–2525, May 2011. doi: 10.1109/ICRA.2011.5980409.

[62] Daniel Mellinger, Quentin Lindsey, Michael Shomin, and Vijay Kumar. Design, modeling, estimation and control for aerial grasping and manipulation. In *International Conference on Intelligent Robots and Systems (IROS)*, pages 2668–2673. IEEE, September 2011. ISBN 978-1-61284-456-5. doi: 10.1109/IROS.2011.6094871.

[63] Daniel Mellinger, Alex Kushleyev, and Vijay Kumar. Mixed-integer quadratic program trajectory generation for heterogeneous quadrotor teams. *International Conference on Robotics and Automation (ICRA)*, pages 477–483, May 2012. doi: 10.1109/ICRA.2012. 6225009.

[64] Daniel Mellinger, Nathan Michael, and Vijay Kumar. Trajectory generation and control for precise aggressive maneuvers with quadrotors. *The International Journal of Robotics Research*, 31(5):664–674, January 2012. doi: 10.1177/0278364911434236.

[65] Kaisa Miettinen. Nonlinear multiobjective optimization, 1998.

[66] Cleve Moler and Charles Van Loan. Nineteen dubious ways to compute the exponential of a matrix, twenty-five years later. *SIAM review*, 45(1):3–49, 2003. doi: 10.1137/S00361445024180.

[67] Gérard Petit and Brian Luzum. IERS conventions (2010). IERS technical note; 36, Bundesamts für Kartographie und Geodäsie, 2010. ISBN 3-89888-989-6.

[68] X. Ping. Output feedback robust MPC based on off-line observer for LPV systems via quadratic boundedness. *Asian Journal of Control*, 19(4):1641–1653, 2017. doi: 10.1002/ asjc.1469.

[69] X. Ping, P. Wang, and Z. Li. Quadratic boundedness of LPV systems via saturated dynamic output feedback controller. *Optimal Control Applications and Methods*, 38(6):1239–1248, 2017. doi: 10.1002/oca.2328.

[70] Paul Pounds, Robert Mahony, and Peter Corke. Modelling and control of a quad-rotor robot. *Proceedings Australasian Conference on Robotics and Automation 2006*, 2006.

[71] Paul Pounds, Daniel R. Bersak, and Aaron M. Dollar. Grasping from the air: Hovering capture and load stability. In *International Conference on Robotics and Automation (ICRA)*, pages 2491–2498. IEEE, May 2011. ISBN 978-1-61284-386-5. doi: 10.1109/ICRA.2011.5980314.

[72] Caitlin Powers, Daniel Mellinger, Aleksandr Kushleyev, Bruce Kothmann, and Vijay Kumar. Influence of aerodynamics and proximity effects in quadrotor flight. In *13th*

International Symposium on Experimental Robotics, ISER, pages 289–302, 2012. doi: 10.1007/978-3-319-00065-7_21.

[73] Morgan Quigley, Ken Conley, Brian Gerkey, Josh Faust, Tully Foote, Jeremy Leibs, Rob Wheeler, and Andrew Ng. ROS: an open-source Robot Operating System. In *ICRA workshop on open source software*, volume 3, page 5. Kobe, Japan, 2009.

[74] Robin Ritz, Mark W. Müller, Markus Hehn, and Raffaello D'Andrea. Cooperative quadrocopter ball throwing and catching. In *International Conference on Intelligent Robots and Systems (IROS)*, pages 4972–4978. IEEE, October 2012. doi: 10.1109/IROS.2012.6385963.

[75] Fabio Ruggiero, Jonathan Cacace, Hamid Sadeghian, and Vincenzo Lippiello. Impedance control of VToL UAVs with a momentum-based external generalized forces estimator. In *IEEE International Conference on Robotics and Automation (ICRA)*, pages 2093–2099, May 2014. doi: 10.1109/ICRA.2014.6907146.

[76] Fabio Ruggiero, Jonathan Cacace, Hamid Sadeghian, and Vincenzo Lippiello. Passivity-based control of VToL UAVs with a momentum-based estimator of external wrench and unmodeled dynamics. *Robotics and Autonomous Systems*, 72:139–151, 2015. doi: 10.1016/j.robot.2015.05.006.

[77] Angel Santamaria-Navarro, Joan Sola, and Juan Andrade-Cetto. High-frequency MAV state estimation using low-cost inertial and optical flow measurement units. In *International Conference on Intelligent Robots and Systems (IROS)*, pages 1864–1871. IEEE/RSJ, 2015. doi: 10.1109/IROS.2015.7353621.

[78] Stanley F. Schmidt. Application of state-space methods to navigation problems. In *Advances in control systems*, volume 3, pages 293–340. Elsevier, 1966. doi: 10.1016/B978-1-4831-6716-9.50011-4.

[79] Jin-Hua She, Mingxing Fang, Yasushiro Ohyama, Hiroshi Hashimoto, and Min Wu. Improving disturbance-rejection performance based on an equivalent-input-disturbance approach. *Transactions on Industrial Electronics*, 55(1):380–389, 2008. doi: 10.1109/TIE.2007.905976.

[80] Stanley W. Shepperd. Quaternion from Rotation Matrix. *Journal of guidance and control*, 1(3):223–224, 1978.

[81] Sara Spedicato, Giuseppe Notarstefano, Heinrich H Bülthoff, and Antonio Franchi. Aggressive Maneuver Regulation of a Quadrotor UAV. In *The 16th International Symposium on Robotics Research*, Singapore, 2013. doi: 10.1007/978-3-319-28872-7_6.

[82] John Stuelpnagel. On the parametrization of the three-dimensional rotation group. *SIAM review*, 6(4):422–430, 1964. doi: 10.1137/1006093.

[83] Jinya Su, Wen-Hua Chen, and Baibing Li. High order disturbance observer design for linear and nonlinear systems. In *International Conference on Information and Automation*, pages 1893–1898. IEEE, 2015. doi: 10.1109/ICInfA.2015.7279597.

[84] Bruno O.S. Teixeira, Jaganath Chandrasekar, Leonardo A.B. Tôrres, Luis A. Aguirre, and Dennis S. Bernstein. State estimation for equality-constrained linear systems. In *46th Conference on Decision and Control (CDC)*, pages 6220–6225. IEEE, 2007. doi: 10.1109/CDC.2007.4434800.

[85] Bart Theys, G. Dimitriadis, T. Andrianne, Patrick Hendrick, and Joris De Schutter. Wind tunnel testing of a VTOL MAV propeller in tilted operating mode. In *Unmanned Aircraft Systems (ICUAS), 2014 International Conference on*, pages 1064–1072, May 2014. doi: 10.1109/ICUAS.2014.6842358.

[86] Panagiotis Tsiotras and James Longuski. Comments on a new parameterization of the attitude kinematics. In *Astrodynamics Specialists Conference*, page 3627, 1996. doi: 10. 2514/6.1996-3627.

[87] D.A. Turner, I.J. Anderson, J.C. Mason, and M.G. Cox. An Algorithm for Fitting an Ellipsoid to Data. Technical report, School of Computing and Mathematics, University of Huddersfield, 1999.

[88] Roberto G. Valenti, Ivan Dryanovski, and Jizhong Xiao. Keeping a good attitude: A quaternion-based orientation filter for imus and margs. *Sensors*, 15(8):19302–19330, 2015. doi: 10.3390/s150819302.

[89] Charles Van Loan. Computing integrals involving the matrix exponential. *Transactions on Automatic Control*, 23(3):395–404, Jun 1978. ISSN 0018-9286. doi: 10.1109/TAC.1978. 1101743.

[90] Yuan Wang and Eduardo D. Sontag. On two definitions of observation spaces. *Systems and Control Letters*, 13:279–289, 1989. doi: 10.1016/0167-6911(89)90116-3.

[91] Zidong Wang, Biao Huang, and Heinz Unbehauen. Robust H_∞ observer design of linear state delayed systems with parametric uncertainty: the discrete-time case. *Automatica*, 35 (6):1161–1167, 1999. doi: 10.1016/S0005-1098(99)00008-4.

[92] Stephan Weiss and Roland Siegwart. Real-time metric state estimation for modular vision-inertial systems. In *International Conference on Robotics and Automation (ICRA)*, pages 4531–4537. IEEE, 2011. doi: 10.1109/ICRA.2011.5979982.

[93] Stephan M Weiss. *Vision based navigation for micro helicopters*. PhD thesis, ETH Zurich, 2012. doi: 10.3929/ethz-a-007344020.

[94] Marcin Witczak, Mariusz Buciakowski, and Christophe Aubrun. Predictive actuator fault-tolerant control under ellipsoidal bounding. *International Journal of Adaptive Control and Signal Processing*, 30(2):375–392, 2016. doi: 10.1002/acs.2567.

[95] Marcin Witczak, Damiano Rotondo, Vicenç Puig, Fatiha Nejjari, and Marcin Pazera. Fault estimation of wind turbines using combined adaptive and parameter estimation schemes. *International Journal of Adaptive Control and Signal Processing*, 32(4):549–567, 2017. doi: 10.1002/acs.2792.

[96] Drew Woodbury and John Junkins. On the consider kalman filter. In *Guidance, Navigation, and Control Conference*, page 7752. On the consider Kalman filter, 2010. doi: 10.2514/6. 2010-7752.

[97] Burak Yüksel, Cristian Secchi, Heinrich H. Bülthoff, and Antonio Franchi. A nonlinear force observer for quadrotors and application to physical interactive tasks. In *International Conference on Advanced Intelligent Mechatronics (AIM)*, pages 433–440. IEEE/ASME, 2014. doi: 10.1109/AIM.2014.6878116.

[98] Renato Zanetti and Christopher D'Souza. Recursive Implementations of the Schmidt-Kalman 'Consider' Filter. *The Journal of the Astronautical Sciences*, 60(3-4):672–685, 2013. doi: 10.1007/s40295-015-0068-7.

[99] Longge Zhang, Xiangjie Liu, and Xiaobing Kong. State estimators for uncertain linear systems with different disturbance/noise using quadratic boundedness. *Journal of Applied Mathematics*, 2012, 2012. doi: 10.1155/2012/101353.

[100] Tao Zou and Shaoyuan Li. Stabilization via extended nonquadratic boundedness for constrained nonlinear systems in Takagi–Sugeno's form. *Journal of the Franklin Institute*, 348 (10):2849–2862, 2011. doi: 10.1016/j.jfranklin.2011.09.007.